



Universitat Autònoma de Barcelona

ADVERTIMENT. L'accés als continguts d'aquesta tesi queda condicionat a l'acceptació de les condicions d'ús establertes per la següent llicència Creative Commons:  http://cat.creativecommons.org/?page_id=184

ADVERTENCIA. El acceso a los contenidos de esta tesis queda condicionado a la aceptación de las condiciones de uso establecidas por la siguiente licencia Creative Commons:  <http://es.creativecommons.org/blog/licencias/>

WARNING. The access to the contents of this doctoral thesis it is limited to the acceptance of the use conditions set by the following Creative Commons license:  <https://creativecommons.org/licenses/?lang=en>



On the upscaling of organic solar cells based on non-fullerene acceptors

Enrique Pascual San José

PhD Thesis

PhD in Materials Science

Supervisors: Dr. Mariano Campoy Quiles and Dr. Marco Stella

Tutor: Dr. José Antonio Ayllón Esteve

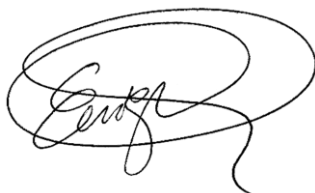
Department of Physics

Faculty of Science

June 2020



This thesis is submitted in partial fulfilment of the requirements for the degree of *Doctor of Philosophy* by the Universitat Autònoma de Barcelona

A handwritten signature in black ink, consisting of several overlapping loops and a trailing flourish, enclosed within a large, irregular oval shape.

Mr. Enrique Pascual San José

Checked and accepted

Dr. Mariano Campoy Quiles

Co-director

Dr. Marco Stella

Co-director

Dr. José Antonio Ayllón Esteve

Tutor

Bellaterra, 19th of June 2020

A mis padres y mis hermanos

*“I have not failed. I have just found
10.000 ways that won’t work”*

Thomas A. Edison

*“We cannot solve a crisis without treating it as a crisis. We need to
keep fossil fuels in the ground, and we need to focus on equity. And
if solutions within the system are so impossible to find, maybe we
should change the system itself.”*

Greta Thunberg

ABSTRACT

Over the last years, organic photovoltaic technology (OPV) has drawn the attention of both the scientific and industrial communities due to their increasing performances, currently over 18%. These high efficiencies have been achieved thanks to the chemical development of the small molecular acceptors, also known as non-fullerene acceptors (NFA). Besides the efficiency, NFA-based OPV offers colour and transparency tuneable properties, low embodied energy, and good long-term stability. These unique properties make OPV a suitable technology for their commercialisation as a part of *building-integrated photovoltaic* systems (BIPV) or for powering the so-called *Internet of Things* (IoT).

This thesis covers some of the critical issues that need to be addressed for OPV to become a truly competitive technology. Firstly, we studied theoretically the strategies for tuning the colour appearance of OPV films. With the aid of an optical model and a genetic algorithm, we predicted the characteristics that photoactive materials should have in order to exhibit a desired colour. The use of non-fullerene acceptors (NFA) for the photoactive blends turned out to be the most effective colour-tuning strategy. As a result, NFAs-based devices were intensively studied in this thesis. Moreover, as an intermediate step towards a large printing scale, the doctor blade technique was employed for most of this thesis work.

Due to their synthetic flexibility, there are many NFAs and their processing conditions that are worth studying. Two examples of combinatorial screening using high throughput techniques are given. First, 1D gradients are applied to devices based on NFAs and polythiophene (P3HT), one of the cheapest and most studied polymers. 1D gradients enabled the fabrication of more than 1000 blade-coated devices with controlled variations in thickness or post-annealing temperature at the photoactive layers. For the most efficient system, we studied and ranked the sensitivity of the different manufacturing parameters.

Second, we extended this to 2D gradients and explored both low bandgap polymers and NFAs. A simple method was developed based on controlled and simultaneous variations of the parameters of interest. With the aid of co-local optoelectronic characterisation techniques, 2D optimisation maps enable fast identification of the optimum thickness and blend composition values. Long term stability was also studied on selected devices, as a relevant factor for OPV upscaling, together with manufacturing fully roll-to-roll modules.

Transparency is another relevant characteristic feature that could enable OPV integration into the potential photoactive windows of the future. Semitransparent laser-patterned modules were fabricated with a NFA that contributes to extend the blend optical absorption up to the near-infrared region. With the aim of developing a sustainable manufacturing process, modules were manufactured following preferences of large-scale printing industry including non-halogenated solvents, air processing and low energy consumption. In summary, in this thesis we provide new insights into the upscaling of NFAs based OPV that pave the way towards an efficient transfer from record lab-devices to fully solution-processed modules.

RESUMEN

En los últimos años, la tecnología fotovoltaica orgánica (*OPV*, por sus siglas en inglés) ha despertado la atención de las comunidades científica e industrial debido a sus altas eficiencias de conversión en continuo aumento, superando actualmente el 18%. Éstas, en parte, se han logrado gracias al gran desarrollo de pequeñas moléculas aceptoras, también conocidos como aceptores no basados en fullereno (*NFA*, por sus siglas en inglés). Además de la eficiencia, la *OPV* basada en *NFAs* ofrece gran flexibilidad para modificar el color y presenta buena estabilidad a largo plazo. Estas propiedades hacen de la fotovoltaica orgánica una tecnología muy prometedora para su intensiva comercialización, bien integrada en edificios (*BIPV*, por sus siglas en inglés) o como fuente de alimentación para sensores en el llamado Internet de las Cosas (*IoT*, por sus siglas en inglés).

Esta tesis aborda algunas de las cuestiones críticas de la fotovoltaica orgánica que deben ser evaluadas para que ésta se convierta en una tecnología comercialmente atractiva. En primer lugar, estudiamos teóricamente las estrategias para controlar la estética de las capas finas absorbentes. Con la ayuda de un modelo óptico y un algoritmo genético, predecimos las características (composición y espesor) que las mezclas de materiales deben tener para que la capa muestre un color previamente elegido. El uso de capas basadas en *NFAs* resultó ser la estrategia más eficaz para modificar el color de la capa activa. Como resultado, los dispositivos basados en *NFAs* fueron estudiados en profundidad a lo largo de esta tesis. Además, como paso intermedio hacia el escalado industrial, la técnica de raqueta (*blade-coating* en inglés) se empleó en la mayoría de los casos para la fabricación de celdas solares.

Debido a la flexibilidad sintética de los *NFAs*, hay una gran variedad de nuevas moléculas que merece la pena estudiar. Se muestran dos ejemplos de cribado combinatorio utilizando técnicas de alto rendimiento. En primer lugar, se aplican gradientes 1D a dispositivos basados en *NFAs* y politiofeno (*P3HT*, por sus siglas en inglés), por ser uno de los polímeros más baratos y más estudiados. Los gradientes 1D

han permitido la fabricación de más de 1.000 dispositivos con variaciones controladas de espesor o temperatura post-recocido en las capas fotoactivas. Para el sistema más eficiente, estudiamos y clasificamos la sensibilidad a los parámetros de fabricación.

En segundo lugar, extendimos los gradientes 1D a 2D y exploramos los polímeros más eficientes con NFAs. Se desarrolló un método simple basado en variaciones controladas y simultáneas de los parámetros de interés. Con la ayuda de técnicas de caracterización optoelectrónicas y co-locales, dicho método permite una rápida identificación de los valores óptimos de espesor y composición de la mezcla a través de los mapas 2D de optimización. También se estudió la estabilidad a largo plazo del sistema más eficiente por ser un factor crítico para su escalado industrial. De igual forma, se fabricaron módulos con técnicas de impresión industrialmente relevantes como la impresión rotativa (*roll-to-roll*, en inglés).

La potencial semitransparencia del OPV se demostró fabricando módulos con un NFA que extiende su absorción óptica hasta la región del infrarrojo cercano. Con el fin de desarrollar un proceso de fabricación sostenible y escalable e industrialmente relevante, los módulos se fabricaron siguiendo las directrices de la industria de la impresión, incluyendo el uso de disolventes no halogenados, la fabricación en atmósfera normal y técnicas de bajo consumo energético. En resumen, en esta tesis proporcionamos nuevos conocimientos sobre el escalado de la tecnología fotovoltaica orgánica, basados en NFAs y que allanan el camino hacia una transferencia eficiente de los dispositivos de la escala laboratorio a una escala industrialmente relevante.

RESUM

En els últims anys, la tecnologia fotovoltaica orgànica (OPV, per les seves sigles en anglès) ha despertat l'atenció de tant la comunitat científica com la industrial, a causa de les seves altes eficiències de conversió energètica, que continuen creixent avui dia, superant actualment el 18%. Aquestes eficiències, en part, s'han aconseguit gràcies a el gran desenvolupament de les petites molècules acceptors, també conegudes com acceptors no basats en fullerè (NFA, per les seves sigles en anglès). A més de l'eficiència, la OPV basada en NFA ofereix gran flexibilitat per a modificar el color i l'estabilitat a llarg termini. Aquestes propietats úniques fan de la fotovoltaica orgànica una tecnologia molt prometedora per a la seva intensiva comercialització, ja sigui com a tecnologia integrada en edificis (BIPV, per les seves sigles en anglès) o com a font d'alimentació per a sensors en l'anomenat Internet de les Coses.

Aquesta tesi aborda algunes de les qüestions crítiques de la fotovoltaica orgànica que han de ser avaluades perquè aquesta es converteixi en una tecnologia comercialment atractiva. En primer lloc, hem estudiat teòricament les estratègies per controlar l'estètica de les capes fines actives, que absorbeixen la llum. Amb l'ajuda d'un model òptic i un algoritme genètic, hem predit les característiques (composició i gruix) que les barreges de materials han de tenir per a que la capa mostri un color prèviament seleccionat. L'ús de capes basades en NFA ha resultat ser l'estratègia més eficaç per a modificar el color de la capa activa. Com a resultat, els dispositius amb NFA han estat estudiats intensament al llarg d'aquesta tesi. A més, com a pas intermedi cap a l'escalat industrial, la tècnica de deposició assistida amb fulla (blade-coating en anglès) s'ha utilitzat en la majoria dels casos per a la fabricació de cel·les solars en aquesta tesi.

A causa de la flexibilitat sintètica dels NFA, hi ha una gran varietat de noves molècules que val la pena estudiar. Es mostren dos exemples de cribratge combinatori utilitzant tècniques d'alt rendiment. En primer lloc, s'apliquen gradients 1D a dispositius basats en NFA i politiofè (P3HT), per ser un dels polímers més barats i més estudiats. Els gradients 1D han permès la fabricació de més de 1.000 dispositius amb variacions controlades de

gruix o temperatura post-recuit en les capes fotoactives. Per al sistema més eficient, estudiem i classifiquem la sensibilitat als paràmetres de fabricació.

En segon lloc, hem estès els gradients 1D a 2D i hem explorat els polímers més eficients amb NFA. S'ha desenvolupat un mètode simple basat en variacions controlades i simultànies dels paràmetres d'interès. Amb l'ajuda de tècniques de caracterització optoelectròniques i co-locales, aquest mètode permet una ràpida identificació dels valors òptims de gruix i composició de la mescla a través de mapes 2D d'optimització. També s'ha estudiat l'estabilitat a llarg termini del sistema més eficient per ser un factor crític per l'escalat industrial. De la mateixa manera, s'han fabricat mòduls amb tècniques d'impressió industrialment rellevants com la impressió rotativa.

La potencial semitransparencia de la OPV s'ha demostrat fabricant mòduls amb un NFA que estén la seva absorció òptica fins a la regió de l'infraroig proper. Per tal de desenvolupar un procés de fabricació sostenible i escalable i industrialment rellevant, els mòduls s'han fabricat seguint les directrius de la indústria de la impressió, incloent l'ús de dissolvents no halogenats, la fabricació en atmosfera normal i tècniques de baix consum energètic. En resum, en aquesta tesi, proporcionem nous coneixements sobre l'escalat de la tecnologia fotovoltaica orgànica, basats en NFA i que aplanen el camí cap a una transferència eficient dels dispositius de l'escala del laboratori a una escala industrialment rellevant.

ACKNOWLEDGEMENTS

Me gustaría dedicar mis primeras palabras de agradecimiento a mis directores de tesis. Gracias Mariano por ser un guía y referente en el ámbito científico, pero aún más en el personal. Gracias por transmitirme tu pasión, confianza y ánimos durante estos cuatro años. Han sido inolvidables. Gracias por transformar a un ingeniero en científico y acogerme en la tripulación de los ‘Forematics’. Gracias Marco por darme la oportunidad de hacer escalado preindustrial y autonomía en el laboratorio. ¡Gracias a ti, la tesis tiene una orientación más industrial! Te agradezco tu paciencia, tesón y tiempo en la corrección de la tesis y por todo lo que me has enseñado dentro del laboratorio. Gracias a los dos por dedicar vuestro tiempo y esfuerzo por ayudarme a conseguir esta tesis.

En segundo lugar quiero agradecer a dos personas que no siendo directores han actuado como si lo hubieran sido. Eugenia Martínez por contagiarme tu perfección y pulcritud en el trabajo. Ignasi Burgués siempre estaré en deuda contigo por cómo me trataste en Southampton. Gracias por guiarme, trabajar codo con codo conmigo y por tu cercanía. De Merck no sólo me llevé la experiencia laboral sino también un gran aprendizaje humano. Gràcies de cor. El legado del ‘Capitán’ traspasa fronteras.

I would like to thank my *Forematic* mates (*Finders of needles in the organic haystack*) who have helped me throughout my thesis. Especially, Xabier for being a sport and scientific inspiration, Toni for your help at the beginning, Martí for being the ideal workmate. Without your endless inventions, life in the lab would have been much more challenging. Alex for your kindness and your unique sense of humour. Adrián for being more than an officemate, a true friend. The credits of the cover are all yours. Thanks! Rana for sharing hours struggling with R2R experiments and in the same way to the rest of Mariano’s group Osnat, Paula, Germán, Fatma, Laura, Iván, Bernhard, Valentina, Albert, Miquel, José and Jose. I want to extend my acknowledgements to the rest of the Nanopto group especially to the paddle mate Sebas, Luis, Agustín, Alejandro, Isabel, Cristiano, Pau, Mayte and Camilla. Similarly, I want to extend my thanks to the Eurecat staff for hosting me very nicely Marta, Laura, Pol, Laia, Xavi and Dani.

I want to express my gratitude to the whole OPV team at Merck-Southampton that you made me feel like one more from the very beginning. Especially, to my supervisors Ignasi, Golnaz and Graham for their guidance, fruitful discussions and help throughout my doctoral stay. Thanks to the rest of the guys for having such an amazing atmosphere Luca, Priti, Kornel, Michal, Sebastian, Dorothée, Léa, Mylene, Li Wei, Duncan, Christoph, Andreas, Max, Charles, Sarabjot and Keith. Finally, thanks to my Italian bestie, Pierluigi Mondelli. Thank you ‘Cavaliere’ for all your help and support. The experience at Merck was truly rewarding that I am sure I will never forget.

I would like to express my gratitude to our collaborators from Imperial College London, Professor Martin Heeney and Dr. Zhuping Fei and to Dr. Roger Guimerà from the Rovira i Virgil University for introducing us in the wonderful world of artificial intelligence.

Thanks to the funding agencies the European Research Council through project ERC CoG648901 and Eurecat Technological Centre that made this PhD possible.

También quiero dar las gracias, a mis amigos de fuera del grupo Begoña, Edu, Jan, Francesco, Juanan, Isa y Javi. Tampoco me puedo olvidar de las personas del ICMAB que hacen un trabajo silencioso pero imprescindible para conseguir que una tesis también salga adelante, personal de administración, limpiadoras, técnicos de laboratorio y servicio de informática. Ni de Raúl y su coral por haber puesto la nota musical a mi doctorado.

Fuera del ámbito académico, me gustaría dar las gracias a Pau, Sol, Bea, Jacobo, Agustín, Jess, Curro y Adrián. A los compañeros running del SAF por ser la vía de escape. Y a los amigos del colegio y equipo de balonmano que, a pesar de la distancia y del tiempo, sé que somos una verdadera familia. Gracias a Daniel, Sergio, Miguel, Juan Pablo, Eduardo, Pablo, Alejandro, Alberto y Luis por animarme y dedicarme vuestro tiempo durante estos cuatro años. ¡Esto lo tenemos que celebrar!

En último lugar quiero agradecer a mi familia, a mi padre y madre por darme todas las oportunidades del mundo y su amor. A mis hermanos Javier y Esther por quererme tanto y tan bien desde la distancia. Sabéis que un trocito de esta tesis tiene el sello Pascual San José. Finalmente, a Pepa por ser mi compañera fiel, por estar siempre apoyándome estoicamente día tras día sin importarte los kilómetros o los días de confinamiento. Por ser la luz que alegra mis días y hace que luche por mis sueños. Gracias de corazón.

LIST OF PUBLICATIONS

- ^[I] E. Pascual-San-José, A. Sánchez-Díaz, M. Stella, E. Martínez-Ferrero, M.I. Alonso and M. Campoy-Quiles, Comparing the potential of different strategies for colour tuning in thin film photovoltaic technologies, *Science and Technology of Advanced Materials*, **19**, 1, 823–835, 2018.
- ^[II] E. Pascual-San-José, X. Rodríguez-Martínez, R. Adel-Abdelaleim, M. Stella, E. Martínez-Ferrero and M. Campoy-Quiles, Blade coated P3HT:non-fullerene acceptor solar cells: a high-throughput parameter study with a focus on up-scalability, *Journal of Materials Chemistry A*, **7**, 20369–20382, 2019.
- ^[III] X. Rodríguez-Martínez, E. Pascual-San-José, Z. Fei, R. Guimerà, M. Heeney and M. Campoy-Quiles, Predicting the photocurrent-composition dependence in organic solar cells. *This work in progress will be submitted in 2020.*
- ^[IV] E. Pascual-San-José, G. Sadoughi, L. Lucera, M. Stella, E. Martínez-Ferrero, G.E. Morse, M. Campoy-Quiles and I. Burgués-Ceballos, Towards photovoltaic windows: Scalable fabrication of semitransparent modules based on non-fullerene acceptors via laser-patterning. Accepted in *Journal of Materials Chemistry A*, 2020 (DOI: 10.1039/d0ta02994g).
- ^[V] Z. Bi, X. Rodríguez-Martínez, C. Aranda, E. Pascual-San-José, A.R. Goñi, M. Campoy-Quiles and A. Guerrero, Defect tolerant perovskite solar cells from blade coated non-toxic solvents, *Journal of Materials Chemistry A*, **6**, 39, 19085–19093, 2018.

TABLE OF CONTENTS

| | |
|--|----------|
| <i>ABSTRACT</i> | i |
| <i>RESUMEN</i> | iii |
| <i>RESUM</i> | v |
| <i>ACKNOWLEDGEMENTS</i> | vii |
| <i>LIST OF PUBLICATIONS</i> | ix |
| TABLE OF CONTENTS..... | xi |
| LIST OF FIGURES | xv |
| LIST OF TABLES..... | xix |
| LIST OF ABBREVIATIONS | xxi |
| | |
| Chapter 1 General introduction | 1 |
| 1.1 Energy resources | 2 |
| 1.1.1 Potential and availability of energy sources | 2 |
| 1.1.2 Current scenario of energy consumption | 2 |
| 1.2 Photovoltaic energy..... | 4 |
| 1.2.1 Photovoltaic technologies..... | 4 |
| 1.2.2 Device characterisation..... | 8 |
| 1.3 Organic photovoltaics | 11 |
| 1.3.1 Working principles of organic solar cells..... | 12 |
| 1.3.2 Structure of the photoactive layer..... | 14 |
| 1.3.3 OPV architectures..... | 16 |
| 1.3.4 Photoactive materials..... | 17 |
| 1.3.5 State-of-the-art in OPV..... | 19 |
| 1.4 OPV companies and applications..... | 21 |
| 1.4.1 OPV companies | 21 |
| 1.4.2 OPV applications..... | 22 |
| 1.5 Motivation and structure of the thesis | 25 |

| | |
|---|-----------|
| 1.5.1 Motivation..... | 25 |
| 1.5.2 Structure..... | 26 |
| Chapter 2 Materials and Methods..... | 29 |
| 2.1 Materials..... | 30 |
| 2.1.1 Electrode materials..... | 31 |
| 2.1.2 Electron and hole transport materials..... | 31 |
| 2.1.3 Solvents..... | 32 |
| 2.1.4 Photoactive materials..... | 32 |
| 2.2 Lab-scale processing techniques..... | 35 |
| 2.2.1 Cleaning..... | 35 |
| 2.2.2 Large scale processing techniques..... | 40 |
| 2.3 Characterisation techniques..... | 43 |
| 2.3.1 Electrical characterisation..... | 43 |
| 2.3.2 Spectroscopic characterisation..... | 45 |
| 2.3.3 Morphological characterisation..... | 45 |
| 2.4 Optical modelling..... | 46 |
| 2.4.1 Transfer matrix method..... | 46 |
| 2.4.2 Colour and transparency calculations..... | 48 |
| 2.4.3 Genetic algorithm..... | 50 |
| Chapter 3 Colour tuning in thin-film technologies..... | 53 |
| 3.1 State of the art..... | 54 |
| 3.1.1 Objective..... | 55 |
| 3.2 <i>Direct problem</i> for OPVs..... | 55 |
| 3.3 <i>Direct problem</i> for perovskite solar cells..... | 64 |
| 3.4 Colour tuning effectiveness..... | 67 |
| 3.5 <i>Inverse problem</i> for OPVs..... | 70 |
| 3.6 Conclusions..... | 73 |
| Chapter 4 Upscaling P3HT:NFA solar cells..... | 75 |
| 4.1 P3HT based OPV. State of the art..... | 76 |
| 4.1.1 Objective..... | 78 |
| 4.2 Physical properties of photoactive materials..... | 79 |
| 4.2.1 Optical properties..... | 79 |

| | |
|--|------------|
| 4.2.2 Energy levels | 80 |
| 4.3 Performance of P3HT based solar cells..... | 81 |
| 4.4 Studied parameters | 84 |
| 4.4.1 Selection | 84 |
| 4.4.2 Sensitivity analysis | 85 |
| 4.5 Meta-analysis of P3HT based solar cells..... | 88 |
| 4.6 Morphology control of P3HT:O-IDTBR solar cells..... | 90 |
| 4.6.1 Solvent study | 90 |
| 4.6.2 Thermal annealing study | 95 |
| 4.6.3 Study of casting temperature | 98 |
| 4.6.4 Understanding the relationship between solvent and annealing temperature | 99 |
| 4.7 Ageing study on P3HT:O-IDTBR devices..... | 102 |
| 4.7.1 Photovoltaic parameters | 102 |
| 4.7.2 Understanding the degradation mechanisms in P3HT:O-IDTBR..... | 104 |
| 4.8 Towards P3HT:O-IDTBR R2R modules | 110 |
| 4.8.1 Intermediate scale | 110 |
| 4.9 Proof-of-concept P3HT:O-IDTBR R2R modules | 117 |
| 4.9.1 Losses upon up-scaling..... | 120 |
| 4.10 Conclusions | 123 |
| Chapter 5 High-throughput screening by 2D gradient maps..... | 125 |
| 5.1 State-of-the-art of high-throughput screening methodologies..... | 126 |
| 5.1.1 Objective | 129 |
| 5.2 Meta-analysis of PBDB-T:NFA solar cells – 1D approach..... | 129 |
| 5.3 Raman modelling | 132 |
| 5.3.1 Introduction | 132 |
| 5.3.2 Mathematical framework..... | 133 |
| 5.4 Manufacturing of gradient solar cells..... | 135 |
| 5.4.1 2D thickness-composition gradient films | 135 |
| 5.4.2 2D thickness-composition gradient solar cells | 137 |
| 5.4.3 Characterisation of 2D gradient maps | 138 |
| 5.4.4 Complementary photocurrent map | 140 |
| 5.4.5 Reproducibility of the combinatorial method..... | 143 |
| 5.4.6 2D optimisation maps and optical absorption..... | 145 |
| 5.4.7 Validation with 1D gradient discrete devices | 147 |

| | |
|--|------------|
| 5.5 Generalisation of the method | 150 |
| 5.6 Conclusions..... | 153 |
| Chapter 6 Laser patterned semitransparent OPV modules..... | 155 |
| 6.1 Requirements for BIPV..... | 156 |
| 6.1.1 Aesthetical requirements..... | 156 |
| 6.1.2 Geometrical requirements for BIPV modules | 159 |
| 6.1.3 Objective | 160 |
| 6.2 Selection of photoactive materials | 160 |
| 6.2.1 Colour and transparency..... | 162 |
| 6.3 Solution-processed devices | 163 |
| 6.3.1 Adapting to industry requirements | 163 |
| 6.3.2 Semitransparent and opaque devices..... | 164 |
| 6.4 Laser-patterned modules | 168 |
| 6.4.1 Cell-to-cell interconnection..... | 168 |
| 6.4.2 Combinatorial optimisation of laser patterning parameters..... | 170 |
| 6.4.3 Optoelectronic characterisation of modules | 175 |
| 6.4.4 Geometrical parameters of modules..... | 177 |
| 6.4.5 Geometry optimisation by co-local techniques | 181 |
| 6.4.6 PAL thickness tolerance in modules | 184 |
| 6.4.7 Flexible assessing of modules | 185 |
| 6.5 Conclusions..... | 187 |
| Chapter 7 General conclusions and perspectives..... | 189 |
| 7.1 Conclusions..... | 189 |
| 7.2 Perspectives | 193 |
| Appendix A..... | 195 |
| Appendix B..... | 197 |
| Appendix C..... | 199 |
| References | 201 |

LIST OF FIGURES

| | |
|---|----|
| Figure 1.1. Evolution of the record efficiency for different photovoltaic technologies. | 4 |
| Figure 1.2. Evolution of certified lab-scale device in OPV. | 6 |
| Figure 1.3. Current-voltage characteristics of an organic solar cell under dark and illumination conditions. | 8 |
| Figure 1.4. Sketch of a general organic solar cell. | 11 |
| Figure 1.5. Power generation processes in organic solar cells. | 13 |
| Figure 1.6. Organic solar cell architectures. | 14 |
| Figure 1.7. Device architecture of organic solar cells. | 16 |
| Figure 1.8. Absorption tunability of OPV materials. | 17 |
| Figure 1.9. General chemical structure of A-D-A NFAs. | 18 |
| Figure 1.10. Examples of OPV for applications in the Internet of Things (IoT). | 22 |
| Figure 1.11. Examples of OPV applications for building-integrated photovoltaics. | 23 |
| Figure 1.12. Workflow of the thesis highlighting the most relevant topics. | 27 |
| Figure 2.1. Top-view and cross-section sketches for different device scales. | 30 |
| Figure 2.2. Chemical structure of the donor materials used in this thesis. | 32 |
| Figure 2.3. Chemical structure of the acceptor materials used in this thesis. | 34 |
| Figure 2.4. Sketch of the solution-processed techniques. | 36 |
| Figure 2.5. Thickness-graded films by blade-coating. | 37 |
| Figure 2.6. Reproducibility of doctor-bladed devices with a thickness gradient. | 38 |
| Figure 2.7. Position-dependent thermal annealing. | 39 |
| Figure 2.8. Slot-die coater. | 40 |
| Figure 2.9. Screen printer. | 41 |
| Figure 2.10. Laser machine used for film ablation in Chapter 6. | 42 |
| Figure 2.11. Equipment and an example of co-local measurements. | 44 |
| Figure 2.12. Sketch for the transfer matrix method formalism. | 46 |
| Figure 2.13. Illuminant sources. | 48 |
| Figure 2.14. CIE 1931 colour matching functions. | 49 |

| | |
|---|-----|
| Figure 2.15. Flowchart of a genetic algorithm. | 51 |
| Figure 3.1. Scheme of the colour prediction tool for thin-film solar cells. | 56 |
| Figure 3.2. Optical properties and colour coordinates of OPV materials. | 57 |
| Figure 3.3. Colour dependence on the stoichiometry and thickness of thin films. | 59 |
| Figure 3.4. Colour of binary blends based on donor:PC ₇₀ BM system. | 60 |
| Figure 3.5. Example of predicted CIE colour coordinates for a ternary system. | 61 |
| Figure 3.6. Complex refractive indices of simulated dyes. | 62 |
| Figure 3.7. Colour tuning in OPV using ternary blends. | 63 |
| Figure 3.8. Colour prediction for perovskite film. | 64 |
| Figure 3.9. Colour prediction for hybrid perovskite films. | 65 |
| Figure 3.10. Colour tuning upon shifting the bandgap of MAPb(I _c Br _{1-c}) ₃ | 66 |
| Figure 3.11. Sketch of the geometric parameters involved in the colour tuning effectiveness. | 67 |
| Figure 3.12. <i>Inverse problem</i> based on genetic algorithm fitting for P3HT:PC ₇₀ BM using a piece of brick as targeted colour. | 70 |
| Figure 3.13. <i>Inverse problem</i> for OPV reproducing material colours. | 71 |
| Figure 4.1. The research interest of P3HT and NFAs over years. | 76 |
| Figure 4.2. Absorption and aesthetics of materials used in this chapter. | 79 |
| Figure 4.3. Energy levels of the studied systems are extracted from the literature. | 80 |
| Figure 4.4. Photovoltaic characterisation of the best P3HT-based devices. | 81 |
| Figure 4.5. Theoretical (HOMO _{acceptor} -LUMO _{donor}) and measured V _{oc} | 82 |
| Figure 4.6. Multiparametric processing study of the P3HT:O-IDTBR based devices from the database. | 87 |
| Figure 4.7. Summary of P3HT based solar cells. | 88 |
| Figure 4.8. Processing solvent study on P3HT:O-IDTBR films. | 91 |
| Figure 4.9. Contact angle measurements of P3HT, O-IDTBR and blends with different solvent systems. | 92 |
| Figure 4.10. AFM measurements of P3HT:O-IDTBR blends as a function of the solvent system. | 92 |
| Figure 4.11. Optical characterisation of P3HT:O-IDTBR devices processed from CB and CB:DCB (1:1). | 93 |
| Figure 4.12. X-Ray diffraction spectra of the P3HT:O-IDTBR. | 94 |
| Figure 4.13. Annealing effect on P3HT:O-IDTBR solar cells processed from CB:DCB. | 95 |
| Figure 4.14. P3HT:O-IDFBR study upon thermal annealing. | 97 |
| Figure 4.15. Casting temperature study for P3HT:O-IDTBR based devices. | 98 |
| Figure 4.16. Sketch of the proposed drying kinetics of formulations. | 101 |
| Figure 4.17. Ageing test of P3HT:O-IDTBR solar cells. | 103 |
| Figure 4.18. Effect of encapsulation via photocurrent images. | 106 |

| | |
|--|-----|
| Figure 4.19. Raman shift of P3HT excited at 488 nm of higher and lower performing areas of the non-encapsulated device of Figure 4.18..... | 107 |
| Figure 4.20. Thickness effect via photocurrent images..... | 108 |
| Figure 4.21. Ageing study via EQE measurements..... | 109 |
| Figure 4.22. Solvent screening of P3HT:O-IDTBR formulations..... | 113 |
| Figure 4.23. Microscope pictures of P3HT:O-IDTBR films processed from the so-called intermediate scale..... | 114 |
| Figure 4.24. Large scale devices (industrial scale). | 117 |
| Figure 4.25. Picture of a R2R module of P3HT:O-IDTBR with an area of 108 mm ² | 118 |
| Figure 4.26. Absorption spectra of R2R modules with different PAL thickness. | 118 |
| Figure 4.27. Photovoltaic parameters of P3HT:O-IDTBR R2R modules as a function of PAL thickness. | 119 |
| Figure 4.28. Picture of a flexible P3HT:O-IDTBR module fabricated by roll-to-roll (R2R)..... | 119 |
| Figure 4.29. The optical density of P3HT:O-IDTBR devices processed from different scales. | 122 |
| Figure 5.1. Summary of PBDB-T based solar cells. | 130 |
| Figure 5.2. Raman fingerprints of the OPV materials employed in this chapter..... | 133 |
| Figure 5.3. Sketch of basic steps to fabricate composition-graded photoactive layer (PAL)..... | 135 |
| Figure 5.4. Manufacturing protocol of composition and thickness-graded solar cells..... | 137 |
| Figure 5.5. Sketch of the <i>Rambic</i> measurement on a thickness-composition-graded device. ... | 138 |
| Figure 5.6. Example of the generation of <i>Rambic</i> co-local maps. | 139 |
| Figure 5.7. Illuminant sources and material absorption. | 141 |
| Figure 5.8. Comparison of photocurrent measurements: <i>Rambic</i> vs <i>whiteBIC</i> | 142 |
| Figure 5.9. Reliability of the high-throughput method. | 143 |
| Figure 5.10. Correlation between photocurrent distribution and overlapping of the extinction coefficients. | 146 |
| Figure 5.11. Verification of combinatorial photocurrent-composition maps. | 148 |
| Figure 5.12. Combinatorial screening of 12 low-bandgap:acceptor systems..... | 152 |
| Figure 6.1. Optical absorption of pristine and blended photoactive materials. | 160 |
| Figure 6.2. Colour and transparency of the PAL as a function of the thickness (PBDTZZT-stat-DBTT-8 and 4TICO)..... | 161 |
| Figure 6.3. Transparency contribution of each layer..... | 162 |
| Figure 6.4. Colour CIE coordinates of photoactive layer films. | 163 |
| Figure 6.5. Comparison between opaque and semitransparent (ST) electrodes..... | 164 |
| Figure 6.6. Performance (PCE) as a function of the thickness of the PAL. | 166 |
| Figure 6.7. Sequential steps for monolithic cell-to-cell interconnection..... | 168 |
| Figure 6.8. Laser-patterned modules..... | 169 |

| | |
|---|-----|
| Figure 6.9. General combinatorial method for the optimisation of the laser patterning parameters..... | 170 |
| Figure 6.10. Optimisation of P1 with increasing laser excitation power. | 172 |
| Figure 6.11. Feature of the laser-patterned groove. | 173 |
| Figure 6.12. P2 and P3 optimisation of laser patterning conditions. | 174 |
| Figure 6.13. Microscope images of the laser patterned organic films for photoactive layer thicknesses. | 175 |
| Figure 6.14. Co-local optoelectronic characterisation on a subcell at different wavelengths. | 176 |
| Figure 6.15. JV characteristics of modules with 2, 3 and 4-mm L_{cell} | 179 |
| Figure 6.16. Geometry optimisation via co-local electrical and optical mapping..... | 181 |
| Figure 6.17. Transversal cross-section images from Figure 6.16. | 182 |
| Figure 6.18. Layout of the laser patterning design. | 185 |
| Figure 6.19. Module performance and transparency. | 186 |

LIST OF TABLES

| | |
|---|-----|
| Table 1.1. Current scenario for non-renewable and renewable electricity production. | 3 |
| Table 1.2. Overview of the current photovoltaic technologies. | 5 |
| Table 1.3. State-of-the-art of top-performing OPV systems. | 20 |
| Table 1.4. Current leading OPV manufacturer companies. | 21 |
| Table 1.5. Largest OPV installations in the world. | 24 |
| Table 2.1. General blade coating recipes for AZO/ZnO, PAL and PEDOT:PSSs. | 38 |
| Table 2.2. Evaporation recipes for MoO ₃ and Ag. | 39 |
| Table 2.3. General recipes for slot-die coating. | 41 |
| Table 3.1. Photoactive layer thickness and error of the corresponding CIE coordinates. | 58 |
| Table 3.2. Colour tuning effectiveness of the different strategies to tune the colour in thin-film solar cells. | 68 |
| Table 3.3. Results of the <i>inverse problem</i> combined with GA. | 72 |
| Table 4.1. Literature review of P3HT-based devices. | 77 |
| Table 4.2. Photovoltaic parameters of the bladed champion solar cells. | 83 |
| Table 4.3. Sensibility analysis of processing parameters. | 86 |
| Table 4.4. Raman peaks analysis of P3HT:O-IDTBR films from Figure 4.11. | 94 |
| Table 4.5. Raman peaks analysis of P3HT:O-IDTBR films from Figure 4.13(a). | 96 |
| Table 4.6. Hansen parameters of solvents and distance in Hansen space. | 100 |
| Table 4.7. Photovoltaic parameters of P3HT:O-IDTBR fresh and degraded solar cells. | 104 |
| Table 4.8. Summary of the specific printing features of lab, intermediate and industrial scale. | 111 |
| Table 4.9. Summary of solvent screening of P3HT:O-IDTBR formulations fulfilling the intermediate scale conditions (Table 4.8). | 115 |
| Table 4.10. Literature review of publications of P3HT-based modules. | 120 |
| Table 4.11. Photovoltaic parameters of champion P3HT:O-IDTBR devices processed from different solvents, manufacturing scales. | 121 |
| Table 4.12. The optical density values of P3HT:O-IDTBR films processed from CB:DCB and toluene. | 122 |

| | |
|---|-----|
| Table 5.1. State-of-the-art of combinatorial screening in OPV. | 127 |
| Table 5.2. Best photovoltaic blade-coated and spin-coated photovoltaic parameters of PBDB-T based solar cells. | 131 |
| Table 5.3. Photovoltaic parameters of PBDB-T:EH-ITIC and PTBT7-Th:ITIC solar cells. | 150 |
| Table 6.1. Specific requirements for the integration of OPV modules into semitransparent windows and curtains. | 156 |
| Table 6.2. State-of-the-art of semitransparent organic solar cells. | 158 |
| Table 6.3. Preferred technical requirements for the manufacturing of OPVs following the request from printing industrial manufacturers. | 164 |
| Table 6.4. Photovoltaic parameters of the optimised opaque and semitransparent (ST) solar cells. | 166 |
| Table 6.5. Fine-tuned values for the laser patterning of P1, P2 and P3. | 174 |
| Table 6.6. Photovoltaic ST modules and lab-cell (reference) parameters as a function of the cell length (L_{cell}). | 180 |
| Table 6.7. Photovoltaic parameters of semitransparent modules consisting of 4 subcells interconnected in series ($L_{\text{cell}}= 3 \text{ mm}$) and lab-devices. | 184 |
| Table 7.1. Results achieved in the thesis benchmarked with the state-of-the-art results. | 191 |

LIST OF ABBREVIATIONS

| | |
|----------|--|
| AA | Active area |
| AFM | Atomic force microscopy |
| AgNW | Silver nanowires |
| AZO | Aluminium doped zinc oxide |
| BHJ | Bulk heterojunction |
| BIPV | Building integrated photovoltaics |
| BrA | p-Bromoanisole |
| CB | Chlorobenzene |
| CRI | Complex refractive index |
| CTE | Colour tuning effectiveness |
| D:A | Donor:acceptor |
| DB | Doctor blade |
| DCB | o-dichlorobenzene |
| DIO | 1,8-diiodooctane |
| EH-IDTBR | (5Z,5'Z)-5,5'-(((4,4,9,9-(2-ethylhexyl)-4,9-dihydro-s-indaceno[1,2-b:5,6-b']dithiophene-2,7-diyl)bis(benzo[c][1,2,5]thiadiazole-7,4-diyl))bis(methanylylidene))bis(3-ethyl-2-thioxothiazolidin-4-one)) |

| | |
|---------|--|
| EH-ITIC | 3,9-bis(2-methylene-((3-(1,1-dicyanomethylene)-6/7-methyl)-indanone))-5,5,11,11-tetrakis(2-ethylhexyl)-dithieno[2,3-d:2',3'-d']-s-indaceno[1,2-b:5,6-b']dithiophene |
| EMA | Effective medium approximation |
| EPBT | Energy payback time |
| EROI | Energy return on investment |
| ETL | Electron transport layer |
| EQE | External quantum efficiency |
| FF | Fill factor |
| FWHM | Full width at half maximum |
| GFF | Geometrical fill factor |
| GA | Genetic algorithm |
| HTL | Hole transport layer |
| HOMO | Highest occupied molecular orbital |
| HPT | Human perception transmittance |
| ICBA | 1',1'',4',4''-Tetrahydro-di[1,4]methanonaphthaleno [1,2:2',3',56,60:2'',3''] [5,6]fullerene-C ₆₀ |
| IPA | 2-propanol |
| ITO | Indium-tin-oxide |
| ITIC | 3,9-bis(2-methylene-(3-(1,1-dicyanomethylene)-indanone))-5,5,11,11-tetrakis(4-hexylphenyl)-dithieno[2,3-d:2',3'-d']-s-indaceno[1,2-b:5,6-b']dithiophene |
| ITIC-M | 3,9-bis(2-methylene-((3-(1,1-dicyanomethylene)-6/7-methyl)-indanone))-5,5,11,11-tetrakis(4-hexylphenyl)-dithieno[2,3-d:2',3'-d']-s-indaceno[1,2-b:5,6-b']dithiophene |

| | |
|---------------------|--|
| ITIC-4F | 3,9-bis(2-methylene-((3-(1,1-dicyanomethylene)-6,7-difluoro)-indanone))-5,5,11,11-tetrakis(4-hexylphenyl)-dithieno[2,3-d:2',3'-d']-s-indaceno[1,2-b:5,6-b']dithiophene |
| J _{sc} | Short circuit current density |
| JV curve | Current density and voltage curve |
| LBIC | Light beam induced current |
| LUMO | Lowest unoccupied molecular orbital |
| MoO ₃ | Molybdenum trioxide |
| NFA | Non fullerene acceptor |
| O-IDFBR | (5Z,5'Z)-5,5'-((7,7'-(6,6,12,12-tetraoctyl-6,12-dihydroindeno[1,2-b]fluorene-2,8-diyl)bis(benzo[c][1,2,5]thiadiazole-7,4-diyl))bis(methanylylidene))bis(3-ethyl-2-thioxothiazolidin-4-one) |
| O-IDTBR | (5Z,5'Z)-5,5'-(((4,4,9,9-tetraoctyl-4,9-dihydro-s-indaceno[1,2-b:5,6-b']dithiophene-2,7-diyl)bis(benzo[c][1,2,5]thiadiazole-7,4-diyl))bis(methanylylidene))bis(3-ethyl-2-thioxothiazolidin-4-one)) |
| O-ITIC | 3,9-bis(2-methylene-((3-(1,1-dicyanomethylene)-6/7-methyl)-indanone))-5,5,11,11-tetrakis(4-octyl)-dithieno[2,3-d:2',3'-d']-s-indaceno[1,2-b:5,6-b']dithiophene |
| OPV | Organic photovoltaics |
| OSC | Organic solar cell |
| P3HT | Poly(3-hexylthiophene-2,5-diyl) |
| PAL | Photoactive layer |
| PBDB-T | Poly[(2,6-(4,8-bis(5-(2-ethylhexyl)thiophen-2-yl)-benzo[1,2-b:4,5-b']dithiophene))-alt-(5,5-(1',3'-di-2-thienyl-5',7'-bis(2-ethylhexyl)benzo[1',2'-c:4',5'-c']dithiophene-4,8-dione)] |
| PC ₆₀ BM | [6,6]-Phenyl-C ₆₁ -butyric acid methyl ester |
| PC ₇₀ BM | [6-6]-Phenyl-C ₇₁ -butyric acid methyl ester |

| | |
|-------------|--|
| PCDTBT | Poly[N-9'-heptadecanyl-2,7-carbazole-alt-5,5-(4',7'-di-2-thienyl-2',1',3'-benzothiadiazole)] |
| PCE | Power conversion efficiency |
| PCPDTBT | Poly[2,6-(4,4-bis-(2-ethylhexyl)-4H-cyclopenta[2,1-b;3,4-b']dithiophene)-alt-4,7(2,1,3-benzothiadiazole)] |
| PEDOT:PSS | Poly(3,4-eoly(3,4-ethylenedioxythiophene)-poly(styrenesulfonate) |
| PET | Poly(ethylene terephthalate) |
| PffBT4T-2OD | Poly[(5,6-difluoro-2,1,3-benzothiadiazol-4,7-diyl)-alt-(3,3'''-di(2-octyldodecyl)-2,2';5',2'';5'',2'''-quaterthiophen-5,5'''-diyl)] |
| PL | Photoluminescence |
| PTB7-Th | Poly[4,8-bis(5-(2-ethylhexyl)thiophen-2-yl)benzo[1,2-b;4,5-b']dithiophene-2,6-diyl-alt-(4-(2-ethylhexyl)-3-fluorothieno[3,4-b]thiophene)-2-carboxylate-2-6-diyl] |
| p-Xyl | p-Xylene |
| R2R | Roll-to-roll |
| RamBIC | Raman and LBIC technique |
| RMS | Root mean square |
| R_s | Series resistance |
| R_{sh} | Shunt resistance |
| TMM | Transfer matrix method |
| Tol | Toluene |
| UV-Vis | Ultraviolet-visible |
| V_{oc} | Open circuit voltage |
| ZnO | Zinc oxide |
| XRD | X-ray diffraction |

Chapter 1 General introduction

ABSTRACT

The current energy landscape, mostly dominated by fossil fuels, will be shortly driven to a not sustainable scenario. Fossil fuels resources are limited and their effects after their intensive consumption have driven the world to a dangerous warming situation with important consequences for humankind. Fortunately, the good news is that we are still on time to mitigate the effects of the so-called climate emergency by researching and developing clean and sustainable energy alternatives.

Among renewable resources, solar energy has the potential to meet the yearly global energy demand in 1 hour. However, solar energy is dispersed (compared with non-renewable alternatives), and thus it requires an intensive photovoltaic/thermosolar deployment to shift the dependence from fossil to renewable energy. Although silicon panels are currently governing the photovoltaic market, there is room for other photovoltaic technologies that offer complementary features such as mechanical flexibility, light-weight and aesthetics. This thesis focuses on the upscaling of organic photovoltaics (OPV) based on non-fullerene acceptors. In particular, we study three relevant topics for the full deployment of OPV into the market: aesthetics, high-throughput screening, and optimisation methods and upscaling techniques. In this introductory chapter, an overview of the photovoltaic technologies, theoretical background, state-of-the-art and potential applications of OPV are given to facilitate the reading of this thesis. The chapter concludes with the motivation and the structure of the discussed issues in the thesis.

1.1 Energy resources

1.1.1 Potential and availability of energy sources

In the late XIX century, the industrial revolution boosted an intensive use of fossil fuels for electricity, heating and transport.^[1] Since then, fossil fuels have dominated the energy landscape over the last centuries despite their limited availability and environmental impact.^[2] According to forecasts, coal reserve is pointed as the most abundant fossil fuel while uranium, oil and natural gas would last less than 20 years each (Table 1.1).^[2,3] Consequently and according to these forecasts, if only these non-renewable resources were exploited, these reserves would last less than 105 years, assuming a very optimistic scenario with constant global energy consumption in the next decades, see Table 1.1.^[2]

Beyond their limited availability, the consequences of the intense consumption of carbon-based sources are nowadays noticeable in a significant increase in the CO₂ emissions, and thus the global warming.^[4,5] Some indicators that assess quantitatively the effects of the climate emergency revealed an increase of 1°C of the global averaged temperature in comparison to the previous century.^[6] This has adverse consequences that affect animals, plants and oceans, and, consequently, humankind's way of life.

To mitigate, or ideally reverse, this alarming future perspective, clean renewable energy sources are being promoted as efficient alternatives to fossil fuels. Among the renewable sources, tidal, wave, geothermal, hydro and biomass sources show a relatively low energy potential compared to solar and wind energy (Table 1.1).^[2] These resources are able to meet to meet the global energy demand many times by themselves, see Table 1.1.

1.1.2 Current scenario of energy consumption

The largest energy consumption in the world is dedicated to heating and cooling (51%), while the other half is employed for electricity generation (32%) and fuel for transport (17%).^[7] The penetration level of renewable energies in the market varies according to their final use. While 26% of the electricity in the world was produced from 'clean' resources, only 9.8% was employed in heating and cooling, and 3.3% in transport.^[7] The reason behind that it is because transport relies mostly on combustion engines fuelled by oil, diesel, petrol, kerosene, etc. whereas coal or natural gas are the preferential choices

for heating. Renewable resources will play a crucial role in the transition to sustainable transport, for example through the full deployment of electric vehicles. Additional efforts will be required for the electricity generation and its storage such as electric batteries. Regarding electricity generation, one-quarter of world production comes from renewable resources, mostly hydro (16%) and wind (4%). By contrast, coal is the most employed resource for electricity generation (38%) followed by natural gas (23%), see Table 1.1.

When looking at Spain in particular, the use of renewable resources is more optimistic as electricity produced by hydro, wind and solar resources is almost double the world share, 38% and 23%, respectively. In addition, the Spanish production share from non-fossil fuels (including nuclear) reaches 64.6% in comparison to 34.7% in the world. On the other hand, the penetration of solar energy in the electricity market (photovoltaic and thermal) is still very poor (4.6%) despite a large amount of solar radiation striking on the Spanish territory in comparison to other countries. The large irradiance would motivate further PV installations in the Spanish territory.

Table 1.1. Current scenario for non-renewable and renewable electricity production.

| | Resource | Energy potential ^[2] (TW-y) | Global share ^[8] (%) | Spanish share ^[9] (%) | Spanish Equiv. power density* ^b (W/m ²) | EROI* ^c |
|-----------|-------------|---|------------------------------------|-------------------------------------|---|------------------------------------|
| Finite | Coal | 900 | 38.3 | 13.5 | 100-110 ^[10] | 15-80 ^[11] |
| | Natural gas | 215 | 22.9 | 10.2 | 120-1000 ^[10] | 10-25 ^[12] |
| | Nuclear | 90-300 | 10.2 | 20.6 | 100-130 ^[10] | 5-15 ^[13] |
| | Oil | 240 | 3.3 | 11.2 | 90-120 ^[10] | 5-10 ^[12] |
| Renewable | Hydro | 3-4* ^a | 16.3 | 13.2 | 11 ^[14] | 50-200 ^[12,15] |
| | Wind | 25-70* ^a | 4.4 | 19 | 1-4 ^[14] | 20-40 ^[12] |
| | Biomass | 2-6* ^a | 2.3 | 1.4 | 0.03-0.2 ^[10] | 1-10 ^[12] |
| | Solar | 23000* ^a | 1.8 | 4.6 | 5-20 ^[14] | 7-15* ^c ^[16] |

*^a Units of renewable resources are TW-year/year; global energy consumption 16 TW-year.^[2] Global electricity production ('Global share') and in Spain ('Spanish share') data is from 2018. *^b Equiv. power density stands for output of electrical power per unit land or water area.^[10] *^c The energy-returned on investment (EROI) values for the solar resource is calculated based on silicon-photovoltaics.

1.2 Photovoltaic energy

The different PV technologies, as well as the general characterisation methods, are explained in this section.

1.2.1 Photovoltaic technologies

As it was previously mentioned, solar energy is one of the few renewable resources with the largest potential scale to meet our future energy demand. The potential of the incoming solar irradiation on Earth in 1 hour equals our current annual energy consumption. In practical terms, a rough estimation, considering 25% of land share on Earth, an average photovoltaic conversion efficiency of silicon modules of 10% and 430 EJ^[17] as total yearly energy consumption, points out that covering 2% of the land on Earth would be enough to provide electricity only from solar panels. This area represents the full coverage with photovoltaic (PV) panels equivalent to countries such as Kazakhstan (2.700 km²) or Algeria (2.400 km²).

Although the solar radiation that reaches Earth is abundant, its effective power density is very low, 5-20 W_{electricity}/m² according to calculations done by van Zalk *et al.*,^[10] since the overall installation for the electricity production requires covering large areas.

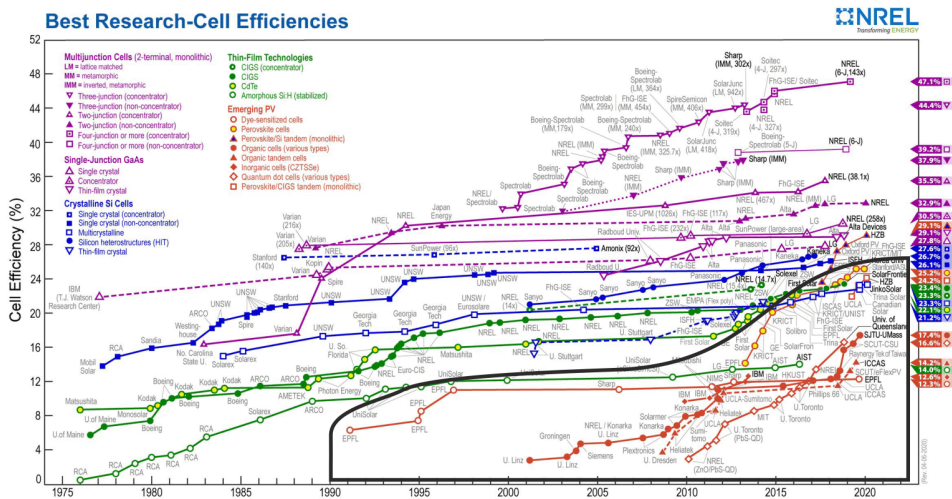


Figure 1.1. Evolution of the record efficiency for different photovoltaic technologies. The chart ‘Best Research-Cell Efficiencies’ is reprinted with permission by the National Renewable Energy Laboratory from Ref ^[18]. Emerging photovoltaic technologies are highlighted with a black rectangle.

An average of 10 W/m² of electrical power density (considering the full PV installation) is generated by silicon-PV (Si-PV) while 3.7 W/m² is generated in the case of solar thermal energy, resulting in more diffuse resources than other non-renewable technologies (>100 W/m²).^[10] To compensate for the diffuse solar energy, a PV technology should be chosen that maximises the metric called energy return of investment (EROI) which is the ratio between the amount of obtained energy and the energy employed for the production of the device (Table 1.1). This metric accounts the efficiency, lifespan and employed energy for the PV device production. Thus, the more efficient and stable a PV technology is, the higher the EROI value. However, in some specific cases, the final choice depends on the specifications of the application. On the other hand, for the intensive deployment of PV, another relevant feature as important as the aforementioned ones is the sustainability of the manufacturing processes and the use of raw abundant and non-toxic materials.

Among the existing PV technologies, monocrystalline and polycrystalline Si-PV have dominated the energy landscape (93% market share) over years due to high efficiencies (> 20%), long lifespans (>25 years) and moderate cost.^[19] Besides Si-PV, cadmium telluride (CdTe) and copper indium gallium selenide (CIGS) PV technologies have also reached the PV market. However, their penetration is very low compared to Si-PV (Table 1.2). Regarding the efficiency, gallium arsenide panels (GaAs-PV) are the most efficient,^[20] however, their use is limited to satellites and aircrafts applications due to low degradation under space radiation and a sector with minor economic limitations.^[21]

Table 1.2. Overview of the current photovoltaic technologies. Market share, lifespan, efficiency and area of certified modules, energy payback time (EPBT) and energy return on investment (EROI) for different PV technologies.

| Type | Market share ^[22] (%) | Lifespan ^[23] (Years) | Efficiency ^{*a} ^[23] (%) | Area ^[23] (cm ²) | EPBT ^[24] (Years) | EROI ^[24] |
|--------------------|-------------------------------------|-------------------------------------|---|--|---------------------------------|------------------------------------|
| Silicon | 93 ^{*c} | 25 | 20.4 | >14000 | 1.5-3 ^{*c} | 7-15 ^{*c} ^[16] |
| CdTe | 5 | 10-15 | 19.0 | >14000 | 0.5-1.5 | 10 |
| CIGS | 2 | 10-15 | 19.2 | 800-6500 | 1-2 | 30 |
| GaAs ^{*b} | - | 20 ^[25] | 31.0 | 800-6500 | N.A. | N.A. |
| Perovskite | - | 0.5-1 ^[26] | 16.1 | 800-6500 | 0.25 ^[27] | 10-20 |
| Organic | - | 1-9 | 11.7 | 200-800 | 0.1-0.5 ^[28] | 20-120 ^[28,29] |

^{**} Efficiency stands for best module efficiency and the area of the reported module extracted from NREL.^[23] ^{*b} GaAs refers to three junctions no-concentrator. ^{*c} Silicon refers to all type of Si PV (monocrystalline to polycrystalline 56%, monocrystalline 36% and amorphous 2%). Emerging PV technologies (perovskite and organic) are separated vertically.

Although Si-PV exhibits high efficiencies and is based on abundant materials (Si), its manufacturing temperatures are extremely high ($> 900^{\circ}\text{C}$) leading to extended energy payback times (EPBT). On the other hand, despite the high performance of GaAs-PV, this technology mostly relies on scarce materials on Earth crust such as Ga (0.019%) and As (0.00021%), thus limiting their intensive deployment.^[30]

For these reasons, emerging PV technologies (dye-sensitised, perovskite, organic and quantum dots technologies) have been explored as top-performing and cost-effective novel semiconductor materials. These PV technologies exhibit high lab-scale performances such as 15% for dye-sensitised PV,^[31] 16% for quantum-dots PV,^[32] 18% for organic PV^[33] and 25% for hybrid perovskite PV,^[18] see Figure 1.1. Although perovskite-based devices currently show the highest performance, the lead present in the absorber layer might threaten their eventual commercialisation.^[34]

Organic photovoltaics (OPV), the second top-performing PV emerging technology, has experienced an unprecedented increase in performance, going from 7% to more than 18% conversion efficiency in less than 10 years (Figure 1.2), while employing no harmful elements.^[35] Regarding the efficiency, Figure 1.2 shows the performance evolution for certified OPV lab-scale devices. We identified three stages in their development. (i) 5% efficiency devices were achieved by the development of polythiophene and fullerene semiconductors together with a control of the morphology.

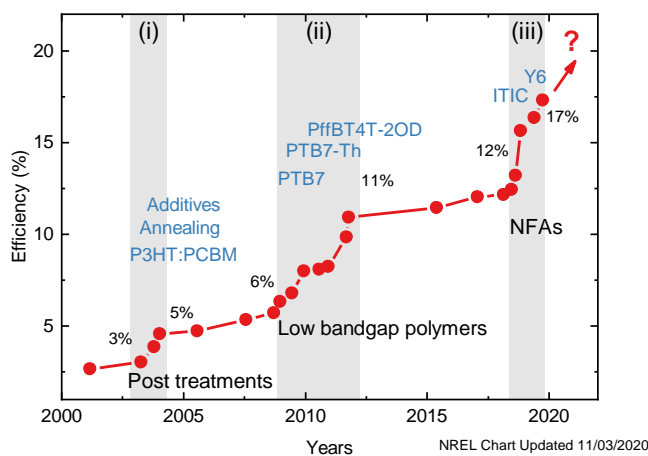


Figure 1.2. Evolution of certified lab-scale device in OPV. Data is extracted from the chart ‘Best Research-Cell Efficiencies’ by the National Renewable Energy Laboratory from Ref ^[18]. Highlighted periods (i, ii, iii) are described in the main text.

(ii) Development of low-bandgap polymers that led to 11% efficiency devices. Then from 2012 to 2018, most of the interest shifted away from OPV to perovskite resulting in a slow-down of the OPV development. (iii) In 2018, after the irruption of efficient non-fullerene acceptors (NFAs), OPV field has experienced continuous progress going from performance of 12% to almost 18% in two years.^[33] See more details about OPV materials in the next section.

Regarding the material abundance, organic photo-absorbing materials are mostly based on oxygen (46%), carbon (0.18%) and hydrogen (0.15%) which are between the most abundant chemical elements on Earth crust, as well as others elements with a minor presence in OPV materials such as fluorine (0.054%), sulphur (0.042%), chlorine (0.017%) and nitrogen (0.002%).^[30] On the other hand, materials for electrodes are not as abundant as photoactive material elements including indium ($1.6 \cdot 10^{-5} \%$) and silver ($7.9 \cdot 10^{-6} \%$).^[30] However, carbon-based electrodes have been investigated as efficient metal-based electrode replacement.^[36,37]

Another main advantage of OPV over traditional Si-PV is that OPV is a solution-processed technology being even processable from non-halogenated solvents. Moreover, the maximum processing temperatures do not surpass 150°C, leading to extremely low embodied energy.^[38-40] Precisely this allows OPV to have a potential short energy payback times (EPBT) of just a few weeks and EROI values up to 100 (Table 1.2).^[28,41] The facts of the low manufacturing temperatures and solution-process technology make OPV printable on flexible plastic substrates by means of industrial rotative equipment also known as roll-to-roll (R2R). Therefore, we conclude that OPV is a quite relevant and cost-effective technology to study due to the sustainability of its manufacturing processes and the employment of Earth-abundant semiconductor materials while exhibiting competitive lab-scale efficiencies up to 17% and 11.7% in large-scale modules. Hence, it is worth studying the upscaling of OPV based on NFAs.

1.2.2 Device characterisation

1.2.2.1 IV curve

The performance assessment of solar cells is common to all solar cell technologies. A comprehensive explanation of the PV device characterisation is here given. In dark conditions, solar cells behave like a usual diode being almost zero under reverse bias ($V < 0$) and with a rectifying effect that yields the current to increase exponentially under forwarding bias ($V > 0$), see blue line in Figure 1.3.

Upon light illumination, the rectifying behaviour is maintained although photocurrent is generated and delivered to an external circuit (red line in Figure 1.3). All solar cell parameters are extracted from the current-voltage (IV) curve or, considering the active area of the device, density current-voltage (JV), see Figure 1.3(a).

The power conversion efficiency (PCE) is the parameter employed to evaluate and compare the performance of photovoltaic devices on a quantitative basis. The parameters involved in the calculation of PCE are highlighted in Figure 1.3(a) and listed below.

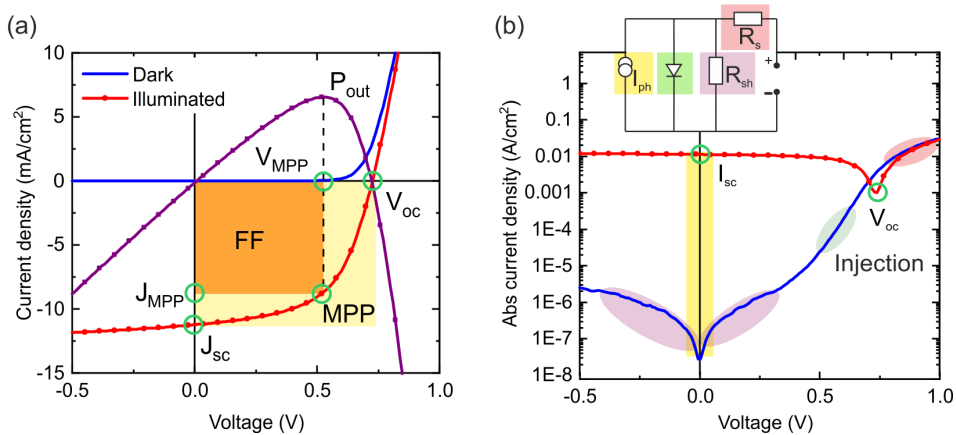


Figure 1.3. Current-voltage characteristics of an organic solar cell under dark and illumination conditions. The relevant characteristic parameters of the device are highlighted in both (a) linear and (b) semi-logarithmic scale. Inset in (b) shows the simplified equivalent circuit of a solar cell. The example of the JV curve corresponds to a P3HT:O-IDTBR OPV device. More details about this system in Chapter 4.

- Short-circuit current density (J_{sc}) is the generated current that flows in short-circuit conditions ($V=0$) divided by the photoactive area of the device. Generally, J_{sc} is proportional to the absorbed light in the device.
- Open-circuit voltage (V_{oc}) is the voltage to be applied in order to have no global current flowing because the diode current is counterbalanced by the photogenerated one. This parameter is defined, in the case of organic materials, by the difference in energy levels of the photoactive materials, a further discussion is given in the next section.
- Maximum power point (MPP): Between short-circuit and open-circuit conditions the device generates electrical power. The point in which the product of voltage and current density is maximised is known as the MPP and the corresponding voltage and current as V_{MPP} and J_{MPP} . This point is the normal operating condition for a commercial photovoltaic module.
- The fill factor (FF) is defined as the ratio between the operating MPP and the hypothetical maximum power for an ideal device, see Eq. 1.1. Visually, FF can be described by the geometrical ratio between the orange and yellow squares in Figure 1.3(a). The FF is an indirect way to evaluate the transport properties in the devices, determined by the processes of charge transport and extraction at the electrodes of the photogenerated charge carriers.

$$FF = \frac{V_{MPP} J_{MPP}}{V_{oc} J_{sc}} \quad (1.1)$$

- Power conversion efficiency (PCE) is the parameter that defines the overall performance of the device. PCE is the ratio between the output power (P_{out}) and the incident light power (P_{in}). PCE can be rewritten in terms of the aforementioned parameters, see Eq. 1.2.

$$PCE = \frac{P_{out}}{P_{in}} = \frac{V_{oc} J_{sc} FF}{P_{in}} \quad (1.2)$$

For standard characterisation, P_{in} matches the incident spectral irradiance of sunlight at Earth namely Air Mass1.5 Global spectrum (AM 1.5G), with an average power density of 1000 W/m². See the solar spectrum in Figure 1.8.

- Series resistance (R_s) is the slope of the JV characteristics at higher voltages than V_{oc} , red-highlighted area in Figure 1.3(b).
- Shunt resistance (R_{sh}) is the slope of the JV characteristics at low voltages, purple-highlighted area in Figure 1.3(b).

Generally, the IV/JV characteristics of a photovoltaic device can be described by adapting the Shockley diode equation (Eq. 1.3):^[42]

$$I(V) = I_0 \left[e^{\frac{q(V-IR_s)}{nkT}} - 1 \right] - \frac{V - IR_s}{R_{sh}} - I_{ph} \quad (1.3)$$

where I_0 is the dark current, q the elementary charge, V the applied voltage, n the diode ideality factor, kT the thermal energy, R_s the series resistance, R_{sh} shunt resistance, and I_{ph} is the photocurrent which represents a shift of the IV curve down with respect to dark current. The corresponding equivalent electric model is depicted in the inset of Figure 1.3(b).

1.2.2.2 Quantum efficiency

The quantum efficiency (QE) of a photovoltaic device is the probability that an incident photon of certain energy (wavelength) will be converted into an electron within the PV device. Therefore, QE is a quantitative metric of energy conversion. The internal quantum efficiency (IQE) is the ratio between the generated charges and the number of absorbed photons at a given wavelength. In this case, the effective incident power (P_i) accounts for the losses by reflection, scattering or transmitted light.

The external quantum efficiency (EQE) is the ratio between the number of collected charges and the number of incident photons in the PV device at each wavelength. Expressing the incident energy as a function of wavelength, $E(\text{eV}) \cong 1240/\lambda$ (nm), the corresponding expression is given by Eq. 1.4.

$$EQE = \frac{\eta_{electrons}}{\eta_{photons}} = 1240 \frac{J_{sc}}{\lambda \cdot P_{in}} \quad (1.4)$$

1.3 Organic photovoltaics

Organic photovoltaics (OPV), also known as plastic solar cells, are characterised by the organic small molecules or polymers used as light-harvester materials. OPV devices are constituted by a structure of thin-layered films, each layer in the range of tens-hundreds of nanometres thickness, with a total stack (full OPV device) thickness of ~ 500 nm. An example of the typical OPV architecture is shown in Figure 1.4.

The photoactive layer (PAL), or active layer, is obtained by blending two semiconductors, known as the *electron donor* (D) and the *electron acceptor* (A), that for simplicity are named just as donor and acceptor, respectively. The PAL is where light is absorbed with consequent charge carrier generation, followed by their extraction at the electrodes (see more details in 1.3.1). In order for the light to reach the active layer, at least one semitransparent electrode is required, as it is shown in Figure 1.4.

Photoactive materials, which are conjugated systems, form PAL in OPV. In general, a conjugated organic molecule is characterised by having alternating single, and double bonds between carbon atoms. The single bonds are σ type whereas the double ones are formed by 1 σ and 1 π bonds and triple bonds have 1 σ and 2 π bonds. As a consequence of the bonding, π orbital and a π^* antibonding orbital are created. The π orbital is the highest occupied molecular orbital (HOMO) that has electrons in it whereas π^* orbital is the lowest unoccupied molecular orbital (LUMO) which is the lowest energy place to excite an electron upon excitation.^[43]

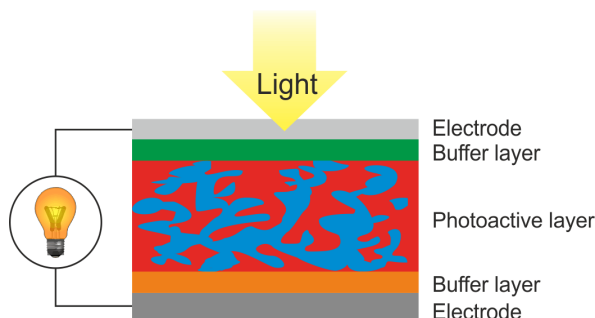


Figure 1.4. Sketch of a general organic solar cell.

1.3.1 Working principles of organic solar cells

Photoactive materials are characterised by their HOMO and LUMO energy levels (Figure 1.5(a)). The difference between such levels is what defines the bandgap (E_g) of an organic semiconductor. An electron can be photoexcited, taken from the HOMO to the LUMO, only when a photon has equal or higher energy than the bandgap of the material. For a blend of donor and acceptor materials sandwiched between an anode and a cathode, it is accepted that the difference between the LUMO of the acceptor and the HOMO of the donor defines the theoretical maximum open-circuit potential (V_{oc}^*), see Figure 1.5(a).^[44]

Traditionally, donor materials have been the main responsible for light absorption, whereas fully-conjugated ball-like acceptor called fullerenes have had a minor contribution, see more information in Chapter 2.^[45] However, after the irruption of the novel small-molecule acceptors materials called non-fullerene acceptors (NFAs) in the OPV field (section 1.3.4), both donor and acceptor materials have similar light absorption contribution in the PAL (Figure 1.5(a)).

We can divide the mechanisms that occur in a device, from light absorption to current extraction, into several steps (Figure 1.5(b)). In Figure 1.5(b,i), for simplicity indicated as (i), photons are absorbed by the photoactive materials in the device, resulting in photo-generated electron-hole pairs (*i.e.* excitons). As a consequence of the photoexcitation, an electron can jump from HOMO to LUMO energy levels. In contrast to inorganic semiconductors, where photoexcitation leads directly to separated charge carriers, in OPV these carriers are still bounded by Coulomb forces. This is due to the lower dielectric constant of organic materials compared to their inorganic counterparts. (ii) These excitons diffuse towards the donor:acceptor (D:A) interface. (iii) At the interface, the charge transfer from the donor to the acceptor occurs. (iv) Then, the electron-hole pair dissociates into free charges. (v) The free carriers, holes and electrons, are transported through donor and acceptor domains, towards the respective electrodes. (vi) Finally, the charges are collected at the electrodes. Unfortunately, some inherent losses are affecting all these steps.

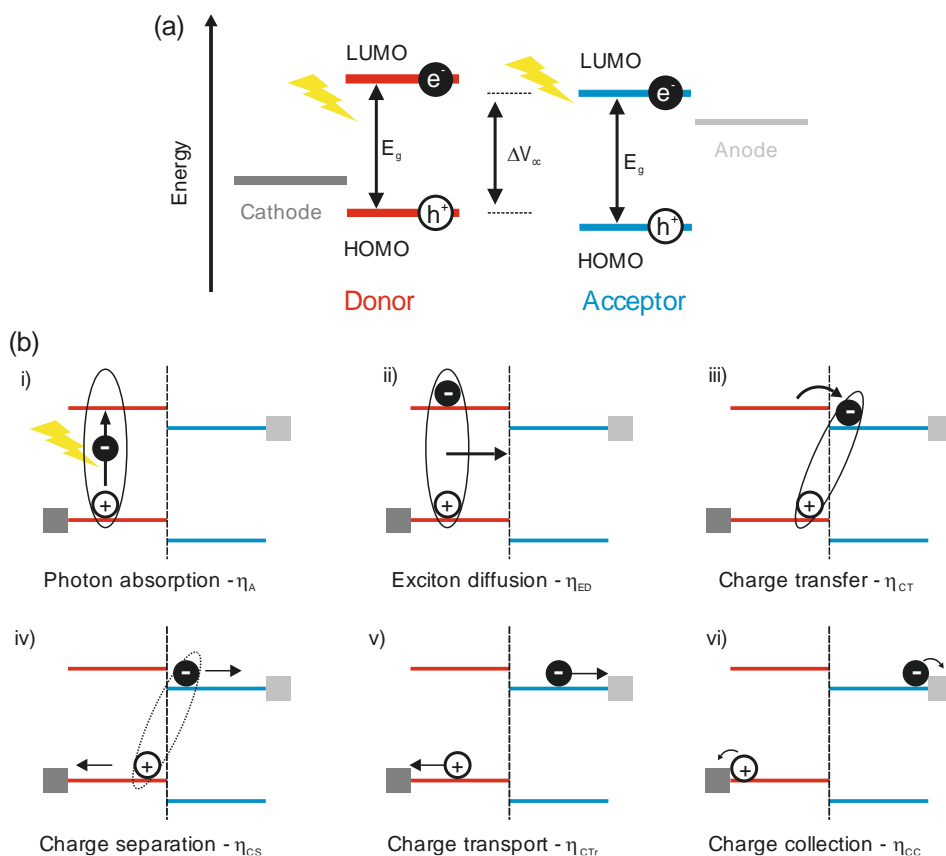


Figure 1.5. Power generation processes in organic solar cells. (a) Schematic of energy levels in a binary donor:acceptor system. (b) Steps in which the current generation and collection mechanisms can be divided: (assuming donor as the main light-harvester semiconductor). (i) Photon absorbed by donor and exciton is generated, (ii) exciton diffusion towards the donor:acceptor interface (highlighted with a vertical dashed line), (iii) charge transfer from the donor to the acceptor, (iv) exciton dissociation into free charges (charge separation), (v) charge transport of free carriers towards the electrodes and (vi) charge collection in electrodes.

For instance, not absorbed photons in (i). Non-radiative (thermalisation) and radiative (monomolecular) recombination of the exciton in (ii), (iii) and (iv). Moreover, free charges can recombine with opposite charges along the path towards the electrode (bimolecular recombination) or can fall into traps in (v). As a result, an efficiency value can be associated with each step and the product of all the efficiencies gives the PCE.

$$PCE = \eta_A \eta_{ED} \eta_{CT} \eta_{CS} \eta_{CTr} \eta_{CC} \quad (1.5)$$

These associated efficiencies of each of the processes shown in Figure 1.5(b) are namely absorption (η_A), exciton diffusion (η_{ED}), charge transfer (η_{CT}), charge separation (η_{CS}), charge transport (η_{CTr}) and charge collection (η_{CC}), see Eq. 1.5.

Among all the factors that influence the process efficiency, PAL structure has a strong impact on the steps that go from exciton generation to charge collection at the electrodes.

1.3.2 Structure of the photoactive layer

The first organic solar cells were sublimated molecules sandwiched between two metal electrodes with different work functions.^[46] Due to the low exciton diffusion length for most organic semiconductors (<20 nm), in such structures only those excitons generated in areas close to the electrode contribute to the photocurrent of single-junction devices, see Figure 1.6(a).^[47]

As an alternative to overcome the inefficient charge separation, a planar bilayer heterojunction device was proposed,^[48] see Figure 1.6(b). The combination of a *p-type* (electron donor) and a *n-type* (electron acceptor) materials enables the creation of the so-called p-n junction. In this case, the splitting of excitons into free charges occurs at the interface between the donor and acceptor materials. While representing an improvement because of a more effective exciton dissociation than homojunction, this configuration is still affected by the already mentioned short exciton diffusion length (~10 nm) that makes the majority of excitons decay before reaching the interface.^[49] As a consequence, an optimised bilayer structure requires a very thin PAL thickness (<40 nm) which reduces significantly the light absorption in the device.

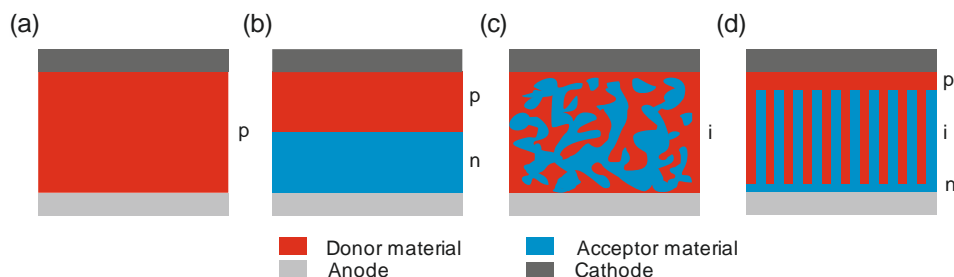


Figure 1.6. Organic solar cell architectures. (a) Single junction (homojunction), (b) bilayer heterojunction, (c) bulk heterojunction and (d) ideal interdigitated heterojunction.

To improve the light absorption capabilities of the bilayer structure, the so-called bulk heterojunction structure was proposed,^[50] see Figure 1.6(c). The essence of bulk heterojunction is similar to the bilayer structure in terms of materials with the same donor (*D*) and an acceptor (*A*) materials. In this case, a significant increase of the interface *D:A* area is obtained through the mixing of domains of each material.^[51] As a result, the bulk heterojunction strategy enables a higher charge separation efficiency and the possibility to manufacture more efficient thicker devices (>80 nm).^[52]

Ideally, the most efficient charge transport microstructure is a bulk interdigitated domains of alternating donor and acceptor materials, as depicted in Figure 1.6(d). *D:A* interface area is maximised while, at the same time, *D* and *A* pathways are optimised to efficiently collect the charges at the electrodes. Unfortunately, such ideal blend morphology is challenging to achieve experimentally. Nevertheless, some strategies such as the use of additives or post-thermal treatment or solvent treatment, have been reported to improve the preferential segregation of photoactive materials (*D:A* phase separation) and thus more favourable pathways for charge transport.^[53-55]

Besides controlling blend morphology, the use of interfacial or buffer layers are employed to improve hole and electron selectivity at the electrodes. The so-called electron and hole transport layers are characterised by their intermediate energy levels in between those of electrodes and PALs (understood as energy levels of donor and acceptor, Figure 1.5(a)). This cascade alignment enables the selective transport of one charge type, acting as a barrier for the opposite charge. The thickness of these interlayers ranges from a few nanometres up to 50 nm depending on the conductivity of the material.^[56] Moreover, these buffer layers limit the diffusion of electrode material into the PAL, preventing short-circuiting of devices.^[22,57] Very recently, the use of exfoliated WS₂ was demonstrated as an efficient PEDOT replacement with extremely high performance.^[58] Generally, buffer materials are oxides of inorganic materials (ZnO, MoO₃) or organic materials (PEDOT). More details about ETL and HTL materials are given in the following section.

1.3.3 OPV architectures

Conventional and inverted architectures are the two main strategies employed for the design of the stack of organic solar cells, see Figure 1.7. In the conventional configuration, positive charges (holes) are collected in the transparent electrode, typically indium tin oxide (ITO), with the aid of a hole selective transport layer (HTL). On the opposite side, negative charges (electrons) are collected at the top electrode, through the electron transport layer (ETL). By contrast, in the inverted configuration, the charge carriers flow is the opposite, with the electrons being collected at the bottom transparent electrode and the holes transported to the top and low work function electrode.

The use of Ag-based cathodes enables a better resistance to oxidation compared to Al-based ones due to the greater stability, attributing an important advantage to the inverted structure respect to the standard one.^[59]

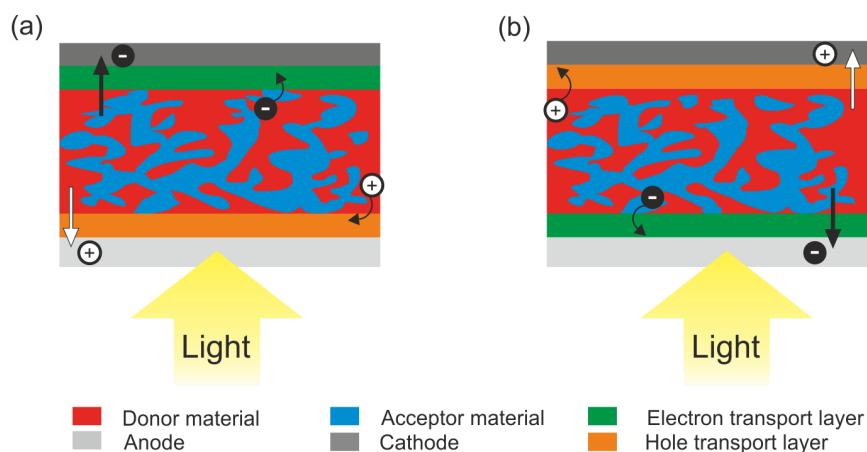


Figure 1.7. Device architecture of organic solar cells. (a) Conventional and (b) inverted configurations.

1.3.4 Photoactive materials

As discussed before, in less than 10 years the performance of OPV devices has overcome the milestone of 18%.^[33] This significant increase could not have been achieved without the development of the small molecular acceptors, namely non-fullerene acceptors (NFA), see Figure 1.2.

Before the intense NFA development, the fully conjugated ball-like fullerene acceptors with solubilisation chains (PC₆₀BM and PC₇₀BM) blended with a conjugated polymer donor were the most employed choice for top-performing systems.^[60-62] The conception of fullerenes was to facilitate charge extraction due to their high mobility, even with a limited light-harvesting contribution compared to polymeric donor materials, see Figure 1.8. For years, the OPV workhorse was polythiophene (P3HT, polymeric donor) blended with a fullerene (acceptor material, PC₆₀BM, PC₇₀BM or ICBA). This system, that enabled efficiencies over 6%, were employed in the first large-scale and fully solution-printed demonstrator.^[62,63]

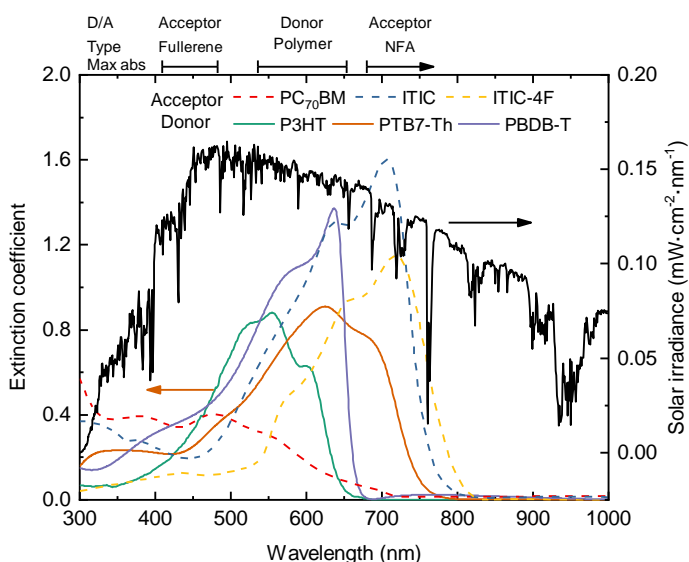


Figure 1.8. Absorption tunability of OPV materials. The extinction coefficient of some relevant OPV materials: PC₇₀BM, ITIC, ITIC-4F, P3HT, PTB7-Th and PBDB-T. Complex refractive indices were measured by Mr. Xabier Rodríguez-Martínez and Dr. Mariano Campoy-Quiles. On the top axis highlighted the maximum peak for the different type of OPV materials. Solar irradiance AM 1.5G (right axis). More details about these specific OPV materials in the experimental section.

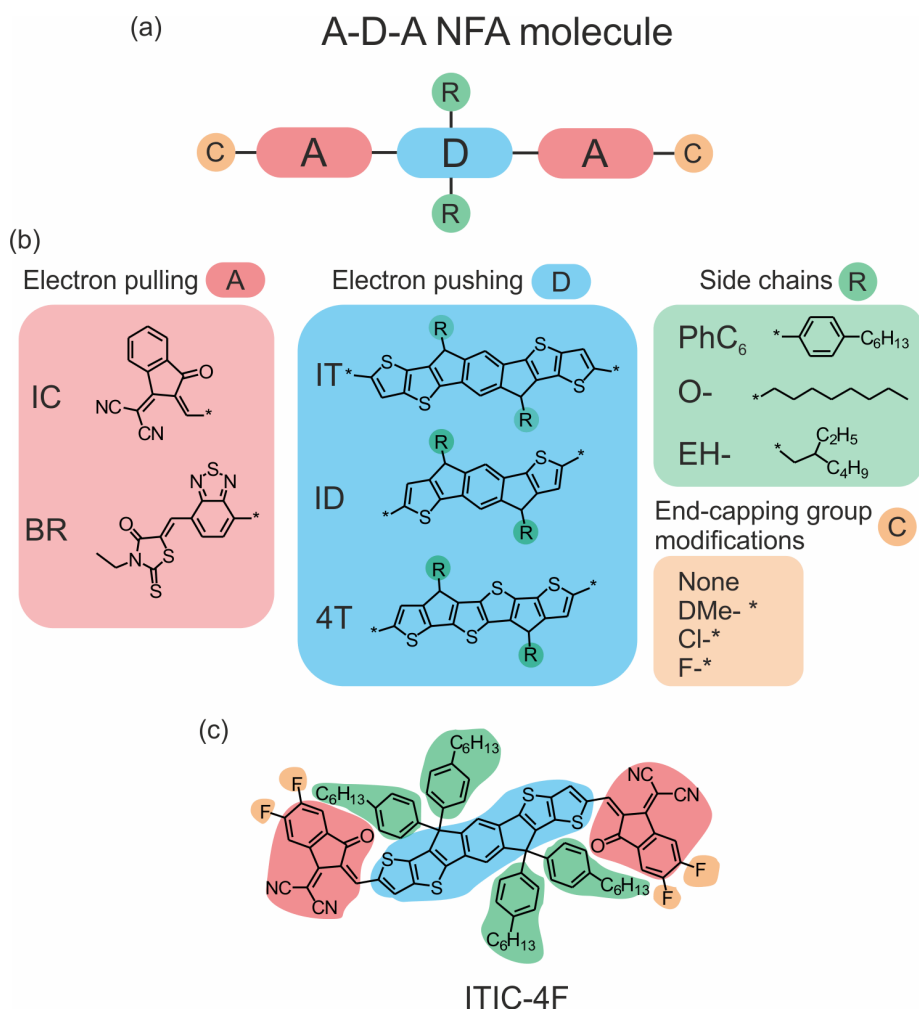


Figure 1.9. General chemical structure of A-D-A NFAs. (a, b) Building blocks that form the NFA molecule based on an electron pushing backbone (D) with radical side chains (R) and flanked by symmetrical electron pulling moieties (A) that can be modified by end-capping groups (C). O- refers to linear octyl whereas EH- to branched 2-ethylhexyl side chains. (c) Example of an NFA called ITIC-4F identifying its building blocks.

Polymeric donors were originally designed to harvest light in the solar spectrum regions with a higher power density (450-600 nm, Figure 1.8). To extend the light absorption of polythiophenes, novel conjugated polymers were synthesised. They are characterised by a lower bandgap enabling harvesting light in the near-infrared (see examples of PTB7-Th and PBDB-T in Figure 1.8). With this strategy, efficiencies over 9% were reported blending a low bandgap polymer with a fullerene acceptor.^[64]

One of the initiatives conducted to overcome the 12% milestone was the development of NFAs exploiting the intramolecular *push-pull* effect by alternating the presence of donor

and acceptor donating moieties (A-D-A), see Figure 1.9.^[65] This effect is achieved by attaching units with different electron affinity including a central electron-pushing core (donor unit, flanked by electron-pulling building blocks (acceptor unit), resulting in strong π - π interactions.^[65]

As an additional way of improving NFA properties, specific side chains (R) can be attached to the donor unit to improve the control of the solubility of molecules and, therefore, the PAL morphology. Recently, the attachment of chlorine and fluorine (Cl, F) atoms to the end-capping groups has enabled extending the light absorption to the near-infrared allowing efficiencies over 16%.^[66] Thanks to this chemical flexibility, several thousands of new molecules have been recently synthesised.^[65] As an example of the NFA modular design, ITIC-4F (Figure 1.9(c)), is given. Furthermore, recent theoretical work has predicted efficiencies over 20% in NFA-based OPV by reducing electron-hole recombination and having a balanced charge carriers mobilities.^[67]

1.3.5 State-of-the-art in OPV

The current top-performing binary OPV consists of a polymeric donor blended with one NFA (binary combination)^[33,66] or two NFAs (ternary combination)^[35] yielding in both cases efficiencies over 16% (Table 1.3). On the one hand, systems based on both polymeric donor and acceptor semiconductors have reached over 11% of PCE.^[68] The main bottleneck of all-polymer systems is the reduced light-harvesting capabilities of polymeric acceptors, compared with NFAs, as suggested by the low photocurrent values (~ 12 mA/cm² compared to >25 mA/cm² for other blends), see Table 1.3. Despite their relatively low performance compared to NFA-based blends, all-polymer systems are very relevant for commercialisation due to their superior properties including stability, processability (viscosity and wettability) and mechanical resistant. This latter property eases their potential integration into, for instance, foldable photoactive elements.^[68,69]

On the other hand, all-small molecule devices (small molecule donor and acceptor materials) show an impressive performance of over 14% due to the excellent light-harvesting capabilities (24 mA/cm²). However, it exhibits moderate FF values (68%, compared to $>74\%$ for other approaches) as a consequence of the low mobilities of small-molecule donor materials in comparison to polymeric ones.^[70]

Table 1.3. State-of-the-art of top-performing OPV systems. Please see material acronyms in the given references.

| Type | Materials | V _{oc} (V) | J _{sc} (mA/cm ²) | FF (%) | PCE (%) | Area (mm ²) |
|-------------------------|----------------|------------------------|--|-----------|------------|----------------------------|
| Binary ^[66] | PBDB-TF/BTP-F | 0.87 | 25.4 | 75.0 | 16.5 | 9 |
| Binary ^[33] | D18/Y6 | 0.86 | 27.7 | 76.6 | 18.2 | 2.6 |
| Ternary ^[35] | PM6/BTP-M/Y6 | 0.88 | 26.6 | 73.5 | 17.0 | 4 |
| Pol:Pol ^[68] | PTzBI-Si/N2200 | 0.88 | 11.6 | 75.8 | 11.8 | 4 |
| SM:SM ^[70] | ZR1/Y6 | 0.86 | 24.3 | 68.4 | 14.3 | 4 |
| Tandem ^[71] | Binary/Ternary | 1.64 | 14.3 | 72.1 | 17.4 | 4 |
| Module ^[72] | TPD-3F:ITIC-4F | 4.5 | 17.3 | 64.0 | 10.4 | 2040 |
| Module ^[73] | N.A. | 9.98 | 21.3 | 71.1 | 13.2 | 2613 |

Finally, for a thesis focused on upscaling, it is worth highlighting the current record in OPV modules (series on interconnected devices) of 26 cm² with ~13% of PCE.^[73] These modules were manufactured following a similar process to that described in Chapter 6, a combination of blade-coating and laser ablation to obtain the series-connected solar cells. Although the photoactive materials employed for the record OPV devices (neither lab-scale nor module) have not been disclosed, the reduction in performance with the active area is negligible considering the 653-fold increase with respect to the size of the lab-cell devices (Table 1.3). Therefore, these advances have made OPV one step closer to the intensive-commercialisation.

1.4 OPV companies and applications

1.4.1 OPV companies

The main market niches for organic photovoltaics are the so-called Internet-of-Things (IoT) and building-integrated photovoltaics (BIPV). There are already OPV companies commercialising OPV technology for both markets, Table 1.4. It is noteworthy that there is a similar number of companies developing solutions for BIPV and IoT. While in general BIPV requires opaque or semitransparent modules with a large area, IoT can be smaller and typically opaque to maximise indoor light harvesting.

Regarding printing techniques (solution and evaporation-based), one main conclusion is that most OPV companies rely on solution processes due to the lower embodied energy and therefore the lower energy return on investment (EROI), assuming similar performances, see Table 1.4.^[74-76] Alternatively, to the best of our knowledge, Heliatek is the only company that manufactures evaporated-based OPV in a fully roll-to-roll process under vacuum with reliable results.^[77] However, the development of an evaporation-based pilot line requires a higher initial investment than the solution-based counterpart. Avoiding evaporation steps for manufacturing OPV devices reduce the embodied energy for the fabrication and consequently the EPBT.^[78]

Table 1.4. Current leading OPV manufacturer companies.

| Company | Country | Business | Printing technology | Reference |
|-------------------------|----------------|----------|---------------------|-----------|
| Sunew | Brasil | BIPV | Solution | [74] |
| Heliatek | Germany | BIPV | Evaporated | [77] |
| Armor/Opvius | France-Germany | BIPV/IoT | Solution | [76] |
| Enerthing | Germany | IoT | Solution | [75] |
| Epishine | Sweden | IoT | Solution | [79] |
| InfinityPV | Denmark | BIPV/IoT | Solution | [80] |
| Savvy Science | UK | IoT | Solution | [81] |
| Kolon Industries | South Korea | BIPV/IoT | Solution | [82] |
| Dracula Technologies | France | IoT | Solution | [83] |
| Toyobo | Japan | IoT | Solution | [84] |
| Solar window technology | USA | BIPV | Solution | [85] |
| Eni | Italy | BIPV | Solution | [86] |
| Ribes tech | Italy | IoT | Solution | [87] |

1.4.2 OPV applications

OPV has the potential to energise IoT devices, helping to increase the lifespan of batteries or even substitute them.^[88,89] The mechanical flexibility enables OPV to be integrated as part of clothes (wearables)^[90] or as a portable sun-battery that can be rolled and used in areas with no electricity,^[80] see Figure 1.10.

In other outdoor applications, OPV can exploit their intrinsic mechanical flexibility when deposit on a flexible substrate to be conformally applied into complex and non-flat shapes such as automobiles, aeroplanes, trains and ships or other vehicle skins exposed to intense solar exposure.^[91] Similarly, OPV can take part of self-powering portable electronics in the context of textiles or backpacks applications.^[90]

One of the envisioned applications for OPV is to drive low power off-grid electronics. As explained in section 1.3.4, NFA-based OPV can be chemically designed to harvest light in a specific range of the spectrum. As a result, OPV show significantly better performance under indoor illumination (LED, incandescent, fluorescent) than conventional Si-PV technologies.^[92] Interestingly, NFA-based devices show efficiencies over 20% under indoor illumination.^[93,94]

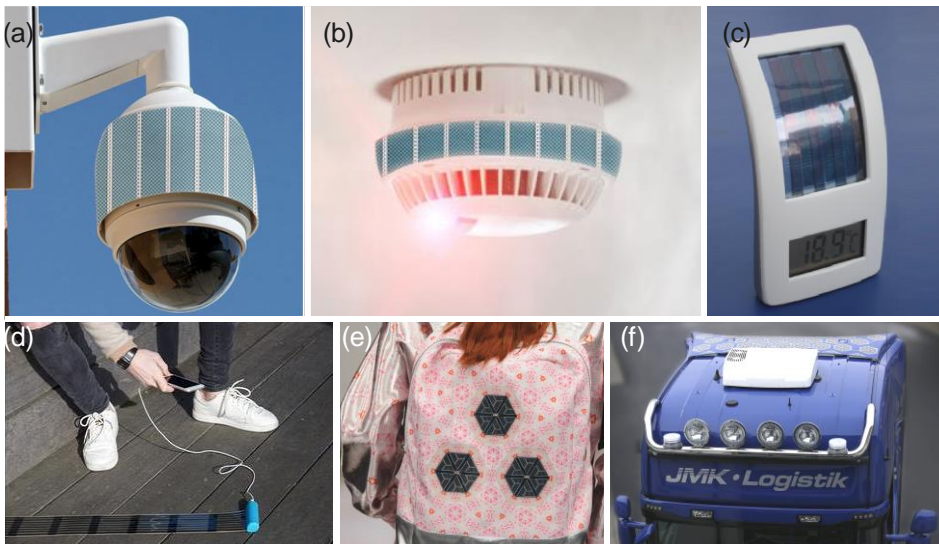


Figure 1.10. Examples of OPV for applications in the Internet of Things (IoT). (a) Powering monitoring systems^[76], (b) sensing^[76], (c) thermometers^[79], (d) foldable solar chargers^[80], (e) wearables^[90] and (f) vehicles^[91].

Thanks to this, OPV modules are implemented into electronic devices such as screens, calculators and interactive labels, among others. Therefore, this is an efficient way of *light recycling*.^[92,93] On the other hand, from the BIPV perspective, OPV offers great potential to be exploited as a key technology to create active light-harvesting surfaces on a very large scale. BIPV has become one of the main business areas of recent OPV applications.^[95]

Factors like the ease of tuning the appearance, the degree of transparency, lightweight and the free-device design make OPV an optimal choice for BIPV such as windows or curtains.^[96] For instance, OPV can be found integrated as part of opaque architectural elements such as urban furniture, façades or building skins, see Figure 1.11.

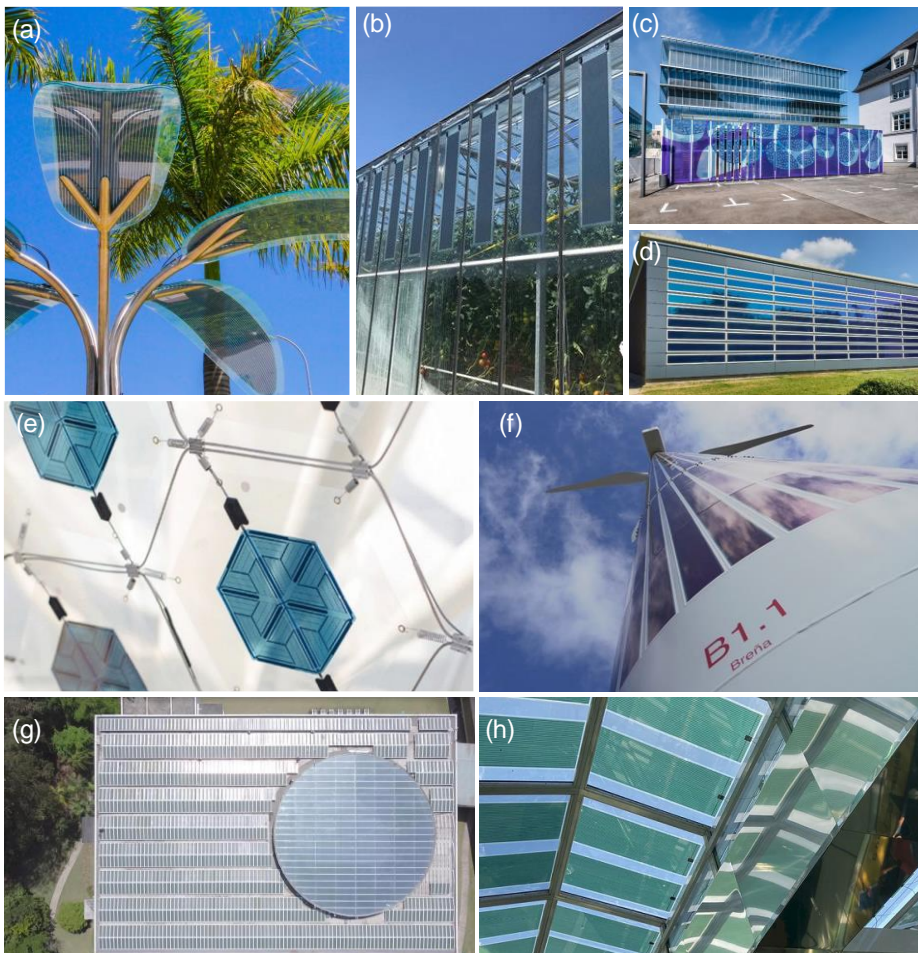


Figure 1.11. Examples of OPV applications for building-integrated photovoltaics. Urban furniture,^[97] (b) greenhouse^[98]; (c)^[99] and (d) ^[100] façades, (e) solar tree,^[101] (f) tower of a wind turbine,^[102] (g) opaque^[103] and (h) semitransparent^[104] rooftops.

Table 1.5. Largest OPV installations in the world.

| Company | Installation | Year | Area (m ²) | Installed power (kW) | Printed technology | Ref. |
|----------|----------------------------------|------|------------------------|----------------------|--------------------|-------|
| Sunew | Natura (Brasil) | 2019 | 1800 | N.F.* | Solution | [103] |
| Sunew | Shopping da Bahia (Brasil) | 2019 | 125 | N.F. | Solution | [104] |
| Heliatek | Pierre Mendes School (France) | 2019 | 500 | 22.5** | Evaporated | [105] |
| Heliatek | Duisburger Hafen (Germany) | 2018 | 185 | N.F. | Evaporated | [106] |
| Heliatek | Breña Wind Farm Albacete (Spain) | 2020 | 173 | 9.36 | Evaporated | [102] |
| Opvius | Expo Milan (Italy) | 2015 | >250 | >5 | Solution | [101] |

* Not found (NF) but it is estimated 73.4 MWh of energy a year. ** 23.8 MWh of electricity will be generated annually.

Non-opaque OPV offers the possibility of integration into semitransparent elements including glazings, windows, rooftops or greenhouses.^[107] Very recently in Spain, an OPV demonstrator was installed on part of a wind turbine tower in order to harvest sunlight from this unused surface.^[102] This example reveals the great synergy potential between two renewable technologies combined in a single installation.^[102]

During the year 2019 new records were achieved with both lab-scale devices and modules. For instance, Sunew company has manufactured a rooftop coverage in Brasil with the largest global OPV installation known until now.^[103] Similarly, modules from Heliatek effectively harvest area of 500 m² in France.^[105] According to these promising demonstrators, nowadays OPV has proven to be a truly upscalable technology with a fully printed milestone covering a surface nearly to 2000 m².^[103]

1.5 Motivation and structure of the thesis

1.5.1 Motivation

As it was discussed throughout the general introduction, the field of organic photovoltaics (OPV) has recently achieved two very relevant milestones: 18% performance for lab-scale devices and the first $\sim 2.000\text{ m}^2$ installation. These examples highlight the unprecedented advancement that the field has experienced during the last few years. These achievements can be explained, at least in part, by the intense development of the so-called non-fullerene acceptors (NFAs).

Despite OPV having already reached the market, its penetration is still at the prototyping/demonstrator level (Table 1.5). The majority of the studies at lab-scale are focused on optimising the device performance; however, other technologically relevant features need to be addressed for its full deployment. For instance, substituting ITO electrode with a cost-effective alternative, understanding the degradation mechanisms under real-operating conditions, optimising the synthesis of organic semiconductors, assessment of aesthetics for the integration as part of BIPV or IoT applications and reducing the lab-to-fab gap. Among the mentioned topics, this thesis deals with the aesthetics, high-throughput screening and upscalability of two NFA-based systems from mm^2 -scale devices to cm^2 -scale modules manufactured by industrially-relevant techniques such as slot-die coating and laser ablation.

Note that this upscaling thesis has been developed within the collaboration framework between Dr. Mariano Campoy's group at the Institute of Materials Science of Barcelona (ICMAB) and the Printed Electronics department of the Technological Centre of Catalunya (EURECAT) under the supervision of Dr. Marco Stella and Dr. Eugenia Martínez. Additionally, a 3-month PhD stay was carried out at Merck Chemicals Ltd (Southampton, UK) under the guidance of Dr. Ignasi Burgues, Dr. Graham Morse and Dr. Golnaz Sadoughi. In this respect, most of the lab-scale studies were carried out at ICMAB, whereas the upscaling experiments were carried out at EURECAT and Merck Chemicals.

1.5.2 Structure

This thesis is structured in seven chapters and follows the flowchart as depicted in Figure 1.12.

The processing methods, materials, device fabrication details, characterisation techniques and mathematical framework employed in this thesis are presented in Chapter 2.

In Chapter 3, a mathematical framework is developed and validated to investigate the colour tuning capability in organic solar cells. Three different colour tuning strategies are explored: interference effects at the active layer, D:A ratio and specific materials evaluation, and ternary combination of semiconductors. Finally, a genetic algorithm is used for the identification of solar cells characteristics (thickness and composition) whose appearance reproduces a desired colour.

A systematic study of the influence of several processing parameters on the performance of solar cells based on P3HT:NFAs binary systems is conducted in Chapter 4. The fabrication of one dimensional (1D) graded photoactive layers films allows to speed-up the optimisation process and analyse in a combinatorial way the performance sensitivity on manufacturing conditions while reducing the experimental resources. We investigate possible relationships between active layer thickness and degradation. Finally, as a proof-of-concept, we demonstrate the up-scaling of P3HT:O-IDTBR modules by roll-to-roll.

Chapter 5 extends the 1D combinatorial gradient (Chapter 4) to 2D graded films with simultaneous variations in two parameters of interest (thickness and composition). In order to show the potential, we apply these 2D gradient maps to 10 OPV systems consisting of donor/acceptor pairs chosen between two low bandgap polymers and five different NFAs. A Raman-based methodology is presented to deduce photoactive layer characteristics, which is measured co-locally with light beam induced current used to assess the local photocurrent. With this high-throughput methodology, a significant reduction in terms of raw semiconductors and experimental time are achieved.

Chapter 6, the last experimental chapter discusses the fabrication of semitransparent modules with low-cost manufacturing processes. The detailed sequential laser ablation and coating steps with the optimisation of the module geometry and laser parameters are presented. A further co-local optoelectronic characterisation of modules is also given.

Finally, Chapter 7 summarises the general conclusions and provides future perspectives that arise from this work.

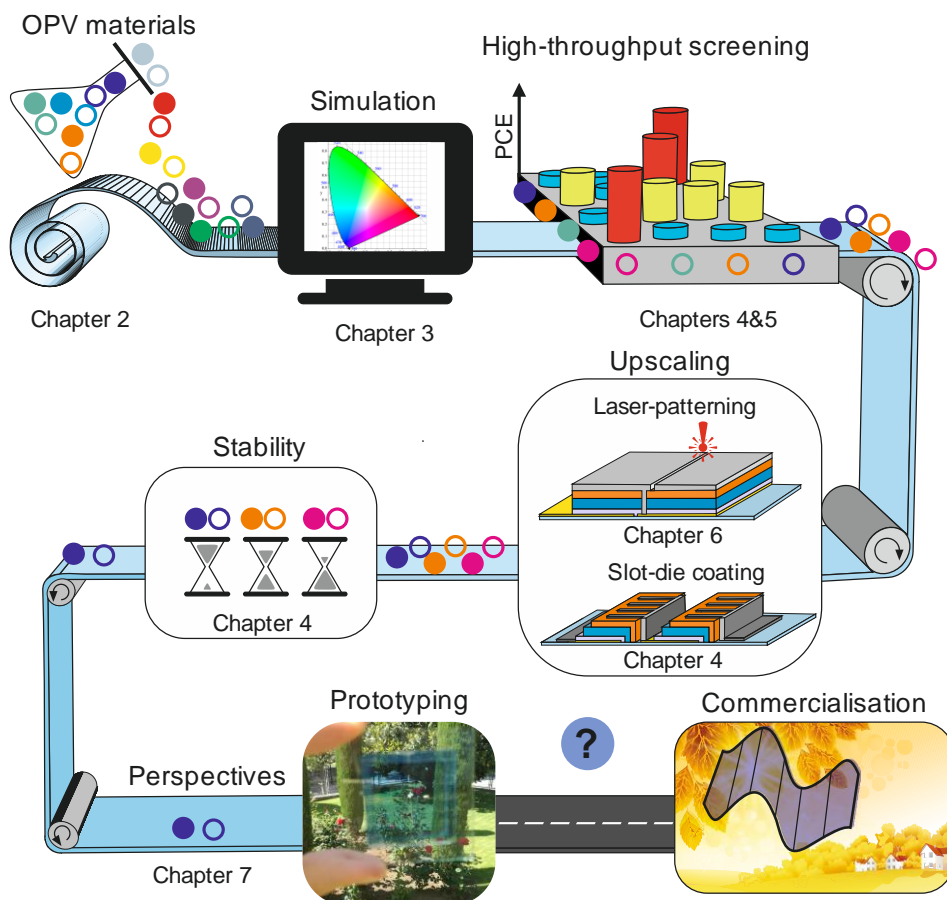


Figure 1.12. Workflow of the thesis highlighting the most relevant topics.

Chapter 2 Materials and Methods

ABSTRACT

The processing methods, device fabrication, materials and characterisation techniques used throughout this thesis are described here. Special emphasis is set on high-throughput and solution-process techniques to manufacture graded devices in the parameters of interest (thickness, post-thermal annealing and composition). This enables to speed up the screening and optimisation process of OPV materials at very low embodied cost. In order to facilitate the transference from lab-to-fab, we used only manufacturing techniques compatible with large-scale production such as blade coating and slot-die. In the section dedicated to characterisation, advanced co-local maps (light beam induced current, LBIC) were used to correlate the performance of OPV materials with its optical properties (Raman scattering and photoluminescence). Finally, a detailed description of the optical modelling to predict thin-film colour is given. It is worth highlighting that a database was designed and developed to store more than 5000 JV curves during the thesis.

Parts of this chapter have been published in [I], [II], [III], [IV], [V].

2.1 Materials

All OPV devices manufactured in this thesis followed the inverted architecture. A simplified sketch of the sequential manufacturing process of OPV devices is depicted in Figure 2.1. For the vast majority of lab-scale devices, electron transport layer (ETL) and photoactive layer (PAL) were blade-coated whereas the hole transport layer (HTL) and top-electrode were thermally evaporated (except HTL in Chapter 6). Note that OPV samples have glass slide dimensions (7.5x2.5 cm). With this particular sample design, each lab-scale device contains 24 pixels, 12 in each side of the sample leading to 24 devices with an 8-mm² active area (Figure 2.1(a)). In the majority of lab-scale experiments, we took advantage of it and we employed a high-throughput combinatorial approach to manufacture photoactive layers with variations in the parameters of interest (thickness, composition or thermal annealing).

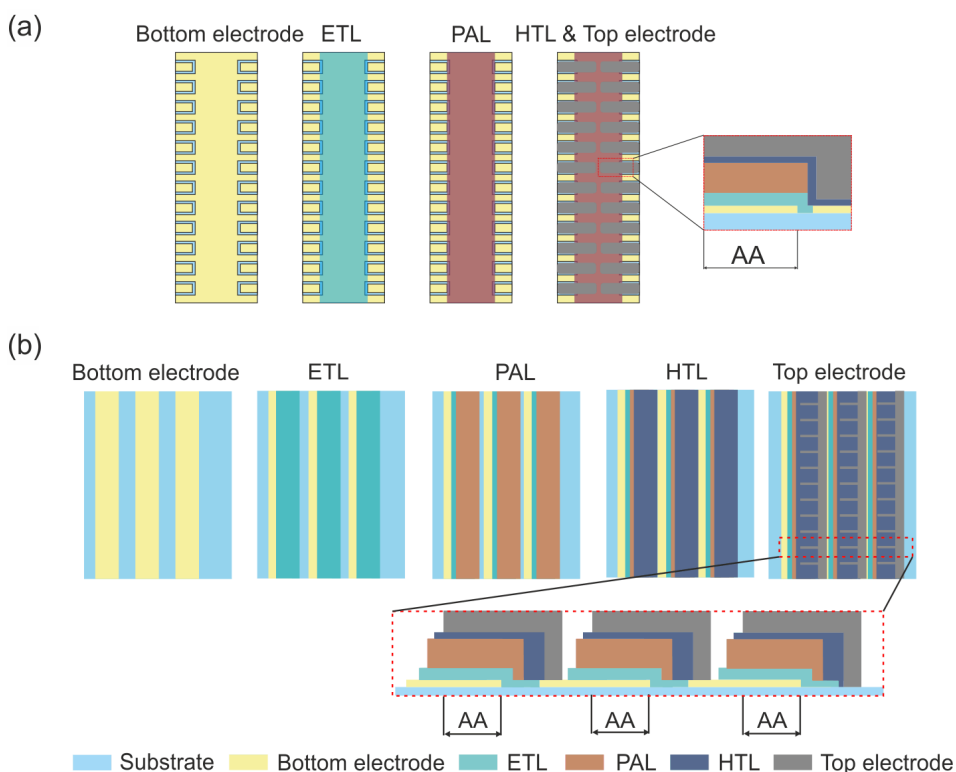


Figure 2.1. Top-view and cross-section sketches for different device scales. (a) Lab-scale and (b) large-scale (roll-to-roll) OPV devices. In lab-scale devices, ETL and PAL films are wiped out from selected areas before the evaporation of HTL and top electrode materials. AA shows the length of the device active area.

Thanks to this, it is possible to easily explore the relevant OPV parameters in a very limited time and reducing significantly the material consumption.

On the other hand, large-scale devices consist of a sequential fully-printed layered structure with a controlled horizontal offset that ensures a series of interconnection between cells (Figure 2.1(b)). A detailed explanation of R2R modules is given at the end of Chapter 4. Note that other type of module design, laser-patterned, is described in Chapter 6. In the following sections, OPV materials used in this thesis are listed following: bottom electrode or (anode)/ETL/PAL/HTL /top electrode (cathode).

2.1.1 Electrode materials

The following listed materials were employed as opaque/semitransparent electrode.

- Pre-patterned ITO coated glass (25x75 mm) with $20 \Omega/\square$ and 100 nm thickness, provided from Ossila.
- ITO strip coated PET with $50 \Omega/\square$ and 150 nm thickness, provided by Technifilm.
- Ag: Thermally evaporated (pellets from Kurt J. Lesker) lab-scale devices and Ag screen-printed paste 5025 from DuPont for roll-to-roll (R2R) experiments.
- Clevios PH1000: Highly conductive PEDOT from Heraeus used in semitransparent devices in Chapter 6.

2.1.2 Electron and hole transport materials

As electron transport materials, ZnO and AZO nanoparticles dispersion (N-10, N-20X, Avantama) in isopropanol (IPA) were used. Depending on the manufacturing technique, different hole transport materials were used.

- Evaporation-process: Molybdenum trioxide (MoO_3) from Alfa Aesar.
- Solution-process: Two types of PEDOT:PSS: Clevios PVP Al 4083 (Chapter 6) and Clevios FHC Solar for R2R (Chapter 4), both provided from Heraeus.

2.1.3 Solvents

All solvents were purchased from Sigma-Aldrich and were used without further purification. In particular, the solvents were chlorobenzene (CB), *o*-dichlorobenzene (DCB), toluene and *o*-xylene. Common cleaning solvents such as acetone, 2-propanol and ethanol were purchased from Labbox.

2.1.4 Photoactive materials

The studied photoactive blends consist of a binary mixture between electron donor and acceptor materials. Some of the photoactive materials used in this thesis were commercially available, others synthesised by collaborating groups. All these materials were processed from solution in a total concentration of 15 mg/mL and, typically, in 1:1 (w:w) D:A ratio and once blended stirred overnight at 80°C.

2.1.4.1 Donor materials

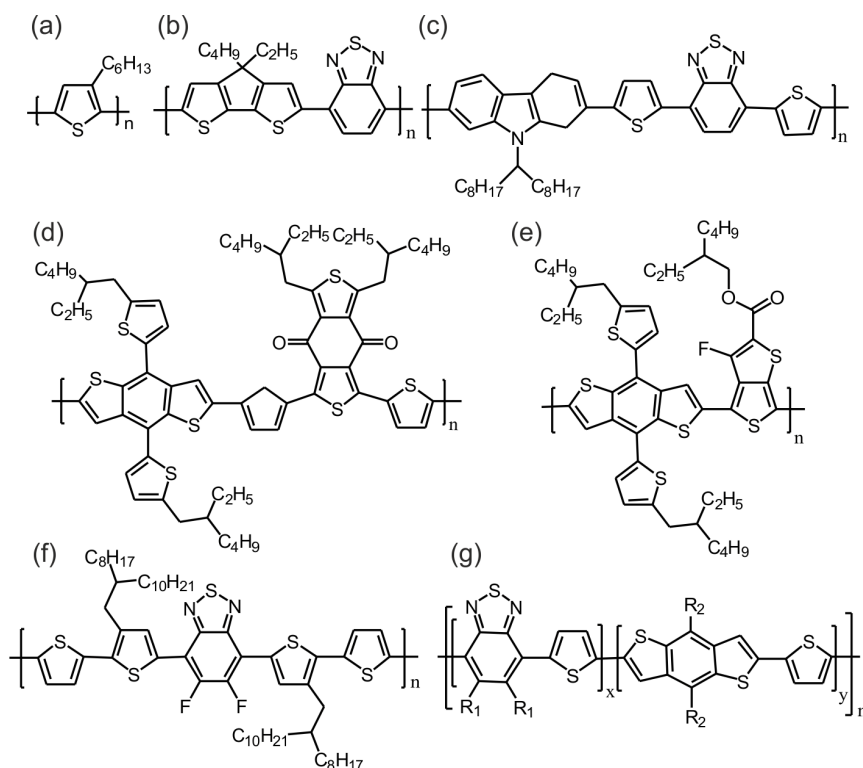


Figure 2.2. Chemical structure of the donor materials used in this thesis. (a) RR-P3HT, (b) PCDTBT, (c) PCPDTBT, (d) PBDB-T, (e) PTB7-Th, (f) PffBT4T-2OD and (g) PBTZT-stat-BDIT-8

The chemical structures of the polymers used in this thesis are given in Figure 2.2. The polymers used for upscaling were regioregular poly(3-hexylthiophene-2,5-diyl) (RR-**P3HT**), Chapter 4, provided by Sigma Aldrich for lab-scale devices, (regioregularity >96%, $M_w = 20\text{-}50$ kDa) and Rieke Metals for R2R experiments (regioregularity 91-94%, $M_w = 50\text{-}70$ kDa) and **PBTZT-stat-BDTT-8**, in Chapter 6 provided by Merck Chemicals GmbH ($M_w = 49.5$ kg/mol). The complete IUPAC nomenclature of PBTZT-stat-BDTT-8 is not available. The side chains R_1 and R_2 have not been disclosed.

The polymer poly[N-9'-heptadecanyl-2,7-carbazole-alt-5,5-(4',7'-di-2-thienyl-2',1',3'-benzothiadiazole)] (**PCDTBT**, from Ossila), poly[2,6-(4,4-bis(2-ethylhexyl)-4H-cyclopenta[2,1-b;3,4-b']dithiophene)-alt-4,7-(2,1,3-benzothiadiazole)] (**PCPDTBT**, from Sigma Aldrich) and poly[(5,6-difluoro-2,1,3-benzothiadiazol-4,7-diyl)-alt-(3,3''-di(2-octyldodecyl)-2,2';5',2'';5'',2'''-quaterthiophen-5,5'''-diyl)] (**PffBT4T-2OD**, namely PCE11 from Sigma Aldrich) were used in colour simulations (0).

The polymers poly[4,8-bis(5-(2-ethylhexyl)thiophen-2-yl)benzo[1,2-b;4,5-b']dithiophene-2,6-diyl-alt-(4-(2-ethylhexyl)-3fluorothieno[3,4-b]thiophene)-2-carboxylate-2,6-diyl)] (**PTB7-Th**, also known as PCE10 from Ossila) and poly[(2,6-(4,8-bis(5-(2-ethylhexyl)thiophen-2-yl)-benzo[1,2-b;4,5-b']dithiophene))-alt-(5,5-(1',3'-di-2-thienyl-5',7'-bis(2-ethylhexyl)benzo[1',2'-c:4',5'-c']dithiophene-4,8-dione)] (**PBDB-T** namely PCE12 from 1-Material), were used in the high-throughput screening section (Chapter 5).

2.1.4.2 Acceptor materials

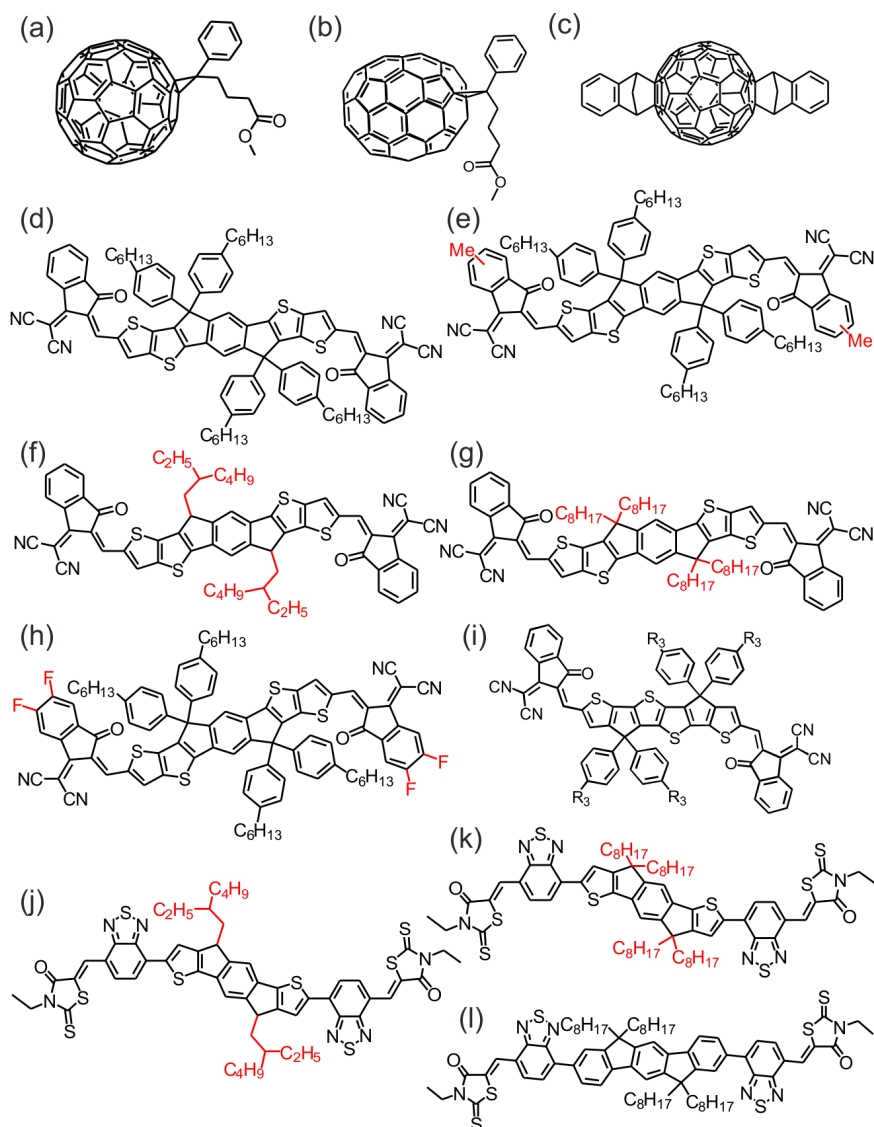


Figure 2.3. Chemical structure of the acceptor materials used in this thesis. (a) PC₆₀BM, (b) PC₇₀BM, (c) ICBA, (d) ITIC, (e) ITIC-M, (f) EH-ITIC, (g) O-ITIC, (h) ITIC-4F, (i) 4TICO, (j) EH-IDTBR, (k) O-IDTBR and (l) O-IDFBR. Highlighted in red the modifications in the backbone and side chains of molecules with the same core.

The chemical structures of the acceptor materials employed in this thesis are shown in Figure 2.3. As acceptor fullerenes, [6,6]-phenyl-C₆₁-butyric acid methyl ester (**PC₆₀BM**), [6,6]-phenyl-C₇₁-butyric acid methyl ester (**PC₇₀BM**) and 1',1'',4',4''-tetrahydro-di[1,4]methanonaphthaleno[1,2:2',3',5,6:2'',3'']-[5,6]fullerene-C₆₀ (**ICBA**), were used

and all of them purchased from Solenne BV. As small molecule acceptors, also called non-fullerene acceptors (NFAs), 3,9-bis(2-methylene-(3-(1,1-dicyanomethylene)-indanone))-5,5,11,11-tetrakis(4-hexylphenyl)-dithieno[2,3-d:2',3'-d']-s-indaceno[1,2-b:5,6-b']dithiophene (**ITIC**), 3,9-bis(2-methylene-((3-(1,1-dicyanomethylene)-6/7-methyl)-indanone))-5,5,11,11-tetrakis(4-hexylphenyl)-dithieno[2,3-d:2',3'-d']-s-indaceno[1,2-b:5,6-b']dithiophene (**ITIC-M**), 3,9-bis(2-methylene-((3-(1,1-dicyanomethylene)-6,7-difluoro)-indanone))-5,5,11,11-tetrakis(4-hexylphenyl)-dithieno[2,3-d:2',3'-d']-s-indaceno[1,2-b:5,6-b']dithiophene (**ITIC-4F**), (5*Z*,5'*Z*)-5,5'-(((4,4,9,9-(2-ethylhexyl)-4,9-dihydro-s-indaceno[1,2-b:5,6-b']dithiophene-2,7-diyl)bis(benzo[c][1,2,5]thiadiazole-7,4-diyl))bis(methanylylidene))bis(3-ethyl-2-thioxothiazolidin-4-one)) (**EH-IDTBR**), (5*Z*,5'*Z*)-5,5'-(((4,4,9,9-tetraoctyl-4,9-dihydro-s-indaceno[1,2-b:5,6-b']dithiophene-2,7-diyl)bis(benzo[c][1,2,5]thiadiazole-7,4-diyl))bis(methanylylidene))bis(3-ethyl-2-thioxothiazolidin-4-one)) (**O-IDTBR**) and (5*Z*,5'*Z*)-5,5'-((7,7'-(6,6,12,12-tetraoctyl-6,12-dihydroindeno[1,2-b]fluorene-2,8-diyl)bis(benzo[c][1,2,5]thiadiazole-7,4-diyl))bis(methanylylidene))bis(3-ethyl-2-thioxothiazolidin-4-one)) (**O-IDFBR**) were employed and purchased from 1-Material.

On the other hand, ITIC with side chains modifications, 3,9-bis(2-methylene-((3-(1,1-dicyanomethylene)-6/7-methyl)-indanone))-5,5,11,11-tetrakis(4-octyl)-dithieno[2,3-d:2',3'-d']-s-indaceno[1,2-b:5,6-b']dithiophene (**O-ITIC**) and 3,9-bis(2-methylene-((3-(1,1-dicyanomethylene)-6/7-methyl)-indanone))-5,5,11,11-tetrakis(2-ethylhexyl)-dithieno[2,3-d:2',3'-d']-s-indaceno[1,2-b:5,6-b']dithiophene (**EH-ITIC**), were provided by the group of Prof. Martin Heeney (Imperial College London). 4TICO was provided by Merck Chemicals GmbH. The complete IUPAC nomenclature of 4TICO is not available. R₃ side chains have not been disclosed.

2.2 Lab-scale processing techniques

2.2.1 Cleaning

All lab-scale glass substrates, ITO-coated glass, were cleaned by sequential ultrasonication baths of 5 minutes each in acetone, 10% vol. Helmanex solution in H₂O, isopropanol and finally 10% w/v NaOH in water solution. Finally, substrates were dried with compressed air.

2.2.1.1 Blade-coating

Although the OPV record solar cells were spin-coated^[58] (Figure 2.4(a)), this technique is limited to sheet-to-sheet manufacturing with low material yield. In this work, ETL and PAL and, HTL and top electrode layers, in some cases like in Chapter 6, were blade-coated (Figure 2.4 (b)) due to their easy transfer from lab to large scale.

Blade-coating, also known as doctor blading, is a very relevant deposition method frequently used in OPV research.^[108-110] Figure 2.5(a) shows a sketch of the blade coating process. A volume of ink (V) is deposited close to the gap (G) between the applicator and the substrate where a meniscus is formed. By moving the automatic coater (ZUA 2300, Zehntner), the solution is distributed along the substrate forming a wet film. The drying kinetics are controlled by adjusting the platform temperature (from 40°C to 150°C).

$$d = \frac{1}{2} \frac{G c}{\rho} \quad (2.1)$$

The empirical relationship for the dried film thickness is shown in Eq. 2.1 where G is the blade-substrate gap, c is the ink concentration and ρ is the ink concentration.^[111] From a practical standpoint, cast volume (V) and blade speed (v) also affect the final film thickness.

In our group, Dr. Bernhard Dörfling modified the commercial blade coater machine (ZUA 2000, Zehntner) by coupling a home-made speed controller to the equipment in order to obtain acceleration or deceleration during the deposition process, see Figure 2.5(a). Photoactive films were cast by decelerating the blade from 99 mm/s to 1 mm/s during solution spreading across the substrate length (7.5 cm).

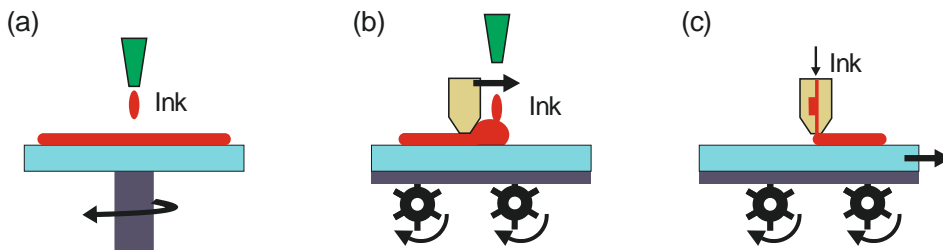


Figure 2.4. Sketch of the solution-processed techniques. (a) Spin-coating, (b) blade-coating and (c) slot-die coating.

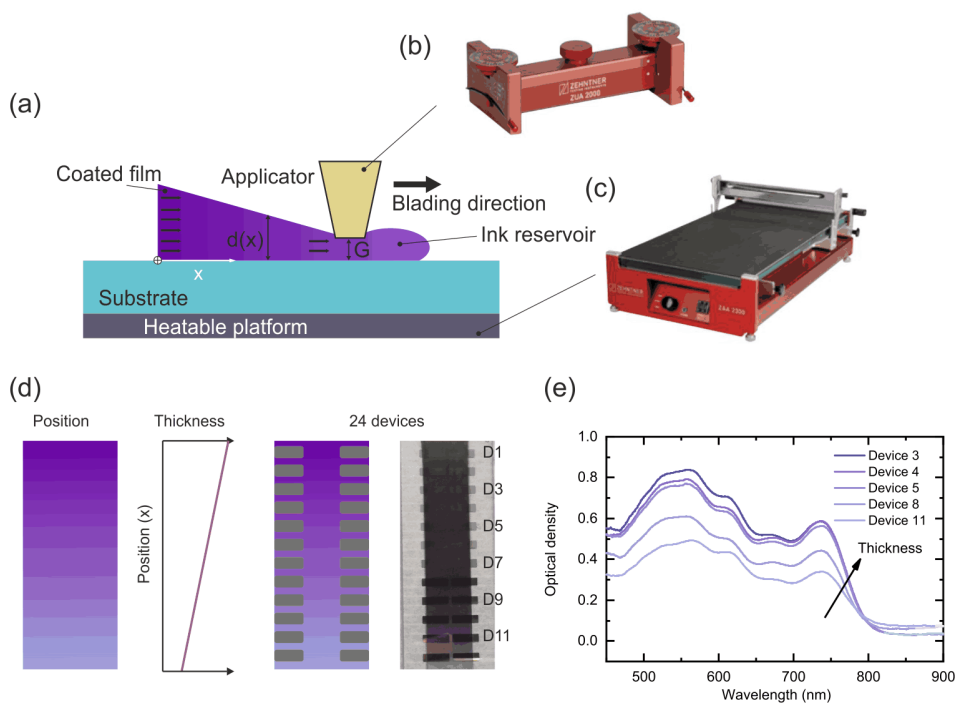


Figure 2.5. Thickness-graded films by blade-coating. (a) Sketch for making thickness gradient films by decelerating the applicator when passing along the substrate. Picture of the (b) applicator and (c) blade coater. (d) Sketch of the graded devices on a single substrate and a real photograph. (e) Optical density spectra of a thickness-graded photoactive layer of P3HT:O-IDTBR.

This variable speed approach enables the exploration the thickness-performance dependence in one sample. Such a strategy can be applied to all the solution-processed layers, but in this thesis, it has been only applied to PAL optimization. Although the final film thickness depends on the processing parameters and the choice of donor/acceptor materials, typically the thickness gradient in the PAL can vary from 200 to 50 nm, see Figure 2.5. The results obtained with thickness graded solar cells are fully explained in Chapter 4 and Chapter 5. In order to check the reproducibility of this method, we prepared three batches of P3HT:O-IDTBR devices with the same processing conditions but on different days. For the range of explored PAL thickness (from 50 nm to 180 nm, see Figure 2.6), the results are reproducible and lie within 5% of standard deviation. Additionally, in our group, we also developed a simple fabrication platform based on blade coating to manufacture films with donor:acceptor (D:A) composition gradients.

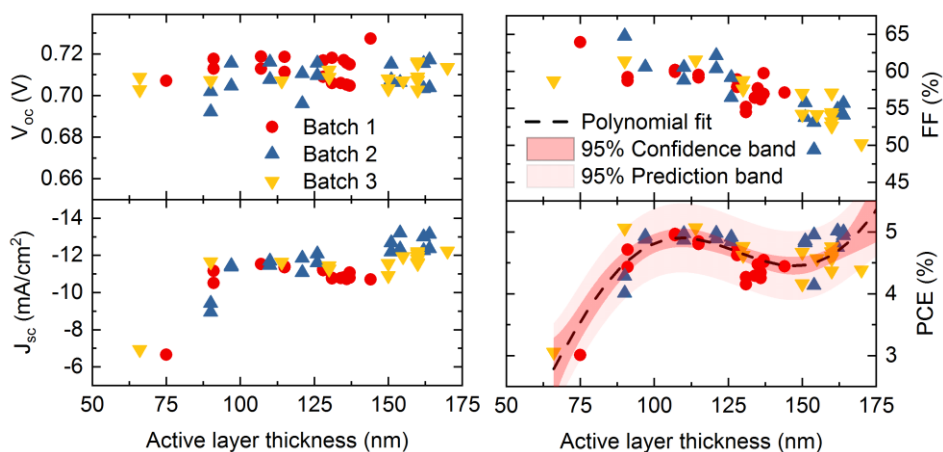


Figure 2.6. Reproducibility of doctor-bladed devices with a thickness gradient. Photovoltaic parameters (V_{oc} , J_{sc} , FF and PCE) of devices from three different batches with photoactive layer thickness gradient. The photoactive layer is P3HT:O-IDTBR.

In contrast to the one-drop conventional blading, two or more drops of the pristine materials are cast. A comprehensive explanation of the manufacturing of graded-stoichiometry films is given in Chapter 5. Finally, Table 2.1 shows the recipes for all the blade coated materials including ETL (AZO/ZnO), PAL with thickness gradient, PEDOT:PSS and PH1000 as semitransparent top electrode.

Table 2.1. General blade coating recipes for AZO/ZnO, PAL and PEDOT:PSSs.

| Ink | AZO/ZnO | PAL | PEDOT 4083 | PH1000 |
|------------------------------------|---------|--------|------------|--------|
| Volume (μL) | 40 | 70 | 150 | 100 |
| Gap (μm) | 50 | 100 | 575 | 200 |
| Blade speed (mm/s) | 4 | 99->5 | 20 | 15 |
| Temperature ($^{\circ}\text{C}$) | 40 | 90 | 65 | 65 |
| Final thickness (nm) | 40 | 200-50 | 50 | 150 |

2.2.1.2 Thermal evaporation

The final step in the fabrication of lab-scale OPV devices consisted in the sequential evaporation of the MoO_3 (HTL) and Ag (top electrode) through a shadow mask at high vacuum ($<1 \cdot 10^{-6}$ bar). A thermal evaporator (ECOVap, MBraun) attached to a nitrogen glovebox was used. The thickness of the layers and the evaporation rate was controlled using a quartz crystal.

Table 2.2. Evaporation recipes for MoO₃ and Ag.

| Material | Rate (Å/s) | Thickness (nm) |
|------------------|---------------|-------------------|
| MoO ₃ | 1 | 10 |
| Ag | 3 | 100 |

The active area of the device was 8 mm², defined by the overlap of all the layers composing the device. The evaporation parameters are summarised in Table 2.2.

2.2.1.3 Thermal annealing

Controlling the morphology of the PAL is crucial to achieve high performances in OPV.^[55,112] One of the most common approaches is to subject the final device to a thermal annealing process to achieve a more favourable blend morphology. In this thesis, in most of the cases, constant-temperature annealing was performed for 20 minutes on a homogenous temperature hot-plate (SD162, Stuart) inside of the glovebox. On the other hand, to analyse the annealing temperature effect on the device performance, a variable post-deposition thermal gradient annealing is carried out for 20 minutes on samples with homogeneous thickness by using a Kofler bench (Lab Logistics Group GmbH), see Figure 2.7. This Kofler bench is a hot plate with a position-dependent temperature. The Kofler bench exhibits a thermal gradient of 6.7°C/cm and a temperature range extending from 30°C to 200°C. The 12 devices in each side of the glass slice size sample (the same as thickness-gradient devices) are all exposed to slightly different temperatures through the annealing gradient. Please refer to Figure 4.13 and Figure 4.14 for practical examples.

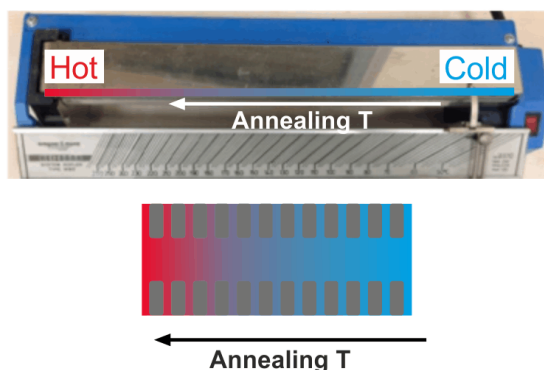


Figure 2.7. Position-dependent thermal annealing. (top) Picture of the variable temperature Kofler bench (bottom) sketch of the device with colour-dependent scale.

2.2.2 Large scale processing techniques

2.2.2.1 Slot-die coating

Roll-to-roll (R2R) based slot-die system is one of the most used strategies for upscaling flexible OPV.^[96,113,114] In Figure 2.8(a), a picture of the complete machine is shown. A simplified scheme (Figure 2.8 (d)) illustrates the main components: (1) unwinder, (2) web aligner, (3) corona treatment, (4) slot-die station, (5) hot-air dryer and (6) rewinder.

Slot-die is a method which produces continuous wet films or, with the help of properly designed masks, structured layers in form of stripes. The ink is pumped into the slot die head with the aid of a pressure system (see Figure 2.8), and, from there, it flows through the slot-die print-head onto the substrate. A dry film is formed after the evaporation of solvent content of the wet film inside of the hot air drying station.

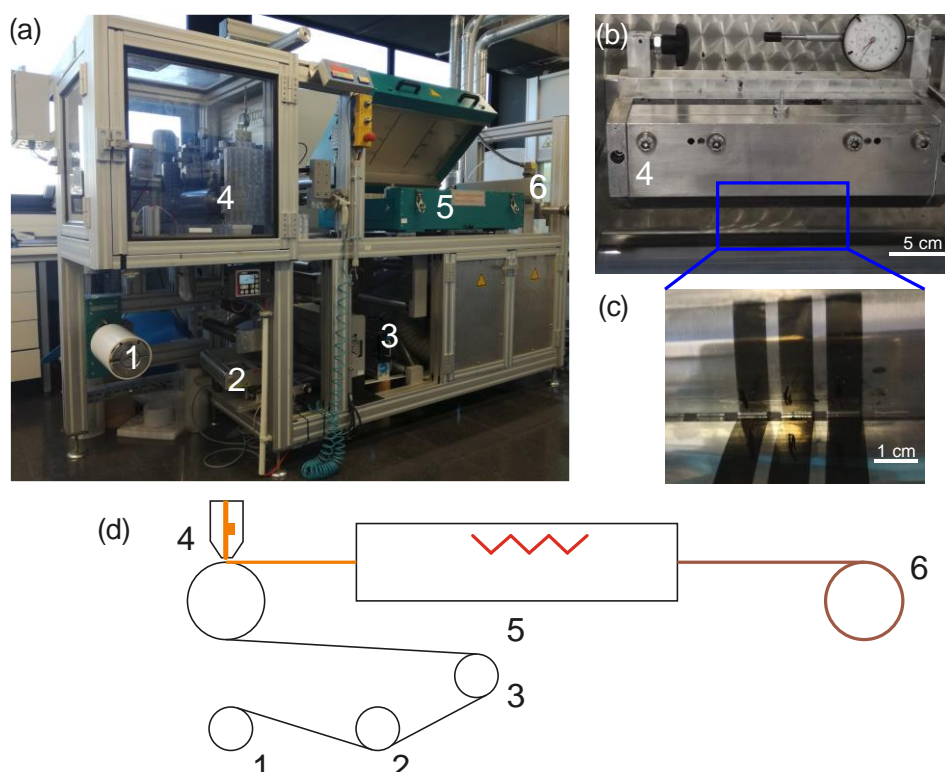


Figure 2.8. Slot-die coater. (a) Picture of the machine. (b) Picture of the 27-cm-width slot-die head and (c) detail of printing three stripes with the slot-die. (d) Simplified sketch of the R2R slot-die coater: (1) unwinder, (2) web aligner, (3) corona treatment, (4) slot-die station, (5) hot-air dryer and (6) rewinder. Orange and brown colours in the sketch represent wet and dry films, respectively.

Table 2.3. General recipes for slot-die coating.

| Ink | AZO | PAL | PEDOT:PSS |
|-----------------------|-----|------|-----------|
| Volume rate (mL/min) | 0.2 | 0.25 | 0.3 |
| Web speed (m/min) | 1.2 | 1.4 | 0.8 |
| Oven temperature (°C) | 100 | 130 | 140 |
| Final thickness (nm) | 80 | 300 | 200 |

Then, the substrate is rolled again in the rewinder. The thickness of the coated film is controlled by ink feeding rate, ink concentration and web speed. Besides the slot-die station and the oven, the R2R equipment includes a web aligner, which controls substrate lateral position during the whole process, and a corona treatment unit used to improve the contact angle of the inks. Although most of the research effort was focused on blade coated organic devices at lab scale, proof of concept flexible modules were successfully manufactured by slot-die coating (see Chapter 4).

2.2.2.2 Screen-printing

Screen-printing is a versatile printing technique enabling 2D featuring and can be used in both sheet-to-sheet and R2R processes. A moving squeegee makes the paste pass through the uncovered area of the pre-patterned textile. Then, the screen-printing paste is cured with heat or UV-light. The viscosity and the squeegee pressure are relevant parameters to control the printed features. Additionally, a reliable positioning between the modules and the screen is crucial to interconnect satisfactorily each of the module subcells, and thus, ensuring working devices. This printing technique was used to obtain the Ag top electrode of the flexible R2R modules (Chapter 4). The machine used for this purpose is a screen-printer AT-60PD model by ATMA (see Figure 2.9).

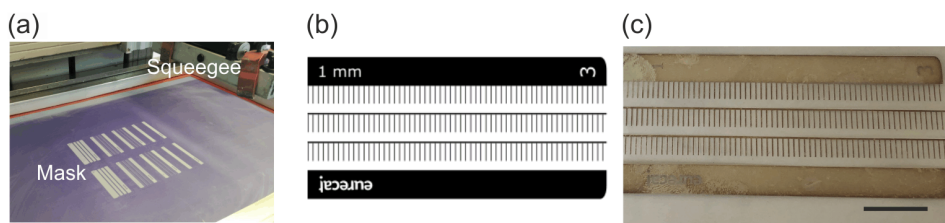


Figure 2.9. Screen printer. (a) Screen printer and (b) mask design with a 1 mm spacing between fingers. (c) Photograph of a screen-printed electrode on a flexible substrate. Scale bar corresponds to 1 cm.

2.2.2.3 Laser patterning

Laser scribing has shown to be one of the best choices for upscaling OPV technology.^[115] The combination of sequential coating and precise ablation steps enable the serial interconnection of module subcells and thus, modules over 1V. The ablation resolution is given, among others, by laser spot size (typically around 40-60 μm diameter). The narrow patterned lines (<100 μm) together with the accurate spatial resolution enable to increase the geometrical yield in modules in comparison with slot-die counterpart. In particular, geometrical fill factors (GFF) over 90% can be reached in an interconnection length of less than 300 μm . Moreover, lasers can be mounted on R2R systems to avoid printing stripes.^[63,96,114] In our study, industrial compatible equipment (Easy Mark Compact Laser Engraver, RoFin) with a 1064 nm laser and a minimum pulse width of 1 μs at repetition rates up to 200 kHz was used to pattern the modules described in Chapter 6.^[116] Groove features are controlled by two terms: laser power and overlapping factor. The power density of the incident laser was controlled by the laser current providing up to 30 A. The laser overlapping factor was controlled by the frequency, speed, pulse length and line width. More experimental details are given in Chapter 6.



Figure 2.10. Laser machine used for film ablation in Chapter 6.

2.3 Characterisation techniques

The characterisation techniques used in this thesis were divided into electrical, spectroscopic and morphological.

2.3.1 Electrical characterisation

The electrical techniques employed to evaluate the performance of OPVs were JV-characteristics, external quantum efficiency (EQE) and light beam induced current (LBIC).

2.3.1.1 JV characterisation

The current-voltage characteristics (IV) of the OPV devices were extracted by using a Keithley 2400 Sourcemeter and an Arduino based multiplexer and switcher. All the electronic components were automatically controlled with a LABVIEW software tool (designed by Mr. Martí Gibert). This allows the fast measurement of 24 devices in less than 6 minutes. As an illumination source, a solar simulator (XES-100S, SAN-EI Electric) under AM 1.5G (Air Mass 1.5 Global) and 100 mW/cm² illumination was employed. This solar simulator is AAA class, which ensures a homogenous illumination in a 10 cm x 10 cm area, needed for the accurate evaluation of the gradient-based OPV devices. The solar simulator was calibrated with a certified silicon solar cell (Oriel, Newport).

It is worth highlighting that a home-made database was employed to store all the JV measurements throughout the thesis. The Access database has more than 5000 measured JV characteristics such as the manufacturing and characterisation details including materials, solvents, solvents casting temperature and blade speed. This tool was used to analyse the sensitivity of the processing parameters, as described in Chapter 4 and Chapter 5.

2.3.1.2 External quantum efficiency

External quantum efficiency (EQE) was measured with a home-made system (developed by Mr. Martí Gibert) that uses a Supercontinuum light source (LLTF contrast, Fianium) coupled to a monochromator filter and normalised by the light power as measured by a

silicon diode. EQEs were recorded from 400 nm to 900 nm excitation wavelength by focusing the 50 μm diameter laser spot. This set-up was also controlled with LABVIEW-based software.

2.3.1.3 Light beam induced current

Light beam induced current (LBIC) was measured adapting the WITec alpha 300 RA+ microscope equipment (Figure 2.11). The sample was illuminated locally by a monochromatic nm laser. The optical measurement (Raman/Photoluminescence) signal was recorded with a spectrometer (CCD camera) and co-locally the photocurrent response (LBIC) with a source meter. This co-local technique refers to *RamBIC* (Raman and LBIC) or *whiteBIC* when the built-in white light of the microscope is used. As an additional work during the thesis, local PL and LBIC measurements were employed to correlate the performance and the microstructure of the blade-coated and spin-coated perovskite solar cell.^[IV]

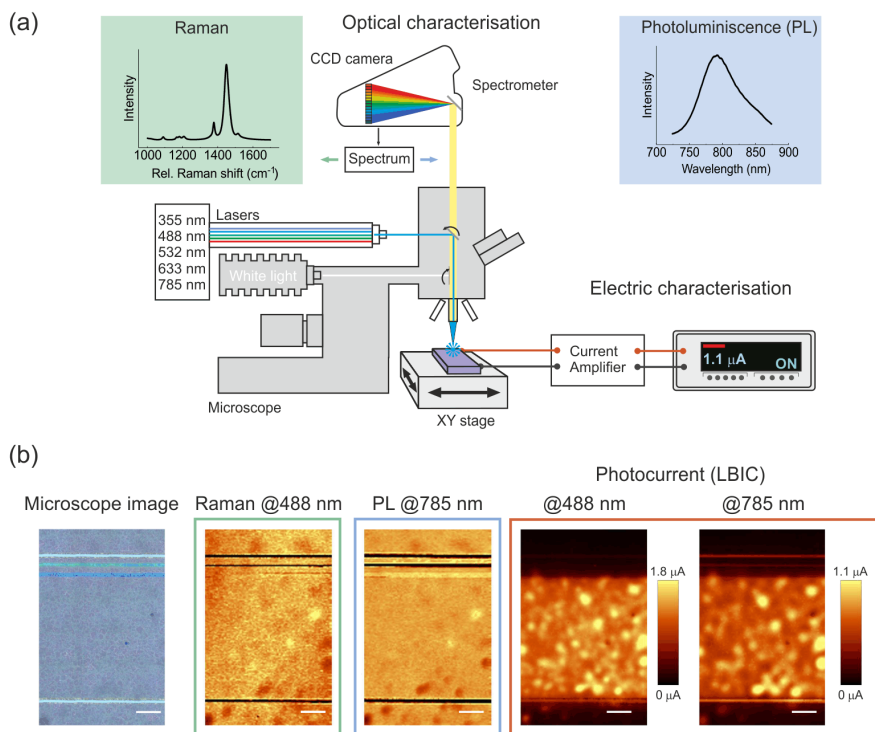


Figure 2.11. Equipment and an example of co-local measurements. (a) Simplified scheme of WITec microscope for optical imaging (Raman and PL) and simultaneously, electrical response (LBIC). (b) Example of co-local optoelectronic images from Figure 6.14.^[IV] Scale bar corresponds to 400 μm .

In this thesis, this technique has been fully exploited in the characterisation of heterogeneous graded devices understanding the degradation (Chapter 4), for high-throughput evaluation (Chapter 5) and verification of subcells interconnections of modules (Chapter 6).

2.3.2 Spectroscopic characterisation

Raman scattering and photoluminescence (PL) spectra were acquired using a WITec alpha 300 RA+ confocal Raman setup. The samples were excited through a 10X objective using two solid-state lasers centred at 488 nm and 785 nm. The Raman spectra were analysed using WITec Project FOUR software and fitted with Fityk piece of software.^[117] Complex refractive indices were measured and analysed by Dr. Mariano Campoy and Mr. Xabier Rodríguez with a variable angle spectroscopic ellipsometer (VASE) from Semilab Sopra GES5E. The modelling of the ellipsometry data was performed using the Winelli II software package from SOPRALAB. The optical properties of the thin films (absorption, reflection and transmission) were measured with both Vis-NIR Fourier-transform spectrophotometer (Vertex 70, Bruker) and UV-Vis OceanOptics USB2000+.

2.3.3 Morphological characterisation

X-ray diffraction (XRD) spectra of the films were collected using an X-ray diffractometer (A25 D8 DISCOVER, Bruker) with grazing incidence geometry by the ICMAB technician Mrs. Anna Crespí. The surface morphology of the organic films was examined using atomic force microscopy (AFM) in tapping mode configuration (Keysight 5100, Agilent) by the ICMAB technician Mr. Andrés Gómez. The film thickness was measured with two mechanical profilometers Dektak 150 (Veeco) and P16+ (KLA Tencor). Contact angle measurements (DSA 100, KRÜSS) were carried out using 50 μ L distilled water drop that was monitored by image analysis software in order to extract the contact angle value. Microscope images were acquired with a Nikon Eclipse LV100D.

2.4 Optical modelling

OPV technology has the potential to tune the aesthetics of the devices with limited effect on the performance due to the wide range of organic materials. The potential colour gamut for the semitransparent OPV devices was studied using the well-established transfer matrix method (TMM).

2.4.1 Transfer matrix method

Inganäs *et al.* firstly reported the TMM method applied to thin-film organic solar cells which enables precise quantification of the electric field distribution inside of the OPV device.^[118] For the simplification of the TMM equations, multi-layered structures with isotropic and homogenous layers and parallel-plane interfaces can be described by 2x2 matrices due to the fact the equations governing the propagation of the electric field are linear and the tangential component of the electric field is continuous.^[118]

We consider a planar multi-layered structure with m layers between the semi-infinite ambient and the optically thick substrate, see Figure 2.12. Each layer j has a d_j thickness and its optical properties are described by the complex refractive index, $\tilde{n}_j = n_j + ik_j$, which depends on the wavelength of the incident light. The electric field propagating in the stack has two terms: one in the positive x direction (E_j^+) and other in the negative direction (E_j^-).

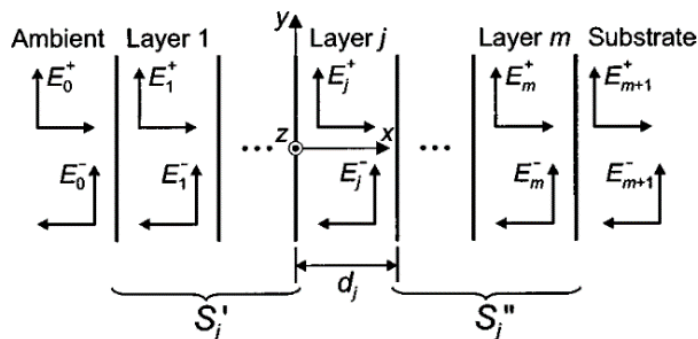


Figure 2.12. Sketch for the transfer matrix method formalism. A general multilayer structure having m layers between a semi-infinite transparent ambient and an optically thick substrate. Each j layer has a d_j thickness and its optical properties are described by its complex refractive index. The electrical field that is propagating in the two directions is indicated by E_j^+ and E_j^- . Scheme reproduced from ^[118].

The modelling of the interface between the layer j and $j-1$ is described as the matrix of refraction ($I_{j,j-1}$) given by Eq. 2.2.

$$I_{j,j-1} = \frac{1}{t_{j,j-1}} \begin{bmatrix} 1 & r_{j,j-1} \\ r_{j,j-1} & 1 \end{bmatrix} \quad (2.2)$$

where $r_{j,j-1}$ and $t_{j,j-1}$ are the Fresnel complex refraction and transmission coefficients at the interface $j,j-1$. As we consider the incoming light with the electric field perpendicular to the plane of incidence (transverse electric (TE) waves), the Fresnel coefficients can be simplified and rewritten in terms of the \tilde{n}_j (Eq. 2.3 and 2.4).

$$r_{j,j-1} = \frac{\tilde{n}_j - \tilde{n}_{j-1}}{\tilde{n}_j + \tilde{n}_{j-1}} \quad (2.3)$$

$$t_{j,j-1} = \frac{2 \tilde{n}_j}{\tilde{n}_j + \tilde{n}_{j-1}} \quad (2.4)$$

The phase matrix describing the propagation of the electric field through layer j is given by

$$L_j = \begin{bmatrix} e^{-i\xi_j d_j} & 0 \\ 0 & e^{i\xi_j d_j} \end{bmatrix} \quad (2.5)$$

where $\xi_j = \frac{2\pi\tilde{n}_j}{\lambda}$ and λ is the incident wavelength

By combining the interface matrix (Eq. 2.2) and the phase propagation matrix (Eq. 2.5), we can write the transfer matrix A of the full system (Eq. 2.6, 2.7) relating the electric field from the ambient side to the substrate.

$$\begin{bmatrix} E_0^+ \\ E_0^- \end{bmatrix} = A \begin{bmatrix} E_{m+1}^+ \\ E_{m+1}^- \end{bmatrix} \quad (2.6)$$

$$\mathbf{A} = \begin{bmatrix} A_{11} & A_{12} \\ A_{21} & A_{22} \end{bmatrix} = \left[\prod_{v=1}^m I_{(v-1)v} L_v \right] I_{m,m+1} \quad (2.7)$$

For the total layered structure, the reflection (R) and transmission (T) coefficients can be expressed as

$$R(\lambda) = \frac{E_0^+}{E_0^-} = \frac{A_{21}}{A_{11}} \quad (2.8)$$

$$T(\lambda) = \frac{E_{m+1}^+}{E_0^-} = \frac{1}{A_{11}} \quad (2.9)$$

The transmitted coefficient (T) as a function of the wavelength is used as input to calculate the colour coordinates. The practical implementation of the TMM formalism was carried out in MATLAB software.^[118] As the first approach, the TMM was simplified to three layers (optically thick glass, photoactive layer and air) in Chapter 3.

2.4.2 Colour and transparency calculations

Colour and transparency features are the most relevant aesthetic parameters for the integration of OPV into translucent architectonic elements. The colour calculation depends basically on three terms: the illuminant, the object and the observer. For the quantification of the colour, the illuminant (D65 or AM 1.5G, Figure 2.13) and the observer (human eye response \tilde{y} in Figure 2.14) were determined by the CIE standard.^[119]

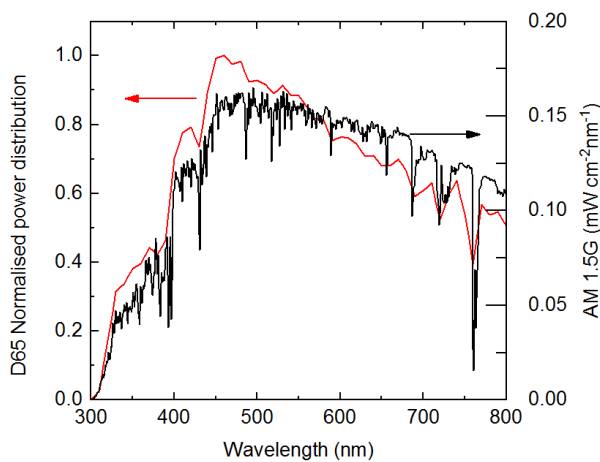


Figure 2.13. Illuminant sources. D65 (red line, left scale) and AM 1.5G (black line, right scale).

Note that for all colour simulations AM 1.5G illuminant source was used. The object features, in the case of semitransparent thin films, were given by the transmission spectrum (T) generated from the TMM formalism. In Chapter 3, we investigate in detail the colour tuning strategies for thin-film technologies. From the transmission spectrum, it is possible to determine the colour coordinates (XYZ tristimulus values) according to the CIE standard.

$$X = \int_{380 \text{ nm}}^{780 \text{ nm}} \tilde{x}(\lambda) T(\lambda) S(\lambda) d\lambda \quad (2.10)$$

$$Y = \int_{380 \text{ nm}}^{780 \text{ nm}} \tilde{y}(\lambda) T(\lambda) S(\lambda) d\lambda \quad (2.11)$$

$$Z = \int_{380 \text{ nm}}^{780 \text{ nm}} \tilde{z}(\lambda) T(\lambda) S(\lambda) d\lambda \quad (2.12)$$

where \tilde{x} , \tilde{y} and \tilde{z} are the colour matching function (Figure 2.14), $T(\lambda)$ and $S(\lambda)$ are the transmitted spectra and the illuminant, respectively.

Normalising the tristimulus values X , Y and Z , we obtain the CIE coordinates (x, y) to plot on the CIE chromaticity diagram.^[119]

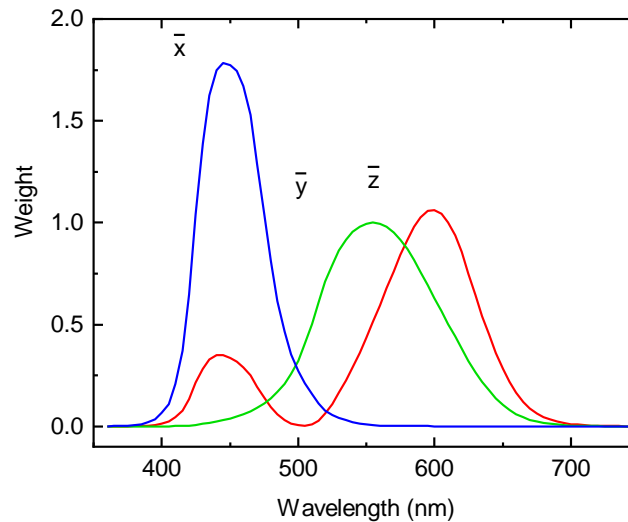


Figure 2.14. CIE 1931 colour matching functions.

$$x = \frac{x}{x+y+z} \quad (2.13)$$

$$y = \frac{y}{x+y+z} \quad (2.14)$$

The transparency is very relevant for the OPV into translucent elements. There are several metrics to quantify the transmission such as average visual transmittance (AVT, Eq. 2.15), the human perception of transmittance (HPT, Eq. 2.16) or the transmission value at 550 nm, the wavelength in which the human eyes show higher sensitivity (see \tilde{y} in Figure 2.14). In this thesis, however, the transmission was calculated considering the human eye response. Note that the human eye response is modelled by the \tilde{y} matching function. Equation 2.14 was used to calculate the transparency of the thin films and semitransparent OPV devices. The election between different metrics would not change significantly the level of transparency as depicted in Chapter 6.

$$AVT = \frac{\sum_{i=380\text{ nm}}^{780\text{ nm}} T_i(\lambda)}{780 - 380} \quad (2.15)$$

$$HPT = \frac{Y}{K} = \frac{\int_{380\text{ nm}}^{780\text{ nm}} \tilde{y}(\lambda) T(\lambda) S(\lambda) d\lambda}{\int_{380\text{ nm}}^{780\text{ nm}} \tilde{y}(\lambda) S(\lambda) d\lambda} \quad (2.16)$$

2.4.3 Genetic algorithm

The aesthetics of the OPV is crucial for minimising the visual impact upon the integration into architectonic elements. For that reason, we developed a colour predictive platform to identify the characteristics of the OPVs that reproduce, if possible, desired colours. Fitting problems are, in general, computationally expensive especially for those having more than two dimensions. For generalisation, the problem of finding the best combination of thickness and composition and, at the same time, a genetic algorithm was employed. This genetic algorithm (GA) is a computational method for solving optimisation problems that avoid local minima in fitting processes. The GA is inspired by the natural selection process, the natural process that drives biological evolution. The

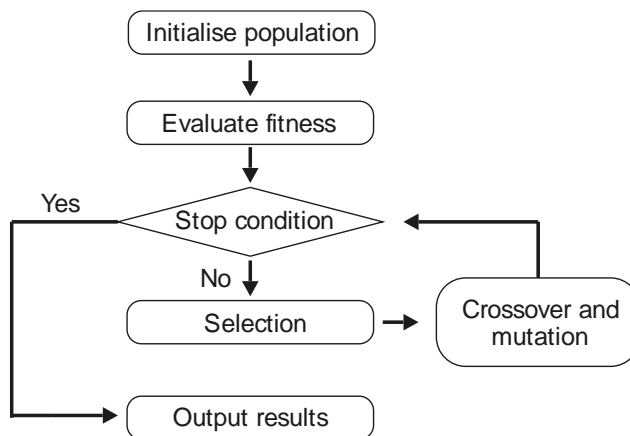


Figure 2.15. Flowchart of a genetic algorithm.

GA, which was used in chapter 3 to reproduce natural colours given by its CIE coordinates, starts with a first-generation population of randomly generated pair of candidates (thickness and composition) of the active layer (Figure 2.15).

Each thickness/composition pair corresponds to certain CIE coordinates which are calculated through the direct method described in the next chapter. Typical size of each generation is 10 pairs. We found that this number is often more critical than the number of generations for the algorithm to converge, 10 is a good compromise in terms of computing time. Then, the evaluation the objective equation or goodness of these new candidates is evaluated by an error function defined as the Euclidean distance between each of the generated CIE coordinates and the target CIE coordinates (desired colour). The best 5 candidates of each generation are used as seed for the next generation of 10 new candidates, generated by the main three genetic operators selection, crossover (0.9 probability) and mutation (0.1 probability). In all cases, we found good convergence after 8 generations. For the implementation of the GA, a previously reported Matlab code was adapted from X. Blasco's PhD Thesis for our needs.^[120] The combination of the optical simulation and GA code enables to exploit theoretically the aesthetics of thin-film solar technologies.

Chapter 3 Colour tuning in thin-film technologies

ABSTRACT

The full deployment of photovoltaic technology requires amenability to be installed in all types of environments. Building-integrated photovoltaics is forecast as an emerging market niche for emerging PV technologies. OPV offers to power the existing non-photoactive elements, such as façades or glazings, while minimising the visual impact. Although the performance of the solar cells has been the most studied topic, for the building integration of OPVs the aesthetics and transparency are as important as the performance.

In this chapter, we theoretically assess the potential of different strategies to tune the colour in organic and perovskite thin films. More precisely for OPV, we evaluate the potential of varying the photoactive layer features thickness, stoichiometry, and ternary mixing. The implemented methodology, using as input the complex refractive index of the materials and the thickness of each layer, combines transfer matrix method (TMM) formalism with the colour theory to calculate the colour coordinates of thin films of organic and perovskite materials. We conclude using a genetic algorithm to find the materials and geometry that reproduce a targeted colour.

*Parts of this chapter have been published in ^[1] [E. Pascual-San-José](#), A. Sánchez-Díaz, M. Stella, E. Martínez-Ferrero, M.I. Alonso and M. Campoy-Quiles. *Science and Technology of Advanced Materials*, 19, 1, 823–835 (2018).*

3.1 State of the art

Most efforts of the scientific photovoltaic (PV) community have been dedicated to the performance ^[66,121] and stability ^[122,123] of emerging PV technologies. However, other relevant features for commercialisation as part of BIPV, such as aesthetics, have received much less attention.^[96] Emerging PV technologies, such as OPVs and perovskite solar cells (PSCs), offer great potential to tune its appearance due to their synthetic flexibility. Depending on the type of modification, the colour tuning strategies can be divided into two approaches: 1) changes in the optical properties of the PAL materials and 2) changes in the device structure (photonic effects).

As a first approach, the chemical structure of the semiconductors is one of the main factors affecting the optical absorption in the PAL (not considering blend morphology, photonics or absorption of metals). The synthesis of specifically designed materials or blending existing materials with different optical properties is an efficient approach to modify the cell colour. For instance, in the field of OPV, a wide range of colours were achieved by blending the different polymers P3HT, PCDTBT, and PBDTTT-T-T as donors, and the fullerene derivatives PC₆₀BM and PC₇₀BM as acceptors.^[124] Alternatively, doping the PAL with small amounts of photoactive dye led to an effective way to fine-tune the cell appearance.^[125] The use of a third component, ternary blends, enabled to span from blue-green to purple-red controlling the loading of an acceptor dye (ASSQ) within PTB7-Th:N2200 binary system.^[126] On the other hand, by engineering the Br/I ratio the appearance of perovskite solar cells was modified from red (I rich) to yellow (Br rich).^[127-129]

The device structure defines the distribution of the electric field within the layered stack. Optical interference effects critically depend on the exact thicknesses of the device and complex refractive indices of the materials. Therefore, the device appearance can be varied by modifying the thickness of each layer or adding a multilayer stack. One common approach is the use of sequential metal-dielectric multilayers that enables modifying the optical cavity resonances and thus the electric field distribution within the layered stack.^[130] Dielectric multilayers with photonic crystal properties were used in OPVs^[124,131-134], PSCs^[135-138] and quantum dots^[139]. Although this approach does not affect the optimised PAL, it requires precise control of the evaporated dielectric film

thickness. Thus, achieving structural colour with photonic approaches might be challenging to further upscale to roll-to-roll (R2R) solution process.

Only a few studies investigated intensively the theoretical chromatic design in solar cells using fitting algorithms. Recently, Arinze et al. optimised the photocurrent, the degree of transparency and colour employing multi-objective algorithm within quantum dot solar cells.^[139] Also recently, a high-throughput optical method has been employed to yield high transparency and performance optimising photonic crystal structure in OPVs.^[140]

3.1.1 Objective

This chapter aims to evaluate theoretically the potential of different strategies based on PAL materials to tune the colour in organic and perovskite thin-film solar cells. For the case of OSC, we assess the potential of varying PAL parameters thickness, stoichiometry, the use of fullerene or non-fullerene acceptors (dyes), and ternary mixing. And for PSC, we compare blending with alloying blending approaches. The implemented methodology is based on the transfer matrix method (TMM), and uses as input parameters the material/blend complex refractive index (\tilde{n}) (refractive index, n , and extinction coefficient, k) and the thickness of each layer. Interestingly, our methodology enables also to address the *inverse problem*, in which the materials and geometry that produce a targeted colour are obtained by a fitting routine. We demonstrate this by deducing device structures that can reproduce naturally occurring stone colours.

3.2 *Direct problem for OPVs*

The so-called *direct problem* establishes the relationship between the geometrical parameters of the PV device and its corresponding CIE colour coordinates. The selected device parameters are limited to those of the for the PAL namely thickness and composition. As discussed in the theory of colour presented in section 2.4.2, the calculation of the CIE coordinates requires the convolution of three terms: the illuminant, an object spectrum (reflectance or transmittance) and the human eye perception model. The reflectance or transmittance spectra can be either measured experimentally or simulated theoretically by TMM A schematic diagram of the *direct problem* is shown in Figure 3.1.

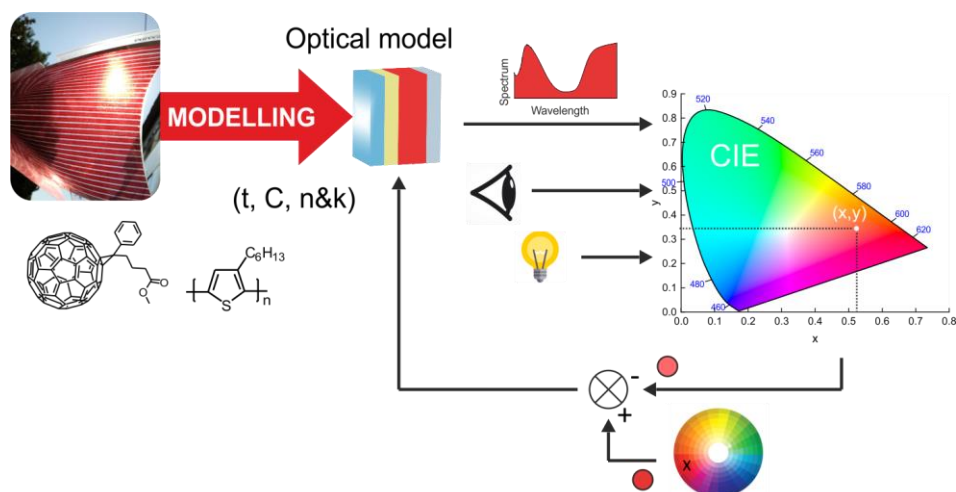


Figure 3.1. Scheme of the colour prediction tool for thin-film solar cells. The top part represents the *direct problem*, in which TMM is employed to calculate the transmission and reflection of a given stack. As model input parameters the complex refractive indices and thicknesses of all layers are needed. This spectrum is then convoluted with the illuminant and eye perception model to define the corresponding CIE colour coordinates (x,y). The bottom part illustrates the *inverse problem*, which is a procedure to find solar cell parameters that yield a targeted colour (x,y) in the CIE chromaticity diagram. As an example of used OPV materials, PC₆₀BM and P3HT chemical structures are shown.

Note that the only input parameter required to predict the colour of the solar cell is the complex refractive index of each layer extracted from variable angle ellipsometry (VASE). They were measured and analysed by Xabier Rodríguez and Dr. Mariano Campoy. Some representative \tilde{n} spectra of organic materials (donors and acceptors) employed in the optical simulations are given in Figure 3.2(a). Others, such as DPPTTT, APFO-Green and O-IDTBR are not shown here. P3HT, PCDTBT, PCPDTBT, PffBT4T-2OD and PTB7-Th, as donor materials, exhibit efficiencies ranging from 3% up to 11% when combined with acceptor materials.^[65] Besides the high high-performing potential, This set of donors offers a broad optical absorption from 500 nm to 800 nm enabling different solar cell appearance. As acceptors, PC₆₀BM and PC₇₀BM were selected as the workhorse of fullerenes in OPV.

The next step for calculating the colour coordinates is to simulate the transmission and reflection spectra from the TMM. The former describes semi-transparent cells, whereas the latter is more suitable for opaque ones. In order to simplify the discussion throughout this thesis, we focussed on transmission.

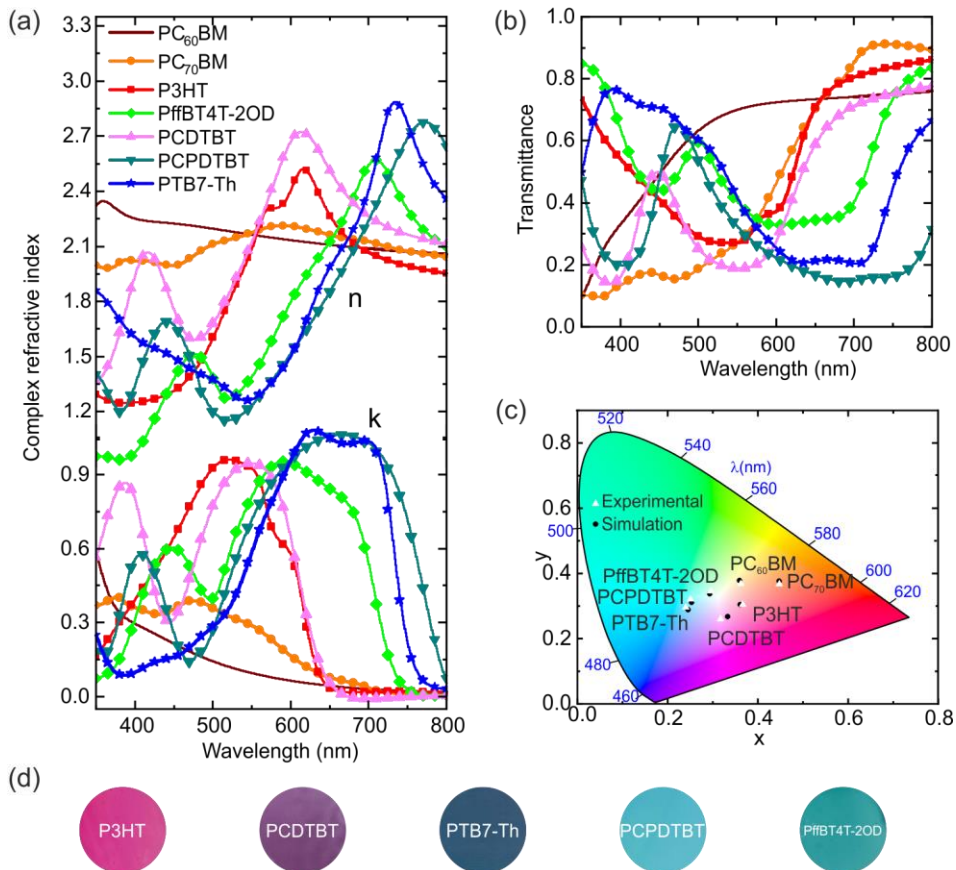


Figure 3.2. Optical properties and colour coordinates of OPV materials. (a) Complex refractive index of the materials and (b) simulated transmittance spectra of PC₆₀BM, PC₇₀BM, P3HT, PffBT4T-2OD, PCDTBT, PCPDTBT and PTB7-Th. (c) CIE chromaticity diagram comparing colour coordinates from simulated (black dot) and measured transmittance spectra (white triangle) for the aforementioned materials.

Note that the R2R devices are typically semi-transparent because the top electrode is a metallic grid that does not fully cover the active area of the device and, thus, could be employed as a partially transparent architectonic element, see OPV module in Figure 3.1.

The simulated transmitted spectra of the aforementioned organic materials are shown in Figure 3.2(b). The theoretical and experimental transmittance spectra were used to calculate the colour coordinates in Figure 3.2(c). The error between the theoretical and experimental CIE₀₀ colour coordinates was calculated as the Euclidean distance between them (see Table 3.1).

For the majority of the materials, this error in CIE coordinates is below 1% which is lower than the human eye sensitivity, understood as the eye capacity to distinguish between two similar colours. In contrast, PCDTBT has an error of 2% in CIE coordinates that might be associated with the film morphology, however, we should dedicate further efforts to fully understand this discrepancy. We demonstrated that, in the majority of cases, the predicted colour coordinates for neat OPV materials are in good agreement with both the simulations and the pictures of the materials (Figure 3.2(d)).

Regarding the film thickness, it is shortly correlated with the distance with respect to the centre of the CIE chromaticity diagram which corresponds to the illuminant. Thinner films (< 100 nm) tend to locate closer to the neutral colour coordinate ($x=0.33$, $y=0.34$) in the CIE plot whereas thicker films lead to saturated colours located at the edges of the CIE diagram. The colour coordinates of P3HT and PffBT4T-2OD films are located in the low colourfulness area providing a neutral colour feeling when looking through these films (Figure 3.2(d)).

Once the colour prediction method has been satisfactorily validated, we then investigate theoretically the effect of PAL characteristics (composition and thickness) on visual aesthetics. Note that throughout this section, we span the PAL parameter range as wide as possible to theoretically explore the colour gamut. Some of these combinations, however, will not result in good-performing devices, when PAL is incorporated as part of the solar cell.

Table 3.1. Photoactive layer thickness and error of the corresponding CIE coordinates. Film thicknesses were deduced from the measured and simulated transmittance spectra of the organic materials shown in Figure 3.2(c).

| Material | Thickness (nm) | Error in CIE coordinates* (%) |
|---------------------|-------------------|----------------------------------|
| PffBT4T-2OD | 50 | 1 |
| P3HT | 52 | 1 |
| PCDTBT | 70 | 2 |
| PTB7-Th | 70 | 1 |
| PCPDTBT | 110 | 1 |
| PC ₆₀ BM | 110 | 1 |
| PC ₇₀ BM | 165 | 1 |

*Error in CIE coordinates refers to the Euclidean distance between the CIE colour coordinates of simulated and measured transmission spectra.

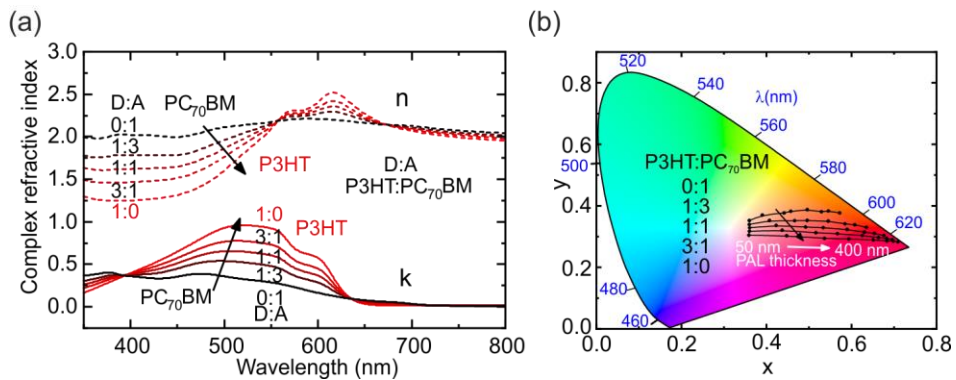


Figure 3.3. Colour dependence on the stoichiometry and thickness of thin films. (a) Complex refractive indices of the binary blend for the different ratio between donor (P3HT) and acceptor (PC₇₀BM) (b) Colour coordinates in the CIE chromaticity diagram as a function of volume ratio and thickness (50 - 400 nm) for P3HT:PC₇₀BM.

Firstly, we inspect the effect of the PAL thickness and composition, donor:acceptor (D:A) volume fraction. The blend complex refractive indices were estimated by the Bruggeman effective medium approximation (EMA).^[141] In particular, we evaluated the colour gamut of the well-known blend P3HT:PC₇₀BM. Figure 3.3(a) shows the complex refractive index of P3HT:PC₇₀BM for blends with D:A variations later used in the colour calculations (Figure 3.3(b)). The performance of thicker PALs usually drops for blend thicknesses above 100 nm, which usually correspond to the first interference maximum. However, the relatively good carrier mobility of P3HT compared with other OPV polymers enables to process films up to 300 nm with no strong effect on the performance. The visual appearance of neat PC₇₀BM films goes from light-brown to dark-brown as the thickness increases from 50 to 400 nm whereas P3HT varies from light reddish to dark-red. The colour coordinates of the blends with intermediate compositions are located between the pristine (P3HT and PC₇₀BM) colour coordinates. For this specific system, the variation of thickness turns out in a relatively larger shift in colour than the volume ratio alternative.

The neutral colour of the PC₇₀BM indicates that primarily the donor material defines the colour of the blend. We study the aesthetics of fullerene-based blends (*donor:PC₇₀BM*) simulating the colour coordinates at equal volume ratio and thickness varying from 50 nm to 400 nm as shown in Figure 3.4.

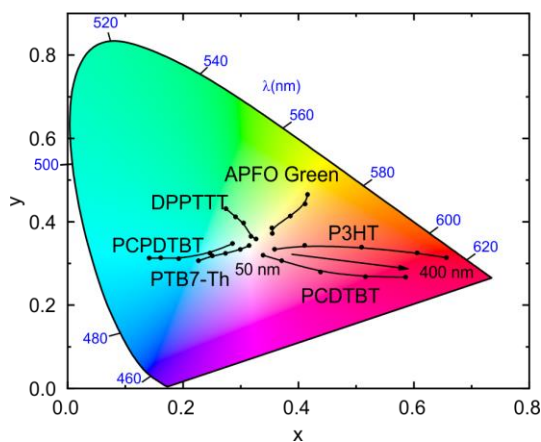


Figure 3.4. Colour of binary blends based on donor:PC₇₀BM system. The donor:acceptor ratio was fixed to 1:1 (in volume) for APFO-Green, P3HT, PCDTBT, PTB7-Th, PCPDTBT and DPPTTT.

Each donor offers a significantly different transmitted colour, ranging from yellow (APFO-Green), red/orange (P3HT), pink (PCDTBT), blue (PTB7-Th), green/blue (PCPDTBT) to green (DPPTTT). We can conclude that the substitution of P3HT by other polymers results in a wider colour exploration of the CIE chromaticity diagram.

The next step towards widening the colour gamut in OPV materials is to explore the ternary blend approach. Although the main role of ternary systems has been to increase the efficiency here, we study the effect on colour.^[142] In order to check the capabilities of ternary mixing for changing the appearance, we added a commercial NFA, O-IDTBR, into the binary of P3HT and PC₇₀BM, and then calculate the CIE coordinates as a function of composition and thickness (50 and 100 nm), see Figure 3.5. These ternaries tune satisfactorily the colour from reddish to almost blue. More details about the chromaticity of P3HT:NFA blends are given in the next chapter. At this point, the proposed ternary blend is only a demonstrator of the potential colour tuning with these materials.

In order to evaluate ternaries based on NFAs more systematically, we introduce a hypothetical dye with a well-defined absorption peak in the visible range of the spectrum whose position is scanned. As an initial approach, the complex refractive index of NFAs can be approximated mathematically by a model of the dielectric function combining Eq. 3.1 and Eq. 3.2.

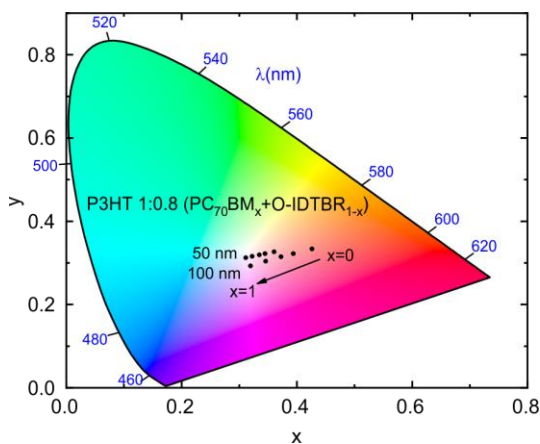


Figure 3.5. Example of predicted CIE colour coordinates for a ternary system. This binary consists of (1:0.8) P3HT : (PC₇₀BM_x:O-IDTBR_{1-x}).

This theoretical ‘dye’ is modelled using a Cauchy law to account for the contribution of UV resonances in the visible (modelled with A, B and C constant in Eq. 3.1), and one Lorentzian peak defined by its wavelength position (λ_0), broadening (γ) and amplitude (D), see Eq. 3.2. This Kramers-Kronig consistent model has the advantage of its mathematical simplicity.

$$\varepsilon_r(\lambda) = A + \frac{B}{\lambda^2} + \frac{C}{\lambda^4} + \frac{D \lambda^2 (\lambda^2 - \lambda_0^2)}{(\lambda^2 - \lambda_0^2)^2 + \gamma^2 \lambda^2} \quad (3.1)$$

$$\varepsilon_i(\lambda) = \frac{D \lambda^3}{(\lambda^2 - \lambda_0^2)^2 + \gamma^2 \lambda^2} \quad (3.2)$$

Moreover, it allows evaluating several dye-based blends by simply shifting the Lorentzian peak position while maintaining overall oscillator strength. The maximum extinction coefficient (A) has been set to 1 since this is a very general value for organic semiconductors.^[143] Two examples of different hypothetical dyes for $\lambda_0=450$ nm and 600 nm are shown in Figure 3.6. We evaluate systematically the effect of the third component (dye) on the CIE coordinates of the binaries based on P3HT, PCDTBT and PffBT4T-2OD, as donors, and PC₇₀BM, as the acceptor.

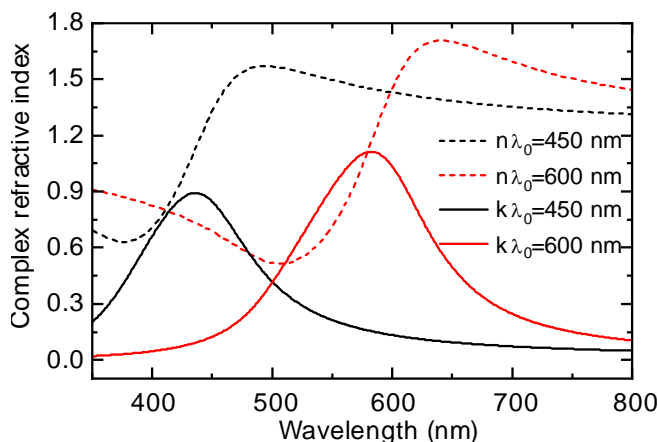


Figure 3.6. Complex refractive indices of simulated dyes. As representative examples, two hypothetical dyes are shown with different absorption maxima 450 nm (black curve) and 600 nm (red curve).

The dye absorption peak was spanned from 380 to 750 nm. As an approximation, the dye is considered as a second acceptor, aiming to reproduce NFAs, and therefore the general formula used for the blend is donor:acceptor [Donor]:[PC₇₀BM_c + dye_{1-c}]_{0.8}, where c is the volume fraction between the PC₇₀BM and dye varying from 0 to 1 (see Figure 3.7(a)). The binary blend made of donor:dye (1:0.8) corresponds $c=0$ whereas the donor:PC₇₀BM (1:0.8) binary blend is for $c=1$. Setting $c=0$ is then an effective way of reproducing an ideal set of NFAs.

We investigate the aesthetics of three examples of ternary blends based on the donors P3HT, PCDTBT and PffBT4T-2OD in which the colour appearance is strongly modified with the addition of a dye/NFA, see Figure 3.7(a,b,c). As the composition of the ternary is varied from fullerene rich ($c=1$) to NFA rich ($c=0$), the CIE coordinates vary dramatically due to the increasing contribution that the strong NFA absorption has on the overall active layer absorption. Since NFAs typically exhibit lower electron mobilities compared to fullerenes, the addition of the third component in the blend may affect the electrical properties. Therefore, we calculate the precise amount of dye/NFA required to produce significant colour changes. To do so, three representative points in the CIE graph namely orange (450 nm), pink (540 nm) and blue (650 nm) were chosen.

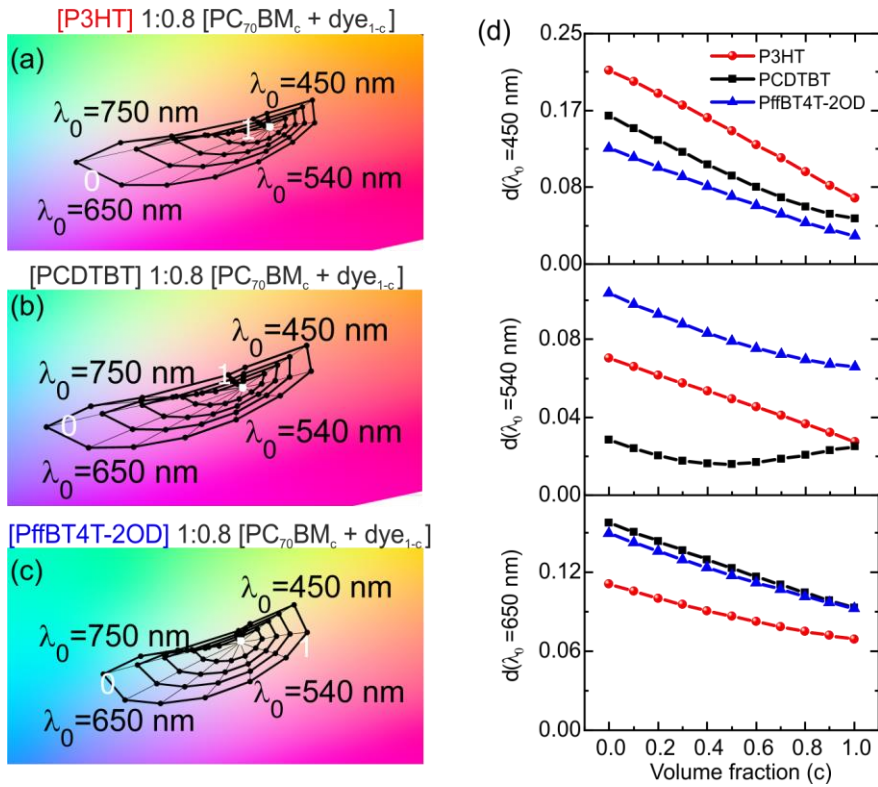


Figure 3.7. Colour tuning in OPV using ternary blends. CIE coordinates in the zoomed CIE chromaticity diagram upon variation of the composition of the ternary blends (donor 1:0.8 [PC₇₀BM:dye]) using as donor (a) P3HT, (b) PCDTBT and (c) PffBT4T-2OD. The film thickness is fixed to 100 nm. (d) Euclidean distance in CIE coordinates for pure 100nm-dye at three representative wavelengths (450 nm, 540 nm and 650 nm) as a function of the volume fraction, *c*.

Then, the Euclidean distance (*d*) in CIE coordinates between the representative colour and the simulated colour coordinates as a function of the dye loading in the ternary blend was calculated, see Figure 3.7(d). For the dye absorbing at $\lambda_0=450$ nm (orange coloured), a shift of 0.08 in CIE diagram requires 40%, 60% and 90% of dye loading for PffBT4T-2OD, PCDTBT and P3HT blends, respectively. In the case of the colour pink target, the PffBT4T-2OD blends cannot reduce the Euclidean distance below 0.06. This is due to PffBT4T-2OD depicts neutral colour and by adding this dye a saturated pink based on PffBT4T-2OD cannot be obtained. On the other hand, blends based on PCDTBT are insensitive to the amount of dye and the distance from the target is always below 0.03. In contrast, for a P3HT-blend the error is reduced with an increasing amount of dye. Apparently, for the binary blend P3HT:dye the error is virtually the same which is found for PCDTBT:dye blends. This coincidence can be explained because of blended P3HT

and PCDTBT with PC₇₀BM result in very close CIE coordinates for the blends. Finally, for the colour blue target, PffBT4T-2OD and PCDTBT again exhibit the same values of error. However, P3HT blends reach the bluish part of the CIE graph more easily. In general, the colour change by the addition of a ternary compound to the binary blend is linear in the graph; moreover, to produce a sensitive colour variation, more than 20% of dye (or NFA) is required in the blend.

3.3 Direct problem for perovskite solar cells

The colour prediction methodology can also be extended to other thin-film technologies such as hybrid perovskite active layers. In particular, we investigate the aesthetics of the most common hybrid organic-inorganic halide perovskite system ($\text{CH}_3\text{NH}_3\text{PbX}_3$) with three different inorganic anions ($\text{X} = \text{Br}, \text{Cl}, \text{and I}$). The complex refractive indices for three types of perovskites are plotted in Figure 3.8(a) and taken from the literature.^[144] The effect of changing the halide element shifts the onset of absorption from 780 nm to 530 nm and 400 nm for I, Br and Cl, respectively. Firstly, optical simulations from pristine perovskite films of 50 nm to 500 nm were performed with the three types of halide elements (Figure 3.8(b)). On the one hand, iodide and bromide perovskite films exhibit the same colour trend as organic materials. For thin films (below 100 nm) associated CIE coordinates are located close to the central colourless area whilst for thicker films, they tend to more saturated colours.

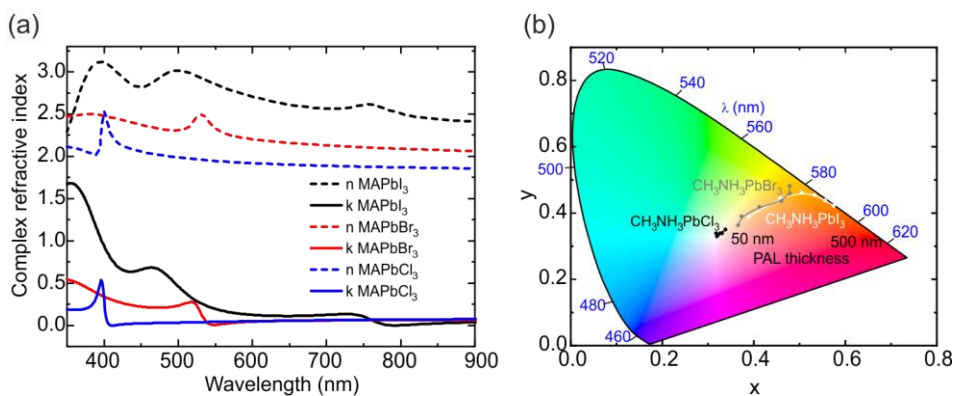


Figure 3.8. Colour prediction for perovskite film. Perovskite colour-simulation with different halogen anions such as iodide (I), bromide (Br) and chloride (Cl). (a) Complex refractive indices of perovskite used for optical simulations. (b) CIE coordinates. (b) CIE coordinates of pure perovskite phase with thicknesses ranging from 50 nm to 500 nm.

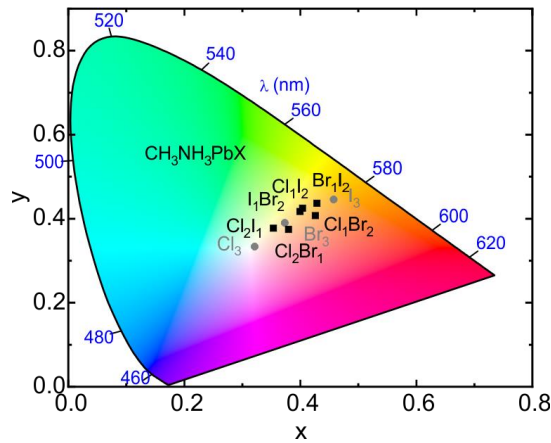


Figure 3.9. Colour prediction for hybrid perovskite films. CIE colour coordinates of 100-nm film using Bruggeman modelling for $\text{CH}_3\text{NH}_3\text{PbX}$ ($X=\text{I}_3, \text{Cl}_3, \text{Br}_3$). Pure perovskite phase is plotted in filled grey circles and mixtures in filled black squares.

On the other hand, simulated colours of chloride-based perovskite are located around the central area of the CIE graph regardless of thickness. This colourless finding for Cl-perovskite is due to the transparency in the visible range (see Figure 3.8(a)). Figure 3.9 depicts CIE chromaticity diagram for perovskite mixtures assuming Bruggeman approximation and 100 nm films. As it was expected, CIE coordinates of mixtures are located between those of pure perovskite phases. Different perovskite anion mixtures based on Bruggeman approximation can be only applied to predict the effective dielectric function if there are still pure perovskite domains of each of the perovskite phase in the final blend. Such structure often results when the perovskite film is manufactured by gas route by sublimating perovskite precursors.^[145] However, solution-processed perovskite mixtures result in alloys whose dielectric functions are defined by bandgap shifting of the absorption onset and thus Bruggeman approximation is not valid.^[146]

For this reason, we approximate the complex refractive index by parametric interpolation of the standard critical points to reproduce perovskite intermediate phases given by the general formula $\text{MAPb}(\text{I}_c\text{Br}_{1-c})_3$, where MA stands for methylammonium (CH_3NH_3), between iodide and bromide whose onsets are 780 nm and 550nm, respectively. The resulting complex refractive indices obtained by the bandgap shifting are shown in Figure 3.10(a) and the corresponding CIE colour coordinates for 100-nm films in Figure 3.10(b).

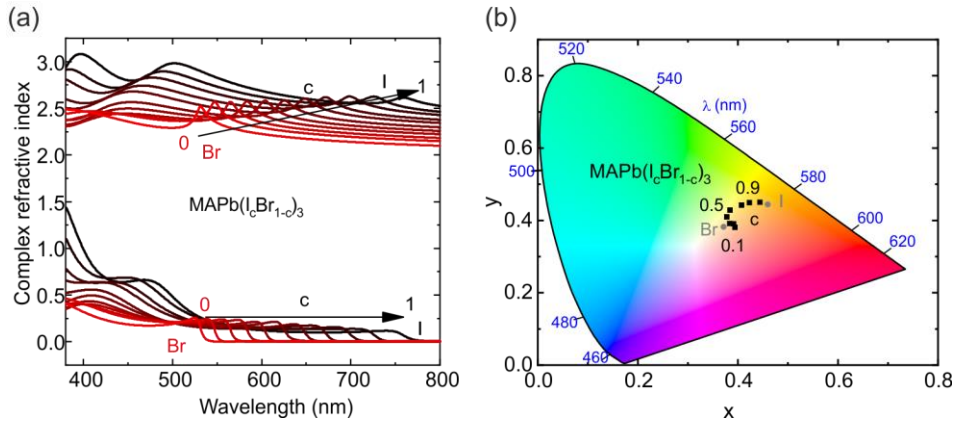


Figure 3.10. Colour tuning upon shifting the bandgap of $\text{MAPb}(\text{I}_c\text{Br}_{1-c})_3$. (a) Complex refractive indices. (b) CIE coordinates for 100 nm mixture films approximated by parametric interpolation of the dielectric function according to $\text{MAPb}(\text{I}_c\text{Br}_{1-c})_3$ where c is the concentration of each phase. Colour coordinates for pure perovskite phase are plotted in filled grey circles and shifted perovskite curve are plotted in filled black squares.

Two main conclusions can be drawn. First, both, blending and alloying of hybrid perovskite produces only a limited colour gamut, centred around the red part of the CIE diagram. Unless other effects, like interference effects, no easy access to blue or green cells is predicted. Secondly, alloying does change colour effectively for iodine-rich stoichiometries, having a clear non-linear colour tuning capability with Br content.

3.4 Colour tuning effectiveness

For a quantitative assessment of the different colour tuning approaches, we define the colour tuning effectiveness (CTE) as the range of colour gamut that a specific system can present. The employed metric for CTE quantification is the covered area of the CIE chromaticity diagram (Table 3.2).

This allows the comparison between different colour tuning strategies, namely, 1) modify the volume ratio and thickness for a given D:A pair; 2) change the donor material keeping the same acceptor; and 3) ternary blending. The simulations shown in Table 3.2 were carried out fixing a film thickness between 50 and 100 nm for easy comparison. Furthermore, we predict the covered area for binary blends as a function of the cylindrical coordinates centred in the illuminant (the central point of the CIE diagram). Eq. 3.3 represents a geometrical approximation for the CIE covered area as a function of the angle (θ_D and θ_A) and distance (ρ_D and ρ_A) of the pristine donor and acceptor materials with the illuminant, respectively (see calculations on Appendix A and Figure 3.11 for an illustration of these parameters).

$$Area = \frac{1}{2} |\sin(\theta_D - \theta_A)| \cdot (\rho_{D2} \cdot \rho_{A2} - \rho_{D1} \cdot \rho_{A1}) \quad (3.3)$$

Note that films based on P3HT:PC₇₀BM with variations in thickness and D:A ratio have less colour variability compared to blends employing different donors with the same acceptor (PC₇₀BM) and volume ratio (1:1).

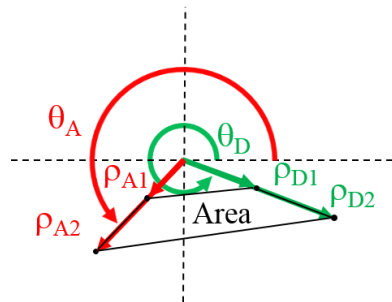


Figure 3.11. Sketch of the geometric parameters involved in the colour tuning effectiveness. Further details are given in Eq. 3.3 for the calculation of the covered area in the CIE diagram.

This can be explained by the limited chromaticity of P3HT compared with the wide gamut afforded by the different donor materials (such as PTB7:Th or PCDTBT). We observe that changing the donor for a fixed donor:PC₇₀BM ratio is more effective in terms of CTE than changing the volume ratio (as observed in the case of P3HT:PC₇₀BM). Changing the ratio might only be effective when donor and acceptor have strong and complementary colours (and far from the centre of the CIE diagram).

According to the results shown in Table 3.2, changing the donor material covers twice the area in the CIE chromaticity diagram compared to changing the D:A ratio.

Table 3.2. Colour tuning effectiveness of the different strategies to tune the colour in thin-film solar cells. Thicknesses were varied from 50 to 100 nm and from 50 to 400 nm (marked by an asterisk) and volume fraction from 0 to 1. The evaluated strategies were thickness and volume ratio (Figure 3.3(b)), changing donors (Figure 3.4), dye addition (Figure 3.7) and perovskite alloy (Figure 3.10(b)).

| Blended materials | CIE covered area | |
|--|------------------|---------------|
| | Measured (%) | Predicted (%) |
| P3HT:PC ₇₀ BM | 1.1 | 0.9 |
| P3HT:PC ₆₀ BM | 1.0 | 0.5 |
| PTB7-Th:PC ₇₀ BM | 0.3 | 0.3 |
| APFOGreen:PC ₇₀ BM | 0.2 | 0.2 |
| Polymer:PC ₇₀ BM | 1.2 | - |
| P3HT:dye ($\lambda_0=450$ nm) | 2.5 | 2.1 |
| P3HT:dye ($\lambda_0=540$ nm) | 0.6 | 0.7 |
| P3HT:dye ($\lambda_0=650$ nm) | 1.1 | 1.5 |
| P3HT:dye ($\lambda_0=750$ nm) | 0.5 | 0.4 |
| [P3HT]1:0.8[PC ₇₀ BM _c dye _{1-c}] $\lambda_0=450$ nm | 0.6 | - |
| [P3HT]1:0.8[PC ₇₀ BM _c dye _{1-c}] $\lambda_0=540$ nm | 0.8 | - |
| [P3HT]1:0.8[PC ₇₀ BM _c dye _{1-c}] $\lambda_0=650$ nm | 0.5 | - |
| [P3HT]1:0.8[PC ₇₀ BM _c dye _{1-c}] $\lambda_0=750$ nm | 0.1 | - |
| P3HT:PC ₇₀ BM:dye | 2.8 | - |
| PCDTBT:PC ₇₀ BM:dye | 2.8 | - |
| PffBT4T-2OD:PC ₇₀ BM:dye | 2.6 | - |
| Perovskite alloy MAPb(I _c Br _{1-c}) ₃ | 0.7 | - |
| P3HT:PC ₇₀ BM* | 5.9 | 6.2 |
| P3HT:PC ₆₀ BM* | 6.4 | 6.1 |
| PTB7-Th:PC ₇₀ BM* | 5.0 | 7.9 |
| APFOGreen:PC ₇₀ BM* | 4.4 | 4.7 |
| Perovskite alloy MAPb(I _c Br _{1-c}) ₃ * | 3.7 | - |

The substitution of PC₇₀BM by NFAs (as represented here by the dye) can also strongly increase the colour tuning capability. For instance, the binary blend of P3HT:NFA (dye, $\lambda_0=450$ nm) is the most suitable combination to tune the colour of P3HT. By adding a third coloured-component (dye) the range of colours covered increases twofold compared to a binary blend approach based on fullerene. Moreover, this enhancement in the covered area of CIE chromaticity diagram appears on all ternary blends based on P3HT, PCDTBT and PffBT4T-2OD with PC₇₀BM as one of the acceptor materials.

According to these results, ternary blends based on dyes are the most promising approach to modify the colour in solar cells. In the next chapter, P3HT:NFA blends will be studied in details. Nevertheless, this last colour tuning approach entails the addition of a third component which must be compatible with the energy levels and miscible with the initial pair of donor and acceptor materials. The performance of the potential devices cannot be predicted with the optical simulations.

3.5 Inverse problem for OPVs

The *direct problem*, as the first approach has been defined in the previous section, enables to theoretically explore the potential device appearance as a function of the manufacturing strategies. By contrast, the here so-called *inverse problem* seeks a specific combination of PAL parameters (thickness and volume ratio) that mimics a targeted colour. One of the main disadvantages of calculating all possible combinations is that the computational cost scales with the number of investigated variables.

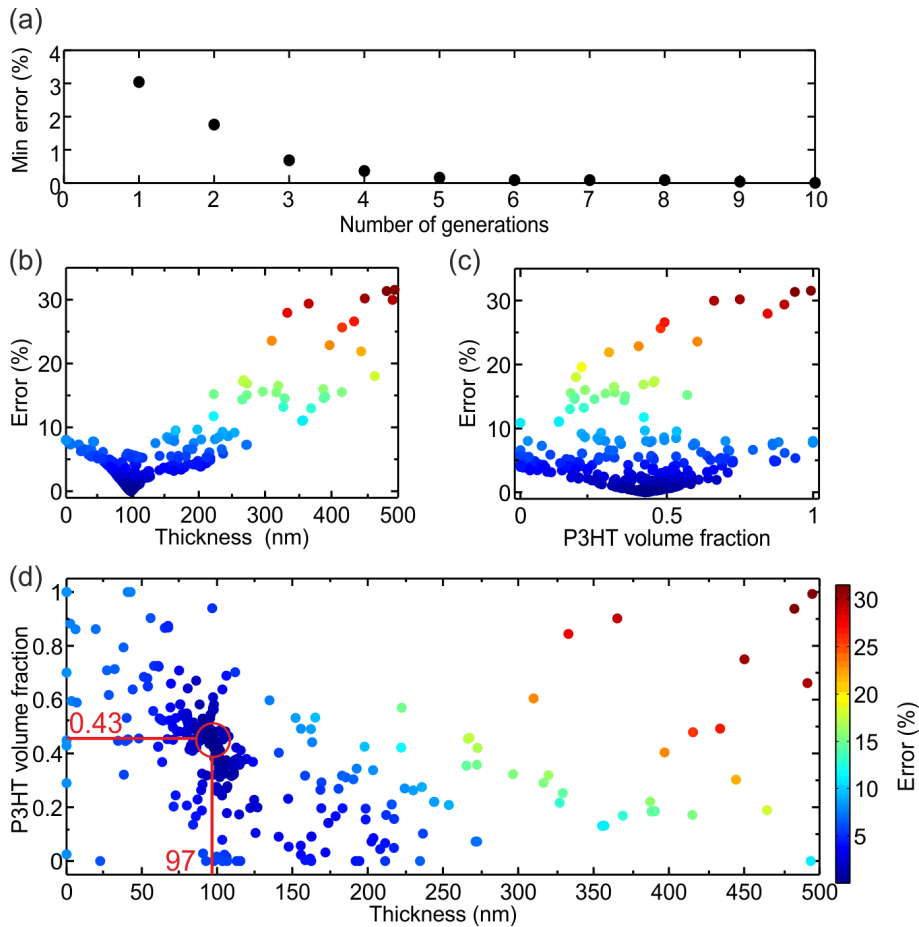


Figure 3.12. Inverse problem based on genetic algorithm fitting for P3HT:PC₇₀BM using a piece of brick as targeted colour. (a) Evolution of the minimum error yielded as a function of the number of generations. (b) Error (Euclidean distance in CIE coordinates) as a function of thickness. (c) Error as a function of P3HT volume fraction. (d) Error mapping as a function of P3HT volume fraction and thickness. The red circle highlights the solar cell parameters (volume fraction and thickness) which mimic a targeted brick colour. The error scale for (b) and (c) is the same as (d).

An alternative to such methodology, we chose a genetic algorithm (GA) to solve the *inverse problem*. We selected a GA, usually employed for multi-objective and non-linear problems. This fitting algorithm avoids local minima and widely explores the space of parameters. As a first case study, the *inverse problem* was applied to find the parameters of P3HT:PC₇₀BM blend that mimics the colour of a brick piece (target colour) whose CIE colour coordinates (0.4117, 0.3555) were extracted from reflectivity measurement.

We found that for a rapid convergence the number of individuals (40) is more important than the number of generations (10). For the brick case, after 3 generations the error associated with the best combination is less than 1% (Figure 3.12(a)). PAL thickness is highly colour sensitive (Figure 3.12(b)) in contrast to volume fraction which is almost colour independent (Figure 3.12(c)). Surprisingly, the PAL parameters (100 nm and 40% vol. of P3HT volume fraction) of the best candidate reproducing the brick appearance yields to optimum efficiency for this specific system.

Alternatively, with all solutions of the GA, it is possible to establish a range of thicknesses and volume fractions where their CIE colour coordinates fall within a certain error value. This post-processing tool could be used in more complex scenarios to cluster solutions and then select the best candidates depending on potential efficiency or other parameters such as the amount of material used or the materials cost.

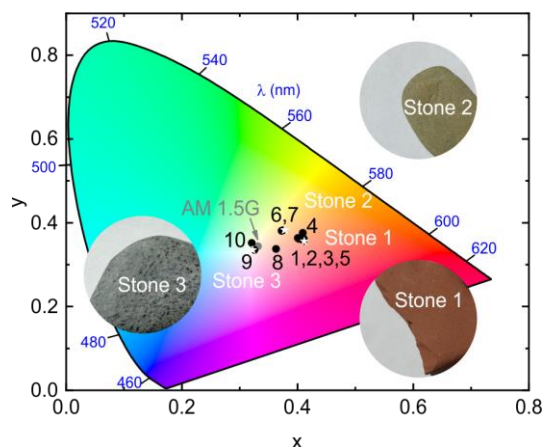


Figure 3.13. *Inverse problem* for OPV reproducing material colours. CIE chromaticity diagram with colour coordinates for three coloured stones (white stars) and the optical simulations guided by a genetic algorithm (filled black circles). See for further details about the simulation number in Table 3.3.

In order to demonstrate the potential of the GA-based methodology, we applied it to reproduce the aesthetics of three relevant construction materials with potential for BIPV namely brick, marble, and slate but using OPV material combinations. For each stone, several combinations of D:A mixture were evaluated and the results are shown in Table 3.3. The simulated CIE chromaticity coordinates compared with the colour coordinates of the real stones are given in Figure 3.13.

For a given photovoltaic material, there is a limited available colour gamut. For instance, P3HT blends cannot reproduce colours of *stones 2* and *3*, having associated errors of 3% and 4%, respectively. In contrast, P3HT mixtures can reproduce easily reddish colours (*stone 1*), as depicts simulation 2, with a 100 nm of thickness and 22% of volume fraction ratio leading to an error in CIE coordinates of only 0.2%. On the one hand, the greener part of CIE (*stone 2*) is accessed with blends based on APFO-Green and DPPTTT with 100 nm and 194 nm, respectively. *Stone 3* exhibits neutral appearance, thus its colour coordinates are located close to the illuminant coordinates (AM 1.5G). To avoid trivial solutions in GA (e.g. zero thickness), 50 nm was set as a lower limit of the thickness range. Consequently, the best candidates of P3HT and DPPTTT mixtures, which are polymers with well-defined colour, correspond to the lowest available thickness. Finally, PTB7-Th blend reproduces accurately the *stone 3* appearance (0.3% of error) with 170-nm film thickness and 38% of donor concentration.

Table 3.3. Results of the *inverse problem* combined with a GA. Different donors and target CIE coordinates were used as shown in Figure 3.13.

| Target stone | Simulation ref | Donor | Acceptor | Thickness (nm) | C donor (%) | Error (%) |
|--------------|----------------|------------|---------------------|----------------|-------------|-----------|
| 1 | 1 | P3HT | PC ₆₀ BM | 99 | 33 | 1.1 |
| | 2 | P3HT | PC ₇₀ BM | 100 | 22 | 0.2 |
| | 3 | PTB7-Th | PC ₇₀ BM | 322 | 23 | 0.6 |
| 2 | 4 | APFO-Green | PC70BM | 315 | 0 | 2.0 |
| | 5 | P3HT | PC ₇₀ BM | 100 | 10 | 2.9 |
| | 6 | APFO-Green | PC ₇₀ BM | 100 | 38 | 0.5 |
| | 7 | DPPTTT | PC ₇₀ BM | 194 | 26 | 0.4 |
| 3 | 8 | P3HT | PC ₇₀ BM | 50 | 33 | 4.1 |
| | 9 | PTB7-Th | PC ₇₀ BM | 170 | 38 | 0.3 |
| | 10 | DPPTTT | PC ₇₀ BM | 50 | 58 | 1.7 |

3.6 Conclusions

We developed a methodology to explore, theoretically, the potential of several strategies to tune the appearance of photovoltaic devices. The studied strategies included simple interference effects (evaluated by PAL thickness), the blend composition, blend materials (e.g. different donors or the use of non-fullerene acceptors), and ternary mixing. In particular, we evaluated in ternary blends the percentage of dye needed to obtain a given colour in a multicomponent system. Additionally, the methodology was satisfactorily validated by comparing (x,y) CIE coordinates deduced from experimental and calculated transmittance.

We define the colour tuning effectiveness as a parameter that quantifies the covered area in the CIE diagram for the different strategies. The addition of a coloured-dye as part of a ternary blend (or replacing the fullerene altogether) turned out to be the most efficient approach to change the colour. Since a relatively large amount of the third component is needed (>20%) to significantly change colour, it is required that the three materials should be photoactive and compatible between them in order to maintain the electronic properties. On the other hand, when focusing on binaries, replacement of fullerenes by NFAs can lead to a larger colour gamut. Changing the D:A ratio is a relatively poor strategy to change colour for fullerene-based OPV but could provide CIE tunability for donor and acceptor molecules with complementary absorptions if performance does not need to be the highest for the given combination. Mixing and alloying hybrid perovskite films appear to have a more limited colour tuning capability than the case of organic films unless several strategies are combined.

Finally, the *inverse problem* allows finding the best combination of thickness and blend concentration that matches a targeted colour. To demonstrate the potential of this methodology, we have evaluated a variety of materials, composition and thicknesses to achieve the colour of different stones, including representative examples for BIPV such as brick, marble and slate.

Chapter 4 Upscaling P3HT:NFA solar cells

ABSTRACT

In this chapter, we investigate the performance and aesthetics of P3HT blended with seven commercially available acceptors namely ITIC, ITIC-M, EH-IDTBR, O-IDTBR, O-IDFBR and PC₆₀BM and ICBA as fullerene references. More than one thousand bladed P3HT:acceptor devices are manufactured using high throughput techniques based on 1D gradients of thickness and annealing temperature. A large dataset is employed to perform a parameter sensitivity to identify the most influential parameters for P3HT based devices. Devices with power conversion efficiencies over 5% show a negligible dependence to casting temperature (40-105°C) and thickness (80-250 nm). Then, with the aid of co-local selective optoelectronic measurements, we analyse the effect of the encapsulation, thickness and the role of each photoactive material on the long-term stability. Finally, as a proof-of-concept, P3HT:O-IDTBR R2R flexible modules are manufactured with large-scale compatible conditions.

Parts of this chapter have been published in ^[1] [E. Pascual-San-José, X. Rodríguez-Martínez, R. Adel-Abdelaleim, M. Stella, E. Martínez-Ferrero and M. Campoy-Quiles. Journal of Materials Chemistry A, 7, 20369–20382, \(2019\).](#)

4.1 P3HT based OPV. State of the art

Poly(3-hexylthiophene), P3HT, is one of the most studied polymers in OPV (chemical structure is given in section 2.1.4.1).^[60,147,148] The simple and optimised synthetic steps enable to produce kilograms of P3HT at a moderate price compared to other conjugated polymers.^[149-151] Traditionally, P3HT has been mixed with fullerene acceptors, such as PC₆₀BM, PC₇₀BM and ICBA, reaching PCEs with lab-scale devices of 3.1%,^[61] 4.4%,^[152] and 6.5%,^[62] respectively. Due to those reasons, P3HT was the first polymeric semiconductor employed in R2R flexible modules.^[153] On the other hand, the development of high performing low-bandgap polymers, typically mixed with NFAs, shifted away the research interest from P3HT (see Figure 4.1). Interestingly, in 2016 a novel NFA, O-IDTBR, was synthesised so that when blended with P3HT reached up to 6.3% of PCE.^[154] O-IDTBR showed a dramatically enhanced absorption as well as good stability compared to fullerene counterparts. Since then, different O-IDTBR studies have been carried out including carrier transport and recombination^[155-157], theoretical solubility by means of machine learning approaches^[158] and the influence of P3HT molecular weight on the OPV performance.^[148] More recently, Baran *et al.* boosted the efficiency up to 7.7% with the addition of the amorphous O-IDFBR into the P3HT:O-IDTBR binary.^[159]

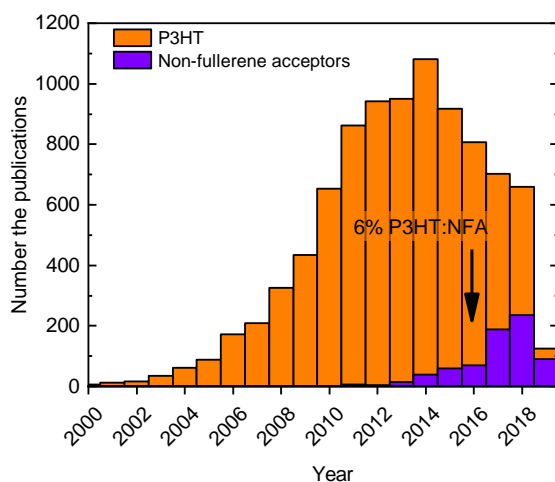


Figure 4.1. The research interest of P3HT and NFAs over years. The number of publications on P3HT and non-fullerene acceptors in the literature over the past years. Source: Scopus accessed 24/02/2019.

Table 4.1. Literature review of P3HT-based devices. Summary of the photovoltaic parameters reported in the literature.

| Acceptor | V_{oc} (V) | J_{sc} (mA/cm ²) | FF (%) | PCE (%) | Reference |
|---------------------|-----------------|-----------------------------------|-----------|------------|-----------|
| PC ₆₀ BM | 0.61 | -9.96 | 51.5 | 3.1 | [160] |
| PC ₇₀ BM | 0.62 | -11.6 | 49.3 | 3.6 | [160] |
| ICBA | 0.84 | -10.6 | 72.7 | 6.5 | [62] |
| O-IDTBR | 0.72 | -13.9 | 60.0 | 6.3 | [154] |
| EH-IDTBR | 0.76 | -12.1 | 62.0 | 6.0 | [154] |
| O-IDFBR | 0.68 | -7.4 | 68.0 | 4.5 | [159] |
| O-IDTBR:O-IDFBR | 0.82 | -14.4 | 64.0 | 7.6 | [159] |
| BTA1 | 1.02 | -7.3 | 70.0 | 5.2 | [161] |
| BTA2 | 1.22 | -6.2 | 60.0 | 4.5 | [162] |
| ITIC | 0.52 | -4.2 | 56.9 | 1.3 | [163] |

Besides the IDTBR family, there are other examples reported in the literature of P3HT blended with NFAs, see Table 4.1. For instance, a benzotriazole molecule (BTA2) mixed with P3HT exhibited V_{oc} values over 1 V leading to an efficiency of 4.5%.^[162] Moreover, devices with similar P3HT:benzotriazole modified with octyl side chains (BTA1) reached 5.2% of PCE.^[161] As shown in Table 4.1, some devices based on P3HT:NFA exhibit very high J_{sc} and FF with values over 12 mA/cm² and 60%, respectively. This can be explained due to the extraordinary synthetic flexibility of NFAs that enables to tune both absorption and energy levels in comparison to the traditional fullerene acceptors.^[164] However, there are other examples in the literature that the combination of P3HT and NFAs does not result in efficient devices. For instance, despite ITIC show very promising results in systems with a low-bandgap polymer, when ITIC is blended with P3HT show very low electron mobility^[165], and consequently PCEs below 2%.^[163]

From the manufacturing perspective, most of the reported solar cells were manufactured by spin-coating, hence limiting the large-scale transition.^[157,159] Very recently, Strohm *et al.* manufactured P3HT:O-IDTBR laser-patterned modules by blade-coating and slot-die.^[166] In that work, a detailed solvent screening identified efficient ‘greener’ alternatives such as methyl anisole and cymene to halogenated solvents. This work, as well as other papers, points out that the whole manufacturing scheme needs to be adapted in the transference to blade coating.^[108,167] Therefore, further studies of devices

manufactured with large-scale techniques are highly demanded to reduce the lab-to-fab gap. Very recently, Corzo *et al.* demonstrated high performing (>6%) devices of the same system but manufactured by inkjet printing.^[168]

4.1.1 Objective

The next sections of this chapter aim to further advance in the scalability of P3HT-based solar cells. First at lab-scale, we make use of the high throughput methods to screen five doctor-bladed P3HT:NFA systems with more than 1000 solar cells. Once we identified the best acceptor to blend with P3HT, the relevant parameters for the scalability such as thickness dependence, solvent system, annealing temperature and casting temperature were studied. Then, a long-term stability test as a function of the photoactive layer (PAL) thickness and encapsulation was carried out. The latter study is very relevant for the industrial point of view since we find that the most efficient devices are not necessarily correlated to the most long-term stable devices. To conclude this chapter, a first approach for the transition between lab-scale and intermediate-scale is discussed as a strategy to further upscale mm²-devices. Finally, as a proof-of-concept, R2R modules were manufactured from non-halogenated solvents.

4.2 Physical properties of photoactive materials

4.2.1 Optical properties

The specific acceptor material used in the photoactive layer has a decisive influence on the overall absorption of the device. The extinction coefficients for the different materials employed in binary blends are shown in Figure 4.2(a). Whereas fullerene molecules, PC₆₀BM and ICBA, are known to barely contribute to the optical absorption, NFAs exhibit a great light-harvesting potential even overcoming P3HT absorption capabilities. For this set of NFAs, light can be efficiently harvested from 450 nm to 750 nm depending on the nature of acceptor. Their chemical structures are given in section 2.1.4.2.

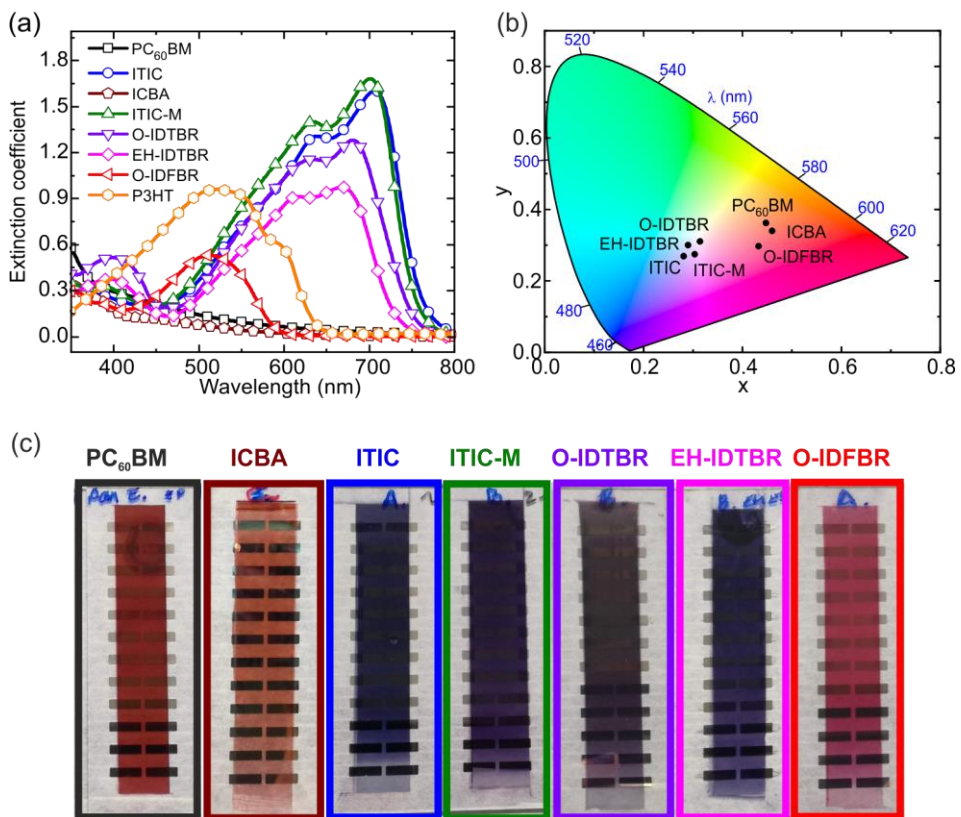


Figure 4.2. Absorption and aesthetics of materials used in this chapter. P3HT and acceptors (PC₆₀BM, ICBA, ITIC, ITIC-M, O-IDTBR, EH-IDTBR, O-IDFBR). (a) Extinction coefficient measured by VASE by Mr. Xabier Rodríguez and Dr. Mariano Campoy, (b) CIE colour coordinates of P3HT-based blends and (c) pictures of thickness-graded blends. The size of each sample is 7 cm x 2.5 cm.

This tuneable and high absorption of NFAs can be employed to tune the aesthetics of P3HT-based devices. Binaries of P3HT blended with fullerenes typically exhibit brownish or wine-like appearance. However, the use of NFAs based blends allows to widen the appearance of P3HT devices from purple (ITIC, ITIC-M, EH-IDTBR, O-IDTBR) to reddish (O-IDFBR), see Figure 4.2(b,c). The specific NFA side chains have a relevant impact on the absorption (Figure 4.2(a)). For instance, in the IDTBR family, octyl side chains (O-) exhibit both red-shifted and stronger absorption compared to the ethyl-hexyl (EH-) counterparts. The solubilisation chains affect the molecular packing, and thus, the degree of crystallinity of the two variants.^[154,169] On the other hand, the influence of methyl-end-capped group (ITIC-M) on ITIC is negligible in light absorption (Figure 4.2(a)). Note that, except O-IDFBR, this choice of NFAs has complementary absorption to P3HT, which enables broadening light absorption from 400 nm to 800 nm. Thus, a higher short-circuit current (J_{sc}) is expected in such systems, compared to fullerene-based devices.

4.2.2 Energy levels

In general, the optical gaps deduced from absorption are in good agreement with the reported energy levels (see Figure 4.3). Unlike the side chains effects described for the absorption, end-capped groups (ITIC vs ITIC-M) are more sensitive to the energy levels than side chains modifications (O-IDTBR vs EH-IDTBR).^[44,154]

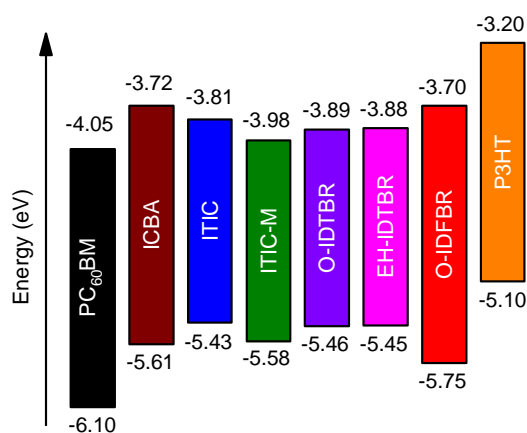


Figure 4.3. Energy levels of the studied systems are extracted from the literature.^[44,154,159]

The methyl end-capping group shifts up to 0.17 eV and 0.15 eV the LUMO and HOMO levels, respectively. In contrast, the modification of the side chains barely modifies energy levels of IDTBR. The acceptor type, in this case, is not the most relevant factor. Whereas the LUMO of PC₆₀BM and ICBA lies at -4.05 eV and -3.72 eV, respectively, energy levels of NFA can be also customised and designed from -3.70 eV (O-IDFBR)^[159] to -3.98 eV (ITIC-M). The increase of the acceptor LUMO levels (keeping constant HOMO levels) leads to an enhancement in the open-circuit voltage (V_{oc}) if only similar levels of recombination are assumed. For instance, and as reported, the increment of O-IDFBR and ICBA LUMO level to -3.70 eV and -3.72 eV (compared to -4.05 eV of PC₆₀BM) leads to an enhanced V_{oc} of 0.9 V and 0.83 V, respectively, of the corresponding solar cell (c.f. 0.6 V for PC₆₀BM^[159]).

4.3 Performance of P3HT based solar cells

According to the efficiency results, two main groups can be defined: P3HT working systems and P3HT non-working systems (see JV characteristics in Figure 4.4(a)). On the one hand, non-compatible P3HT:NFA systems include ITIC and its derivative, ITIC-M, which show low output despite their promising optical properties and their potentially good *a priori* energy level alignment.^[163] ITIC derivatives show a low external quantum efficiency (EQE), below 10%, see Figure 4.4(b). This low performance can be ascribed to a strong recombination process resulting in high voltage losses.

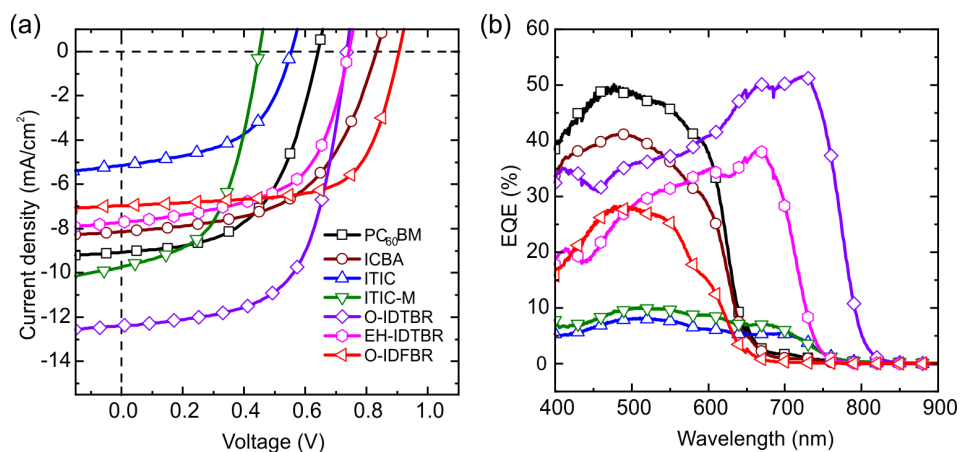


Figure 4.4. Photovoltaic characterisation of the best P3HT-based devices. (a) J-V characteristics. (b) External quantum efficiency (EQE). (a) and (b) share the colour legend.

This interpretation agrees with studies in the literature that similarly reported very low PCE of P3HT:ITIC system due to the excessive degree of crystallinity leading to excessive phase separation.^[163] Figure 4.5 confirms that none of the ITIC-based solar cells follows the expected linear behaviour between the measured and theoretical V_{oc} .^[170] On the other hand, the group of the P3HT compatible acceptors includes PC₆₀BM, ICBA, O-IDTBR, EH-IDTBR and O-IDFBR. As shown in Figure 4.5, the theoretical V_{oc} , herein defined as the energy levels difference between HOMO_{acceptor} and LUMO_{donor}, and measured V_{oc} for the P3HT working systems follows a linear trend indicating low recombination process. Additionally, V_{oc} values for working systems exhibit good agreement with the reported data. The best efficiencies for these systems vary from 3.2% for PC₆₀BM to 5.6% for O-IDTBR. Amongst them, PC₆₀BM solar cells show the lowest PCE values because of the limited V_{oc} compared to NFAs. Whereas PC₆₀BM based system yields 0.64 V, the rest of working NFA systems exceeds 0.7 V, reaching up to 0.9 V for O-IDFBR. This low voltage is explained by the lower LUMO level of PC₆₀BM with respect to NFAs (Figure 4.4(a) and Table 4.2). Unlike PC₆₀BM, the other fullerene reference, ICBA, reaches a 3.7% efficiency due to the large V_{oc} .

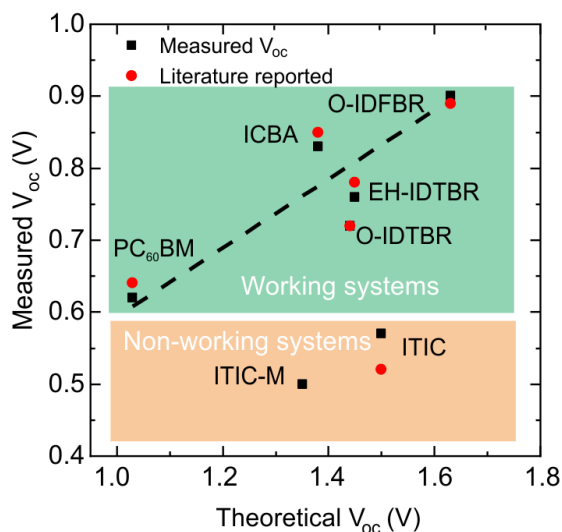


Figure 4.5. Theoretical (HOMO_{acceptor}-LUMO_{donor}) and measured V_{oc} . HOMO and LUMO levels were extracted from the energy levels of P3HT based systems for devices reported in this manuscript (black square) and literature (red circle). P3HT is blended with PC₆₀BM, ICBA, ITIC, ITIC-M, O-IDTBR, EH-IDTBR, O-IDFBR. Note that there is no available reported data for P3HT:ITIC-M system. The energy levels are extracted from the literature (references in the text). The dashed line is plotted as a guide to the eye.

According to the results of Table 4.2, side chains of the NFAs have a strong influence on the final performance. The devices containing an NFA decorated with octyl side chains (O-IDTBR) reach much higher short-circuit current density (12.4 mA/cm^2) than the ethylhexyl (EH-IDTBR) counterpart (7.7 mA/cm^2). Note that, the IDTBR molecule with linear side chains (O-IDTBR) is red-shifted and harvest light at longer wavelengths more efficiently compared to the branched one (Figure 4.4(b)). A larger red-shift associated with linear side chains is also noticeable in the extinction coefficient of Figure 4.2(a). Thus, side chains affect the molecular solubility and, consequently, the resulting PAL morphology. This points to a strong morphology dependence on the device performance, typically observed for semi-crystalline P3HT-based devices. This fact might help to explain the reason for the low efficiency of P3HT:ITIC system.^[163]

Table 4.2. Photovoltaic parameters of the bladed champion solar cells. These devices were manufactured using the high-throughput method shown in section 2.2.1.1. For device statistics and reproducibility of the high throughput method, see high throughput reproducibility in Figure 2.6.

| Acceptor | V_{oc} (V) | J_{sc} (mA/cm^2) | FF (%) | PCE (%) |
|---------------------|-----------------|----------------------------------|-----------|------------|
| PC ₆₀ BM | 0.64 | -9.1 | 54.6 | 3.2 |
| ICBA | 0.83 | -8.2 | 54.8 | 3.7 |
| ITIC | 0.55 | -5.2 | 52.2 | 1.5 |
| ITIC-M | 0.45 | -9.8 | 52.5 | 2.3 |
| O-IDTBR | 0.74 | -12.4 | 61.6 | 5.6 |
| EH-IDTBR | 0.74 | -7.7 | 57.7 | 3.3 |
| O-IDFBR | 0.90 | -6.9 | 67.5 | 4.2 |

4.4 Studied parameters

4.4.1 Selection

In general, the top-performing PALs based on P3HT are cells processed from chlorobenzene (CB), spun-coated and subjected to a post-thermal treatment.^[40] We evaluate the impact of those parameters that have a higher impact when moving from spin-coating to blade-coating. In particular, we explore some of the most relevant blade-coating parameters such as solvent system, the annealing temperature, blade-speed (thickness) and casting temperature.

For a given material system, the device optimisation usually involves careful control of the parameters that affect the crystallinity of the PAL. CB is the most employed solvent system in spin-coating technique. Although in some cases the use of a controlled amount of a solvent additive, such as 1,8-diiodooctane (DIO), can improve the blend morphology by means of adjusting both the material solubility and the degree of phase separation.^[171] The use of additives, however, requires precise control of the solvent volume fraction (typically 1-2% in volume). Therefore, solvent mixtures (assuming volume fraction higher than 10%) are less critical with respect to the exact percentage of additives.

In this section, we compare the effect of both CB and a binary mixture of universal solvents (chlorobenzene:o-dichlorobenzene, CB:DCB), which is a more general choice than the additive alternative. We also looked at the blade casting temperature, as a strategy of modifying the drying kinetics without specifically changing the solvent system. Typically, the top-performing blade-coated solar cells are cast around 80-90°C. In this study, we span the range of the casting temperature from 40°C to 105°C. Besides, to investigate the thickness-performance dependence, the blade speed was varied from 5 to 99 mm/s using a high throughput approach. Finally, the effect of the post annealing was studied varying the annealing temperature gradually from no-annealing to 150°C. Precisely, within this range of temperatures P3HT-based solar cells typically show the optimum post-thermal treatment.

4.4.2 Sensitivity analysis

Many processing parameters are involved in the optimisation process of blade coated P3HT-based devices. To quantitatively assess each parameter of the dataset, a sensitivity analysis was performed to identify the most critical parameter/s. For this purpose, the statistical tool F-statistics, extracted from the one-way analysis of variance (ANOVA), was applied to the developed dataset of 1000 devices.^[172]

$$F = \frac{MS_{between}}{MS_{within}} \quad (4.1)$$

The F statistic is applied individually to each of the studied parameters including acceptor, solvent system, annealing temperature, casting temperature and blade speed. For any of the aforementioned parameters, F statistic compares the variability between the different subsets of the parameter concerning the variability within each of the subsets of the same parameter, see Eq. 4.1. For instance, F statistic applied to the parameter of casting temperature of P3HT:O-ITDTBR (Figure 4.6) is the variability between ($MS_{between}$) the 3 studied casting temperatures (40°C, 80°C and 105°C) concerning the variability within (MS_{within}) each of these casting temperatures. Mathematically, $MS_{between}$ is the mean square between subsets (Eq. 4.2) whereas MS_{within} is the mean square within subsets (Eq. 4.3).

$$MS_{between} = \frac{\sum_{i=1}^k \left(\frac{T_i^2}{n_i} \right) - \frac{G^2}{n}}{k - 1} \quad (4.2)$$

$$MS_{within} = \frac{\sum_{i=1}^k \sum_{j=1}^{n_i} Y_{ij}^2 - \left(\frac{T_i^2}{n_i} \right) - \frac{G^2}{n}}{n - k} \quad (4.3)$$

where

- k: Number of different subsets for a given variable. For casting temperature k=3 equivalent to the different cast temperatures 40°C, 80°C and 105°C.
- G: the grand total or in other words the sum of PCE for all casting temperatures.

- T_i : Group total. Similar to G but applied to subsets. For casting temperature is the sum of PCE for each of the scanned temperatures. T_1 is the sum of PCEs cast at 40°C, T_2 is the sum of PCEs cast at 80°C and T_3 is the sum of PCEs cast at 105°C.
- n_i : Size of each subset (or the number of data) i . For casting temperature there are 151 devices cast at 40°C ($n_1=151$), 53 devices cast at 80°C ($n_2=53$) and 437 devices cast at 105°C ($n_3=437$)
- n : Size of the entire dataset. For casting temperature and only considering P3HT:O-IDTBR devices $n=641$.
- Y_{ij} is an observation or in other words, represents a labelled data of the dataset. For casting temperature, PCE_{ij} is the data of PCE corresponding to casting temperature i varying from 1 to 3 (40, 80, 105°C) and in the position j within that casting temperature.

For this analysis, the selected groups that influence the PCE are acceptor, solvent system, casting temperature, annealing temperature and blade speed. Large F-test values indicate highly sensitive parameters whilst small ones suggest a low-impact parameter in the optimisation process. Besides, F-test values enable to classify the processing parameters as a function of the PCE sensitivity (Table 4.3). According to these results, the most sensitive performance-parameter of P3HT:acceptor based devices is the acceptor material ($F=129$), in agreement with what observed in the previous section. For instance, O-IDTBR devices yield PCE values up to 5.5% (Figure 4.6), meanwhile, the performance of ITIC devices is limited to 1.5%.

Table 4.3. Sensibility analysis of processing parameters. F value for the different processing parameters, as extracted from the one-way variance (ANOVA) analysis. It includes the ANOVA-F for the complete set of devices and the ones with >5% PCE, as well the min-max difference in performance for each parameter.

| | F (all data) | F (PCE>5%) | $\Delta PCE_{\max-\min}$ (%) |
|-----------------------|-----------------|---------------|---------------------------------|
| Acceptor | 129 | - | 4.0 |
| Solvent | 84 | - | 1.7 |
| Annealing temperature | 64 | 1.5 | 0.6 |
| Casting temperature | 40 | 3.1 | 0.3 |
| Blade speed | 4.3 | 1.0 | 0.5 |

Then, the second most sensitive parameter ($F=84$) is the solvent system. For P3HT:O-IDTBR based devices, the performance varies up to 1.7% for a binary solvent system with respect to CB. As the third most sensitive parameter is the effect of the annealing temperature ($F=64$), with variations of PCE of more than 0.6% to yield an adequate balance between crystalline and amorphous domains of both components. Finally, the least sensitive studied parameters are the casting temperature ($F=40$) and, to a lesser extent, the blade speed, equivalent to the PAL thickness. The thickness-performance insensitivity (less than 0.5%) is probably to the relatively high mobility of P3HT. The performance of O-IDTBR devices shows minor dependence with the casting conditions varying less than 0.3% in the scanned temperature range.

As a rule of thumb, our study reveals that the most critical OPV parameters for the studied P3HTbased devices are listed as follow:

- Choice of acceptor material.
- Precise microstructure (solvent system, annealing temperature and casting temperature).
- Geometrical device factors (thickness).

In the following sections of this chapter, we analyse the individual the contribution of each of the parameters starting from the most sensitive ones, solvent system and the acceptor material.

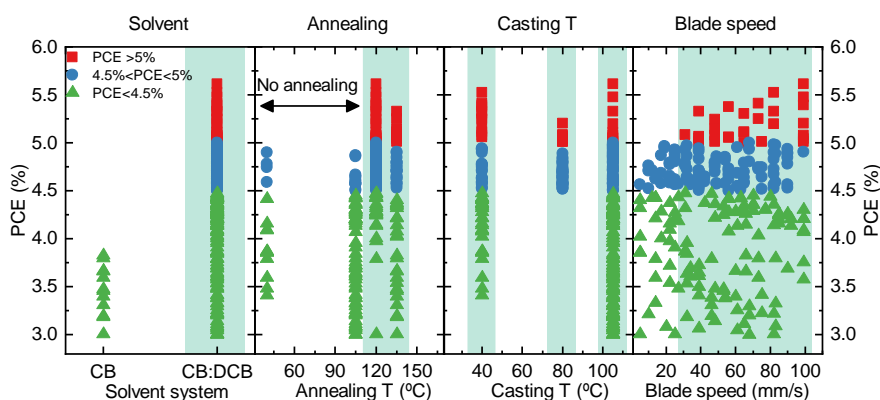


Figure 4.6. Multiparametric processing study of the P3HT:O-IDTBR based devices from the database. The solvent system, annealing temperature, casting temperature and blade speed (from left to right) as a function of PCE. Plot symbols are shape-PCE dependent (red squares over 5%, blue circles from 4.5 to 5% and green triangles below 4.5%). 3% PCE threshold was set to avoid non-working devices.

4.5 Meta-analysis of P3HT based solar cells

We have performed a data science-inspired analysis of P3HT based solar cells. With the aid of an in-home developed database, over a thousand devices comparing the solvent system (CB vs CB:DCB) were considered and depicted in Figure 4.7. For clarity and to rule-out malfunctioning devices, 0.3V V_{oc} , 30% FF and 0.5% PCE thresholds were set. The label in brackets in Figure 4.7 represents the number of devices that overcome the thresholds. For example, although the same number of ITIC and its derivative devices were manufactured, only 1 ITIC based device processed from CB yielded a *PCE* over 0.5%.

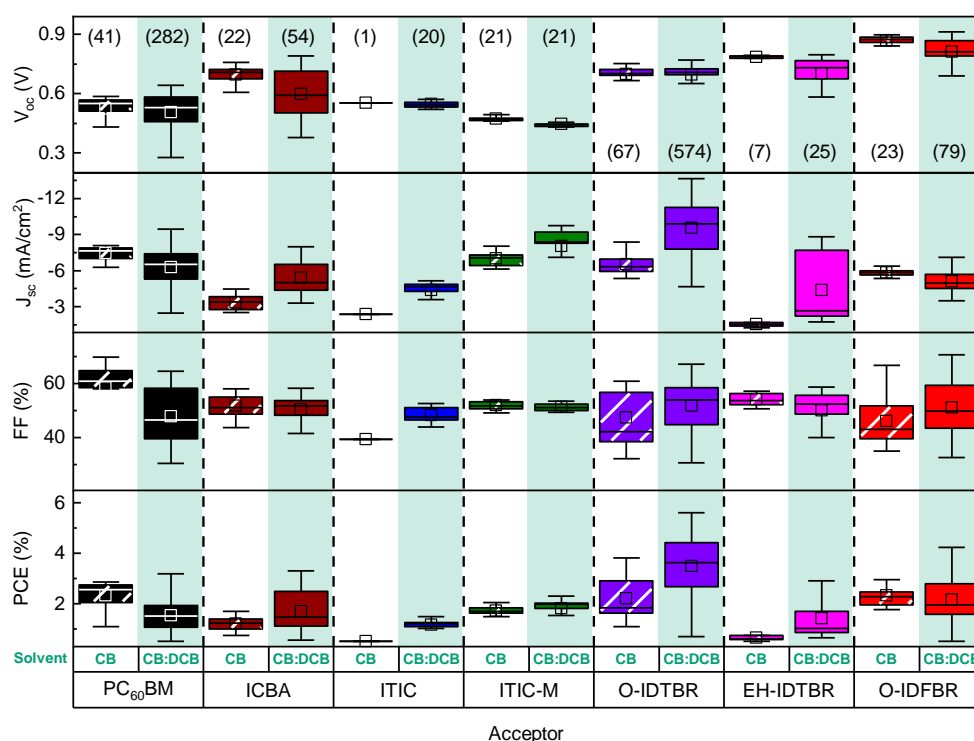


Figure 4.7. Summary of P3HT based solar cells. Box and whisker plot of photovoltaic parameters from 1560 devices of P3HT blended with seven different acceptor materials (PC₆₀BM, ICBA, ITIC, ITIC-M, O-IDTBR, EH-IDTBR, O-IDFBR) as a function of the solvent, namely chlorobenzene (CB) and a mixture of chlorobenzene: dichlorobenzene (CB:DCB). The photovoltaic parameters are open-circuit voltage (V_{oc}), short-circuit current (J_{sc}), fill factor (FF) and power conversion efficiency (PCE). Data include thickness variations, annealing variations, several casting temperatures and various volume ratios. Statistical values are represented by mean (inner empty square), median or 2nd quartile (inner horizontal line), 1st and 3rd (height of the box) and maximum and minimum value (whisker height). The number of devices characterised for each material system appears in brackets (only those which overcome the 0.5% PCE and 30% FF threshold) on the top row.

Furthermore, Figure 4.7 summarises the whole high-throughput optimisation process. The large dispersion of J_{sc} and FF in the box and whisker plot is due to variations in all the studied parameters. As seen in the ANOVA sensitivity analysis, we found that the most sensitive processing parameter for P3HT-based systems is the solvent system. This indicates that controlling drying kinetics is crucial for achieving high performing bladed-solar cells. The addition of a solvent with a higher boiling point (131°C and 180°C for CB and DCB, respectively) delays film formation and hence strongly affects the morphology of films. This first conclusion prompts a detailed investigation of other factors affecting drying kinetics, such as the casting temperature and post-deposition annealing (see following sections).

The first observation of Figure 4.7 is that, consistently, devices processed from a mixture of solvents (CB:DCB) yield to higher J_{sc} and FF values, regardless the choice of NFA, side chains, or end-capping group. In particular, for IDTBR family devices, there is a twofold increase of J_{sc} when processed from CB:DCB compared to CB. Unlike the J_{sc} , FF does not show a strong solvent system dependence. Unsurprisingly, PC₆₀BM and O-IDTBR are the systems with higher dispersion of FF since more than 200 devices were manufactured for each material system. It is worth noting that the amorphous NFA system, O-IDFBR, shows the highest FF (67%) with similar values of spin-coated devices.^[159] However, the limited absorption of O-IDFBR leads to poor performing devices. This problem has been solved with the addition of O-IDTBR in the binary to improve J_{sc} .^[159]

The solvent system barely affects V_{oc} . Both CB and CB:DCB processed devices show similar V_{oc} values, with a small dispersion (below 0.1 V). However, devices processed from CB:DCB lead to a higher V_{oc} in PC₆₀BM and slightly lower V_{oc} in ICBA, EH-IDTBR and O-IDFBR. These small variations in V_{oc} values generally point to small changes in the degree of crystallinity of the PAL.^[55] Finally, the highest PCE values are consistently found for cells based on CB:DCB mixtures. The PCE mainly reflects the dependence of J_{sc} with the solvent system. Additionally, the PCE points out that the top-performing NFA blended with P3HT is O-IDTBR. Despite the many processing parameters involved in the optimisation process, the median PCE of O-IDTBR devices is above 4% while the median of other NFAs blended with P3HT is lower than 3%. Our

finding is in agreement with Strohm *et al.* who reported that mixtures of CB with the additive p-bromoanisole (5.6%) overcome the performance of the formulations from pristine CB (2.6%).^[166] Noticeably, in our study, 4% PCE blade-coated P3HT:O-IDTBR devices were processed from pristine CB.

4.6 Morphology control of P3HT:O-IDTBR solar cells

In the next sections, the processing parameters (solvent system, annealing and casting temperature) that control the PAL morphology of the most promising system, P3HT:O-IDTBR, system are intensively assessed.

4.6.1 Solvent study

To get insights on the best performance of devices processed from the solvent mixture over a pristine solvent, we further study the P3HT:O-IDTBR system. In particular, we analyse the effect of the solvent system on the thickness-performance trade-off, film surface by contact angle measurements and AFM, and crystallinity by Raman spectroscopy, optical absorption and X-ray diffraction.

4.6.1.1 Photovoltaic performance

The effect of the solvent system and PAL thickness on the photovoltaic parameters were assessed using a high-throughput approach (described in section 2.2.1.1). To do so, only two samples with thickness-graded PAL (24 devices) were manufactured enabling to save resources and time.

CB:DCB processed devices exhibit, consistently, higher J_{sc} compared to CB-based devices, and with milder thickness dependence (see Figure 4.8). More precisely, J_{sc} is enhanced by more than 4 mA/cm² for devices processed from the solvent mixture at thicker films (200-300 nm). Unlike J_{sc} , FF and V_{oc} do not show large difference upon the solvent system. The enhancement of straight-forward J_{sc} observed from a mixture of solvents is usually explained by a higher degree of crystallinity, better domain sizes and/or purity or by improved vertical segregation.^[173,174]

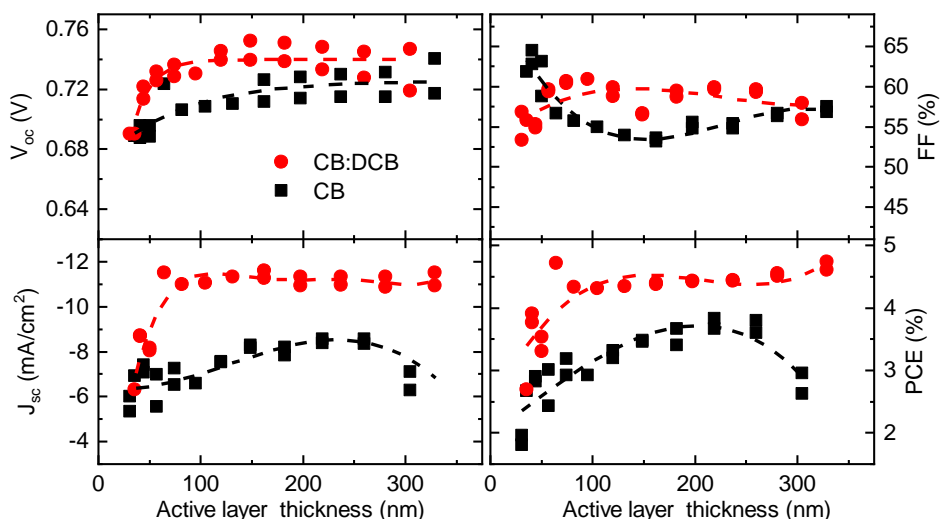


Figure 4.8. Processing solvent study on P3HT:O-IDTBR films. Photovoltaic parameters V_{oc} , J_{sc} , FF and PCE as a function of the thickness of the PAL and solvent system (dashed lines are plotted as a guide to the eye).

4.6.1.2 Topographical studies

In order to unravel the potential surface enrichment of any component, we first measured the water contact angle of the neat donor and acceptor materials, P3HT and O-IDTBR, together with blends deposited from CB and CB:DCB. The contact angle values for neat P3HT and O-IDTBR processed from CB (Figure 4.9(a,b)) are $108^\circ \pm 2.0^\circ$ and $98.1^\circ \pm 1.2^\circ$ respectively, thus easily distinguishable.

Additionally, to rule out the effect of the processing solvent on the wetting properties of the neat material, we measured the contact angle of P3HT film processed from CB:DCB showing a similar value ($107.5^\circ \pm 0.9^\circ$) when processed from CB. In contrast, the contact angle measurement of O-IDTBR processed from the binary solvent could not be assessed due to dewetting tendency of the wet film. As Figure 4.9(c) depicts, the contact angle of the PAL coated from CB corresponds to the average contact angle value of both P3HT and O-IDTBR. Surprisingly, the PAL manufactured from CB:DCB (Figure 4.9(d)) leads to a similar contact angle to that of the neat P3HT. This finding strongly indicates preferential segregation of P3HT domains towards the surface of the PAL.

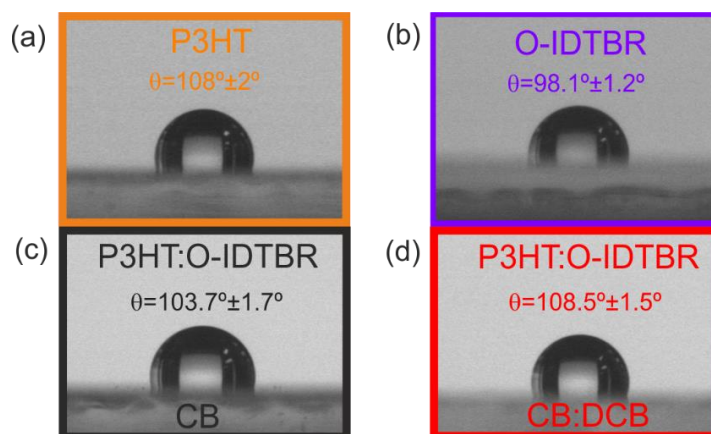


Figure 4.9. Contact angle measurements of P3HT, O-IDTBR and blends with different solvent systems. Measurements carried out on glass for neat materials processed from CB:DCB (a) P3HT (b) O-IDTBR, and blends P3HT:O-IDTBR (c) from CB:DCB and (d) CB.

Moreover, the contact angle measurement could explain the superior performance of devices processed from CB:DCB and consequently supports the construction of the inverted structure of the device where the electron donor (P3HT) material should be placed preferentially close to the HTL. Secondly, atomic force microscopy (AFM) was used to investigate the effect of the processing solvent on the surface of P3HT:O-IDTBR blend films.

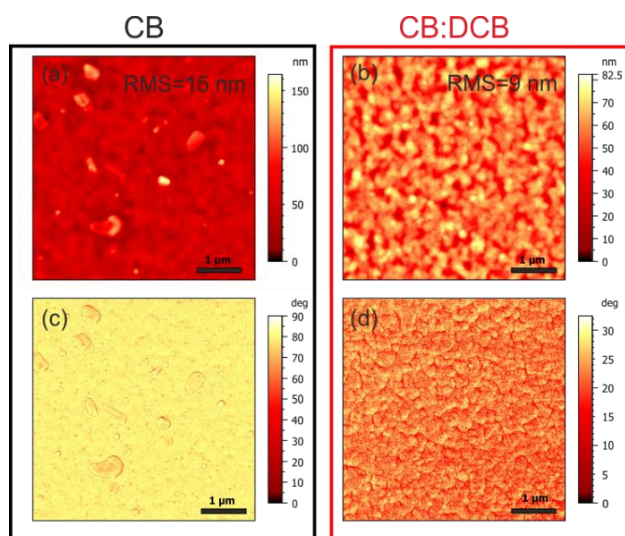


Figure 4.10. AFM measurements of P3HT:O-IDTBR blends as a function of the solvent system. AFM height (a, b) and phase (c, d) images of P3HT:O-IDTBR films processed from CB (a, c) and CB:DCB (b, d). All AFM image scans are 5 μm x 5 μm .

The topography and height images are shown in (Figure 4.10). CB:DCB processed films show a root-mean-square (RMS) roughness of 9 nm lower than CB counterpart (15 nm). Additionally, the CB processed films display large aggregation in the range of micron size, which is typically related to the crystallinity of the material. In contrast, the morphology of the CB:DCB processed films evolves to a more favourable donor-acceptor phase separation.

4.6.1.3 Morphological studies

The degree of crystallinity of films was tackled using optical spectroscopic techniques. Optical absorption measurements show a minor change in the absorption region of O-IDTBR (from 700-850 nm) when going from CB:DCB over CB, see Figure 4.11(a). To unravel the role of P3HT, Raman scattering measurements were also carried out (Figure 4.11(b)). Since the P3HT Raman cross-section is much higher than that of O-IDTBR, the observed Raman peaks can be uniquely attributed to P3HT.

As reported in the literature, we have analysed the main P3HT Raman bands as a superposition of two components, namely regioregular (*RR*) and regiorandom (*RRa*) P3HT, see inset of Figure 4.11(b).^[112] Table 4.4 shows a summary of the Raman peak analysis. The higher *RR*/*RRa* height peak ratio for films processed from CB compared to those made from CB:DCB suggests that the former leads to higher P3HT crystallinity.

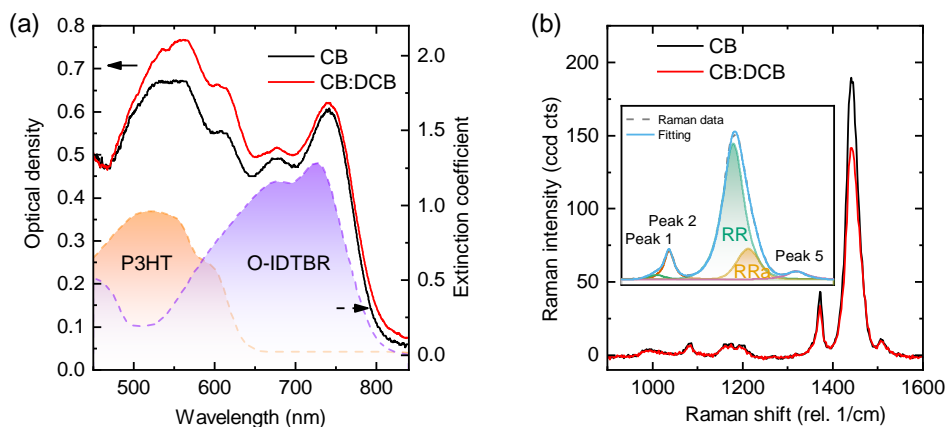


Figure 4.11. Optical characterisation of P3HT:O-IDTBR devices processed from CB and CB:DCB (1:1). (a) Optical density (left axis) of blends and extinction coefficient of neat materials (right axis). (b) Raman shift excited at 488 nm. Inset: Fitting of Raman spectra with 5 peaks. Highlighted P3HT regioregular (*RR*) and regiorandom (*RRa*) C=C symmetric stretching components following the method reported in the literature.^[112]

Table 4.4. Raman peaks analysis of P3HT:O-IDTBR films from Figure 4.11. Gaussian Lorentzian crossed functions are used to fit Raman spectra. All the Raman spectra were fitted with 5 Lorentzian Cross product peaks and subtracting the background in the same way.

| Solvent | P3HT regioregular (RR) | | | P3HT regiorandom (RRa) | | | RR/RRa (height) |
|---------|--------------------------------|--------|------------------------------|--------------------------------|--------|------------------------------|--------------------|
| | Centre (cm^{-1}) | Height | FWHM (cm^{-1}) | Centre (cm^{-1}) | Height | FWHM (cm^{-1}) | |
| CB | 1441.5 | 182 | 13.5 | 1458.8 | 32 | 14.1 | 5.6 |
| CB:DCB | 1441.5 | 137 | 14.3 | 1460.8 | 33 | 14.0 | 4.1 |

The XRD spectra show a P3HT (100) intensity peak centred at 5.3° , which is in good agreement with previous reports.^[175] The intensity of the P3HT peak of films processed from CB is higher than that of a CB:DCB processed film of a similar thickness, with the FWHM of the latter being slightly smaller (0.027 \AA^{-1} and 0.029 \AA^{-1} for CB and CB:DCB, respectively). Therefore, XRD findings and supported by Raman scattering point out an excessive degree of crystallinity of P3HT blends when processed from CB with respect to CB:DCB. Additionally, this help to explain the higher FF of thinner devices ($<100 \text{ nm}$) when processed from CB compared to CB:DCB (Figure 4.8). In summary, Raman spectroscopy, XRD and AFM measurements suggest that the mixture of solvents prevent large scale phase separation, as recently suggested for a different solvent mixture.^[155] The better intermixing morphology together with lower RMS explains the higher J_{sc} and better charge transfer for CB:DCB over CB processed films.

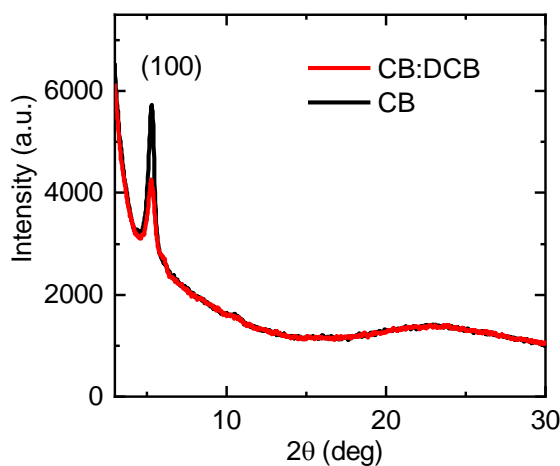


Figure 4.12. X-Ray diffraction spectra of the P3HT:O-IDTBR. For films processed from CB (black) and CB:DCB (red) subjected to post-thermal annealing at 120°C .

4.6.2 Thermal annealing study

The solvent study presented in the previous section clearly shows that the attained blend morphology is a very important parameter determining the final device photocurrent for devices based on P3HT.^[176] Particularly, the CB:DCB solvent system induces a more appropriate degree of P3HT crystallinity yielding higher efficiencies compared to CB. Alternative processing schemes aimed at tuning the morphology of the photoactive layer include the casting temperature and the post-deposition thermal annealing. Here, we investigate the effect of thermal annealing on the performance of P3HT:O-IDTBR solar cells processed from CB:DCB.

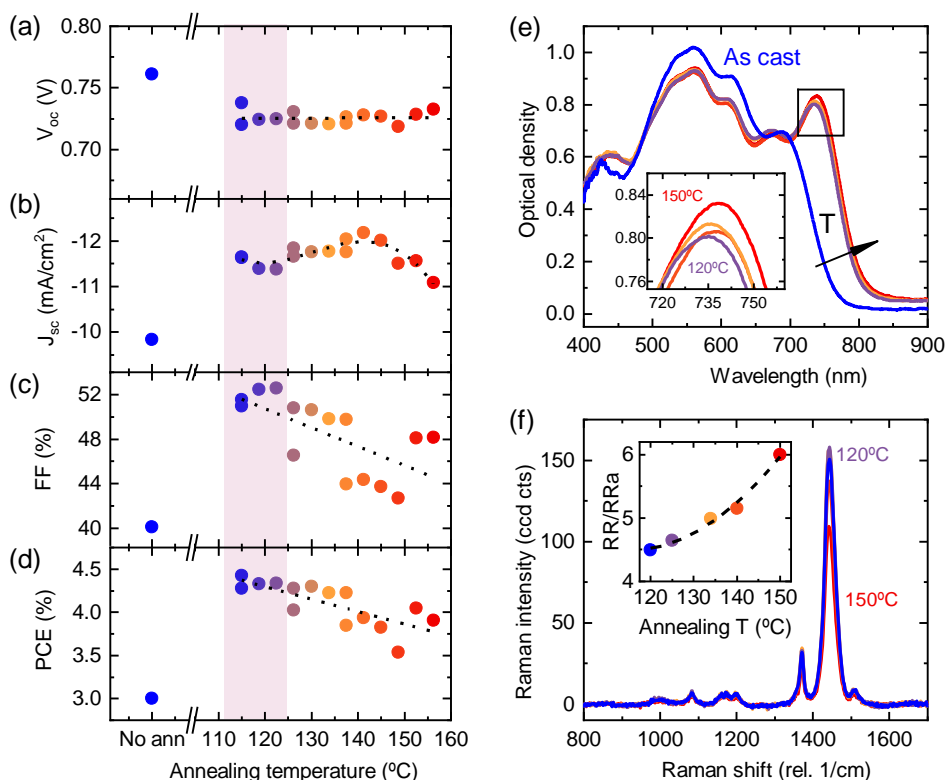


Figure 4.13. Annealing effect on P3HT:O-IDTBR solar cells processed from CB:DCB. Photovoltaic parameters (a) V_{oc} , (b) J_{sc} , (c) FF and (d) PCE as a function of the annealing temperature. (e) Optical density spectra. Inset: absorbance zoom in the wavelength of interest from 715 to 770 nm. (f) Raman shift of photoactive layers annealed at temperatures from 120°C to 150°C. Inset: Raman peak height ratio of P3HT regioregular (RR) and regiorandom (RRa) Raman height ratio of P3HT components. In all graphs, a temperature-colour dependent scale is used. Colours vary gradually from no annealing (blue) to 150°C annealing (red). Dashed lines are plotted as a guide to the eye.

A high throughput approach was again employed; in this case, a sample of constant thickness was exposed to an annealing gradient using a Kofler bench (see section 2.2.1.3). Non-annealed samples show a low FF (40%) and a modest J_{sc} (10 mA/cm²). Interestingly, both PCE (Figure 4.13(d)) and FF (Figure 4.13(c)) have the optimum annealing conditions around 120°C, while the J_{sc} maximises at slightly higher temperatures (Figure 4.13(b)). Note that the minimum annealing temperature (no-annealing) was 105°C, corresponding to the casting temperature. This fact suggests that the FF is the dominant parameter affected by the specific annealing temperature. Increasing the annealing temperature above 120°C leads to a progressive decrease of both FF and PCE, presumably due to the development of larger crystalline domains.

Moreover, the FF (PCE) decreases from 52% (4.3%) to 42% (3.7%) upon annealing at 120°C and 150°C, respectively. Annealing promotes NFA crystallisation, as clearly seen by the bathochromic shift in the absorption spectra produced by annealing (Figure 4.13(e)). Note that the absorption change observed upon annealing occurs at the spectral region corresponding to the NFA absorption, while the overlapping absorption of the two components around 500 to 650 nm makes it difficult to assign changes in P3HT crystallinity with confidence, see Figure 4.11(a). Similarly to the previous section (Figure 4.11(b)), we have performed a study on Raman scattering measurements on the graded temperature annealed sample to analyse the effect of annealing temperature on the crystallinity of P3HT.^[112,130]

Table 4.5. Raman peaks analysis of P3HT:O-IDTBR films from Figure 4.13(a). Gaussian Lorentzian crossed function was used to fit Raman spectra. All the Raman spectra were fitted with 5 Lorentzian Cross product peaks and subtracting the background in the same way.

| Annealing T (°C) | P3HT regioregular (RR) | | | P3HT regiorandom (RRa) | | | RR/RRa (height) |
|---------------------|-------------------------------|--------|-----------------------------|-------------------------------|--------|-----------------------------|--------------------|
| | Centre (cm ⁻¹) | Height | FWHM (cm ⁻¹) | Centre (cm ⁻¹) | Height | FWHM (cm ⁻¹) | |
| 120 | 1441.5 | 141 | 13.9 | 1457.8 | 32 | 14.3 | 4.5 |
| 125 | 1441.5 | 150 | 13.9 | 1458.4 | 32 | 14.0 | 4.6 |
| 134 | 1441.5 | 150 | 13.9 | 1458.2 | 30 | 14.3 | 5.0 |
| 140 | 1441.5 | 133 | 13.7 | 1458.1 | 26 | 13.7 | 5.2 |
| 150 | 1441.5 | 109 | 13.9 | 1459.1 | 18 | 13.9 | 6.0 |

The Raman analysis reveals that the RR/RRa peak height ratio (a proxy of the degree of crystallinity) increases with temperature (Table 4.5). Moreover, the optimum RR/RRa peak height ratio for films of P3HT:O-IDTBR processed from CB:DCB is 4.5. A RR/RRa ratio larger than 4.5 leads to a reduction in the performance of the solar cell. As-cast P3HT:O-IDTBR films from CB show a RR/RRa height ratio (namely degree of crystallinity) of 5.6 and a PCE of 3.5% (Figure 4.13(f)), which are comparable to the 150°C-annealed CB:DCB processed devices leading to a RR/RRa ratio of 6 and 3.8% of PCE. This proves that, for this specific system, similar blend morphology can be obtained through different combinations of the solvent system and annealing temperature.

For completeness, a similar annealing dependent study was carried out for P3HT:O-IDFBR system (details in Figure 4.14). Note that, the optimum annealing temperature is, in this case, around 150°C, which is close to the typical temperature needed to optimise P3HT:PC₆₀BM blends. This has been attributed to the temperature required to crystallise P3HT.^[54]

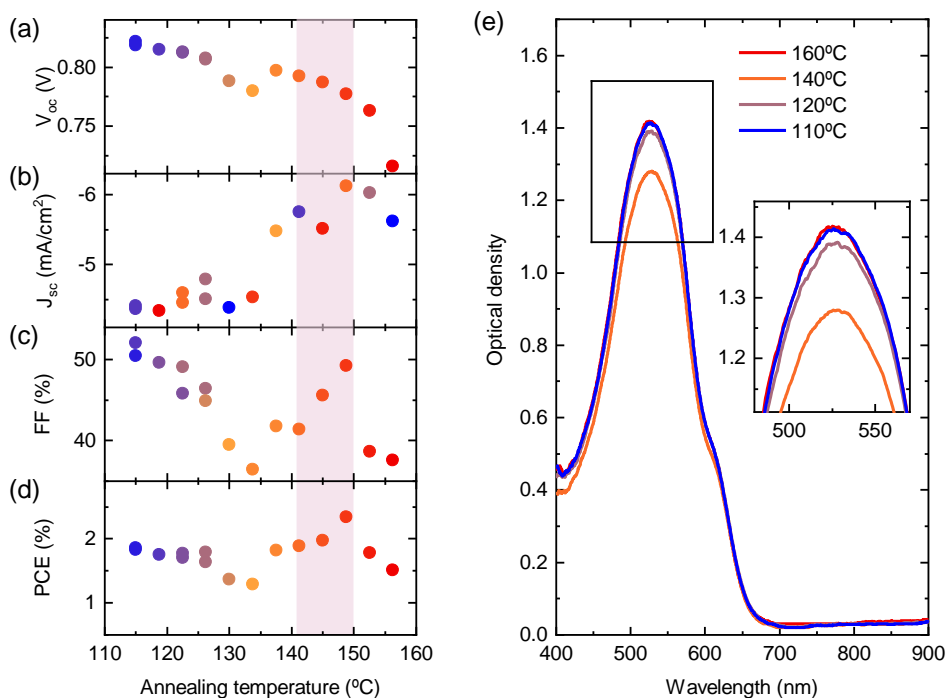


Figure 4.14. P3HT:O-IDFBR study upon thermal annealing. Photovoltaic parameters (a) V_{oc} , (b) J_{sc} , (c) FF and (d) PCE. (e) Optical density of annealed samples from 110°C to 160°C. Colours are temperature-dependent in plot going from 110°C (blue) to 160°C (red).

Considering that O-IDFBR molecules partially prevent P3HT crystallisation, it is reasonable that the required temperature to enhance such crystallinity is higher.^[159] Correspondingly, the photovoltaic efficiency appears to be the combination of J_{sc} and FF, as one may expect from an improving degree of crystallinity and thus charge transport upon annealing.

4.6.3 Study of casting temperature

Figure 4.15(a,b,c,d) shows the photovoltaic parameters of P3HT:O-IDTBR solar cells with a thickness gradient cast at 3 different temperatures (40°C, 80°C and 105°C). All devices were subjected to a thermal annealing at 120°C after casting (the optimum annealing temperature previously found).

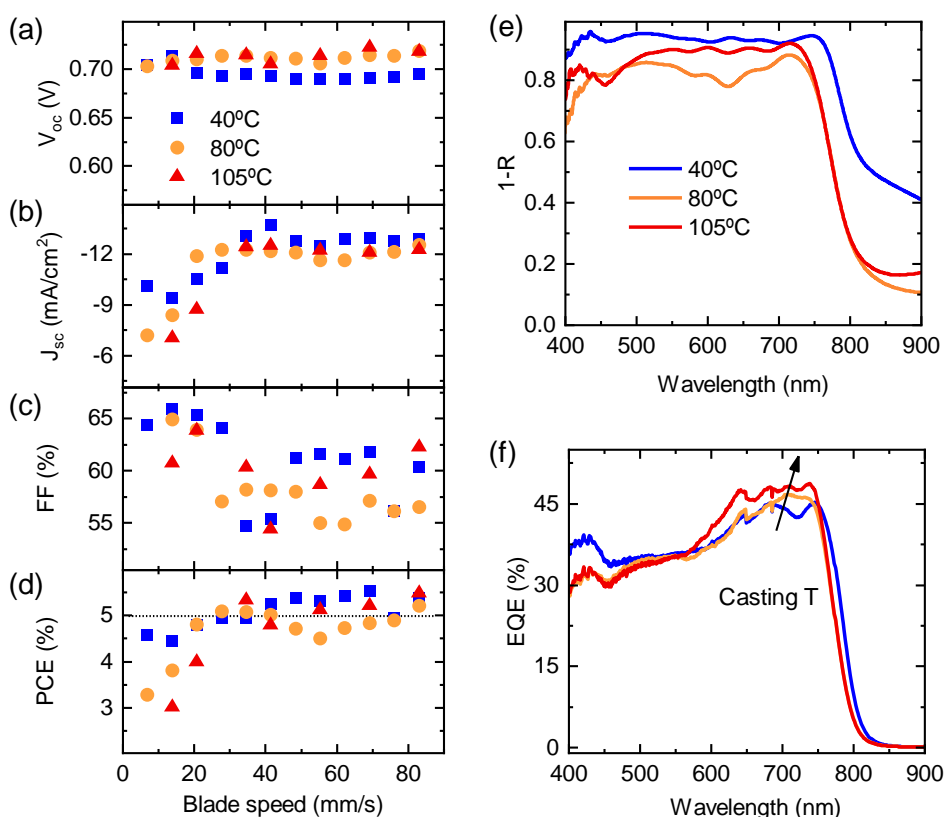


Figure 4.15. Casting temperature study for P3HT:O-IDTBR based devices. (a) Open-circuit voltage (V_{oc}), (b) short-circuit current density (J_{sc}), (c) fill factor (FF), (d) power conversion efficiency (PCE), (e) absorption (1-R) and (f) EQE for 3 different casting temperatures 40°C (square blue), 80°C (circle orange) and 105°C (triangle red).

Devices cast at 80°C and 105°C exhibit a V_{oc} around 0.72 V, whereas devices cast at 40°C show a slightly lower V_{oc} (0.70 V). Moreover, Figure 4.15(e) shows red-shifted absorption peaks for devices cast at 40°C compared to those of samples cast at 80°C and 105°C. This indicates that a slower drying dynamics leads to better phase separation and thus, a higher degree of NFA crystallinity (see FF in Figure 4.15(c)). The J_{sc} of the devices cast at different temperatures exhibits a similar trend with PAL thickness having the first interference peak at a blade speed of 40 mm/s, which corresponds, in our case, to a thickness of 120 nm. The J_{sc} for the devices cast at three different temperatures reaches values of 12 mA/cm². Interestingly, the J_{sc} shows the same increasing trend with no effect of the casting temperature despite the different drying kinetics. This effect indicates that the post-deposition annealing partially erases the previous processing history of the film, provided that the deposition temperature is below the post-deposition annealing.

This type of thermal memory effect has been observed before in conjugated polymers subjected to cycled thermal annealing.^[177] Unlike the J_{sc} , the highest FFs are found for the devices cast at 40°C. This effect might be explained again by the slow drying and thus, longer times for domain formation, in agreement with the EQE and absorption spectra (Figure 4.15(e,f)). Finally, PCE reveals that this combination of semiconductors is not especially sensitive to film thickness. Promisingly, PCE values above 5% are yielded for deposition temperatures ranging from 40°C to 105°C and for blade speeds ranging between 35 mm/s and 80 mm/s. This finding makes this OPV system a suitable candidate for upscaling due to the wide thickness processing window. A proof-of-concept of R2R P3HT: O-IDTBR modules is shown the section 4.9 of this thesis.

4.6.4 Understanding the relationship between solvent and annealing temperature

As discussed before, an appropriate morphology for P3HT-based devices is mainly controlled by the solvent system and post-thermal annealing. The choice of solvent affects the degree of solubility of materials, the boiling point and consequently, the drying dynamics and aggregation degree. Generally, polymers show more difficulties to be dissolved in organic solvents than small-molecule acceptor materials (NFAs). To predict the theoretical solubility of a material in a specific solvent, Hansen solubility parameters (HSP) method can be employed.^[178] The HSP accounts for the dipole-dipole contribution

of the molecular bonding including non-polar bonding or dispersion forces (δ_D), polar dipole forces (δ_P) and hydrogen bonding interactions (δ_H).^[179] The predicted solubility is given by the material-solvent distance (R_a) in the Hansen space described by Eq. 4.4.

$$R_a = \sqrt{4(\delta_{D1} - \delta_{D2})^2 + (\delta_{P1} - \delta_{P2})^2 + (\delta_{H1} - \delta_{H2})^2} \quad (4.4)$$

where the indices 1 and 2 refer to solute and solvent, respectively.

According to the HSP values shown in Table 4.6, P3HT and O-IDTBR show better solubilities in DCB and consequently in CB:DCB (2.3 and 4.2, respectively) than in CB (5.0 and 7.3, respectively) due to the non-polar bonding (δ_D) of DCB. However, the role of CB in the binary formulation is crucial due to two factors. First, the presence of CB in the solution improves the processability of the formulation (avoid dewetting) and second, it reduces substantially the boiling point of the formulation (131°C and 151°C, for CB and CB:DCB, respectively) resulting in a reduction of the drying time.

In terms of drying kinetics, DCB shows a higher boiling point than CB. In the first stage, CB is evaporated and then DCB controls the last drying stage of the wet PAL (Figure 4.16). The similar solubilities of P3HT and O-IDTBR in DCB (2.9 and 2.5, respectively) could explain the little phase separation in PALs processed from a binary solvent system. The drying of both materials occurs at the same pace. By contrast, P3HT and O-IDTBR show higher HSP values in CB than in DCB. Therefore, both materials are less miscible in CB than in DCB. For CB:DCB formulations, the drying and crystallisation of O-IDTBR occurs first followed by P3HT due to the lower miscibility of O-IDTBR in CB with respect to P3HT (see Table 4.6).

Table 4.6. Hansen parameters of solvents and distance in Hansen space. Hansen parameters of P3HT ($\delta_D=18.5$, $\delta_P=4.6$, $\delta_H=1.4$), O-IDTBR ($\delta_D=19.6$, $\delta_P=4.0$, $\delta_H=2.9$) and solvents are extracted from ^[158,166]. All units are in MPa^{0.5}.

| Solvent | δ_D | δ_P | δ_H | R_a P3HT | R_a O-IDTBR |
|--------------|------------|------------|------------|------------|---------------|
| CB | 16.0 | 4.3 | 2.0 | 5.0 | 7.3 |
| DCB | 19.2 | 6.3 | 3.3 | 2.9 | 2.5 |
| CB:DCB (1:1) | 17.6 | 5.3 | 2.7 | 2.3 | 4.2 |

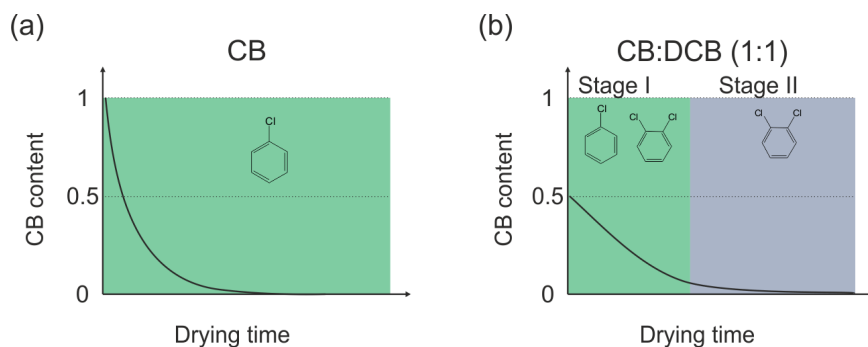


Figure 4.16. Sketch of the proposed drying kinetics of formulations. One solvent (left) and binary solvent system (right).

The significant difference of miscibility of both materials in CB could explain the large phase separation and crystallinity as a consequence of lack of intermixing D:A domains, see AFM images (Figure 4.10) and Raman analysis (Figure 4.11(b)), respectively. To conclude, we identify two mechanisms that control the drying and crystallisation processes of the bladed-P3HT:NFA PALs. While the binary solvent system controls the miscibility, the annealing promotes the phase separation.

- The solvent system controls the miscibility of the semiconductors and enables the solution process with the aid of the casting temperature. In terms of miscibility, similar values of the HSP (DCB) of the photoactive materials in the solvent of higher boiling point (DCB) induce a good mixing. Achieving as-cast pre-mixed domains are pre-requisite for a good donor:NFA interpenetrating network. Moreover, the higher solubility in DCB could explain the lack of dependence on casting temperature and performance for PALs processed from CD:DCB, see section 4.6.3.
- The role of the post-thermal annealing is to promote an appropriate phase separation between donor and acceptor domains after an adequate as-cast D:A mixing. In terms of size, NFAs are bigger molecules than fullerenes thus, limiting the diffusion length of NFAs. By contrast, if once the as-cast domains tend to segregate into large crystals (>50 nm), the post-thermal annealing results ineffective as occurs with CB-processed films due to the large phase segregation induced by the different solubilities of photoactive materials in CB (see AFM images, Figure 4.10).

4.7 Ageing study on P3HT:O-IDTBR devices

Besides efficiency and processability, long-term stability is also a key factor to ensure that OPV penetrates in the photovoltaic market.^[180] To increase the energy return on investment, high-efficiency solar cells should be accompanied by a low embodied energy and a long lifespan.^[159] Given the fact that the processing window is broad to obtain efficient devices, we analysed whether the stability also exhibits a similar trend. Here, following again the gradient approach, we assessed the influence of PAL thickness together with the effect of glass encapsulation in the long-term stability of P3HT:O-IDTBR cells under ambient conditions. In particular, shelf lifetimes were tested by storing samples in the dark under ambient conditions between JV measurements following the guidelines of ISOS-D-1.^[59]

It is worth noting, the non-encapsulated samples enable observation of accelerated degradation processes triggered by intrinsic (photodegradation, diffusion across interfaces, phase separation and remaining of solvent) and extrinsic (temperature, light, oxygen, humidity) mechanisms^[181,182] whereas encapsulated devices mostly reflect intrinsic mechanisms.^[183]

4.7.1 Photovoltaic parameters

As expected, the results point out that the glass encapsulation has a strong effect on stability (Figure 4.17). Most encapsulated devices retain more than 80% of initial PCE after 3000 hours regardless of PAL thickness. On the other hand, the PCE of non-encapsulated devices is reduced to values between 50% and 30% of their initial values after 3000 hours. The degradation in OPV is typically characterised by an initial burn-in stage followed by a linear behaviour.^[184] The initial burn-in decay is seen in the non-encapsulated devices (with no thickness dependence). Moreover, non-encapsulated devices drop exponentially after 1250h, whilst the encapsulated devices exhibit almost a linear degradation over time. This indicates that the burn-in stage is related to the effect of extrinsic factors such as moisture and/or oxygen present in the device.^[185,186]

Figure 4.17(b) also reveals that thicker PAL of P3HT:O-IDTBR (for both encapsulated and non-encapsulated devices) are consistently more sensitive to degradation.

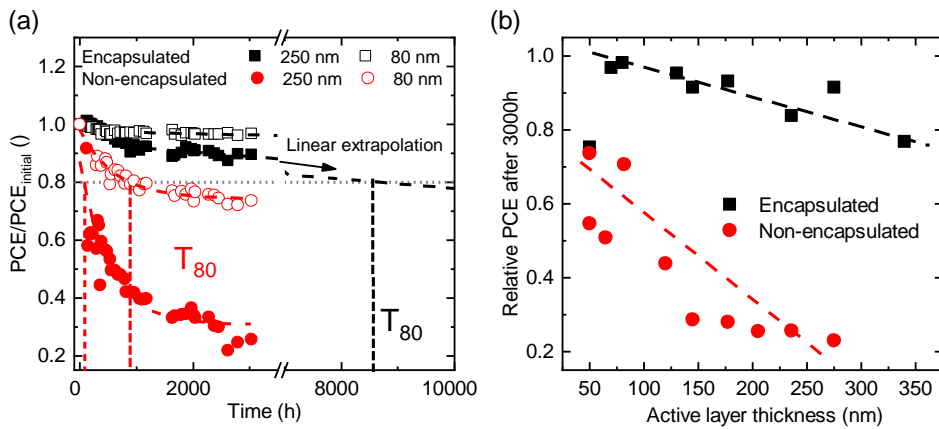


Figure 4.17. Ageing test of P3HT:O-IDTBR solar cells. They were stored in dark (shelf lifetimes) for thinner and thicker photoactive layers and the effect of the encapsulation. (a) Normalised efficiency as a function of time for encapsulated (squares) and non-encapsulated (circles) devices. The dashed line corresponds to a linear extrapolation. (b) Relative PCE vs thickness of the PAL for encapsulated and non-encapsulated devices.

This effect is mainly revealed by the decrease in FF regardless of the encapsulation (Table 4.7). This fact has been interpreted in the literature as an interface degradation.^[181] However, one may expect that interfacial effects will become more important in thinner films due to the relative weight of the interface with respect to the bulk compared to thicker ones. The origin of this effect will be studied in more details in the next section.

The relative PCE values are useful to compare the degradation rates for different thicknesses (Figure 4.17(a)). By contrast, the absolute PCE values obtained for encapsulated devices (Table 4.7) reveal that, despite thinner devices (80 nm) being more stable than thicker ones (250 nm), after 3000 hours the latter still outperform the former. This finding suggests that for long-term stability studies the absolute PCE values are as important as the degradation rate in order to draw a solid conclusion. Furthermore, from Figure 4.17(a) we can also extract relevant information about the degradation of the devices such as the T_{80} parameter. The T_{80} is defined as the time required to achieve 80% of the initial performance. This stability parameter is a good estimation of how rapidly a solar cell degrades. Clearly, Table 4.7 shows that for non-encapsulated devices T_{80} is larger for thinner (700 h) than thicker devices (120 h).

Table 4.7. Photovoltaic parameters of P3HT:O-IDTBR fresh and degraded solar cells. The effects of the encapsulation and thickness of the photoactive layer were evaluated.

| Encap | Status | Thickness (nm) | V _{oc} (V) | J _{sc} (mA/cm ²) | FF (%) | PCE (%) | PCE _{3000h} / PCE _{initial} | T ₈₀ (h) |
|-------|--------------|----------------|---------------------|---------------------------------------|--------|---------|--|---------------------|
| No | Fresh | 250 | 0.72 | -12.5 | 57.7 | 5.2 | 0.15 | 120 |
| | After 3000 h | | 0.42 | -5.8 | 32.7 | 0.8 | | |
| | Fresh | 80 | 0.69 | -8.9 | 56.9 | 3.5 | 0.6 | 700 |
| | After 3000 h | | 0.58 | -7.8 | 46.5 | 2.1 | | |
| Yes | Fresh | 250 | 0.70 | -13.1 | 47.3 | 4.32 | 0.83 | 8300* |
| | After 3000 h | | 0.68 | -12.7 | 41.6 | 3.6 | | |
| | Fresh | 80 | 0.70 | -8.9 | 55.8 | 3.5 | 0.97 | >5years* |
| | After 3000 h | | 0.69 | -8.7 | 55.5 | 3.4 | | |

*Values estimated from linear degradation.

For the encapsulated devices, 3000 hours were not enough to yield the 80% of the initial value and thus, an estimated linear degradation rate was assumed to calculate the corresponding T₈₀. According to the extrapolation, 8500 hours (141 days) and more than 5 years would be required to yield 80% of the initial PCE for thicker (250 nm) and thinner (80 nm) devices, respectively. Considering 25000 working hours (2 years and 300 days), thinner devices overcome the absolute produced energy of thicker devices, providing 13% more accumulated energy. After 3000 hours the relative PCE for P3HT:O-IDTBR solar cells is inversely proportional to PAL thickness, see Figure 4.17(b). Thinner PALs of both encapsulated and non-encapsulated cells degrade more slowly.

4.7.2 Understanding the degradation mechanisms in P3HT:O-IDTBR

In order to get insights on the degradation mechanisms present in P3HT:O-IDTBR devices, we performed co-local photocurrent images on both aged encapsulated and non-encapsulated devices. The light beam induced current (LBIC) maps were measured in short-circuit current conditions with different excitation wavelength (more details about LBIC in 2.3.1.3). Due to the complementary absorption of the PAL materials, LBIC measured at 488 nm and 785 nm enables to assess selectively the photocurrent contribution of P3HT and O-IDTBR, respectively (see Figure 4.11(a)). Additionally, photocurrent maps were also collected using illumination from the white light of a

standard microscope lamp to understand the overall effect of the white light on the device degradation. These experiments herein refer to *whiteBIC* (Figure 4.18).

First, we can observe that there is a significant difference in the magnitude of LBIC maps for the encapsulated and non-encapsulated devices in agreement with the photovoltaic parameters, see Table 4.7. Moreover, the encapsulated device shows a homogeneously-distributed photocurrent map for all the excitation sources. In contrast, the non-encapsulated counterpart exhibits a more heterogeneous photocurrent distribution. This is generally explained as oxidation of the electrode (pinholes), degradation of the PAL evolving from the edge towards the inner part of the device or structural changes of the PAL.^[187] A second observation is that the degradation pace does not seem to be the same for P3HT and O-IDTBR. This is inferred from the photocurrent histograms of the non-encapsulated device, which reveal a parabolic distribution for photocurrent maps at 488 nm and a bimodal distribution obtained at 785 nm excitation. These photocurrent maps suggest that P3HT suffers from a lower degradation rate compared to O-IDTBR. Thus, it is likely that the dominant factor of degradation in the devices is related to O-IDTBR.

White-light photocurrent maps confirm the convolution of the two effects by showing also a bimodal photocurrent distribution.

The bimodal distribution of both photocurrent maps at 785 nm and panchromatic illumination (*whiteBIC*) might be explained with the following factors.

- The oxygen and moisture diffusion from the edges of the device explains the lower photocurrent in the outer area compared to the inner area of the device (non-encapsulated *whiteBIC* of Figure 4.18).
- The trapped solvent in the PAL or partial delamination of the electrode could be the reason for the presence of the isolated darker areas in the *whiteBIC* photocurrent maps.^[187]
- Molecular changes of O-IDTBR. Darker areas of both LBIC at 785 nm and *whiteBIC* photocurrent maps are well correlated pointing to changes in the molecular or chemical structure of O-IDTBR.^[188,189]

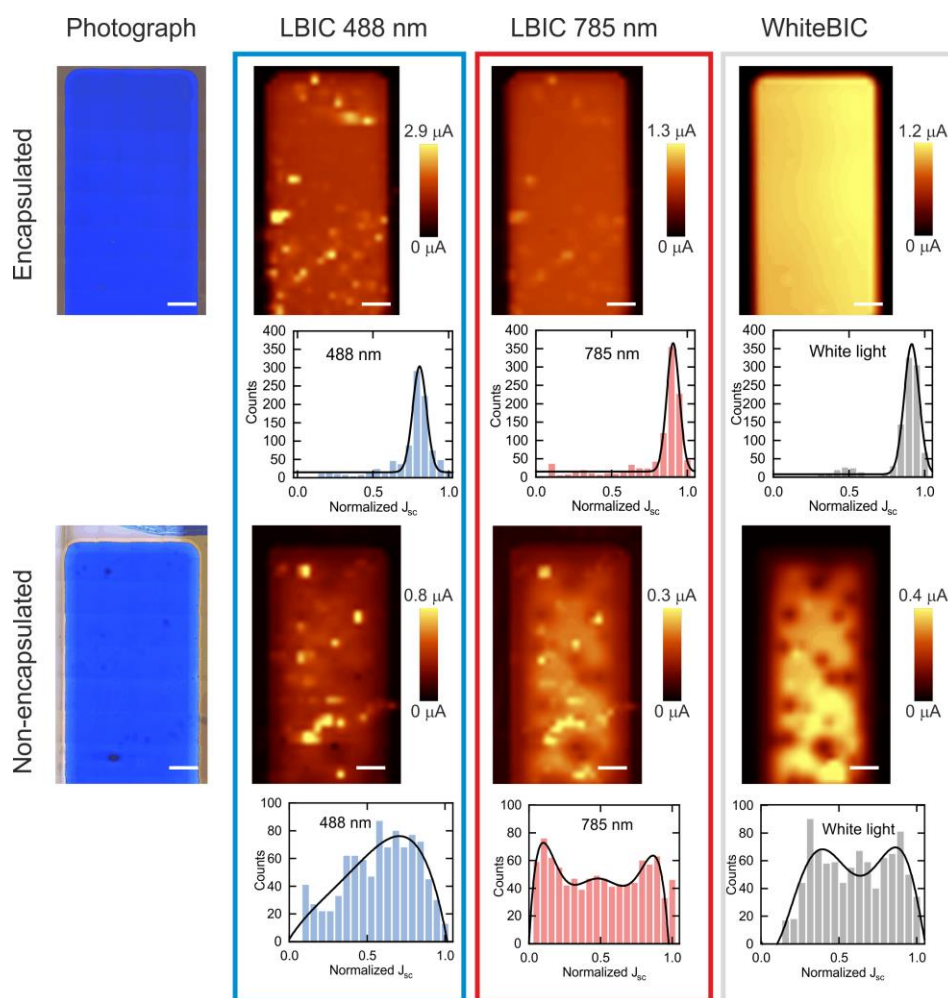


Figure 4.18. Effect of encapsulation via photocurrent images. Encapsulated (top) and non-encapsulated (bottom) thin P3HT:O-IDTBR devices. Photograph, light beam induced current (LBIC) map measured at 488 nm, 785 nm and with white light (*whiteBIC*) (from left to right) The scale bar corresponds to 500 μm . Normalised statistical histogram is under each photocurrent map. Reprinted from [11].

Therefore, it is quite likely that these degradation mechanisms might be triggered by extrinsic agents since these degradation effects are not observed in encapsulated devices. Besides, the dark spots of the photocurrent maps were only found in the non-encapsulated devices and are not correlated with the optical images, thus discarding the effect of pinholes and partial delamination. Moreover, P3HT Raman shift barely varies from top-performing to low performing areas pointing to O-IDTBR as the most sensitive material to extrinsic factors (Figure 4.19).

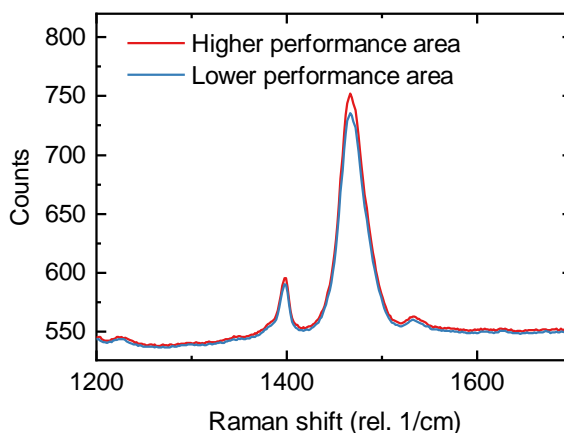


Figure 4.19. Raman shift of P3HT excited at 488 nm of higher and lower performing areas of the non-encapsulated device of Figure 4.18.

On the other hand, we performed a similar study based on a selective excitation to obtain photocurrent maps on thin and thick encapsulated devices (Figure 4.20). The wider photocurrent distribution for thicker devices compared to the thinner ones suggests that the faster degradation factor observed in the thicker devices might be to different self-organisation depending on the thickness of the PAL.^[190]

Finally, to verify that the degradation in thick films of P3HT:O-IDTBR blends evolves faster than in thinner films, wavelength-dependent measurements (EQE) were carried out on non-encapsulated films (Figure 4.21). EQE spectra confirm that thicker P3HT:O-IDTBR devices degrade faster than thinner ones. While the O-IDTBR contribution of the fresh and thick device is higher than the P3HT, in the degraded scenario the EQE spectrum inverts the shape showing clear degradation of O-IDTBR compared to P3HT, which is in agreement with our previous results (Figure 4.21(b)). Similarly, the main reduction of the degraded photovoltaic parameters for non-encapsulated devices is J_{sc} with a reduction of 54% and 12% for thick and thin films, respectively.

The reasons for the degradation of thinner films (80 nm), in contrast to the thicker films (250 nm), are not fully clear since the EQE spectra of both fresh and aged devices maintain the same spectral shape, thus suggesting that a similar degradation pace in both materials. One of the reasons that might explain the relationship between thickness and degradation is the blend morphology.

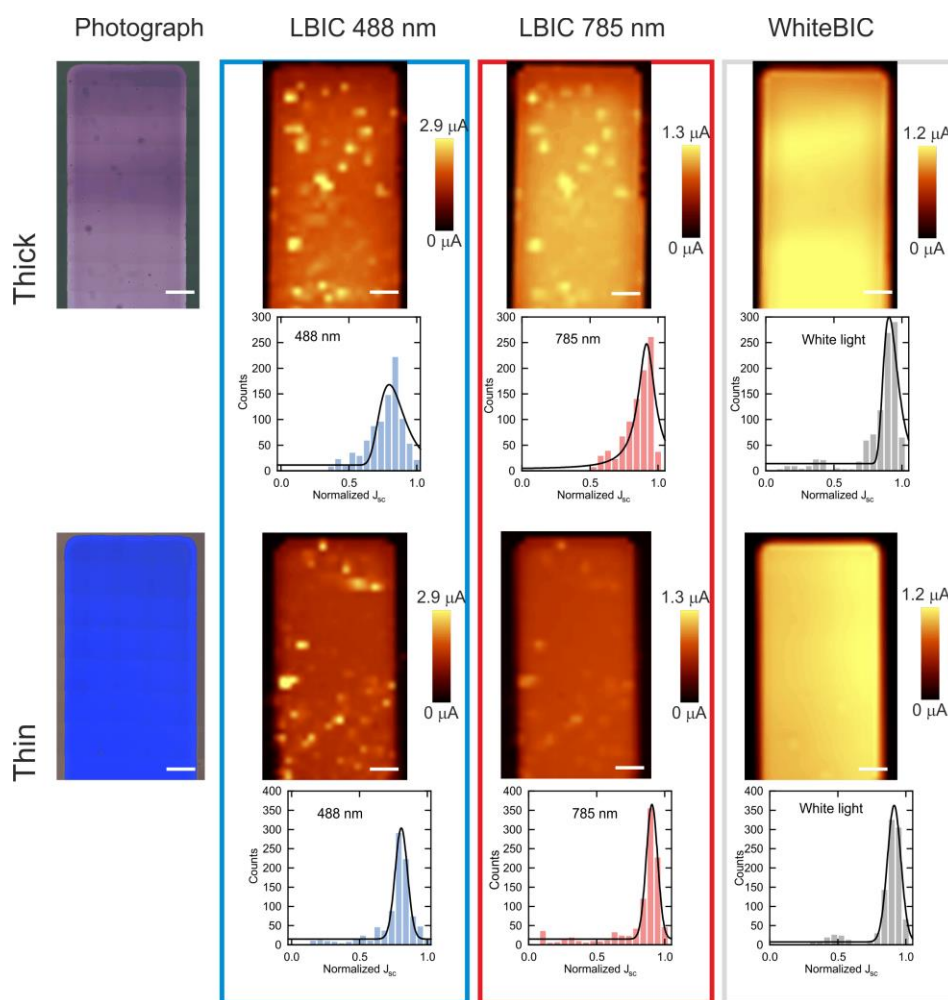


Figure 4.20. Thickness effect via photocurrent images. Thick (top) and thin (bottom) encapsulated films of P3HT:O-IDTBR. Device photo (first column), photocurrent map excited at 488 nm (second column), 785 nm (third column) and with white light (fourth column). Normalised statistical histogram is under each photocurrent map. Scale bar corresponds to 400 μm in all graphs. Reprinted from [11].

We found that thinner (<100 nm) and thicker films (>200 nm) yield to similar PCE, however, there is no proves that both films exhibit the same morphological characteristics. Besides, it is known that thick films (>200 nm) absorb more light but show less favourable morphological organisation (lower crystalline domains) than thin films (<100 nm).^[191] Consequently, the diffusion length of degraded films could be reduced. All in all, further degradation studies are required to fully explain the thickness-degradation dependence; however, these studies are out of the scope of this thesis.

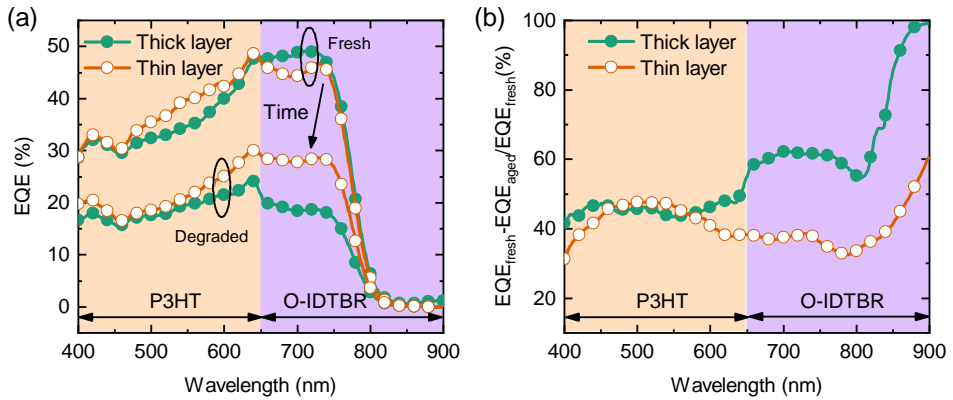


Figure 4.21. Ageing study via EQE measurements. (a) EQE and (b) relative reduction of fresh and aged P3HT:O-IDTBR non-encapsulated devices as a function of the PAL thickness: thick (filled circle) and thin (empty circle). The arrows of the bottom part represent the main absorption contribution of P3HT (400-650 nm) and O-IDTBR (650-800 nm).

We can conclude after evaluating several PAL thicknesses of P3HT:O-IDTBR solar cells, that thinner devices are more stable than thicker ones. This means that not only the studied system takes longer to achieve 80% of its initial PCE but also it requires less material to be manufactured. P3HT:O-IDTBR solar cells with a thinner PAL combine the mentioned advantage of longer T_{80} time with a lower employed material, a factor which makes them economically more attractive. Additionally, the degradation effect is more pronounced in O-IDTBR than P3HT for thick films, albeit for thin films the degradation rate between both materials seems to be the same.

4.8 Towards P3HT:O-IDTBR R2R modules

In this section, P3HT:O-IDTBR were upscaled to modules manufactured by roll-to-roll (R2R). However, the transition from lab-scale to industrial-scale requires intermediate steps in order to mimic/reproduce the specific limitations of the R2R equipment (see section 2.2.2).

4.8.1 Intermediate scale

Herein, the so-called intermediate scale acts a bridge from lab scale to industrial scale. The specific requirements of each manufacturing scale are summarised in Table 4.8. Note that industrial-scale specifications cannot be applied widely since, in our case, it only represents the specific technical limitations of the available R2R equipment used in this thesis. However, this up-scaling protocol can be applied to other large-scale printing techniques as long as considering the technical limitations of the corresponding printing machinery. As a proof-of-concept towards industrial scale, several variables were varied simultaneously when going to lab-scale to intermediate scale (see Table 4.8). Although this is not an ideal approach to draw solid conclusions, this first approach to R2R modules aims to prove the scalability of P3HT:O-IDTBR system. However, further studies will be required to fully understand the contribution of each variable involved in the upscaling process.

4.8.1.1 P3HT supplier

Regioregular P3HT from Rieke Metals (407 €/g)^[192] was employed instead of Sigma Aldrich (380 €/g)^[193] due to available stock in hundreds of grams for R2R experiments. Despite the price is similar for both polymers, the difference in their molecular weight could be a source of performance losses. A recent work has revealed that the optimum molecular weight for P3HT, when blended with O-IDTBR, was 34 kDa, which is in the range of the Sigma Aldrich supplier (20-50 kDa), but not for Rieke Metals (50-70 kDa).^[148]

Table 4.8. Summary of the specific printing features of lab, intermediate and industrial scale.

| Scale | Lab | Intermediate | Industrial |
|-------------------------|--|---|---|
| Coating technique | Doctor blade | Doctor blade | Slot-die |
| Substrate | Glass | Glass/PET | PET |
| ETL | ZnO | AZO | AZO |
| RR-P3HT supplier | Sigma Aldrich (M _w ** 20-50 kDa) | Rieke Metals (M _w ** 50-70 kDa) | Rieke Metals (M _w ** 50-70 kDa) |
| Solvent system* | Halogenated | Halogenated and non-halogenated | Non-halogenated |
| Casting T* | 80-100°C | RT*** | RT*** |
| Drying* | 1' hot plate at casting T | 1' hot plate drying at 130°C | 1' oven drying at 130°C |
| Final Annealing | 10' at 120°C | 10' at 120°C | 10' at 120°C (Ag curing) |
| Annealing conditions | In Glovebox | In air | In air |
| HTL | MoO ₃ | MoO ₃ | PEDOT |
| Top electrode | Evaporated Ag | Evaporated Ag | Screen-printed Ag |

*Referred to PAL processing conditions. **M_w refers to polymer molecular weight. ***RT stands for room temperature-

4.8.1.2 Parameters controlling the blend morphology

Other important parameters, as seen in the previous sections, are those that affect the blend morphology crucial to achieve high-performing devices. In particular, we consider the solvent system (replacement of the halogenated solvent, see next section), annealing and drying temperature of the film. Since the employed slot-die is non-heatable, neither the rolls nor tubes, inks must be cast at room temperature. Similarly, to reproduce this fact at the intermediate scale, inks were processed at room temperature. When moving to a continuous process, annealing and drying stages are carried out in a rotatory oven and in air. In our particular case, since the typical web speed is 1.4 m/min and the length of the oven is 1.5 m, the equivalent heating time is approximately 1 min. Therefore, PAL films processed at intermediate scale were annealed in air for 1 min at 130°C to reproduce

our rotatory oven conditions. The effect of the annealing in air (intermediate and industrial-scale) would require deeper analysis since annealing the PAL is pointed out as the most air-sensitive step.^[194]

4.8.1.3 Substrate

In the so-called intermediate scale, the printability of inks on rigid (glass) and flexible (PET) substrates was evaluated. More details in the solvent screening section.

4.8.1.4 ETL

At lab-scale devices, ZnO was employed as ETL instead of aluminium-doped ZnO (AZO) which was used in intermediate and R2R scale. In principle, the ETL material should not be very performance-sensitive since the use of AZO enables thicker films maintaining the electrical conductivity. However, devices with AZO were reported to exhibit higher air stability than ZnO counterpart.^[195] Besides, some lab-scale devices with ZnO and AZO revealed no difference in performance between these ETLs.

4.8.1.5 Solvent screening

The first step towards OPV large printing scale is the replacement of halogenated solvents of PAL formulations. Despite mixtures of CB:DCB yield PCEs over 5% at lab scale, the use of toxic and hazardous solvents are not suitable due to the strict environmental regulations of the printing industry.^[196] Apart from the toxicity, for the choice of solvent other relevant features need to be considered such as boiling point, viscosity, wetting properties, the solubility of semiconductors and performance. As ‘greener’ solvent alternatives, toluene (Tol) and p-xylene (p-Xyl) and bromoanisole (BrA) were selected and CB and CB:DCB mixtures as halogenated references from the previous section.^[197,198] This set of ‘greener’ solvents enables to reduce the environmental impact as well as investigating the effect of boiling point (from 110°C to 220°C) and miscibility on the device performance when is cast at room temperature. As a starting point, we evaluate the wetting properties of inks when processed following the here called intermediate scale (see Table 4.8). Blade-coated films were processed at room temperature on both PET and glass substrates.

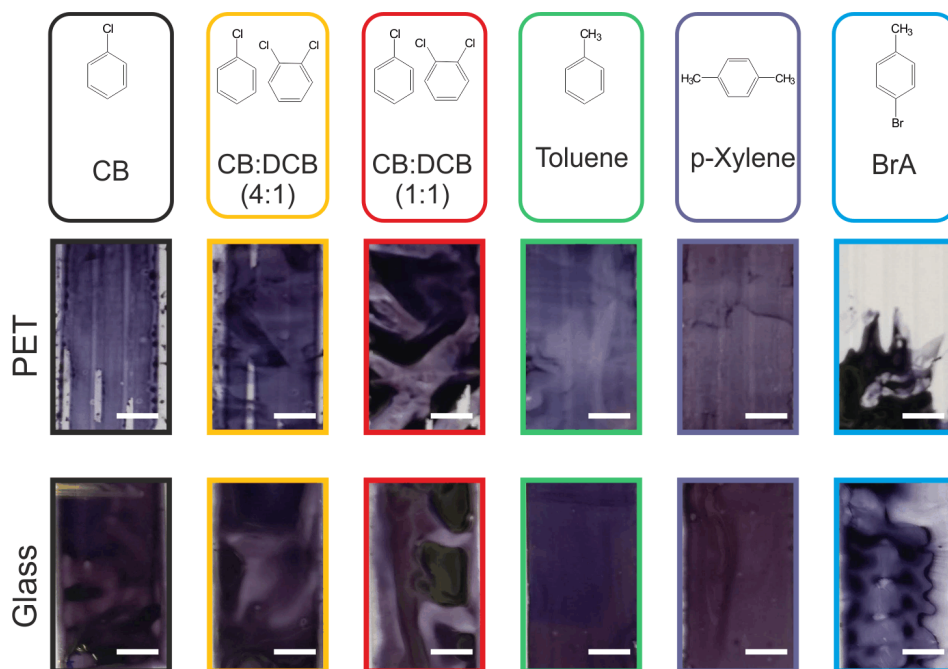


Figure 4.22. Solvent screening of P3HT:O-IDTBR formulations. The upper row represents the molecular structure of the screened solvents (CB, CB:DCB (1:1), CB:DCB (4:1), toluene, p-xylene, bromoanisole). The intermediate and bottom row represent the optical images of blade-coated films on PET/ITO/AZO and glass substrates, respectively. Scale bar represents 1 cm.

Films were cast on PET as a brief estimation of the potential wetting behaviour under similar industrial-scale conditions (see Table 4.8) whereas films on glass were used as solar cells (Figure 4.22). After that, films were subjected to a fast annealing process on a hot plate at 130°C for 1 minute to reproduce the R2R oven conditions. The pictures of films shown in Figure 4.22, reveal that CB based mixtures formulations are not a good choice since as-cast films suffer dewetting on ITO uncovered areas. Besides, BrA is ruled out as host solvent since the PAL processed from BrA does not cover the full area of the substrate. This is due to the fact that BrA is a bad solvent for P3HT (see HSP of BrA in Table 4.9) leading to the gelation of the ink. In contrast, toluene and p-xylene exhibit very homogenous coating along the sample. In terms of microstructure, no significant difference is found in the pictures of films processed from CB, CB:DCB (1:1) and toluene (Figure 4.23).

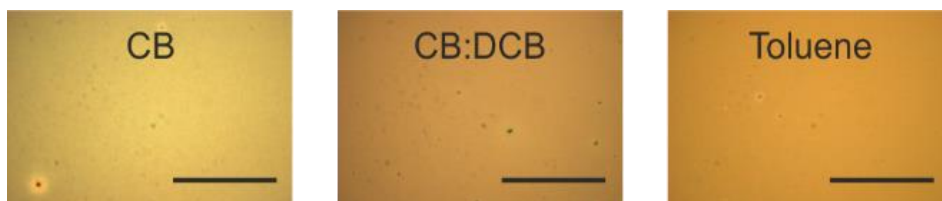


Figure 4.23. Microscope pictures of P3HT:O-IDTBR films processed from the so-called intermediate scale. Solvent system: CB, CB:DCB (1:1) and toluene. Scale bar corresponds to 100 μm .

We can conclude that the most suitable ‘greener’ solvents in terms of wetting properties are toluene and p-xylene based formulations enabling good coverage and homogenous films on both flexible and rigid substrates.

Once assessed the ink wettability on flexible and rigid substrates (intermediate scale), then the solvent-performance dependence for P3HT:O-IDTBR system was tested. For simplicity and a fair comparison with our previous results, solar cells were manufactured in rigid substrate following the standardised manufacturing process on glass (detailed in chapter 2), but using the aforementioned casting conditions for PAL (Glass/ITO/ZnO/PAL/MoO₃/Ag). Note that at this initial screening stage PAL thickness is not optimised for any formulation, hence further optimisation steps are required for each solvent system. Although HTL and top electrode of R2R modules are based on PEDOT and printed silver, respectively; MoO₃ and silver were sequentially evaporated to simplify the comparison with reference lab-devices as well as to limit the number of changes with respect to the lab-scale process.

The first conclusion drawn for intermediate-scale devices is that halogenated and non-halogenated formulations lead to similar efficiencies, proving the availability of ‘greener’ solvent alternatives (Table 4.9). We found that the solvents with the corresponding HSP higher than 5 MPa^{0.5} for P3HT, CB and BrA, show poor performance and wettability. By contrast, the rest of solvents which have similar solubility for P3HT and O-IDTBR (toluene, xylene and DCB-based formulations) yield to comparable PCE. As discussed in section 4.6.4, these results suggest that photoactive materials with similar solubilities prevent phase separation. Secondly, the performance of devices processed from solvent binaries of CB and DCB again overcomes CB formulation, no matter the drying kinetics or production scale.

Table 4.9. Summary of solvent screening of P3HT:O-IDTBR formulations fulfilling the intermediate scale conditions (Table 4.8). The solvent system were CB, CB:DCB mixtures, toluene, p-xylene and bromoanisole.

| Solvent system | As-cast homogeneity | Wetting on PET/ITO | B.P.* (°C) | R _a P3HT (MPa ^{0.5}) | R _a O-IDTBR (MPa ^{0.5}) | PCE (%) |
|----------------|---------------------|--------------------|------------|---|--|---------------|
| CB | ✓ | ✗ | 132 | 5.0 | 7.3 | 1.9±0.4 (2.7) |
| CB:DCB (4:1) | ✓ | ✓ | 142 | 3.8 | 6.0 | 2.8±0.8 (3.9) |
| CB:DCB (1:1) | ✓ | ✗ | 156 | 2.3 | 4.2 | 2.9±0.4 (3.9) |
| Toluene | ✓✓ | ✓✓ | 110 | 3.4 | 4.2 | 3.3±0.3 (4.0) |
| p-Xylene | ✓✓ | ✓✓ | 138 | 4.4 | 5.0 | 2.8±0.4 (3.4) |
| Bromoanisole | ✗✗ | ✗✗ | 223 | 6.9 | 5.5 | - |

Distance in the Hansen space is calculated in the same way as Table 4.6. Statistics with 24 devices. PCE in brackets represents the highest performance. *BP: Boiling point. Wetting legend: ✓✓ very good, ✓ good, ✗ bad and ✗✗ very bad. The ranking is based on images from Figure 4.22.

This can be, again, explained by the superior miscibility of P3HT and O-IDTBR in DCB which is the solvent with a higher boiling point in CB:DCB solvent system (Table 4.9). Thirdly, despite some CB-processed devices yield similar PCE to the toluene formulation (see Table 4.9), these formulations are ruled out because of the toxicity and poor wetting properties on a flexible plastic substrate. Among the non-halogenated alternatives, the top-performing devices were fabricated from toluene showing an average PCE of 3.3% and a maximum of 4.0%. Although both toluene and p-xylene yield efficiencies over 3%, toluene formulation is elected as ‘greener’ alternative to CB based formulations since, in average, toluene (3.3±0.3%) outperforms p-xylene efficiency (2.8±0.4%).

The reasons for the drop in PCE can be attributed to the miscibility of photoactive materials in these solvent systems. The corresponding HSP of P3HT and O-IDTBR in toluene is lower than p-xylene, indicating that the poor solubility of P3HT and O-IDTBR in p-xylene limits the performance. Moreover, the fact that the HSPs of DCB based formulations are similar to that of toluene proves that the miscibility plays a crucial role to achieve high-performing devices. As a proof, the highest PCE of the screened solvents are toluene (3.3%) and CB:DCB, 1:1, (2.9%) exhibiting, at the same time, the lowest HSP values for P3HT (3.4 and 2.3 MPa^{0.5}) and O-IDTBR (4.2 and 4.2 MPa^{0.5}), respectively.

Another relevant factor in the substitution of chlorinated solvents is controlling the drying kinetics. For instance, at lab-scale drying kinetics are controlled by both boiling points

of solvent system and hot plate temperature (blade coater). However, reproducing our specific slot-die conditions (industrial scale, see Table 4.8) with the blade coater leads to films cast at room temperature with inherent longer drying times. Solvents with lower boiling point such as toluene show better performance and wetting properties following our specific technical restrictions. Moreover, formulations with lower boiling and adequate contact angle are suitable for large scale since they avoid unwanted displacement of as-printed wet films, hence improving the resolution of printed stripes.

The comparison between champion devices processed from CB:DCB (1:1) of the two initial upscaling stages reveals a substantial drop in performance, from 5.5% (lab-scale) to 3.9% (intermediate-scale). This difference in PCE could be ascribed as the combination of the synthetic characteristics of P3HT (Sigma, lab-scale and Rieke, intermediate-scale) and the processing parameters, see Table 4.8. The molecular weight and regioregularity of P3HT are reported to a relevant impact on the PCE.^[148]

In terms of processing parameters, the effects of the drying and annealing inside of the oven and in air atmosphere were not proven to be equivalent with respect to the drying and annealing in a controlled atmosphere. An inert annealing atmosphere is typically required for manufacturing high-performing devices. Although no reference of the effect of air-annealing on the OPV performance was found, the effect of air-annealing of poly(9,9-dioctylfluorene) (PFO) results in a thermal-oxidation-induced defect, i.e. the formation of carbonyl (C=O) groups.^[190,199] Therefore, further research is still required to gain insight into the individual contribution of each parameter.

To conclude, we identified toluene as an alternative to chlorinated solvents for the P3HT:O-IDTBR system. We observed that chlorinated and non-chlorinated solvents yield to similar efficiencies in the so-called intermediate scale conditions. Toluene based formulation ensures great P3HT and O-IDTBR solubility, good printing behaviour at room temperature, fast solvent evaporation as well as the highest performance among the screened solvents. Therefore, we can conclude that adapting ink formulation is crucial to control blend morphology, and eventually, reducing the lab-to-fab performance gap.

4.9 Proof-of-concept P3HT:O-IDTBR R2R modules

As the top-view sketch shows in Figure 4.24, the OPV module consists of 3 serially-interconnected subcells by a controlled lateral offset after each coating step that enables the silver-ITO connection of different subcells. The R2R module structure used is PET/ITO/AZO/P3HT:O-IDTBR/PEDOT/Ag. One of the biggest challenges in the upscaling is the substitution of evaporated by a solution-processed electrode. This electrode consists of separated printed silver fingers connected by a busbar, see Figure 4.24 and Figure 4.25. As the optical path is halved without the reflecting electrode fully covering the PAL, an additional effort is required to identify the optimum thickness of PAL. To do so, a PAL thickness-performance study was performed also in large scale geometry. The flow rate pumped in the slot-die was gradually increased over time, and therefore as-cast films become thicker. After calibration, the thickness of PAL was inferred from the optical density value measured at 610 nm, see Figure 4.26.

First, V_{oc} values in Figure 4.27 reveal an efficient module series-interconnection since the average of V_{oc} (2.0 V) scales proportionally with the number of cells connected in series ($3 \times 0.7V$). Additionally, as expected theoretically, V_{oc} does not depend on PAL thickness. Although some modules show V_{oc} values below 1.8 V, those modules also exhibit low FF. Thus, this drop in both V_{oc} and FF suggests strong charge recombination.

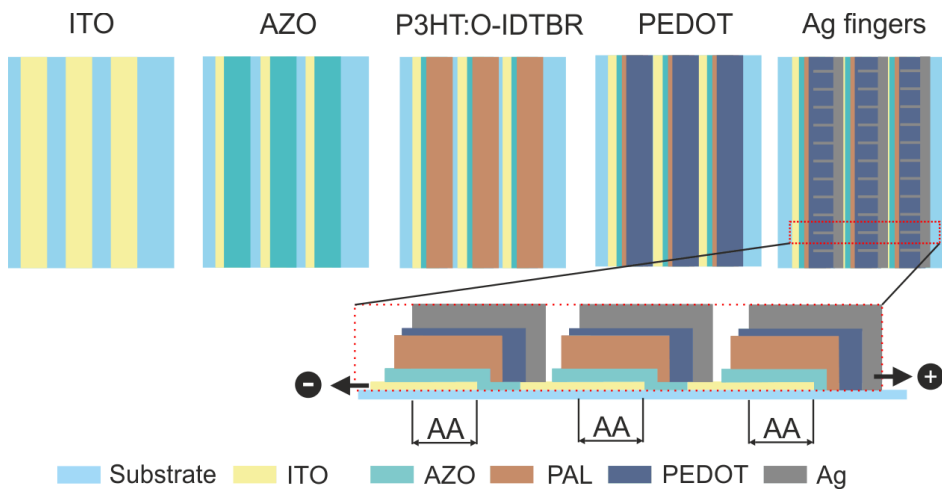


Figure 4.24. Large scale devices (industrial scale). Sketch of top-view and cross-section of sequential layers that form a module manufactured by roll-to-roll (R2R).

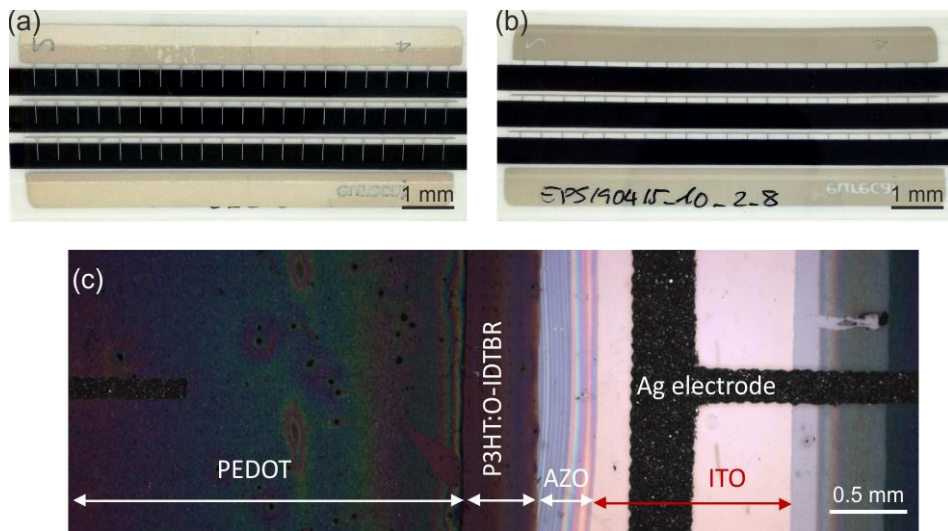


Figure 4.25. Picture of a R2R module of P3HT:O-IDTBR with an area of 108 mm². (a) Back side (top electrode) and (b) front side of the module. (c) Zoomed image of the cell-to-cell interconnection.

Second, J_{sc} increases proportionally with PAL thickness, since thicker PALs (>400 nm) lead to J_{sc} values over 7 mA/cm² whereas thin ones (<300 nm) are limited to 4 mA/cm². Unlike J_{sc} , FF values are reduced from 45% for thinner films down to 30% for thicker PALs. The performance of P3HT:O-IDTBR R2R modules is thus a trade-off between J_{sc} and FF, which show opposite trends with PAL thickness. The existence of a wide thickness operation window for P3HT:O-IDTBR system is proven with modules with 300 nm and 400 nm PALs reaching PCEs over 1.5 %.

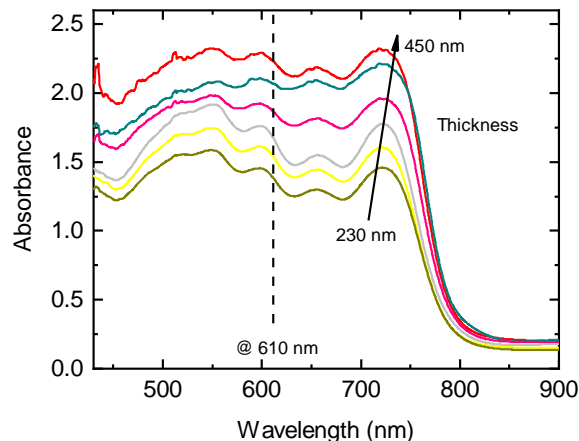


Figure 4.26. Absorption spectra of R2R modules with different PAL thickness. Highlighted with a dashed line the optical density at 610 nm used for predicting the PAL thickness.

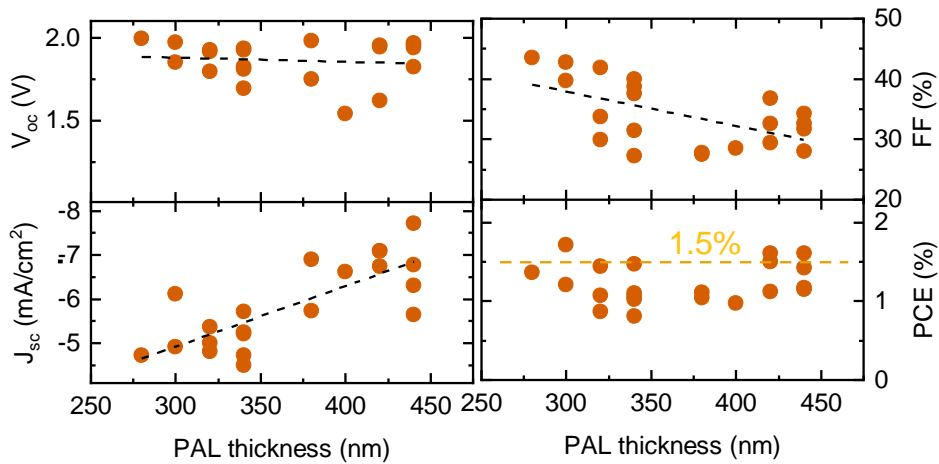


Figure 4.27. Photovoltaic parameters of P3HT:O-IDTBR R2R modules as a function of PAL thickness. PAL thickness was deduced from the optical density values. The dashed lines are plot as a guide to the eye.

We can conclude that our results based on P3HT:O-IDTBR modules are, to the best of our knowledge, the first study in which flexible R2R modules are manufactured by slot-die (Table 4.10). Recently, Strohm *et al.* manufactured laser-patterned P3HT:O-IDTBR modules of on glass by slot-die and doctor blade achieving a PCE around 5%.^[166] Previous to the irruption of NFAs, there are several examples in the literature of R2R modules manufactured with fullerenes (PC₆₀BM and ICBA) and P3HT yielding efficiencies around 2% in flexible substrates.^[200,201] Therefore, our results exhibit similar performance than other studies of modules based on P3HT in flexible substrates. However, further efforts have to be dedicated to reduced to the lab-to-fab gap.

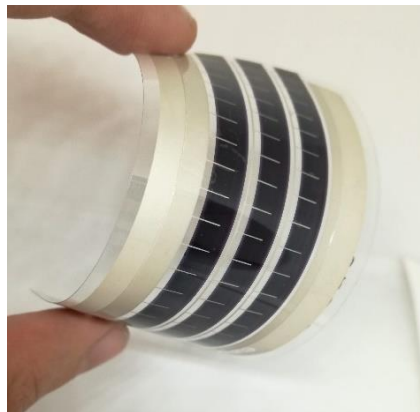


Figure 4.28. Picture of a flexible P3HT:O-IDTBR module fabricated by roll-to-roll (R2R).

Table 4.10. Literature review of publications of P3HT-based modules.

| Structure | Coating technique | PCE (%) | Area (cm ²) | Substrate | Ref. |
|-----------------------------------|-------------------|---------|-------------------------|-----------|-----------|
| ITO/ZnO/PAL1/PEDOT:PSS/AgNW | Slot-die | 4.7 | 59.52 | Glass | [166] |
| ITO/SnO/PAL1/PEDOT:PSS/Ag | Inkjet | 5.0 | N.A | Glass | [202] |
| ITO/ZnO/PAL1/MoO ₃ /Ag | Inkjet | 6.2 | 2 | Glass | [168] |
| ITO/AZO/PAL1/PEDOT:PSS/Ag | Slot-die | 1.7 | 1.08 | PET | This work |
| ITO/ZnO/PAL2/PEDOT/Ag | Gravure | 3.3 | 57 | PET | [200] |
| IMI/ZnO/PAL2/PEDOT/Ag | Slot-die | 2.2 | 21.6 | PET | [201] |
| ITO/ZnO/PAL3/PEDOT/Ag | Gravure | 1.8 | 57 | PET | [200] |

PAL1=P3HT:O-IDTBR; PAL2= P3HT:PC60BM and PAL3=P3HT:ICBA

4.9.1 Losses upon up-scaling

For a successful lab-to-fab transition, it is important to evaluate the associated losses to minimise the potential loss sources. For neat CB formulations, a drop of 29% in PCE occurs when going from lab to intermediate manufacturing conditions. This drop is mainly attributed to a reduction in J_{sc} (24%) and in a lower significantly contribution of V_{oc} (5.3%) and FF (2.3%). Similarly, a reduction of 30% in PCE is observed for DCB based formulations under the same transition pointing out, again, J_{sc} as the most influential factor. This indicates that a more detailed optimisation of PAL at intermediate scale is still required to pave the way towards R2R.

Table 4.11 shows a summary of devices manufactured at three different scales and increase the active area of devices at lab scale (8 mm² cells), intermediate scale (8 mm² cells) and industrial-scale (modules 108 mm²). V_{oc} suffers a systematic reduction, regardless of the formulation, when going from lab-scale to intermediate-scale. Lab-scale devices show V_{oc} of 0.75 and 0.74V for CB and CB:DCB, respectively; whereas the V_{oc} of intermediate-scale devices with the same formulations are 0.71V and 0.71V, respectively. This suggests either a strong recombination activity or an excessive degree of crystallinity. The fact that FF suffers minor reduction points to an excessive degree of crystallinity of PALs when processed following intermediate schemes.

Table 4.11. Photovoltaic parameters of champion P3HT:O-IDTBR devices processed from different solvents, manufacturing scales (lab, intermediate and industrial) and active area.

| Scale | Solvent system | Active area (mm ²) | V _{oc} (V) | J _{sc} (mA/cm ²) | FF (%) | PCE (%) |
|---|----------------|-----------------------------------|------------------------|--|-----------|------------|
| Lab | CB | 8 | 0.75 | -8.6 | 59.9 | 3.8 |
| Intermediate | CB | 8 | 0.71 | -6.5 | 58.5 | 2.7 |
| (Reduction in the lab-inter transition) | | | (5%) | (24%) | (2%) | (29%) |
| Lab | CB:DCB (1:1) | 8 | 0.74 | -12.4 | 61.6 | 5.6 |
| Intermediate | CB:DCB (1:1) | 8 | 0.71 | -9.4 | 58.3 | 3.9 |
| (Reduction in the lab-inter transition) | | | (4%) | (24%) | (5%) | (30%) |
| Intermediate | Toluene | 8 | 0.72 | -9.9 | 55.9 | 4.0 |
| Industrial | Toluene | 108 | 1.97 (0.66*) | -6.1 | 42.7 | 1.7 |
| (Reduction in the lab-inter transition) | | | (8%) | (38%) | (23%) | (58%) |

(*)V_{oc} of the individual subcell of the module. For comparison purposes, the reduction of each parameter with respect to the previous printing scale (lab vs intermediate; intermediate vs industrial) is shown in brackets.

As a first approach to verify the P3HT and O-IDTBR contributions is to measure the optical absorption of the blend (Figure 4.29). Table 4.12 summarises the optical density measurements for P3HT and O-IDTBR at 550 nm and 740 nm, respectively. In particular, P3HT/OIDTBR optical density ratio (ODR) shown in Table 4.12, suggests a balanced crystallinity of both components when processed at lab scale (0.89) in contrast to intermediate scale (0.51). This points out either a non-ideal degree of crystallinity of O-IDTBR due to the non-optimised processing parameters or unbalanced D:A composition in the dried PAL.

Additionally, the fact that the absolute optical density for both components is higher in lab-scale than in intermediate scale suggests thinner films in intermediate-scale devices. Additionally, this could explain the reduction in J_{sc} from 12 to 9 mA/cm² of lab-scale to intermediate-scale devices. Moreover, the small difference in J_{sc} of CB:DCB processed devices (9.4 mA/cm²) and toluene (9.8 mA/cm²) might be attributed to an unbalanced P3HT:O-IDTBR contribution suggested by the ODR (0.51 vs 0.64) of devices processed from the ‘greener’ solvent. To tackle it, further efforts have to be dedicated to intermediate scale in order to achieve a more balanced P3HT and O-IDTBR absorption contributions.

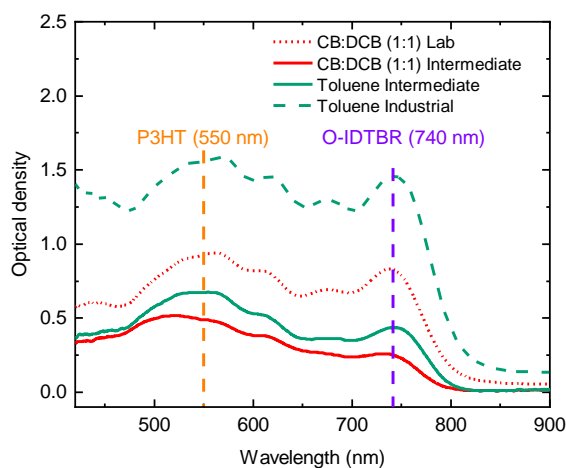


Figure 4.29. The optical density of P3HT:O-IDTBR devices processed from different scales. The most promising formulations (CB:DCB, 1:1 and toluene) and manufacturing scales (lab, intermediate and industrial).

Finally, the fact that the ODR of R2R modules (0.91) and lab cells (0.89) is very similar might point indicate an appropriate blend morphology is achieved in large scale production although the adapted intermediate protocol cannot reproduce the same shape of the optical absorption. Despite the optical absorption of both small and large P3HT:O-IDTBR cells are similar, there is a significant reduction in J_{sc} (12.4 vs 6.4 mA/cm²) and FF values (30%) indicate that the main source of losses upon size scaling derives is related to HTL and electrodes and not PAL morphology. Therefore, further studies on buffer layers and alternative electrodes are required to scale-up P3HT:O-IDTBR successfully. Additionally, the use of highly conducting materials including silver nanowires instead of the silver paste could help to close the gap between champion lab cells and fully R2R modules.

Table 4.12. The optical density values of P3HT:O-IDTBR films processed from CB:DCB and toluene.

| Scale | Solvent system | OD at 550 nm (P3HT) | OD at 740 nm (O-IDTBR) | OD ratio O-IDTBR/P3HT |
|--------------|----------------|------------------------|---------------------------|--------------------------|
| Lab | CB:DCB (1:1) | 0.93 | 0.83 | 0.89 |
| Intermediate | CB:DCB (1:1) | 0.49 | 0.25 | 0.51 |
| Intermediate | Toluene | 0.67 | 0.43 | 0.64 |
| Industrial | Toluene | 1.48 | 1.36 | 0.91 |

4.10 Conclusions

In this fourth chapter, we cover the complete upscaling process from the screening of materials, optimisation of the processing parameters, performing a long-term stability study and finishing with R2R modules of the most promising candidate. We demonstrated the usefulness of high throughput approaches to rapidly screen bladed solar cells based on P3HT and novel NFAs. In particular, we tested seven commercially available acceptors including NFAs (ITIC, ITIC-M, O-IDTBR, EH-IDTBR and O-IDFBR) and PC₆₀BM and ICBA as fullerene references.

The analysis of variance (ANOVA) enabled ranking the sensitivity of each of the studied parameters for P3HT based devices. We found that the most influential parameters, for this specific system, are (in decreasing order): 1) acceptor material; 2) choice of the solvent system; 3) annealing temperature; 4) casting temperature; and 5) active layer thickness. A meta-study with more than one thousand P3HT based samples yielded two main conclusions. Firstly, the most promising P3HT:NFA system is that based on O-IDTBR. Secondly, the processing solvent system (CB:DCB) systematically results in higher efficiency for all bladed P3HT:NFA solar cells. Additionally, this better performance is related to appropriate vertical phase separation of the components of the PAL, as well as a reduction of the surface roughness together with an optimised morphology.

We used the high-throughput methodology applied to thickness and annealing graded devices to further investigate the P3HT:O-IDTBR binary system. We discovered that the solvent system (CB:DCB) and post-annealing temperature are more critical parameters than the casting temperature, being 120°C the optimum temperature. Moreover, we obtained power conversion efficiencies above 5% for this system over a broad photoactive layer thickness range. Finally, encapsulated and thinner P3HT:O-IDTBR devices (PAL around 80-100 nm) also showed a strong potential for improving the stability according to their T₈₀ parameters, retaining more than 95% of the initial PCE after 3000 hours. Interestingly, we found that O-IDTBR degrades faster than P3HT in P3HT:O-IDTBR devices.

Finally, to close up the transition towards large scale production, we tried to reproduce our slot-die coating conditions at lab-scale (casting at room temperature and annealing in air) with the blade coating technique. The first step was to screen several non-halogenated solvents including toluene and p-xylene. We found that toluene is the most promising alternative to chlorinated solvents to manufacture fully R2R P3HT:O-IDTBR modules. Although there is an important reduction in performance upon size increase (from 5.6% in 8 mm² compared to 1.7% in 108 mm²), optical measurements revealed that both P3HT and O-IDTBR yield a morphology that is probably similar to the one obtained with lab-scale devices. This means that further efforts have to be dedicated to the optimisation HTL and top electrode.

Chapter 5 High-throughput screening by 2D gradient maps

ABSTRACT

The screening and optimisation of OPV candidates are often performed empirically through one-variable-at-a-time (Edisonian) experimentation. This approach, however, entails manufacturing hundreds of different devices to fully optimise the microstructure of the photoactive layer by exploring and optimise donor:acceptor (D:A) ratio, thickness, solvent system, additives and post-thermal annealing, among others. Thus, this implies a large consumption of materials, time and human resources.

In this fifth chapter, we extend the 1-dimension (1D) combinatorial methodology presented in the previous chapter to 2-dimensions (2D). As proof of concept, we apply these 2D gradient maps to 10 OPV systems consisting of a low bandgap polymer and a NFA, the current record system in OPV binary system. This methodology, developed by our group, enables to extract, after modelling and fitting the Raman spectra, the thickness and composition from hyperspectral images, and co-locally the photocurrent using the same probing laser or white light to produce photocurrent maps. Finally, after combining the aforementioned maps it is possible to easily identify the optimum parameters for the photoactive layer.

Parts of these data will be published in ^[17]: X. Rodríguez-Martínez, E. Pascual-San-José, Z. Fei, M. Heeney, R. Guimerà and M. Campoy-Quiles (work in progress). This work is a collaboration between PhD students Mr. Xabier Rodríguez-Martínez (characterisation and Raman analysis) and Mr. Enrique Pascual-San-José (manufacturing and characterisation).

5.1 State-of-the-art of high-throughput screening methodologies

As discussed in the general introduction, the intrinsic synthetic flexibility of novel conjugated polymers and small-molecule acceptors offers nearly countless combinations of photoactive materials to overcome the 20% performance milestone in OPV.^[67] The ease modification of the NFA structure including moieties in the backbone, bridging atoms, end-capping groups and the side chains (length and branching points) results in a large number of potential novel acceptors, additional info in Figure 1.9 (Chapter 11).^[65,203] For instance, during the last ten years, several thousands of new molecules have been published although only a few of them have been intensively studied.^[65,204] Although theoretical models can be used to initially pre-screen promising candidates, the final performance generally depends on other properties a priori difficult to predict including the degree of miscibility, domain size, phase segregation, tendency to crystallise or final energy levels upon blending.^[205-207] For a more precise assessment of the aforementioned properties, experimental validation is required. Furthermore, the fine-tuning of a specific system involves further optimisation of ink formulation and manufacturing conditions, as demonstrated in the previous chapter.

Typically, most efforts are devoted to the optimisation of the microstructure PAL by tuning the manufacturing conditions including thickness, donor:acceptor (D:A) composition, annealing temperature, doping, casting conditions, solvent system, additives, etc. However, other parameters need to be considered for the full optimisation of the device such as interlayers (electron and hole transporting layer), geometry, electrodes, etc. Besides, some of these parameters are closely correlated with each other. Traditional one-sample-at-a-time experimentations, also known as Edisonian, find the optimum parameters by manufacturing several samples with small variations between samples for each parameter of interest. As a consequence, the full optimisation of a new system involves a large amount of time and resources.

As an efficient alternative, high-throughput screening methods enable to accelerate the optimisation process while reducing the human and material resources. These methods have recently attracted the attention of the scientific community and some examples applied to OPV are given in Table 5.1. For instance, orthogonal thickness-graded bilayers of CuPc and PTCBI were evaporated sequentially to unravel the optimum thicknesses

combination that leads to the highest efficiency.^[208] Despite the limited amount of semiconductors evaporated in this process, vacuum-assisted deposition methods have intrinsic economic drawbacks for upscaling.^[209]

Unlike evaporation-based techniques, solution-processed alternatives show lower embodied energy and hence, they are more appealing for the printing industry. Several examples exist for the high-throughput evaluation of solution-processed based OPV. An inkjet printer assisted with a robotic arm enabled to cast several PALs with different compositions in a short time.^[210,211] Although this technique offers high material yield compared to spin coating, it is likely to suffer from nozzle clogging upon a fast ink drying. An important observation that opens up new optimisation methods is the fact that the manufacturing time of each device takes several orders of magnitude longer than its photovoltaic characterisation (JV curve).

Table 5.1. State-of-the-art of combinatorial screening in OPV.

| Coating technique | Description | Materials | Parameter of interest | In situ characterisation | Ref |
|-------------------|-------------|--|-----------------------|-------------------------------|-------|
| Evaporation | Bilayer | CuPc, PTCBI | Thickness | Raman, LBIC | [208] |
| Inkjet | Inks | PPE-alt-PPV, DPP-alt-F, P3OT, PCBM | D:A ratio | UV-Vis, emission | [210] |
| Inkjet | Discrete | PCPDTBT, PSBTBT, PCBM | D:A ratio | UV-Vis, PL, PCE | [211] |
| Drop-casting | Robotics | PTB7-Th, P3HT, PCBM, IDTBR | D:A ratio | UV-Vis | [212] |
| Slot-die | Flexible | P3HT, PCBM | Thickness, D:A ratio | PCE | [213] |
| Spray | Graded | P3HT, PCBM | D:A ratio | UV-Vis, LBIC | [214] |
| Blade | Graded | PCDTBT, PCBM | Thickness | PCE | [215] |
| Blade | Tandem | PTB7, PCBM | Thickness | PCE | [216] |
| Blade | Graded | P3HT, NFAs | Thickness, annealing | PCE | [11] |
| Blade | Graded | PCDTBT, PTB7-Th, PffBT4T-2OD, PCBM | Thickness, D:A ratio | LBIC, Raman | [217] |
| Blade | Graded | PBDB-T, ITIC, PC ₇₀ BM, PTB7-Th | Thickness, D:A ratio | <i>whiteBIC</i> , LBIC, Raman | [218] |

For instance, for a parallel batch of 10 samples with several devices in each sample, the manufacture of all lab-scale devices can take up to 6 hours (cleaning, casting sequential layers, evaporation and encapsulation) whereas the JV characterisation takes a few minutes per device. Thus, moving from a fabrication-intensive to a characterisation-intensive protocol would speed up significantly the evaluation time by a factor of 50 while reducing material consumption down to 10 mg of each semiconductor.^[217,218]

Moreover, these types of high-throughput methods will be highly demanded in the upcoming years due to their capabilities to generate a large amount of data at a very low cost. The large datasets generated from high-throughput methods are very useful to feed machine learning (ML) algorithms that typically require large datasets to make predictions out of the training dataset.^[219,220] Alternatively, the manufacturing of devices with continuous gradients in the parameters of interest has reduced dramatically the material consumption for the optimisation of OPVs.^[215,221] For instance, discrete graded devices with different D:A compositions were manufactured by slot-die and spray coating.^[213,214] Although air-assisted deposition techniques are large-scale compatible and widely used in the printing industry, sprayed films are very rough being not a suitable alternative for OPV requirements.^[222] By contrast, slot-die coating technique is typically employed as part of integrated roll-to-roll (R2R) systems. In particular, Krebs group adapted the conventional slot-die coating process to screen OPV semiconductors.^[213] Two pumps controlled the relative donor and acceptor concentration of the resulting ink fed into the slot-die head. As a result, this enabled the fabrication of PALs with variations of composition (differential pumping rate) and thickness (increasing flow rate) along the web. Despite the promising results, the combination of the relatively large consumption of semiconductors (up to 30 mg of each one) and the expensive ITO substrate ITO makes this approach, albeit, not very suitable to explore the parameter space at a moderate cost.

As an alternative to spray and slot-die coating methods, blade-coating was employed to manufacture thickness-graded devices in small areas while reducing material consumption.^[215] Blade-coating is an optimal choice for OPV screening at lab scale serving as an intermediate step towards large-scale, and thus reducing the lab-to-fab gap.^[223] Very recently, sequential PALs with orthogonal thickness gradients enabled a fast optimisation of the OPV tandem structure.^[216] A motorised shadow mask with an

aperture of 1 mm² was used to assess locally the PCE of a thickness-graded device over 16 cm² total dimension. Unfortunately, one limitation of this methodology is the invasive thickness characterisation that requires scratching and peeling off the front absorber layer.^[216] Finally, it is worth highlighting the contribution of Langner *et al.* in the high-throughput experimentation assisted by a robotic arm and data-driven decisions to optimise the stability of multi-components blends.^[212]

5.1.1 Objective

This chapter aims to extend the presented 1D gradient methodology (Chapter 4) to 2D gradients based on controlled variations of the parameters of interest allowing consequently to save both, resources and research time. This methodology consists of three basic steps. First, manufacturing a *D:A* graded composition film and measured through co-local optoelectronic characterisation such as the combination of Raman scattering and light beam induced current (LBIC), with the so-called RamBIC, and LBIC with white light (*also known as whiteBIC*). This non-invasive toolkit extracts the composition and thickness from fitting Raman hyperspectral images and, simultaneously, performs the co-local acquisition of the photocurrent using the same laser so to produce photocurrent images. These images typically contain 20.000 measured points containing the deduced thickness, composition and measured photocurrent values. The comparison between images identifies the optimum values for thickness and composition. Then, the *RamBIC* predictions were verified (and extended to the rest of the cell parameters) by producing doctor-bladed OPV devices with the optimum thickness and composition combinations.

5.2 Meta-analysis of PBDB-T:NFA solar cells – 1D approach

Current top-performing binary solar cells consist of a low-bandgap polymer blended with a NFA.^[65,66] As seen in the previous chapter, NFAs offer a wide range of chemical pathways to modify its structure enabling devices with efficiencies from 10% to 12% for a given polymer, simply by introducing linear solubilisation side chains to the NFA.^[224] We first extract the optimum composition of the state-of-the-art low-bandgap polymer, PBDB-T, from the literature. Then, we compared blade-coated devices with reported data by spin-coating. To do so, we followed the same 1D thickness-gradient methodology

presented in the previous chapter. PBDB-T based devices were studied upon blended with different ITIC derivatives namely O-ITIC (linear side chains)^[224], EH-ITIC (branched side chains), ITIC-M (methyl end-capped groups) and ITIC as reference. Please see the chemical structures of PBDB-T and NFAs in Figure 2.2(d) and Figure 2.3(d-g), respectively. ITIC modifications based solar cells were screened using over 700 devices as a function of the solvent system (CB and CB:DCB), see Figure 5.1 and Table 5.2. According to the results shown in Figure 5.1, ITIC derivative with linear and branched modifications in the side chains (O-ITIC and EH-ITIC) and processed from CB lead systematically to higher efficiencies concerning ITIC-M and the reference (ITIC).

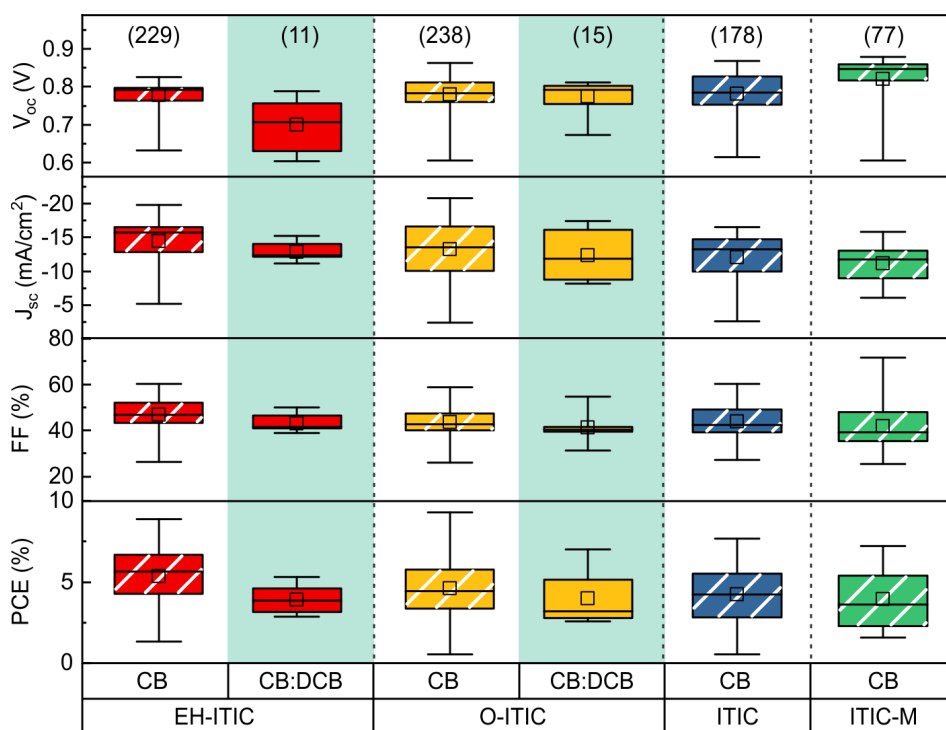


Figure 5.1. Summary of PBDB-T based solar cells. Box and whisker plot of photovoltaic parameters from 748 measured devices of PBDB-T blended with 4 different NFAs (EH-ITIC, O-ITIC, ITIC and ITIC-M) as a function of the solvent, namely chlorobenzene (CB) and the mixture of chlorobenzene:dichlorobenzene (CB:DCB). The photovoltaic parameters are open-circuit voltage (V_{oc}), short-circuit current (J_{sc}), fill factor (FF) and power conversion efficiency (PCE). Data include thickness variations, annealing variations and several casting temperatures. Statistical values are represented by mean (inner empty square), median or 2nd quartile (inner horizontal line), 1st and 3rd (height of the box) and maximum and minimum value (whisker height). The number of devices characterized for each material system appears in brackets (only those which overcome the 0.6 V and 25% FF threshold) on the top row.

The effect of solubilisation side chains is noticeable in J_{sc} values (19 and 19.8 mA/cm² for EH-ITIC and O-ITIC, respectively) which are significantly higher than the non-modified counterparts (15.8 and 14.0 mA/cm² for ITIC and ITIC-M, respectively). However, FF values are comparable with ITIC reference devices. Interestingly, ITIC with linear side chains (O-ITIC) surpasses systematically the branched ones (EH-ITIC), again as occurred in the previous chapter with O-IDTBR and EH-IDTBR. Alternatively, the modification in the end-capping groups (ITIC-M) upshifts the LUMO level and, consequently, increases the V_{oc} (0.87V).^[44] This voltage increase strategy could be useful for specific applications like water-splitting reaction in which maximising the voltage is more relevant than photocurrent.^[225] We conclude that after studying four different PBDB-T:NFA systems (700 devices) octyl solubilisation side chains overcome systematically the branched ones. This is due to better light absorption, suggested by a higher J_{sc} that induces a more favourable morphology and hence performance. Therefore, this points out the relevance of using linear solubilisation side chains to boost device performance.

Similarly to P3HT-based devices, we evaluate solvent-performance effect for top-performing OPV systems (EH-ITIC and O-ITIC). In contrast to the semi-crystalline P3HT systems, the performance of PBDB-T based devices is systematically higher when they are processed from CB than from a mixture of solvents (CB:DCB). This means that the optimised conditions for P3HT based solar cells cannot be extrapolated to other polymers systems.

Table 5.2. Best photovoltaic blade-coated and spin-coated photovoltaic parameters of PBDB-T based solar cells. PBDB-T is blended with four ITIC derivatives processed by a 1D high-throughput screening approach with thickness-graded PAL.

| Acceptor | V_{oc} (V) | J_{sc} (mA/cm ²) | FF (%) | PCE (%) | Ref |
|----------|--------------------------------|-----------------------------------|-----------|------------|-----------|
| ITIC | 0.84 | -15.8 | 58.0 | 7.7 | This work |
| | 0.89 | -17.1 | 65.0 | 9.9 | [224] |
| ITIC-M | 0.87 | -14.0 | 59.3 | 7.2 | This work |
| | 0.94 | -17.4 | 73.5 | 11.5 | [44] |
| EH-ITIC | 0.81 | -19.0 | 57.7 | 8.9 | This work |
| | Not reported in the literature | | | | |
| O-ITIC | 0.80 | -19.8 | 58.5 | 9.3 | This work |
| | 0.86 | -19.7 | 70.0 | 11.9 | [224] |

Therefore, each new OPV material system requires an individualised optimisation process. In the following sections, we present a multi-parametric high throughput combinatorial method that enables a fast exploration of the space of parameters. There are three basic steps in this methodology. First, manufacturing a graded film in the parameter/s of interest, second a co-local Raman scattering and photocurrent characterisation. Finally, the thickness and composition of each point are extracted by fitting Raman spectra through the transfer matrix method (TMM) modelling.

5.3 Raman modelling

The Raman modelling, fully developed by Mr. Xabier Rodríguez *et al.*, is herein used to determine non-invasively PAL compositions and thicknesses of working devices.^[226] This section summarises the method for completeness.

5.3.1 Introduction

The Raman scattering occurs when the light (photons) is scattered inelastically upon its interaction with matter. In this process, the energy of absorbed photons is converted in molecular vibrations. Similarly to Hooke's law, these characteristic vibrational modes of molecules depend on both the strength of the bonds and the mass of the vibrating species. For typical organic materials used in OPV, the most relevant region of the spectrum goes from 1000 to 1700 wavenumbers. Interestingly, this region coincides with most of the associated vibrating modes of bonds that are present in organic semiconductor materials such as C-C, C=C, C-N-C and N-S-N.^[227] Due to the unique vibrational fingerprint of each material, Raman is a material-selective characterisation technique for the chemical identification and quantification of materials even after mixing.^[226] One of the most relevant features of Raman scattering is that it is an in-situ and non-invasive characterisation technique, as long as the laser power is tuned accordingly to avoid photodegradation. Consequently, no damage is induced during the acquisition of Raman spectrum. Raman technique also offers good lateral resolution (diffraction limit) together with large area mapping capabilities when integrated with a motorised XY stage.

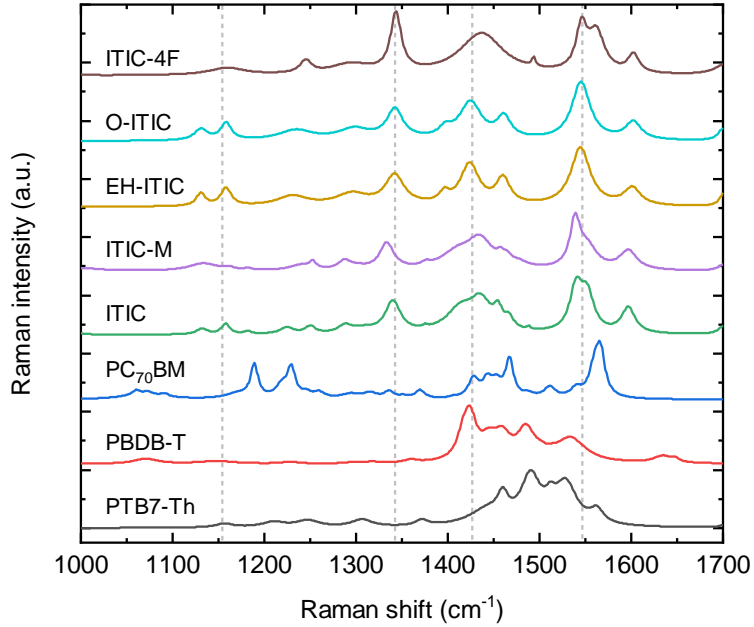


Figure 5.2. Raman fingerprints of the OPV materials employed in this chapter. Vertical dashed lines are guides to the eye to highlight Raman features.

In our particular case, Raman hyperspectral images with 250×100 scanned points over 10 cm^2 can be acquired in less than 1h. Moreover, and as shown in the previous chapter, Raman can be also used to assess the degree of crystallinity of P3HT by tracking the C=C stretching modes as well as monitoring the material phase transitions.^[112,228]

5.3.2 Mathematical framework

The extraction of thickness and composition from Raman hyperspectral images is performed with the aid of a mathematical framework developed in our group by Rodriguez-Martinez *et al.*^[226] This model spans the aforementioned TMM to describe the Raman process in thin films. Rewriting the transfer matrix equation applied to the amplitude of the scattered field (E_R), leaving the film towards the spectrometer, we obtain

$$E_R(x) \propto \left| \frac{t_{10}^R \left(e^{i\xi_1^R x} + r_{12}^R e^{i\xi_1^R (2d-x)} \right)}{1 - r_{10}^R r_{12}^R e^{2i\xi_1^R d}} \right| E_L(x) = t_R |E_L(x)| \quad (5.1)$$

where the superscript R refers to the values attained at the Raman-scattered wavelength (λ_R), i is the imaginary unit, t_{ab}^R and r_{ab}^R are the complex Fresnel transmission and

reflection coefficients of the interfaces between a and b media, $\xi_1^R = 2\pi(n_1 + ik_1)/\lambda_R$, and d is the layer thickness. $E_R(x)$ stands for the emitted Raman-scattered electric field amplitude due to an infinitesimal material slab located at a distance x from the film surface. The total Raman intensity (I_R) generated over the entire film thickness is given by Eq. 5.2

$$I_R(d) = \sigma_R \int_0^d |E_R(x, v_u)|^2 dx \quad (5.2)$$

where σ_R is an empirical effective Raman cross-section that stands for the measured Raman activity. Regarding multi-component mixtures, the intensity of the acquired Raman spectra can be modelled in order to locally determine both film thickness (d) and volumetric composition (v_u) in medium 1. The Raman intensity at any location in the device can be described quantitatively as a linear combination of the reference spectra for the pure components. Generalising Eq. 5.2 for N components we have

$$I_{R,mix}(d, v_u, \bar{\nu}) \propto \int_0^d |E_R(x, v_u)|^2 dx \sum_{u=1}^N v_u \sigma_{R,u} I_{ref,u}(\bar{\nu}) \quad (5.3)$$

where $\bar{\nu}$ is the Raman shift, $I_{ref,u}(\bar{\nu})$ stands for the reference Raman spectrum of component u normalised at the intensity of the mode associated with the cross-section $\sigma_{R,u}$, v_u is the volumetric scattering fraction of component u (which satisfies $\sum_{u=1}^N v_u = 1$) and d refers now to the thickness of the blended thin film in the probed region. For simplicity, the complex refractive indices of Raman-scattered radiation ($E_R(x, v_u)$) are assumed to vary linearly with the volumetric composition as $\varepsilon_{mix} = \sum_{u=1}^N v_u \varepsilon_u$. Although in Chapter 3 for the colour prediction, Bruggeman approximation was assumed for the calculus of the effective optical constant of blends. In this case, to reduce the fitting complexity, linear approximation was instead employed. The non-significant variation between both effective medium approximations lies within the statistical error of the method. To sum up, PAL thickness and volume fraction of blends can be extracted by deconvoluting and fitting the Raman spectra by only using as experimental input the complex refractive indices of all materials ($\tilde{n} = n + ik$) and the Raman cross-section (σ_R).

5.4 Manufacturing of gradient solar cells

The next step is the manufacturing of thickness and composition heterogenous PAL devices which are then co-locally characterised with the aid of the optoelectronic techniques and the aforementioned Raman-based TMM modelling.

5.4.1 2D thickness-composition gradient films

In this section, we span the high-throughput manufacturing method beyond 1D thickness gradient shown in chapter 4. Films with a lateral D:A composition gradient were manufactured as depicted in Figure 5.3. Blade technique is a very useful method to manufacture intended composition-graded PALs. This technique enables an easy transfer from thickness and composition heterogenous films to homogenous ones.

Traditional bladed PALs are usually processed from an ink with pre-mixed materials, as described in chapter 2. By contrast, the use of a multi-nozzle micropipette (or two pipettes) enables to cast simultaneously two or more drops of pristine materials in front of the blade. As the blade moves (Figure 5.3(b)), the two pristine solutions mix, spread along the substrate and after drying a composition gradient from 100% material A to 100% material B is formed in the perpendicular direction of the blade movement (Figure 5.3(c)).

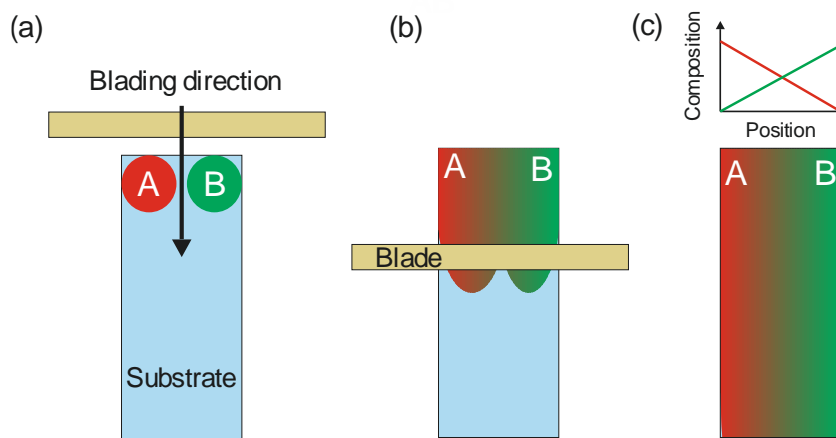


Figure 5.3. Sketch of basic steps to fabricate composition-graded photoactive layer (PAL). (a) Casting two solutions from pristine materials (A and B), (b) blade coating and mixing and (c) final composition gradient sample.

In the case of OPV, 'A' and 'B' labels of Figure 5.3 correspond to donor and acceptor pristine solutions. Note that the mixing process between material A and B can vary depending on the pair of semiconductors and their fluid properties when dissolved. However, the local composition of the heterogeneous PAL is determined experimentally with Raman scattering regardless of the mixing effectiveness. Note that this manufacturing of the composition-graded PALs approach can be applied to other solution-processed technologies with binary components as long as the two materials are mixed in a short distance.

Furthermore, we investigated the window of processing parameters that lead to such composition-graded films. Blade speed and casting temperature were identified as the most critical parameters. Although a detailed study on the sensibility of these two parameters was performed for PTB7-Th:PC₇₀BM system,^[217] we found that similar manufacturing conditions can be extrapolated for different polymer:NFA systems. As a rule of thumb, low blade speeds and low casting temperatures (90-70°C and 5-20 mm/s) produce fully mixed films whereas the opposite conditions of high blade speeds and temperatures yield to phase segregation and dewetting. A general processing window for composition-graded films was identified for blade speeds from 5-20 mm/s and casting temperatures between 90 and 105°C. The applicability of this method based on composition-graded PALs is limited to photoactive materials with *a priori* good level of miscibility upon blading (3-4 seconds, employed in mixing) such as polymer:small molecule (fullerene, NFA) systems. By contrast, solutions with high viscosity, typically polymer:polymer PALs, result more challenging to mix along a few centimetres of the substrate.

One alternative is to preload pure inks with the other pure ink so that the fluid properties of both inks are not that different, and hence it slightly favours the miscibility of two materials during the casting and mixing process. By adding 10% in volume of material A in B and *vice versa* better and more controlled composition-graded films were achieved. As a result, pure materials are not available, although this effect is not crucial. Generally, optimum composition values in OPV show more balanced loadings of donor and acceptor materials.^[229]

Finally, to achieve 2D thickness-composition optimisation maps, an intended thickness variation along the PAL was applied either decelerating the blade (see section 2.2.1.1) or by reducing the volume reservoir cast in front of the blade.^[217] Despite the first option leads to a more pronounced thickness gradient films, the second alternative was selected for simplicity and due to the intrinsic ease to manufacture thickness-graded films by blade coating. Two drops of 30 μL of pristine material solution were cast and bladed at 10 mm/s to produce a graded PAL in both composition and thickness.

5.4.2 2D thickness-composition gradient solar cells

The next step to convert graded PALs to functional solar cells is to adapt the conventional manufacturing protocol shown in the experimental section 2.2. First, instead of commercial pre-patterned ITO substrates, full ITO substrates were employed (Figure 5.4). In this case, ITO corners were etched chemically, and consequently, electrically isolated with Zn and diluted HCl in H_2O . With that, separate contacts of top and bottom electrodes were achieved after evaporation. After ITO etching, a dispersion of ZnO nanoparticles was bladed and annealed as described in the experimental section. Followed by the manufacturing of a graded thickness and composition PAL (section above). Note that one of the most critical points when producing heterogeneous thickness-composition devices is to clean properly PAL for electrode contacts. An excessive PAL cleaned area would eventually lead to the formation of short circuits in the device after Ag evaporation (direct ITO-Ag contact).

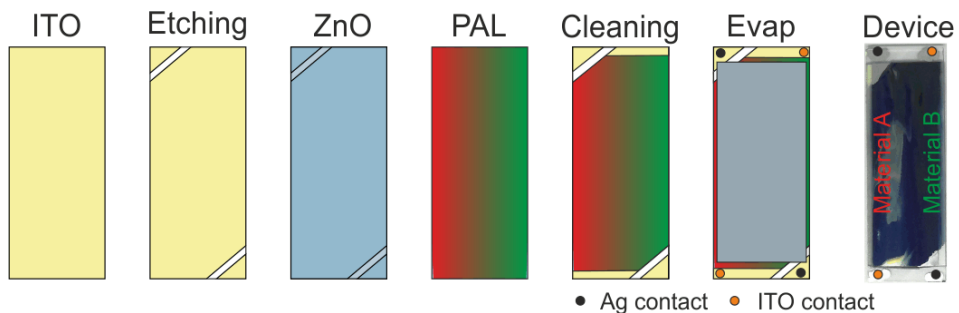


Figure 5.4. Manufacturing protocol of composition and thickness-graded solar cells. Top-view sketch of sequential steps adapting the existing protocol to make composition gradient samples. Photograph of a working graded thickness and composition device. The size of the sample is 2.5 cm x 7.5 cm.

Finally, MoO_3 and Ag were thermally evaporated through a rectangular mask that covers the upper and bottom area for symmetrical electrode contacts, see black (Ag) and orange (ITO) circles in Figure 5.4.

5.4.3 Characterisation of 2D gradient maps

After manufacturing devices with orthogonal thickness and composition PALs, advanced characterisation is required. The combination of co-local optoelectronic techniques enables to assess the PAL characteristics (Raman scattering) and the associated performance at every measured point (photocurrent). A sketch of Raman and LBIC (from herein referred to as *RamBIC*), the co-local characterisation technique herein employed and developed in our group, is given in Figure 5.5.

This technique combines Raman imaging through TMM modelling with co-local photocurrent measured by LBIC technique. The hyperspectral Raman images were analysed and fitted with TMM as shown in section 5.3. As a result, quantitative composition and thickness maps are generated. As an illustrative example of the *RamBIC* methodology, PBDB-T and ITIC-M composition and thickness heterogeneous device is shown in Figure 5.6.

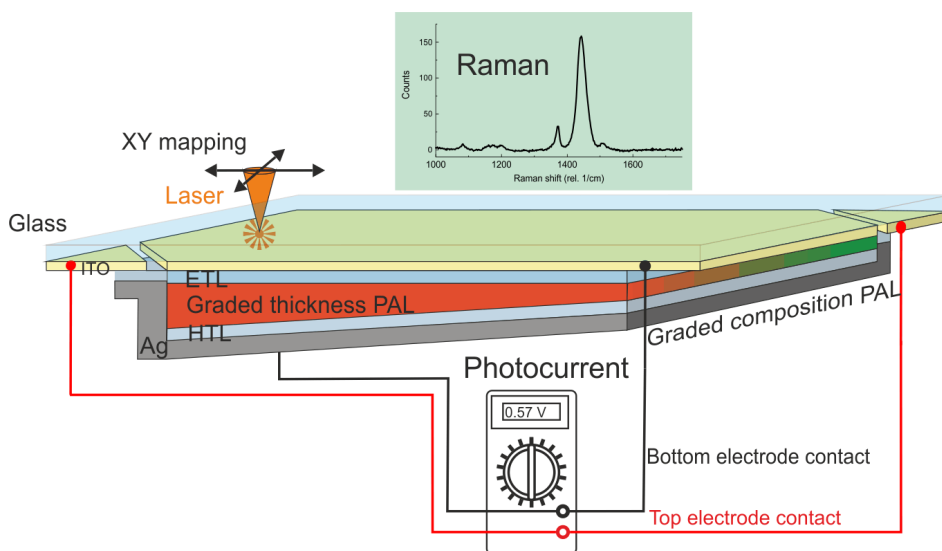


Figure 5.5. Sketch of the *RamBIC* measurement on a thickness-composition-graded device. Raman spectrum and photocurrent are extracted co-locally.

A continuous variation in the PAL composition is observed along the short axis of the device, from PBDB-T rich-areas (left side) to ITIC-M rich-areas (right side). In between them, polymer:NFA intermediate compositions are found (green-yellow in colour scale) in the central part of the sample. The composition map depicted in Figure 5.6(a) demonstrates the effectiveness in creating controlled composition-graded PALs by simple blade-coating technique. Unlike the composition map, PAL thickness map (Figure 5.6(b)) exhibits a limited thickness window. The reason is that the quantification of PAL thickness is based on the interpolation of the scattered Raman intensity in the model which oscillates with the PAL thickness. Therefore, it is not possible to determine unequivocally the PAL thickness beyond the first intensity maximum of the oscillating spectrum. Unfortunately, in working devices, the maximum occurs at ca. 70/80 nm of PAL thickness. This means that beyond this value we cannot predict accurately PAL thicknesses.

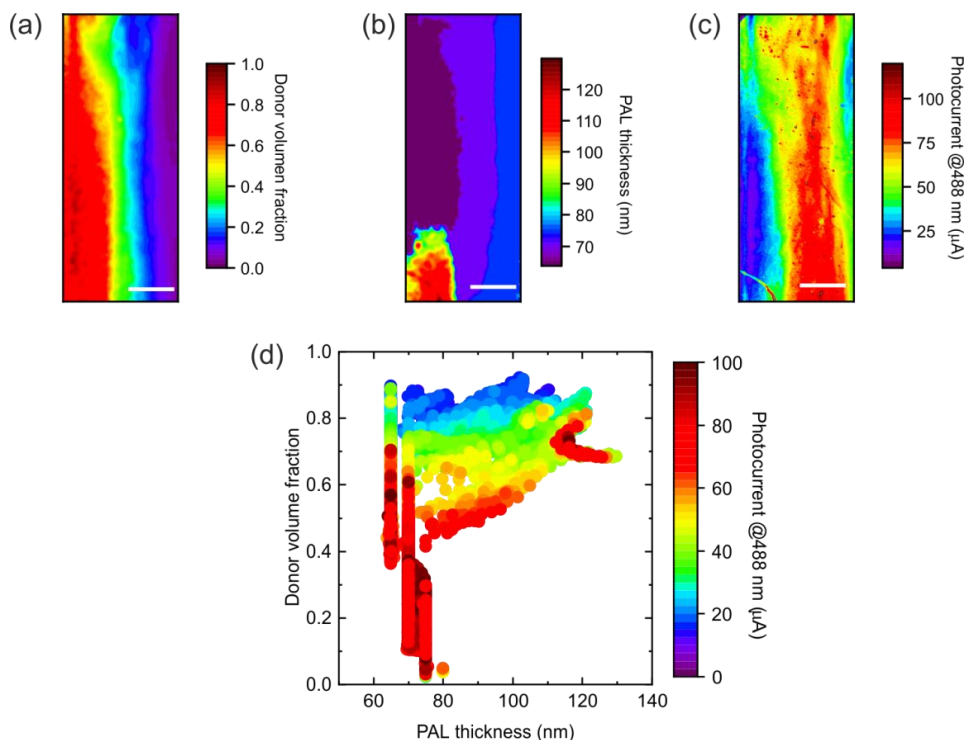


Figure 5.6. Example of the generation of *RamBIC* co-local maps. (a) Volumetric composition, (b) photoactive film thickness and (c) photocurrent maps of a graded composition-thickness solar cell of PBDB-T:ITIC-M. (d) Correlation of previous maps between local photocurrent map and quantitative Raman maps of thickness and composition. The scale bar corresponds to 1 mm.

In principle, this is an intrinsic limitation and drawback of Raman modelling. However, this does not affect significantly the quantification of the composition.^[226] The LBIC photocurrent map measured at 488 nm was employed as an approximation to the overall performance, see Figure 5.6(c). As theoretically expected, the top-performing regions are located in the central area of the device which corresponds to balanced D:A compositions in contrast to lateral areas with unbalanced stoichiometry, and consequently, they exhibit significantly lower photocurrent values. For the sake of better visualisation, the spatial variable is removed and the three extracted maps (composition, thickness and photocurrent) are combined in a single 2D optimisation map, see Figure 5.6(d).

Finally, the active area measured of these samples is 20 mm x 50 mm, defined by the length of the short axis of the device and the maximum stepper motor travel, respectively. Considering the sample size and a typical measurement step of 0.2 mm, more than 20000 measured points were generated containing thickness, composition and photocurrent values in a single device. Therefore, we demonstrate the capacity to generate a large library of data at a very low cost and in a short time.

5.4.4 Complementary photocurrent map

When applying 2D gradient maps to polymer:fullerene-based systems, a single photocurrent measurement was enough to fully characterise the device photocurrent.^[217] This is because in fullerene-based OPV the polymeric donor is the main light harvester. In NFA-based devices, however, both photoactive materials, polymeric donor and NFA, contribute actively to the photocurrent generation. The main reason is the large extinction coefficient of NFAs compared with fullerene counterparts (Figure 5.7).

As a consequence of this fact, an additional photocurrent measurement is required for an accurate assessment of the photocurrent of the NFA-based device. Similarly to the previous chapter, the panchromatic photocurrent measurement was employed using the white light of the microscope (*whiteBIC*). This subsequent complementary photocurrent measurement was performed in the same area as the 488 nm LBIC measurement. Note that *whiteBIC* maps use the same thickness and composition values deduced from *RamBIC* measurement. The only difference is that the photocurrent values were replaced by those measured under white light illumination (*whiteBIC*).

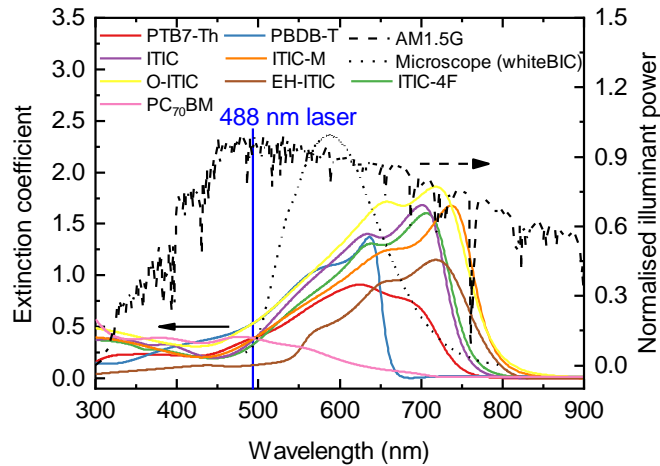


Figure 5.7. Illuminant sources and material absorption. Absorption spectra of the employed semiconductors (left axis) and the normalised illuminant sources AM 1.5G and white light of the microscope, *whiteBIC* (right axis).

As an explanatory example, a comparison between monochromatic (LBIC at 488 nm) and panchromatic (white light of microscope) photocurrent of maps are depicted in Figure 5.8 for PBDB-T and O-ITIC. The absorption coefficient and white light spectrum of *whiteBIC* is given in Figure 5.7 to facilitate the discussion. When comparing both photocurrent images we conclude that the choice of excitation light source (488 nm or white light) plays a crucial role in the identification of high performing areas. In this specific case, the differences in photocurrent cannot be ascribed to the optical absorption since PBDB-T and O-ITIC absorb equally at 488 nm, see Figure 5.7.

On the other hand, the light spot plays a relevant influence. The size of the laser spot (10 μm in diameter) when using monochromatic light (LBIC at 488 nm) is very small. Therefore, it is more likely to scatter light due to dust, scratches or imperfections in the PAL. By contrast, when using white light the spot is much larger (50 μm in diameter) which reduces dramatically the likelihood for scattering phenomena to occur. The scattering of the laser yields many isolated high-performing spots surrounded by low-performing areas in the photocurrent images results that, in our opinion, can be considered an artefact, see Figure 5.8(a).

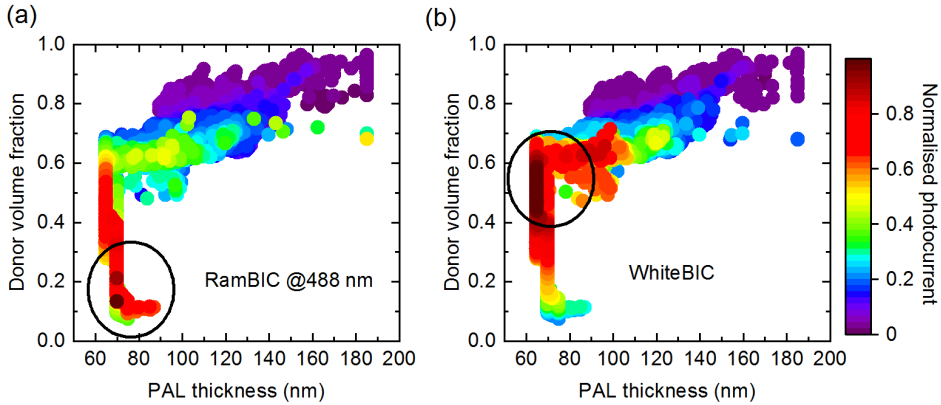


Figure 5.8. Comparison of photocurrent measurements: *Rambic* vs *whiteBIC*. Composition-thickness-performance maps of PBDB-T:O-ITIC system excited at (a) 488 nm laser and (b) with the microscope white light. Both graphs share the normalised colour scale. The highest performing areas are highlighted with a circle.

Consequently, depending on the excitation source for PBDB-T:O-ITIC system each technique suggests different optima thickness-composition values. While wavelength-dependent measurement indicates that the top-performing area corresponds to lower donor loading (0.2 donor volume fraction), the panchromatic measurement indicates a more likely prediction with a more balanced D:A contribution (0.5-0.6 PBDB-T volume fraction), see Figure 5.8(b). Despite *whiteBIC* illumination is spectrally limited (500-750 nm), it provides a more accurate assessment of the photocurrent than 488 nm (Figure 5.7). However, a further characterisation under AMG1.5 is required to evaluate accurately the photocurrent of devices.

To conclude, both co-local optoelectronic measurements are needed for a proper assessment of graded-composition solar cells. As a result, 2D optimisation maps consist of two consecutive and co-local measurements. First, *Rambic* technique pumped at 488 nm enabled to extract the local blend characteristics from Raman scattering (thickness and composition) and, at the same time, an estimation of the photocurrent. Then, a second panchromatic photocurrent measurement (*whiteBIC*), applied over the same measured area, allowed a more accurate evaluation of the photocurrent.

5.4.5 Reproducibility of the combinatorial method.

The intrinsically chaotic nature of the developed mixing process differs from conventional mixing of OPV formulations where donor and acceptor materials are previously premixed and stirred together. In particular, the mixing upon blading could eventually lead to a non-identical thickness-composition window from one experiment to another and different PAL morphologies. To demonstrate the robustness of this method through batch-to-batch reproducibility, we manufactured two similar batches of heterogeneous graded thickness and composition devices of PBDB-T:O-ITIC under the same conditions. As Figure 5.9(a,b) depicts, the space of parameters of the two sets of devices is very similar with a thickness window from 70 to 200 nm and composition ranging from 20% to 90% of PBDB-T. Despite the second batch of composition-graded device covers larger combinations of thicknesses and compositions and the photocurrent values are slightly higher, the top-performing regions coincide in both cases.

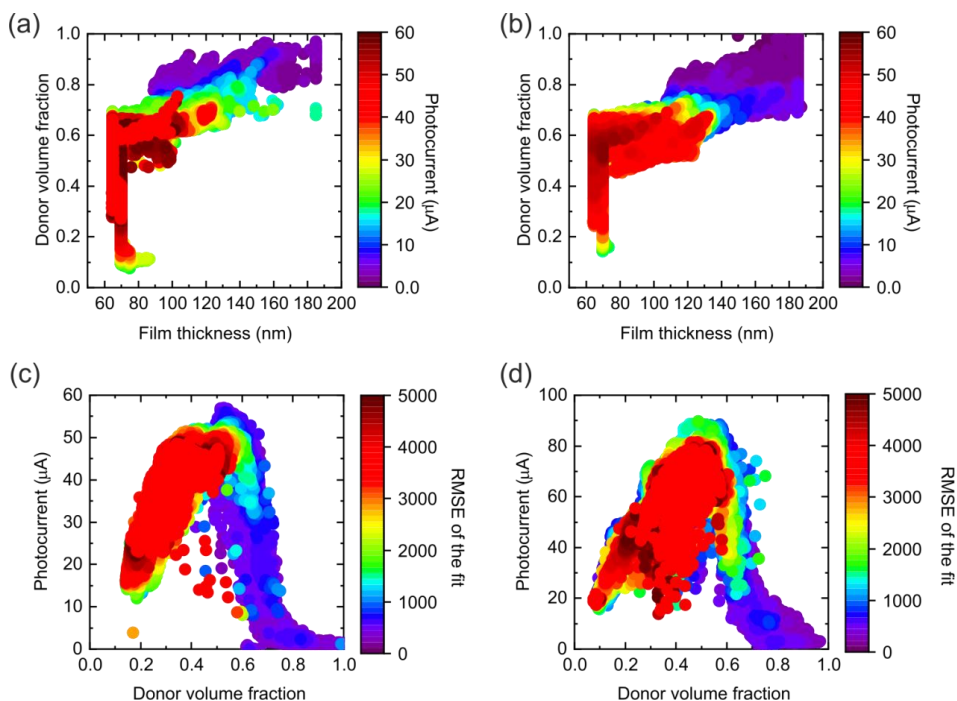


Figure 5.9. Reliability of the high-throughput method. 2D gradient maps (*whiteBIC*) of PBDB-T:O-ITIC systems. Batch 1 (a,c) and batch 2 (b,d) are plotted as a function of photocurrent and composition (top row) and film thickness and volume fraction (bottom row).

This result indicates that the highest performance conditions for PBDB-T:O-ITIC solar cells are reached for film thicknesses between 80 and 130 nm and 50%-60% PBDB-T volume concentration.

Another interesting feature of these maps (Figure 5.9(a,b)) is the wide range of available data for PBDB-T content from 10% to 45 % in volume for 70 nm PAL thickness. This can be explained as a combination of two effects. First, the limited thickness windows of NFA-rich regions (0-0.2 donor volume fraction) appears because of the low ink viscosity typically associated with pristine NFA-based solutions in contrast to viscous polymeric ink. Second, the vertical line for 70 nm PAL might be attributed to factors like the aforementioned difficulty to predict the PAL thickness with enough accuracy due to the oscillation of the scattered intensity with the PAL thickness since the iterative Raman fittings get stuck at the lowest thickness value.

To rule out the uncertainty of the thickness contribution of the 2D optimisation maps, we plot the photocurrent values and the goodness of the fit (root mean square error, RMSE) as a function of the volume composition in Figure 5.9(c,d). In these graphs, the Raman fittings of NFA-rich regions show consistently higher RMSE values than the polymer-rich counterpart. This fact could be explained, again as an effective reduction of the highly complex refractive index of NFAs upon blending. Despite NFAs typically show a very high extinction coefficient, such good absorption features could be diminished when they are blended with a polymer. Finally, the high RMSE values associated with NFA-rich blends was explained as an inaccurate thickness prediction.

Another meaningful information extracted from these 2D maps is the shape of the photocurrent-performance envelope. The fact that both batches exhibit similar shapes proves again the good reliability of this high-throughput screening technique. Both PBDB-T:O-ITIC composition-graded devices exhibit the maximum performance for PBDB-T content between 40% and 60%. Interestingly, there is a sharp drop in performance between 60% and 80% volume fraction of PBDB-T. In contrast to NFA-rich region, the reduction in photocurrent is almost linear with volume fraction. This finding suggests that O-ITIC, the NFA synthesised by Prof. Heeney's group, exhibits excellent light-harvesting capabilities that even blends with low NFA loadings yield high photocurrent values. However, for fullerene acceptors, the optimum composition is

typically shifted towards fullerene-rich blends since fullerenes exhibit limited light absorption.^[230]

The data dispersion shown in the photocurrent concentration map suggests that there could be hidden variables. This is evidenced by the combinations of similar thickness and composition values that yield different photocurrent values. Thus, it is clear that there must be other parameters controlling the photocurrent apart from thickness and composition. We attribute this effect to the difference in blend morphology. This morphological difference could be induced by the blend location in the sample that might induce longer drying time or significantly mixing levels and thus slightly different nanostructure.^[218] We conclude that with 2D graded thickness-composition devices, different morphologies are achieved in the same sample. Further systematic morphological analysis is, however, highly requested to establish a solid performance-morphology relation, although this is out of the scope of this thesis.

Finally, it is worth highlighting that these optimisation maps contain more than 20.000 points measured in a single device. Hence, this method enables fast identification of the window of parameters, in this case, thickness and composition that lead to the highest performance. The generated data through this methodology is further employed to feed the so-called machine learning (ML) algorithms, which typically required several thousands of data for building accurate prediction models.^[231] Moreover, this measuring-intensive high-throughput approach reduces significantly the material consumption down to 10 mg of each new photoactive materials. Furthermore, in terms of manufacturing, the optimisation process can be speeded up by a factor of 100.^[217]

5.4.6 2D optimisation maps and optical absorption

With the aim to correlate the optical absorption the shape of the composition-photocurrent envelope, we investigate systems with complementary (PBDB-T:EH-ITIC) and non-complementary (PTB7-Th:ITIC) light absorption features, see Figure 5.10. The selected NFAs, ITIC and its branched modification (EH-ITIC) exhibit very broad spectral absorption with maximum extinction coefficients over 1.5. Besides, the side chains modifications, in this case, branched ones, have a strong effect on the absorption producing a red-shift and obtaining a more efficient light absorber than the unmodified

ITIC counterpart. This finding points out that the introduction of side chains modifications is a good strategy to improve light absorption capabilities and, consequently, the PCE of devices (as seen in Chapter 4).

Figure 5.10(b,d) shows the photocurrent dependence with donor volume fraction, together with the RMSE of Raman fittings, used to deduce the thickness and composition for each point. It seems that there is a direct correlation between the shape of performance-composition envelope and the optical absorption bands of PAL materials. The system with complementary absorption, PBDB-T:EH-ITIC, exhibits two main peaks with optima composition around 30% and 60% of PBDB-T volume fraction. This bimodal distribution of the photocurrent-composition envelope can be ascribed to the contribution of two effects.

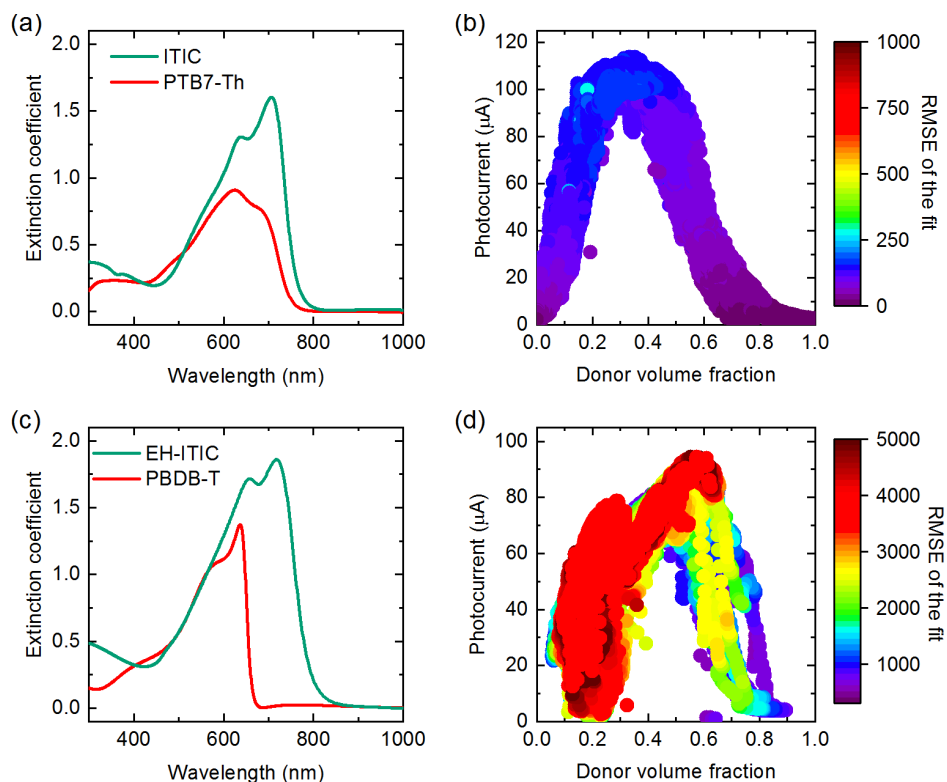


Figure 5.10. Correlation between photocurrent distribution and overlapping of the extinction coefficients. (a) PBDB-T:EH-ITIC and (b) PTB7-Th:ITIC. 2D optimisation maps with photocurrent values and error of fitting (colour scale) as a function of polymer concentration. (a) PTB7-Th:ITIC and (b) PBDB-T:EH-ITIC solar cells.

First, the extraordinary light absorption capabilities of EH-ITIC lead to high photocurrent even with low PBDB-T loading (30% in volume). The second region (60% in vol. of PBDBT) corresponds to the conventional balanced D:A ratio.^[229] On the other hand, the shape the photocurrent-composition envelope for PTB7-Th:ITIC solar cells exhibits a normal distribution of composition centred in 40% volume fraction of PTB7-Th. The normal distribution for this system could be correlated with the fact that both materials have coincident spectral absorption, see Figure 5.10(b). According to these data, top-performing devices could be manufactured in a wide window of compositions from 20 to 50% of the volume fraction of PTB7-Th. This finding is very relevant to predict photocurrent although manufacturing discrete devices is required to verify V_{oc} and FF contribution.

As seen in the previous examples, in both maps the root means square error (RMSE), colour scale in Figure 5.10(b,d), associated to fit Raman spectra is higher for NFA enriched compositions. Again, this high RMSE suggests that an effective reduction of the complex refractive index upon blending with the polymer.^[232] However, this is not the main drawback since it lies within the experimental error of this method. Alternatively, measuring the complex refractive indices of each intermediate D:A mixtures with the only purpose of reducing the associated error would lead to an inefficient approach in terms of material and time consumption, otherwise, this is not the purpose of the high-throughput screening approach.

5.4.7 Validation with 1D-gradient discrete devices

In order to validate the suggested shape of photocurrent-composition by 2D gradients of the previous section, we manufactured several discrete 1D thickness-graded solar cells of PBDB-T:EH-ITIC and PTB7-Th:ITIC going from polymer-rich to NFA-rich compositions, see Figure 5.11(a,b). Discrete devices were characterised electrically by JV curves and optically by Raman spectroscopy. Mr. Xabier Rodríguez carried out the optical characterisation of the best devices on each thickness-graded sample. After Raman modelling and fitting, blend composition in weight was converted to volume fraction with the material density. With that, we can compare in volume fraction the results from 1D gradient devices and 2D maps.

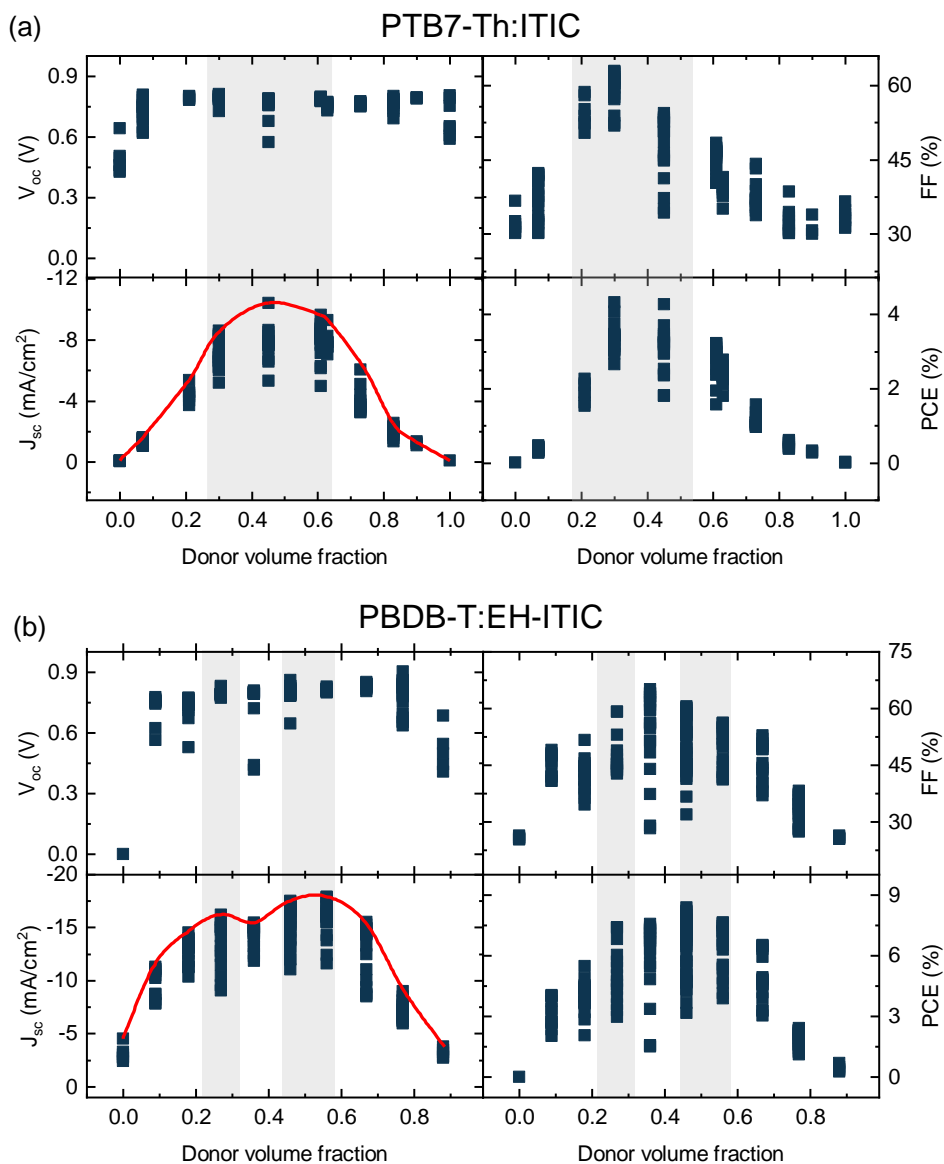


Figure 5.11. Verification of combinatorial photocurrent-composition maps. (a) PBDB-T:EH-ITIC and (b) PTB7-Th:ITIC solar cells. Photovoltaic parameters (V_{oc} , J_{sc} , FF and PCE) from thickness-graded devices at different PBDB-T volume fraction. Highlighted grey areas represent two maxima found in Figure 5.11. The red line in J_{sc} graph highlights the shape of the photocurrent-composition envelope.

PBDB-T:EH-ITIC devices show a significant reduction in V_{oc} (0.75 V to 0.9 V) when going from ITIC-rich blends (20%) to PBDB-T-rich (80%) ones. This fact could be explained as an excessive degree of crystallinity in NFA-rich films and consequently a reduction of V_{oc} . However, further studies are required to fully understand this

phenomenon. By contrast, PTB7-Th:ITIC devices show almost negligible variations of V_{oc} upon composition variations. In the case of fullerene-based solar cells, V_{oc} typically shows a normal distribution for volume fractions around 50%.^[213,229] The FF distribution exhibits a maximum of around 35% polymer volume fraction for both systems (30% for PTB7-Th and 40% for PBDB-T). However, this composition does not match with the optimum conditions for J_{sc} (45% for PTB7-Th and 55% for PBDB-T). This high NFA content required to maximise the FF suggests poor charge mobility of NFAs in comparison with the polymer. By contrast, in some fullerene-based devices the acceptor loading is lower than NFA counterpart due to the higher mobility.^[230]

For PBDB-T:EH-ITIC, the first optimum composition is for blends with 30% volume fraction of PBDB-T. Despite the relative high RMSE of Figure 5.10(a), devices with only 30% loading of PBDB-T yield J_{sc} of 16.2 mA/cm² and 6.8% of PCE, see Table 5.3. This is explained by the superior light-harvesting capabilities of EH-ITIC with respect to PBDB-T. Alternatively, blends with a more balanced stoichiometry (55% PBDB-T volume fraction) have slightly higher J_{sc} and equivalent FF and V_{oc} values, reach efficiencies up to 7.5%. Interestingly, a dramatic difference in performance is observed when comparing enriched EH-ITIC (10% vol) and PBDB-T blends (85% vol), see Table 5.3.

Whereas the former shows very high photovoltaic parameters (J_{sc} =11.5 mA/cm² and PCE=4.9%), the latter exhibits extremely poor performance (J_{sc} =3.8 mA/cm² and PCE=0.7%). Therefore, it is proved the efficient absorption characteristics of EH-ITIC by the small amount of polymer needed to manufacture high performing devices. Additionally, this could open up new strategies for homojunction devices.

PBDB-T:EH-ITIC system depicts two optima compositions for high photocurrent values while PTB7-Th:ITIC shows a single photocurrent maximum centred in 30% polymer volume fraction, as reveal 2D thickness-composition optimisation map. Therefore, it suggests the existence of a correlation between the absorption features of photoactive materials and the shape of photocurrent-composition envelope.

Table 5.3. Photovoltaic parameters of PBDB-T:EH-ITIC and PTBT7-Th:ITIC solar cells. Volume fraction, PAL thickness deduced from Raman fits.

| System | Donor volume fraction (% vol.) | V _{oc} (V) | J _{sc} (mA/cm ²) | FF (%) | PCE (%) |
|--------------------|--------------------------------|---------------------|---------------------------------------|--------|---------|
| PBDB-T: EH-ITIC | 9 | 0.75 | -11.5 | 57.2 | 4.9 |
| | 28 | 0.79 | -16.2 | 53.1 | 6.8 |
| | 55 | 0.81 | -17.9 | 51.8 | 7.6 |
| | 84 | 0.68 | -3.8 | 26.3 | 0.7 |
| PTB7-Th:1 TIC | 10 | 0.70 | -1.62 | 41.5 | 0.5 |
| | 30 | 0.80 | -8.62 | 62.7 | 4.3 |
| | 40 | 0.77 | -10.4 | 45.8 | 3.7 |
| | 50 | 0.80 | -9.62 | 38.9 | 2.8 |
| | 80 | 0.78 | -2.56 | 30.2 | 0.6 |

The shape of the photocurrent-composition envelope from 2D gradient maps (Figure 5.10(a,b)) and 1D discrete devices (Figure 5.11) agree very well. Thus, this is further evidence of the capability of the 2D gradient maps to reproduce the same photocurrent-composition behaviour as Edisonian (sample-to-sample) approach. However, 10 times more photoactive material was employed in the latter approach. Considering the high cost of these new NFAs and their not fully optimised chemical synthesis, the use of high-throughput screening methods can save a significant amount of money in the OPV optimisation process.

5.5 Generalisation of the method

The powerful screening capability of this high-throughput methodology is extended to twelve different systems. In particular, we studied some of the top-performing OPV blends including two low-bandgap polymers, namely PTB7-Th and PBDB-T, mixed with four ITIC derivatives (ITIC-M, O-ITIC, EH-ITIC and ITIC-4F); and PC70BM as fullerene reference (Figure 5.12).

Figure 5.12 reveals that the optimised photocurrent composition for PTB7-Th-based systems is at higher NFA loading than PBDB-T. By contrast, PBDB-T:NFA based system seems to exhibit two maxima, one at 30% and 60%. Another relevant finding that can be extracted through this large dataset is the evaluation of compositional PAL

tolerance with photocurrent. We observe that fullerenes-based systems (PC₇₀BM) exhibit large photocurrent tolerance over a wide range of compositions (10-60% of donor loading). By contrast in some NFA-based systems, the photocurrent distribution is extended for blends with higher donor loadings. For instance, ITIC derivatives systems show high photocurrent values for blends with more than 60% volume content of PBDB-T. The fact of NFAs exhibit photocurrent at higher donor loading might be explained, as mentioned before, due to the higher NFA light-harvesting capabilities with respect to fullerenes.

It is worth highlighting that the dataset of Figure 5.12 consists of more than 300.000 measured data points (25000 points each map by 12 systems) with photocurrent values (LBIC at 488 nm and *whiteBIC*) and the same number of Raman spectra that enable to extract thickness, composition and the associated error after fitting. More impressively, this outstanding dataset was generated with a very little amount of each material (2 mg) resulting in a total amount of 48 mg for the whole dataset. Note that, for this calculus, 133 μ L of pristine material at 15 mg/mL is considered. However, for the fabrication of 2D maps, only 30 μ L of the pristine solution is needed.

As future work derived from this chapter, a further and deeper understanding of this dataset will be performed with the aid of machine learning (ML) algorithms. Several fundamental properties of neat photoactive materials such as energy levels, charge mobility, absorption spectrum are coupled with the composition values and photocurrent of the studied systems. Thanks to this, hidden relationships between photocurrent, blend composition and fundamental properties would be unravelled.

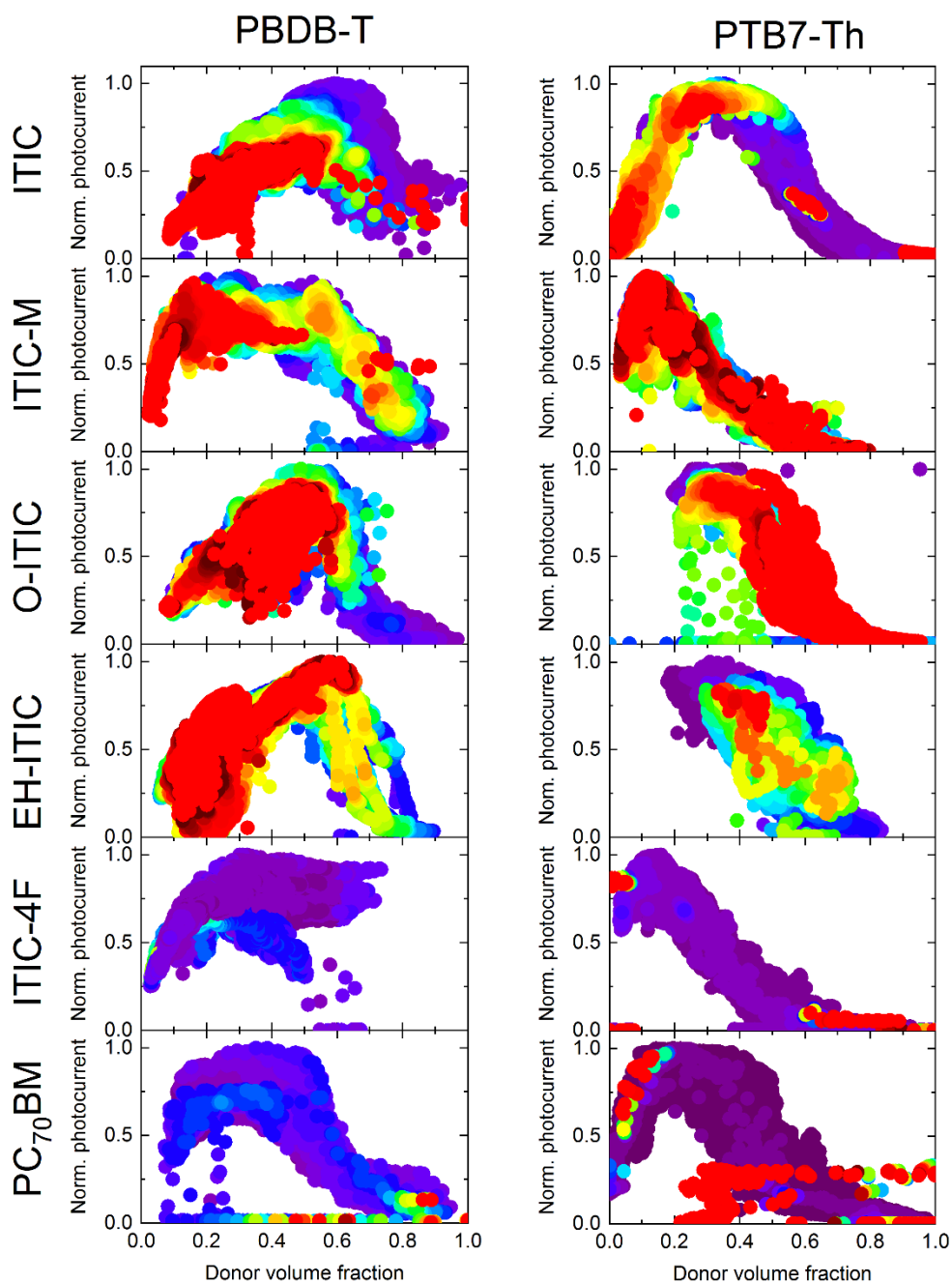


Figure 5.12. Combinatorial screening of 12 low-bandgap:acceptor systems. PBDB-T and PTB7-Th are polymeric donor (columns) and ITIC, ITIC-M, O-ITIC, EH-ITIC, ITIC-4F and PC₇₀BM as acceptors (rows). The colour scale represents the error of fitting going from red (high RMSE) to blue (low RMSE).

5.6 Conclusions

In this chapter, we have extended combinatorial screening to optimise the performance in binary organic solar cells from 1D to 2D gradient approach. With this approach, it is reduced significantly both resources and experimental time. The methodology applied to top-performing binary OPV devices consists of four basic steps. (1) Manufacturing a graded film with intended variations in the parameters of interest, typically thickness and composition. (2) Acquisition of co-local images with two consecutive measurements: a combined Raman scattering and LBIC at 488 nm followed by a panchromatic measurement with white light (*whiteBIC*). (3) Fit the Raman hyperspectral images through TMM modelling to extract the local blend characteristics (thickness and composition) (4) Correlation of thickness, composition and photocurrent maps to easily identify the top-performing blend characteristics.

First, we tested the reproducibility of this screening approach by producing two thickness-composition heterogeneous devices. Despite the chaotic mixing upon blading two photoactive materials from pristine solutions, both heterogeneous devices (from different batches) pointed to the same optimum thickness and composition parameters. This proves the robustness and reliability of the data produced through this combinatorial method. However, one of the main drawbacks of this method is the difficulty to predict accurately the photoactive layer thickness due to the large error when modelling the Raman intensity. Therefore, we focused on photocurrent-composition maps to identify the optimum D:A ratio. The predicted photocurrent-composition envelope was satisfactorily validated for two different NFA-based OPV systems. Note that more than 120.000 measured points from 12 different systems were measured including photocurrent (LBIC at 488 nm and *whiteBIC*), composition, thickness and RMS. The final verification of 2D maps requires an evaluation with homogenous composition devices to determine the effective PCE. Further conclusions will be carried out using the generated dataset with the aid of machine learning (ML) algorithms. For these ML methods, as input parameters, the fundamentals properties of photoactive materials will be introduced so that we might correlate it with the optimum compositions.

To conclude, we have estimated that this combinatorial screening methodology (compared to sample-by-sample counterpart) implies a 10-fold reduction in resources

usage (materials consumption), together with a 10-50-fold in time consumption. Additionally, for the full evaluation of a specific system, a minimal amount of material (<10 mg) per semiconductor is required. Interestingly, this methodology can be extrapolated to optimise other layers or processing parameters. We truly believe that this type of approaches that generate large dataset at a very low cost is going to be a breakthrough in the upcoming decade in order to feed with data the field of data science.

Chapter 6 Laser patterned semitransparent OPV modules

ABSTRACT

The capability of tuning the transparency is one of the most relevant characteristics for the integration of OPV into semitransparent architectonic elements such as windows, curtains and glazings. The recent development of NFAs providing at the same time high efficiency and absorption in the non-visible range paves the way towards the eventual integration of OPV into the buildings of the future.

In this chapter, aesthetical, technical and geometrical parameters of OPV modules are studied to facilitate their integration into semitransparent architectonic elements. To do so, we combine commercial materials such as PBTZT-stat-BDIT-8 and 4TICO with strong near-infrared absorption. The semitransparent and solution-processed devices are further upscaled into 1 cm² modules with a performance exceeding 4%. The module manufacturing process combines effectively sequential laser and coating steps resulting in negligible performance losses upon increasing the active area. These fully bladed modules, with more than 30% of transparency, are fabricated following the low-cost manufacturing processes that are compatible with large-scale production.

Parts of this chapter will be published: *E. Pascual-San-José, G. Sadoughi, L. Lucera, M. Stella, E. Martínez-Ferrero, G. E. Morse, M. Campoy-Quiles and I. Burgués-Ceballos. Journal of Materials Chemistry A, accepted 2020. (DOI: 10.1039/d0ta02994g)*. Some of the results herein shown were achieved during a PhD stay at Merck Chemicals Ltd. in Southampton (UK).

6.1 Requirements for BIPV

As it was mentioned in the general introduction of the thesis, building-integrated photovoltaics (BIPV) is one of the potential markets for OPV, especially for semitransparent architectonic elements.^[95] While most of the efforts of the scientific community are dedicated to improvements in performance and stability, here we also study other relevant technical requirements for the integration of OPV into BIPV, see Table 6.1.^[233-235] In particular, we propose aesthetic features (chromaticity and transparency) and thresholds for prototype geometrical parameters such as geometrical fill factor (GFF) and active area (AA). Note that the efficiency is not considered in these requirements since the higher, the better. Alternatively, opaque modules do not meet the transparency requirements although they might be used in other applications such as walls or rooftops.

Table 6.1. Specific requirements for the integration of OPV modules into semitransparent windows and curtains. The proposed target values correspond to the minimum threshold expected for lab-scale demonstrators. References are given in the main text.

| Item | Target Value |
|-------------------------------|--|
| Chromaticity | Architects prefer blue, green and neutral grey |
| Transparency | $\geq 30\%$ |
| Geometrical fill factor (GFF) | $>90\%$ |
| Active area (AA) | $>1\text{ cm}^2$ |

6.1.1 Aesthetical requirements

From the chromaticity standpoint, OPV materials can theoretically offer any desired colour due to the great synthetic flexibility of the photoactive materials.^[65,236] Blends of OPV materials enable to fully cover the colour palette. For instance, blue^[101] and purple^[166] fully printed modules ($>50\text{ cm}^2$) have been recently reported with efficiencies over 4%. In the particular case of BIPV applications, although colours such as blue, green or neutral grey are the preferential choice of architects, other chromaticities are also employed.^[236,237]

The transparency is another relevant feature for BIPV, especially for semitransparent architectonic elements. Although semitransparent devices are inherently less efficient

than opaque ones due to losses in unabsorbed light (transmitted), for specific applications such as glazing elements the transparency is as relevant as the performance.^[238]

A 30% of average visual transmittance (AVT, Eq.(2.15) or human perception transmittance (HPT, Eq.(2.16) transparency threshold is generally accepted as the benchmark for photoactive windows.^[239,240] More details about the transparency metrics in section 2.4.2. The degree of transparency in OPV can be generally controlled by simultaneously i) reducing the PAL thickness, which consequently limits the overall performance, and ii) with the implementation of semitransparent electrodes. For the latter, the most common strategies include a) reducing the thickness of evaporated electrodes down to 20 nm^[240,241] (non-vacuum free approach), b) screen-printing metallic fingers electrode (noticeable mm-size interconnection and low geometrical fill factor, GFF)^[180,242] and c) printing semitransparent top electrode materials such as highly conductive polymers like PEDOT or metal nanowires like silver (Ag NW).^[243,244]

In Table 6.2, we summarise the recent progress made in semitransparent OPV, classifying the works in respect of the processing of the semitransparent electrode (evaporation vs solution-processing). It is worth highlighting that efficiencies between 6% and 10% have been achieved in semitransparent devices with evaporated electrodes^[241,245-247] (strategy a). In contrast, the efficiency of fully solution-processed semitransparent devices is so far limited to, to the best of our knowledge, 5% (strategy c), see Table 6.3.^[166]

Table 6.2. State-of-the-art of semitransparent organic solar cells.

| | Photoactive layer blend | PCE (%) | Area (cm ²) | Metric | Transparency* (%) | ST electrode | | Reference |
|--------------------------------|--------------------------------|------------|-------------------------|--------------|-------------------|----------------------|----------------------|------------------|
| | | | | | | Materials | Deposition | |
| Evaporated electrode | PDTP-DFBT:FOIC | 4 | 0.04 | HPT | 50 | MoO3/Ag | Evaporation | [245] |
| | PBDTTT-C-T:PCBM | 6 | 0.1 | AVT | 25 | MoO3/Ag | Evaporation | [240] |
| | PBDB-T:ITIC | 7 | 0.12 | AVT | 25 | MoO3/Ag/MoO3 | Evaporation | [241] |
| | PTB7-Th:IHIC | 9.8 | 0.04 | AVT | 35 | MoO3/Au/Ag | Evaporation | [247] |
| | PFBDB-T:O-ITIC | 10 | 0.045 | AVT | 19 | MoO3/Ag/MoO3 | Evaporation | [246] |
| Fully solution-processed | P3HT:PCBM | 1.6 | 84 | - | - | AgNW+PEDOT | Inkjet | [248] |
| | PV2000:PCBM | 4.3 | 1 | @550 nm | 10 | AgNW | Inkjet | [249] |
| | P3HT:Si-PCPDTBT | 2.2 | 0.1 | @550 nm | 30 | AgNW | Blade coating | [250] |
| | P3HT:IDT-2BR | 3.2 | 0.05 | AVT | 53 | PH1000 | Spin-coating | [251] |
| | pDPP5T-2:PCBM | 2.3 | 64 | @550 nm | 52 | AgNW | Slot-die | [252] |
| | PBDTT-DPP:PCBM | 4 | 0.1 | @550 nm | 66 | AgNW | Spin-coating/Spray | [253] |
| | PBTZT-stat-BDTT-8:PCBM | 4.8 | 197.4 | HPT | 10 | AgNW | Slot-die | [254] |
| | PBTZT-stat-BDTT-8:PCBM | 4.5 | 114.5 | AVT | 20 | Ag | Screen-printed | [101] |
| | P3HT:O-IDTBR | 5 | 60 | ISO9050-2003 | 1-6 | AgNW | Blade/Slot-die | [166] |
| | PBTZT-stat-BDTT-8:4TICO | 4.7 | 0.08 | HPT | 20 | PH1000 | Blade coating | This work |
| PBTZT-stat-BDTT-8:4TICO | 3.9 | 1.1 | HPT | 30 | PH1000 | Blade coating | This work | |

*Whenever available this value corresponds to the transparency of the full device, else of the photoactive layer.

6.1.2 Geometrical requirements for BIPV modules

From the manufacturing standpoint, one of the main challenges in the upscaling and mass production of OPV modules is to limit the associated losses when increasing the active area.^[255] The main source of losses arises from the limited conductivity of electrodes, such as ITO or resistive top electrodes, resulting in FF losses upon area increase.^[256] To limit these electrical losses, modules with series-interconnected subcells were proposed to minimise losses derived from the electrical conductivity of the electrodes. The strategies to maximise the active area of these series-interconnected subcells modules include enlarging the cell geometry (width, length and the number of interconnected subcells) and reducing cell-to-cell interconnection. The geometrical fill factor (GFF) is the metric that relates the ratio between the active area and the total area (active area and interconnection area) of the module.

Among the strategies to maximise the GFF, the combination of sequential coating and laser patterning ablation steps result in the most effective approach.^[114,256] With this strategy, the interconnection length can be reduced down to 200 μm in contrast to typical millimetres length of offset and overlapped layers needed for the interconnection with slot-die based coating method.^[40] Therefore, the GFF of modules with laser patterning ablation overcome 90%^[257] whereas printing separate stripes with a controlled lateral offset is limited to 50-70% in the best cases.^[153]

The state-of-the-art of fully solution-processed and laser-patterned modules exhibit GFFs over 90% and active areas larger than 40 cm^2 . For instance, Lucera *et al.* manufactured flexible patterned modules based on PBTZT-stat-BDTP-8:PCBM with more than 98% of GFF.^[258] Recently, P3HT:O-IDTBR laser patterned modules of 50 cm^2 were manufactured delivering 5% PCE, however, they show a very low level of transparency (below 10%) limiting their use as semitransparent element.^[166] When comparing the top-performing lab-scale devices (17%)^[35] and modules (13%),^[73] it is clear that further upscaling studies are required to bridge the gap between hero-lab devices and large-scale modules.

6.1.3 Objective

In this sixth chapter, we propose the technical requirements for the integration of OPV into semitransparent architectural elements. The aesthetics of the solar cells, including colour and transparency, are studied in depth. Semitransparent (ST) devices are manufactured following low-embodied technology demanded by the printing industry namely the use of halogen-free solvents, air processing and evaporation-free steps. In particular, we evaluate the thickness-performance trade-off of semitransparent solar cells based on PBTZT-stat-BDTT-8 blended with 4TICO. Then, ST prototype modules (1 cm^2) are manufactured by blade coating and laser patterning with a minimal reduction in performance upon size increase. Finally, advanced co-local optoelectronic characterisation is used to further evaluate the performance and optimisation of the geometry of the modules.

6.2 Selection of photoactive materials

The election of photoactive materials is crucial to yield high efficiencies, but also to meet other aforementioned aspects, such as aesthetics, transparency and scalability, see Table 6.1. The commercial materials PBTZT-stat-BDTT-8 and 4TICO developed by Merck Chemicals Ltd. were chosen as electron donor and acceptor materials, respectively (chemical structures are depicted in Figure 2.2(g) and Figure 2.3(i)).^[101,258] PBTZT-stat-BDTT-8 shows great stability when blended with the fullerene derivative PC₆₀BM, and higher carrier mobility compared to other polymeric donors.^[259]

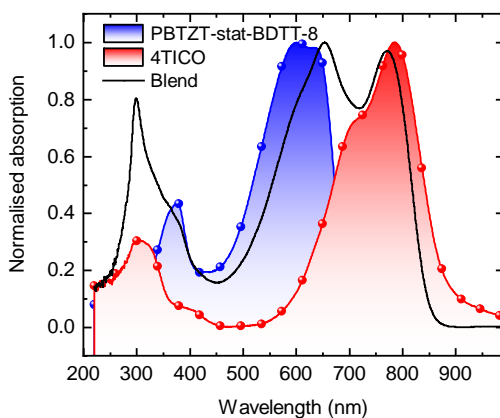


Figure 6.1. Optical absorption of pristine and blended photoactive materials.

Indeed, this enables the manufacturing devices with a relative thick PAL (above 400 nm) while still retaining the device performance over 8%.^[101] As a matter of fact, this polymer has been intensively employed for large-scale demonstrators over 100 cm².^[101,254]

As seen in Chapter 4, despite the extraordinary transport properties of these fullerene-based blends, these type of acceptors barely contribute to the light absorption of the device, thus limiting the light-harvesting capacity, and consequently the device performance. To partially overcome this limitation, we incorporate the newly developed NFA, 4TICO, with the same core structure as reported IHIC but including a modification in the solubilisation side chains.^[247,260] The complementary optical absorption of the PBTZT-stat-BDTTT-8:4TICO PAL with thicknesses ranging from 30 nm to 300 nm is shown in Figure 6.1. PBTZT-stat-BDTTT-8 absorbs light in most of the visible region from 300 nm to 700 nm^[101] whereas 4TICO exhibits a strong absorption from 650 nm to 900 nm with the maximum absorption in the NIR.

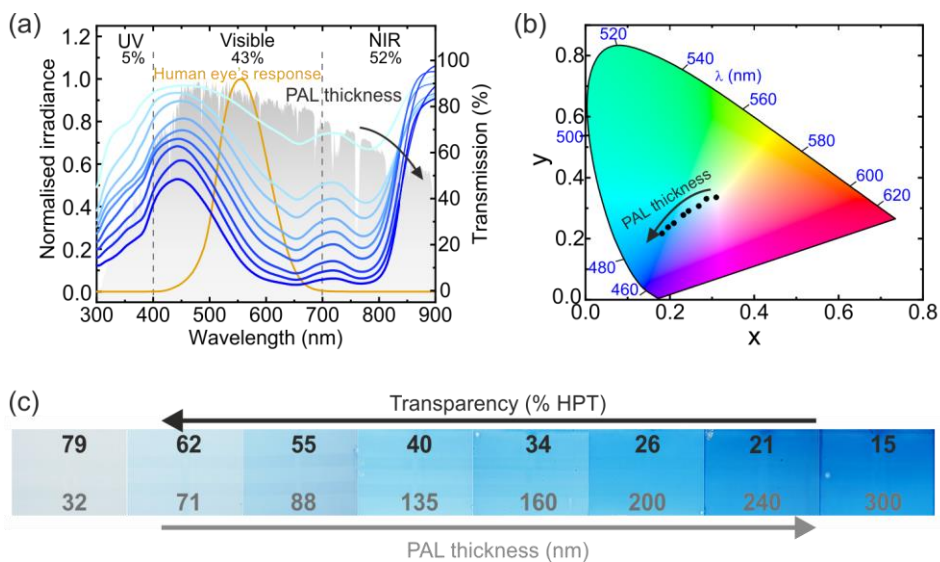


Figure 6.2. Colour and transparency of the PAL as a function of the thickness (PBDTZT-stat-DBTT-8 and 4TICO). (a) Optical transmission. The percentage of irradiance in each of the three regions of the spectrum, ultraviolet (UV), visible and near-infrared (NIR), indicated with the vertical dashed lines are given in the upper part. Normalised human eye's response and AM 1.5G spectra are also given. (b) Colour coordinates in transmission in CIE chromaticity diagram. (c) Pictures of thin films with increasing PAL thickness, labelled with the corresponding HPT values (top) and thickness (bottom). The size of each sample is 5 cm x 5 cm.

6.2.1 Colour and transparency

From the aesthetic perspective, the fact that 4TICO extends the blend absorption up to the near-infrared (NIR) favours the transparency of the device while retaining a weak absorption in the visible range compared to fullerenes or others NFAs strongly absorbing in the visible range. Thus, one of the main advantages of using blends based on NFAs with strong NIR absorption is that the appearance is primarily defined by the polymeric material (Figure 6.2). The colour coordinates of the blend were calculated and plotted in the CIE chromaticity diagram (Figure 6.2(b)) using the transmission spectra from Figure 6.2(a) and an AM 1.5G light source from Figure 6.2(a).

The CIE colour coordinates of the PAL are in good agreement with the pictures shown in Figure 6.2(c) covering a wide range of the blue gamut of the CIE chromaticity diagram. As seen in Chapter 3, the CIE coordinates of thinner films are located close to the centre of the chromaticity diagram, whereas thicker films tend to locate closer towards the edge of the diagram. Additionally, the HPT considering simply the photoactive films was calculated as a function of the thickness varying from 80% to 15% for film thicknesses of 30 and 300 nm, respectively (Figure 6.2(c)). Then, we calculated the deviation from those values considering all the layers of the device (Figure 6.3 and Appendix B). Our data indicate that the colour is mainly defined by the PAL, with a minor influence of PEDOT 4083 and the ST top electrode (Figure 6.4).

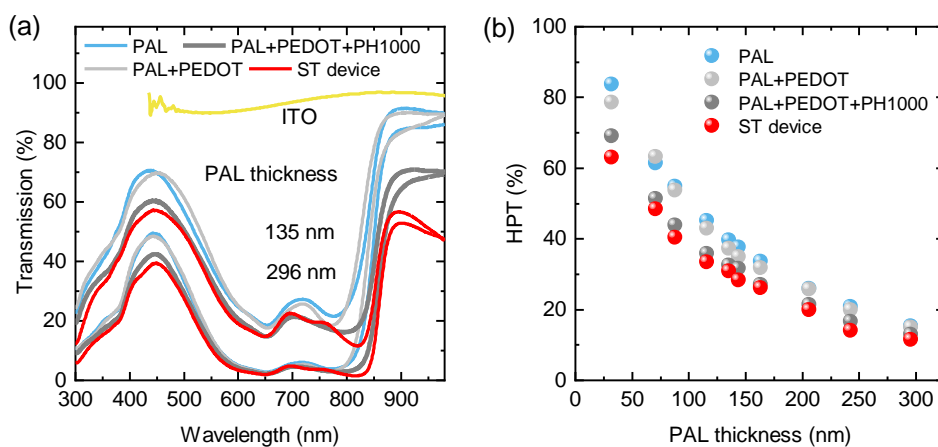


Figure 6.3. Transparency contribution of each layer. The included layers are photoactive layer (PAL), PEDOT:PSS 4083, PEDOT PH1000 and full semitransparent device (ST device). (a) For two PAL thicknesses 135 nm and 296 nm. (b) Human perception transmittance (HPT) as a function of the PAL thickness for each layer.

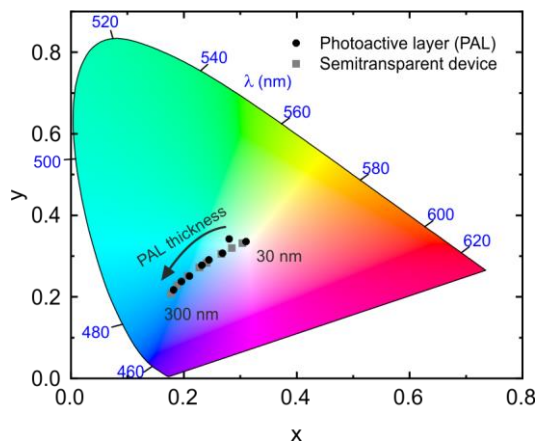


Figure 6.4. Colour CIE coordinates of photoactive layer films (as depicted in Figure 6.2) and semitransparent device (with the contribution of electrodes).

6.3 Solution-processed devices

6.3.1 Adapting to industry requirements

The next stage towards upscaling PBDTZT-stat-DBTT-8 and 4TICO is to adapt the manufacturing process to the printing industry requirements, see Table 6.3.^[40,180,223,255] With that purpose, only large-scale compatible techniques were employed in this chapter. The buffer layers (ETL and HTL), PAL and semitransparent top-electrode were likewise blade-coated in air, thus reducing the associated cost of the printing process. Thus, it enables to avoid the use of a controlled atmosphere, otherwise frequently required for processing top-performing OPVs.^[66,110,261]

Another critical aspect in order to meet industrial printing regulations is to avoid the use of harmful and hazardous halogenated solvents.^[197,256] Both PBDTZT-stat-DBTT-8 and 4TICO were originally designed and synthesised to exhibit great efficiency and solubility in non-halogenated solvents such as *o*-xylene.^[197] Besides, the processing temperature should not exceed 150°C in flexible plastic substrates although in rigid substrates can be higher due to the good thermal stability of these photoactive materials.^[101] The highest casting and annealing temperatures were 65°C and 140°C, respectively.

Table 6.3. Preferred technical requirements for the manufacturing of OPVs following the request from printing industrial manufacturers. References are given in the main text.

| Item | Target |
|------------------------|--|
| Coating technique | Scalable such as slot-die or blade coating |
| Casting atmosphere | In air |
| Top electrode | Solution processing |
| Formulation | Non-halogenated solvents |
| Processing temperature | < 150°C |

6.3.2 Semitransparent and opaque devices

Efficient alternatives to evaporated silver electrodes are highly requested to reduce the drop in performance in the transition from vacuum-processed to solution-processed electrodes.^[244]

We propose the use of a highly conductive PEDOT:PSS (PH1000) due to a good balance between electrical conductivity and transparency.^[260] Furthermore, PH1000 electrode is a metal-free material and can be processed from solution as the rest of the layers. As a result, the layered and inverted architecture employed is Glass/ITO/AZO/PAL/PEDOT:PSS and evaporated Ag (for opaque) or PH1000 (for semitransparent devices), see Figure 6.5(a). Figure 6.5(b) shows the best JV curves for semitransparent (ST) and opaque (used as reference) devices, see also Table 6.4.

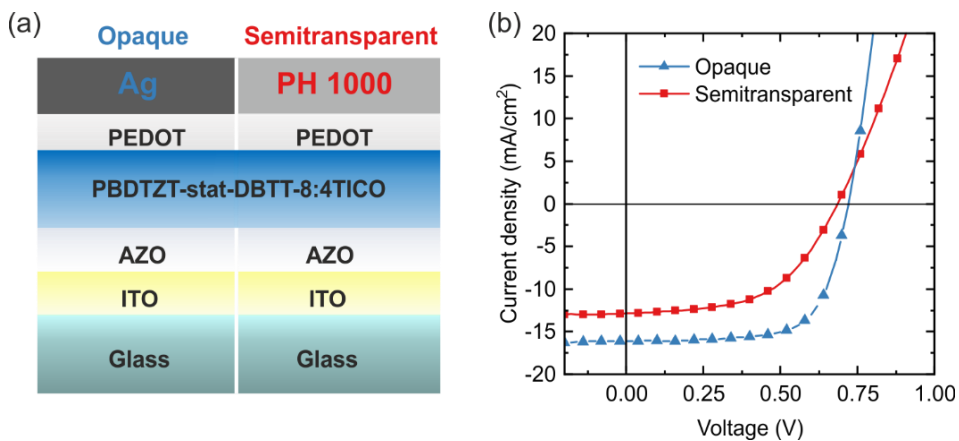


Figure 6.5. Comparison between opaque and semitransparent (ST) electrodes. (a) Sketch of the device architectures and (b) JV characteristics of both devices.

The optimum PAL thickness is mainly governed by the trade-off between fill factor (FF) and short-circuit current density (J_{sc}), having a minor effect the reduction in open-circuit voltage (V_{oc}). On one side, opaque devices yield FF and J_{sc} values of 68.7% and 16.5 mA/cm², respectively; on the other side, ST devices show values of 48.2% and 13.3 mA/cm², for the same parameters. A significant drop of 30%, in the case of FF, and 20%, in the case of J_{sc} , is observed when comparing ST and opaque devices. The drop affecting the FF in ST devices could be explained by the combination of three factors.

The first element to be considered is the back reflection at the electrode. The evaporated silver electrode introduces an optical enhancement effect in opaque devices. Incoming light is multiple-times absorbed in the PAL due to the reflection at the mirror-like silver layer, thus enhancing the overall absorption in the PAL. In ST devices, by contrast, the less pronounced back reflection is compensated with an increase of the absorber layer. Hence, increasing J_{sc} unavoidably sacrifices the FF due to limited transport properties.

As a consequence of the halved optical path in ST devices, thicker PALs tend to inherently have lower FF, especially in systems with limited mobility. Charge recombination processes are more likely to happen before charge collection occurs. Despite the moderately high mobility of the polymer,^[259] this effect is non-negligible in the resulting optimum PAL thicknesses with 100 nm for opaque devices and 200 nm for ST devices. Additionally, the replacement of fullerene derivatives with NFAs might also limit the mobility in the PAL.^[262]

The second factor is the electrical conductivity of the top electrode, which determines the charge collection efficiency. There are three orders of magnitude difference between the electrical conductivity of PH1000 (10^4 S/m) and evaporated silver (10^7 S/m).^[263] In a previous work, the effect introduced by the electrical resistivity of the ST electrode material was estimated to be responsible for more than 70% of the electrical losses in FF.^[256]

In terms of efficiency, the observed drop is from 6.7% to 4.4% in the transition from opaque to solution-process semitransparent devices. A similar decrease in performance from 6% to 3.8% was recently reported using the same polymer, PBDTZO-stat-DBTT-8, blended with a fullerene acceptor.^[264]

Table 6.4. Photovoltaic parameters of the optimised opaque and semitransparent (ST) solar cells. Statistics of 8 devices. The values of the champion devices are in brackets.

| Type | V_{oc} (V) | J_{sc} (mA/cm ²) | FF (%) | PCE (%) | Thickness (nm) | HPT (%) |
|-----------------|---------------------|-----------------------------------|--------------------|------------------|-------------------|------------|
| Opaque | 0.72±0.01 (0.72) | 16.5±0.6 (16.1) | 68.7±0.1 (68.8) | 7.6±0.3 (8.0) | 95 | 0 |
| Semitransparent | 0.69±0.01 (0.69) | 13.3±0.3 (12.9) | 48.2±2.8 (53.3) | 4.4±0.2 (4.7) | 210 | 15 |

In that case, silver nanowires (Ag NW) embedded in a matrix of PEDOT:PSS were used as the top electrode.^[264] In other cases, a bilayer of Ag NW on top of PEDOT:PSS was reported to potentially improve the electrode conductivity by one order of magnitude, yet retaining the transparency of the device.^[63,166] These pieces of evidence demonstrate that further investigations on highly conductive ST electrodes could be important in order to reduce the electrical losses associated with the top electrode, and consequently improve the PCE. Ideally, one of the prerequisites for a potentially scalable OPV system is thickness-performance insensitivity to mitigate the drop in performance upon the intrinsic thickness variations associated with large-scale printing techniques (c.f. slot-die).^[153,265] In order to evaluate this feature in the proposed PBDTZT-stat-DBTT-8:4TICO system, devices with PAL thicknesses from 50 to 300 nm were manufactured. PAL was cast varying the blade speed from 2 to 30 mm/s. Please refer to Appendix C for the specific manufacturing details.

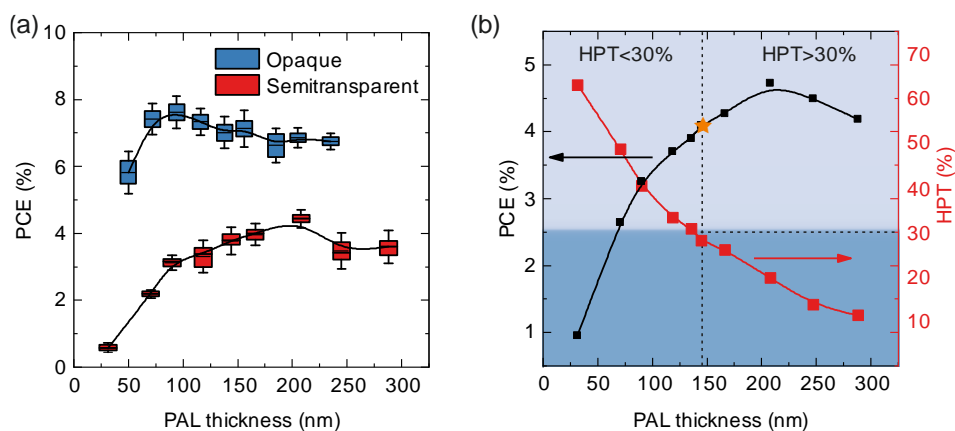


Figure 6.6. Performance (PCE) as a function of the thickness of the PAL. (a) Comparison of opaque and semitransparent devices. (b) PCE of the best ST devices and their calculated transparency measured with the human perception transmittance (HPT).

This small thickness-performance dependence is demonstrated by 70% of opaque and 65% of ST devices loss less than 10% in the PAL range between 100 and 200 nm with respect to their maximum performance. Therefore, the thickness-performance tolerance of PBDTZT-stat-DBTT-8:4TICO suggests that this system is a potential candidate for upscaling (Figure 6.6(a)).

We calculated the degree of transparency with HPT metric (see more details in section 2.4.2), of the full ST stack as a function of the PAL thickness, see Figure 6.6(b). As expected, the HPT decreases inversely proportional to the PAL thickness. Considering the target HPT value for BIPV (transmittance $\geq 30\%$, see Table 6.1) as a minimum requirement, the studied OPV system could deliver performances over 4.1%. Although the best performing ST devices have 200 nm thickness PALs, the HPT of those devices is 20%, which is below the mentioned target of 30% HPT. Consequently, the maximum PAL thickness was reduced down to 150 nm in our subsequent experiments. We believe that this could improve further by engineering the top electrode with more conductive ST materials. Further details about the device transparency in Appendix B.

6.4 Laser-patterned modules

The preliminary upscaling study towards ST modules was carried out following the same optimised stack for ST lab cells (ITO/AZO/PAL/PEDOT/PH1000) while fulfilling the requirements of Table 6.1 (HTP<30%, max. PAL thickness=150 nm). In the following section, the laser patterning steps and their optimisation (P1, P2, P3) are discussed.

6.4.1 Cell-to-cell interconnection

The sequential coating (AZO, PAL, PEDOT and PH1000) and ablation steps ([P1], [P2] and [P3]) needed for subcell series-interconnection are given in Figure 6.7 (ITO/[P1]/AZO/PAL/PEDOT/[P2]/PH1000/[P3]). In particular, ITO is structured with P1 laser ablation, followed by coatings of AZO, PAL and PEDOT, then P2 structuration followed by PH1000 coating and finally P3 structuration of the top electrode.

The module prototype consists of 3 or 4 individual subcells that are monolithically interconnected in series with an area of around 1 cm² (the exact value depends on the cell length and the number of connected cells). Figure 6.8(a) depicts a schematic cross-section of the module design shown in Figure 6.8(b).

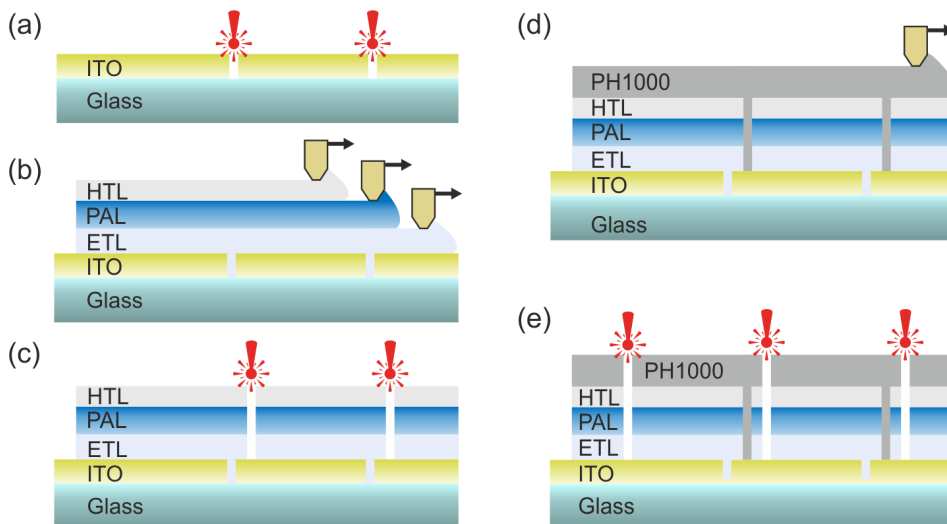


Figure 6.7. Sequential steps for monolithic cell-to-cell interconnection. (a) P1 ITO ablation, (b) coatings of ETL, PAL and HTL, (c) P2 ablation of ETL, PAL and HTL, (d) PH1000 coating and (e) P3 ablation of ETL, PAL, HTL and PH1000.

With this design, either 2 or 4-subcell modules (maximum 3 subcells in case of 4 mm- L_{cell} modules) can be assessed independently, thus enabling a more flexible evaluation of the module performance. The interconnection length (L_i , see Figure 6.8(a,d)), dead area when multiplied by the width of the module (w_{cell}), accounts for the distance between the P1 and P3 resulting grooves. Despite not using an advanced optically assisted nor a XY motorised positioning system, a remarkable interconnection length of 300 μm (Figure 6.8(c)) was achieved. This low interconnection length is benchmarked within the state-of-the-art of publications (100-400 μm) where femtosecond or nanosecond lasers were employed.^[166,266] This is crucial to achieve modules with high GFF. We demonstrate that OPV modules can be patterned with a microsecond industrially-compatible laser equipment. Before the monolithic interconnection of cells that make up the module, films were ablated with an industrially compatible laser equipment pumping at 1064 nm and a minimum pulse width of 1 μs (for more details about the equipment, please refer to 2.2.2.3).^[116]

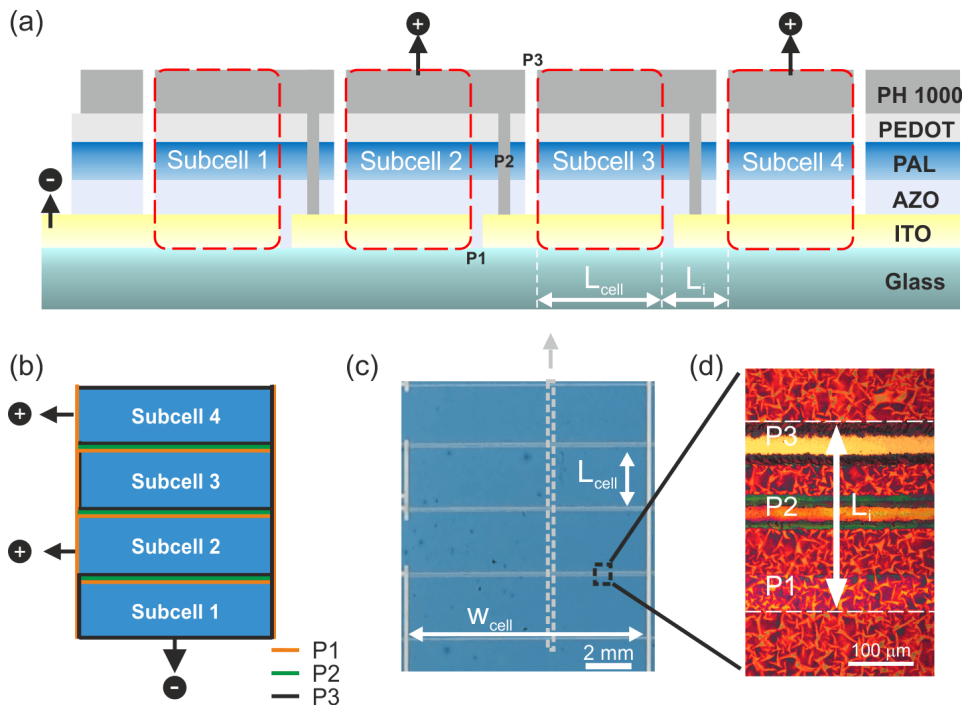


Figure 6.8. Laser-patterned modules. Scheme of the (a) cross-section and (b) top-view of 4 monolithically interconnected (P1-P2-P3) subcells in a module. (c) Top-view image of a module with 4 subcells connected in series (d) Microscope image of the module interconnection (L_i) P1-P2-P3.

Prior to the monolithic interconnection of cells that make up the module, films were ablated with an industrially compatible laser equipment pumping at 1064 nm and a minimum pulse width of 1 μs (for more details about the equipment, please refer to chapter 2).^[116] As ITO and PEDOT strongly absorb at 1064 nm ($k_{\text{ITO}}=0.013$ and $k_{\text{PEDOT}}=0.1$), the whole ablation process is driven by both materials. This implies, in the simplest case, the full ITO sublimation (P1) or controlled heating of ITO and PEDOT to carefully remove the layered stack above ITO (P2 and P3).

6.4.2 Combinatorial optimisation of laser patterning parameters

The use of a general combinatorial method enabled us to rapidly screen the laser parameters space for P1, P2 and P3 in a cost-effective way, as depicted in Figure 6.9(a). The ablation power (laser power), the laser overlapping factor (Figure 6.9(b)) and the focus distance are the most influent laser parameters for the final ablation.

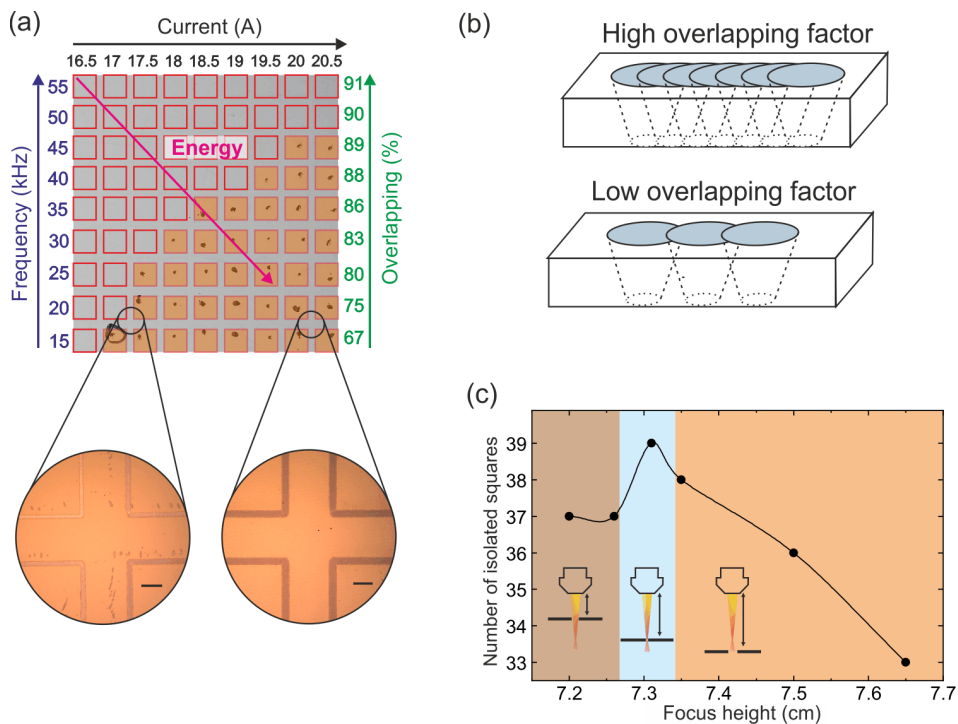


Figure 6.9. General combinatorial method for the optimisation of the laser patterning parameters. (a) Frequency-power laser matrix on ITO film. The dot-marked squares are electrically isolated (higher electrical resistance than 15 M Ω). The patterned substrate is 5x5 cm. Zoomed microscope image of the patterned grooves. The scale bar corresponds to 200 μm . (b) Sketch of the laser overlapping factor. (c) The optimisation process of the focus distance based on the number of isolated squares.

While the applied current controls the incident laser power, the laser repetition (frequency) is a way to control the overlapping factor, see Figure 6.9(b). Other laser parameters that affect the overlapping factor, pulse width (1 μ s), laser speed (100 mm/s) and theoretical line width (20 μ m) were fixed. Taking advantage of the flexibility displayed by laser-based processes, 81 different laser parameters combinations were tested on a single substrate by sweeping the laser power (16.5-20.5A) and frequency (15-55 kHz).

Due to the fact that the employed laser delivers constant power in a fixed time-slot but not in each pulse, the ablation energy increases proportionally with current and inversely proportional with the overlapping factor as the delivered energy is divided between the number of pulses in a given slot of time. For a fixed laser current (power), the laser frequency is reduced (lower overlapping factor) and the delivered energy increases in each pulse, and consequently the ablation power. This effect is demonstrated in Figure 6.9(a).

6.4.2.1 P1 ablation

P1 ablation consists of the ITO removal for the structuration of the bottom electrode. Moreover, P1 is the least critical patterning step since there is no sensitive layer underneath. P1 aims to electrically isolate ITO stripes. The success of the ITO ablation was validated by measuring the electrical resistance between adjacent ITO stripes and considering 15 M Ω as the threshold for a complete ITO isolation.

As an example of the combinatorial method, P1 laser parameters were optimised as shown in Figure 6.9(a). Only 39 out of 81 laser-patterned squares were electrically isolated (electrical resistance higher than 15 M Ω). Despite several combinations of frequency and current lead to electrical isolation of ITO, the feature of grooves are also relevant to avoid cross-talking and short circuits. Generally, lower overlapping factors (60%) and higher applied currents (20 A) lead to electrically isolated and well-defined grooves. Too high laser power results in wider grooves having a detrimental impact on the length of the module interconnection area, and thus lower GFF. Indeed, an extremely high power could eventually damage the substrate, that in the case of flexible plastic

could even break it. Ideally, P1 should be narrow enough as long as it ensures effective structuration at the back electrode (ITO).

In the same way, the P1 ablation step was employed to optimise the sample-laser distance by maximising the number of isolated squares of the frequency-power matrix. 6 different sample-laser distances were scanned (Figure 6.9(c)) being 7.3 cm the best laser powerful distance. This optimised distance for P1 was kept constant for patterning P2 and P3. A detailed optimisation process of the laser parameters was carried out in order to minimise the patterned width, and thus the interconnection length between cells and the GFF. The characterisation techniques employed to assess the quality of the P1 ablation were microscope images, photoluminescence (PL) and light reflection maps (Figure 6.10); and profilometry (Figure 6.11). The microscopes images reveal a good correlation with reflection maps upon an increase in laser power.

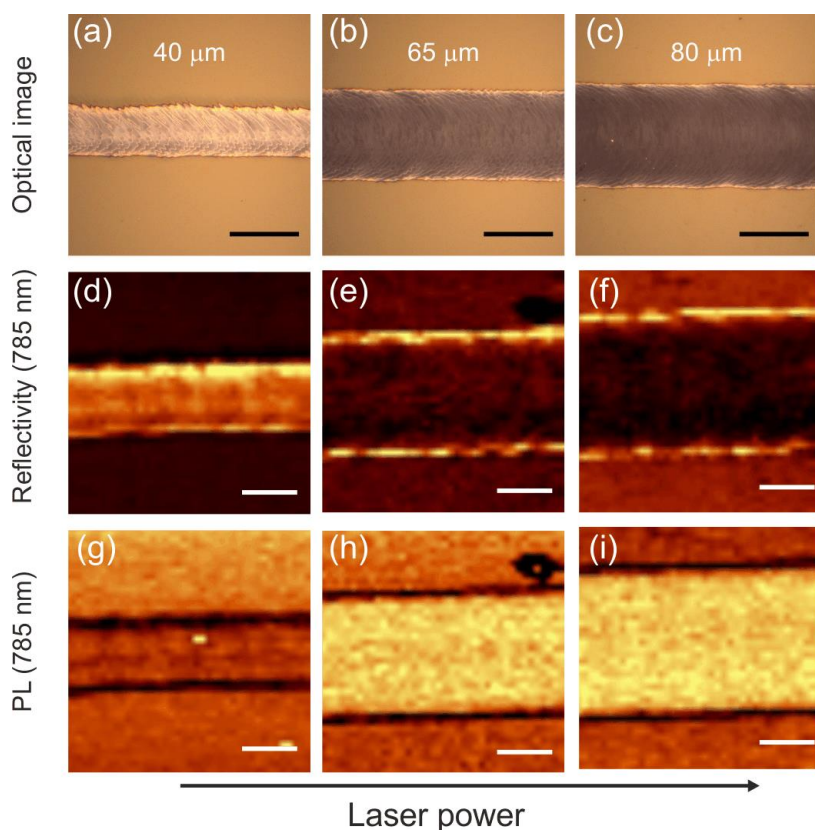


Figure 6.10. Optimisation of P1 with increasing laser excitation power. Microscope images of laser patterned lines (a,b,c), laser reflectivity at 785 nm (d, e, f) and PL (g, h, i) maps of laser patterned ITO with different laser ablation power: 16 A (a), 18 A (b) and 20 A (c). The black scale bar corresponds to 50 μm and the white to 30 μm.

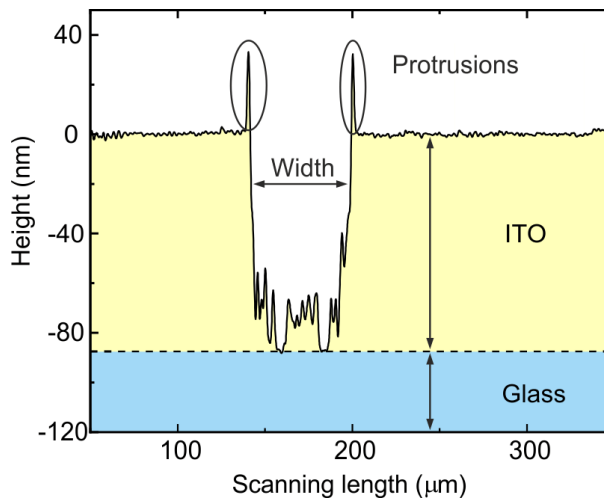


Figure 6.11. Feature of the laser-patterned groove. Groove profile of the optimised P1 groove measured with the mechanical profilometer.

A high enough applied laser power removes completely ITO thickness layer, as proven by the PL and reflection maps (Figure 6.10(e,f,h,i)). By contrast, when laser power is too low, an incomplete ITO removal is obtained, and thus not electrical isolation (Figure 6.10(d,g)). The reflection maps reveal higher ITO signal at the edges of the grooves than in the central part. This fact is well correlated with the presence of spikes at the edge of the groove resulting from the ITO ablation, as observed in the measured profiles (Figure 6.11). These protrusions are unavoidable since are collateral effects of the ITO sublimation. However, the height of those spikes does not exceed 40 nm, and hence the impact of these spikes is minimised since they are fully covered by the subsequent AZO layer which has 40 nm of nominal thickness.

6.4.2.2 P2 and P3 ablation

P2 and P3 patterning steps, however, are more challenging than P1 as they require a precise ablation of the target layers without damaging the ITO underneath. An excessive laser power would reduce dramatically the ITO electrical conductivity, and consequently the module performance (Figure 6.12(c,f)). The P2 patterning step provides a path for the interconnection between the top and bottom electrode, accomplished upon PH1000 coating (Figure 6.12(a,b,c)).

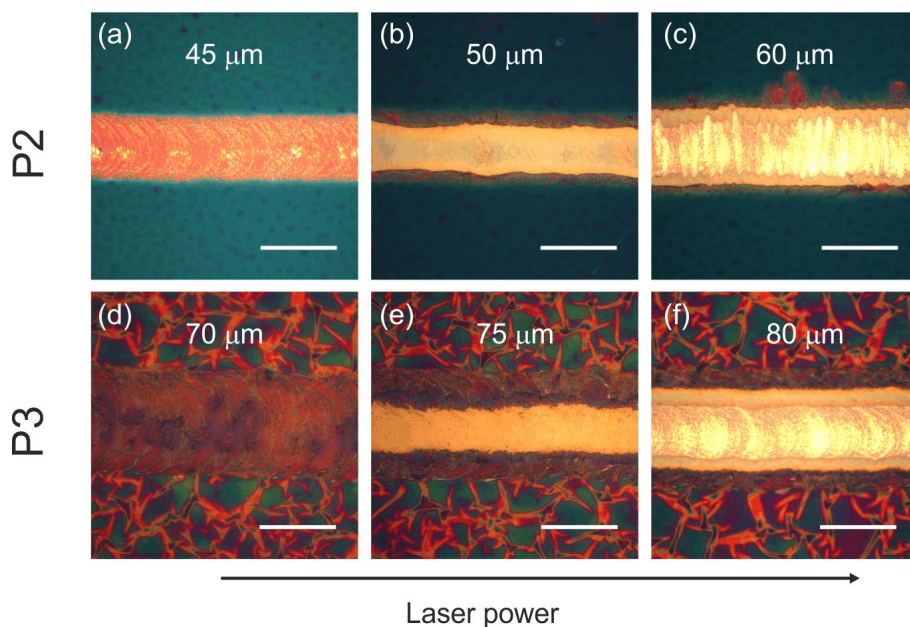


Figure 6.12. P2 and P3 optimisation of laser patterning conditions. Microscope images of laser patterned lines with increasing laser excitation power, which increases the groove width (values in the pictures) (a,b,c) P2 (Glass/ITO/ETL/PAL/HTL) and (d,e,f) P3 (Glass/ITO/ETL/PAL/HTL/PH1000). The scale bar corresponds to 50 μm .

Finally, P3 is equivalent to P1 but electrically disconnecting the top electrode, intending to define the individual subcells Figure 6.12(d,e,f). The optimised widths of the patterned grooves were 65 μm , 51 μm and 74 μm , for P1, P2 and P3, respectively, see Table 6.5.

As a final step, we evaluate the robustness of the optimised P2 laser patterning conditions upon PAL thickness variations because P2 together with P3 are the most challenging patterning steps. Figure 6.13 displays satisfactorily patterned PALs of 120 nm, 140 nm (reference) and 160 nm with the same ablation parameters shown in Table 6.5.

Table 6.5. Fine-tuned values for the laser patterning of P1, P2 and P3.

| Ablation step | Current (A) | Overlap (%) | Frequency (kHz) | Speed (mm/s) | Nominal line width (mm) | Pulse width (μs) | Groove width (μm) |
|---------------|-------------|-------------|-----------------|--------------|-------------------------|-------------------------------|--------------------------------|
| P1 | 18 | 33 | 15 | 100 | 0.01 | 1 | 65 |
| P2 | 18.1 | 90 | 100 | 100 | 0.01 | 1 | 51 |
| P3 | 17.5 | 90 | 100 | 100 | 0.01 | 1 | 74 |

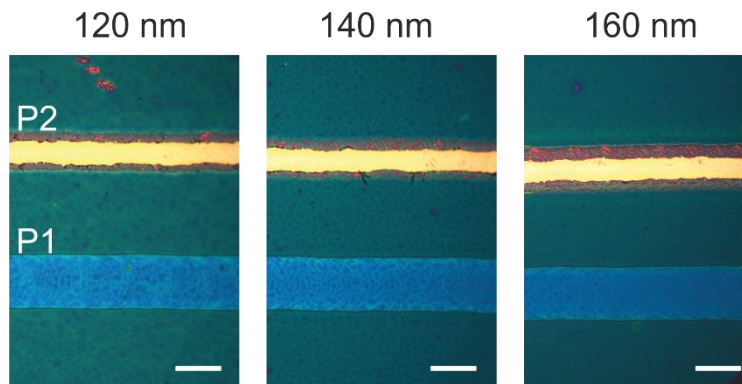


Figure 6.13. Microscope images of the laser patterned organic films for photoactive layer thicknesses. Scale bar corresponds to 50 μm .

Although the groove width is narrower for the thicker film (160 nm) compared to the thinner film (120 nm), the resulting modules with those PALs are functional (see section 6.4.6 for further discussion). This demonstrates that the optimised patterning conditions for 140 nm PAL thickness can be applied within variations of 20 nm. Therefore, it is demonstrated not only PAL thickness-performance tolerance but also a PAL thickness tolerance with the optimised laser parameters.

6.4.3 Optoelectronic characterisation of modules

To evaluate the quality of the module interconnection and the ST module performance, advanced optoelectronic measurements were carried out. More specifically, simultaneous Raman scattering and laser beam induced current (LBIC) maps were measured at 488 nm excitation wavelength in order to correlate the electrical performance with the film morphology.^[V] Additionally, photoluminescence (PL) and photocurrent maps (LBIC) were acquired at 785 nm excitation wavelength. Due to the complementary absorption of the photoactive materials, co-local maps measured at 488 nm correspond mainly to PBDTzT-stat-DBTT-8, whereas 785 nm maps to 4TICO. To facilitate the analysis of the co-local measurements, the scanned area in Figure 6.14 is divided into five different areas: (**Area 1**) full cell stack but electrically disconnected from the subcell, (**Area 2**) P3 groove defining the start of the photoactive area, (**Area 3**) photoactive area also known as subcell, (**Area 4**) cell-to-cell interconnection (P1, P2, P3) (**Area 5**) full stack of photoactive material belonging to the following subcell, equivalent to (**Area 3**) but not evaluated in this measurement.

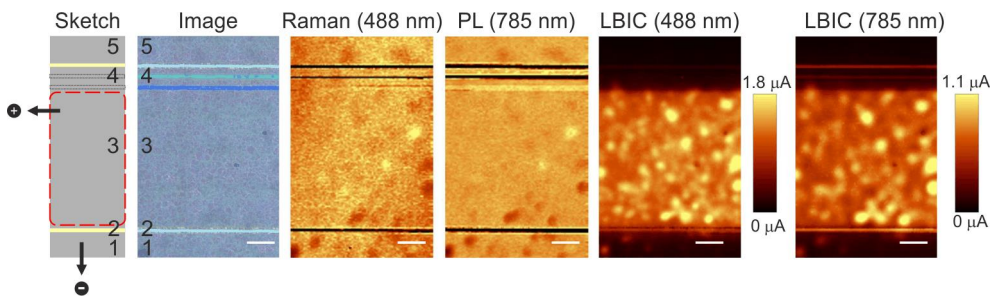


Figure 6.14. Co-local optoelectronic characterisation on a subcell at different wavelengths. (from left to right) Top view sketch, optical image, Raman map excited at 488 nm, PL map excited at 785 nm, LBIC map at 488 nm and 3 mW, and LBIC map at 785 nm at 1 mW. Area legend in the optical image: (1) and (5) non-connected part of the subcell, (2) P3, (3) active area of the subcell and (4) cell interconnection (P1, P2, P3). Scale bar corresponds to 400 μm .

Both Raman and PL maps indicate that **Areas 1** and **5** have the same layered stack as the rest of the module. The fact that such areas are electrically disconnected from the evaluated subcell, is confirmed by the negligible electrical signal exhibited by these areas in both photocurrent maps. Hence, we conclude that the P3 groove (**Area 2**) was well performed since electrical isolation is obtained without damaging the ITO layer underneath. Moreover, P3 defines one edge of the active area, see Figure 6.8(a). The Raman and PL signals in **Area 2** are dramatically low compared to the rest of the module, proving an effective removal not only of PH1000 but also of the PAL. Surprisingly, the electrical contribution of P3 (**Area 2**) is not as low as, one would expect, as seen in both photocurrent maps. Since there is no photoactive material in **Area 2**, the photocurrent enhancement in this region is believed to be an artefact of the measurement originated from scattered light at the rough interconnect which might even waveguide light into the neighbouring PAL. The quality of P3 removal is also shown in the top groove (P3) of **Area 4** exhibiting the same features as P3 in **Area 2**. This finding indicates a spatial reproducibility of the laser patterning procedure.

In **Area 3**, which corresponds to the active area of the subcell, Raman and PL maps show a rather homogenous distribution of photoactive material (thickness and composition) derived from the blade-coating process. Both Raman map and the optical image depict a similar granulated texture appearance. We attribute this to a morphological effect of the PH1000 top electrode rather than to the contribution of the PAL, since this texture is not visible in the PL map, and thus is not related to absorption or other optical effects.

Furthermore, this is supported by the magnified optical microscope image in Figure 6.8(d) which reveals a polycrystal-like structure of PH1000. Additionally, the darker spots in both Raman and PL maps may suggest small thickness reduction leading to lower Raman and PL intensities. These thinner areas are well correlated with the higher photocurrent areas measured in the LBIC maps. Note that, both LBIC photocurrent maps (at 488 nm and 785 nm) exhibit the maximum and minimum performance points in the same positions, thus confirming a similar donor and acceptor contribution.

The complete monolithic cell-to-cell interconnection (**Area 4**, P1-P2-P3) is easily distinguishable with the 3 parallel grooves. The P1 patterning removes the ITO and is followed by the coating of the ETL/PAL/HTL layers, hence they are responsible for the signal detected in the PL and Raman maps in P1. This, however, is slightly lower than in the rest of the image due to the lack of back reflection from the glass compared to the ITO layer. Additionally, P1 delimits the photocurrent generation area, see LBIC maps in Figure 6.14. The absence of signal from the photoactive materials in the Raman and PL maps in Area 4 proves the success of P2 and P3 patterning. The small contribution in P2 and P3 observed in the 785 nm LBIC map is ascribed to light scattering. As it will be shown later these non-expected photocurrent areas disappear when using white light illumination. These results confirm that the laser patterning of the module interconnection was satisfactorily performed, leading to a well-defined active area of the subcells.

6.4.4 Geometrical parameters of modules

Once validated the laser patterning process and the subcell operation, the following step is to explore ways to maximise the geometrical fill factor (GFF). Three relevant geometrical parameters have a direct influence on the module GFF (Eq. 6.1): the cell length (L_{cell}), the interconnection length (L_i) and the number of the interconnected cells (N_{cell}), see Figure 6.8(a).

$$GFF = \frac{A_{active}}{A_{total}} = \frac{L_{cell} \cdot w_{cell} \cdot N_{cell}}{L_{cell} \cdot w_{cell} \cdot N_{cell} + L_i \cdot w_{cell} \cdot (N_{cell} - 1)} = \frac{L_{cell} \cdot (N_{cell})}{L_{cell} \cdot N_{cell} + L_i \cdot (N_{cell} - 1)} \quad (6.1)$$

Note that the GFF is independent of the cell width (w_{cell}), being the only relevant geometrical parameters those in the charge transport direction within the PAL. On the

other hand, w_{cell} directly influences the active area size of the device. As a result, a simple and effective strategy to increase the active area of the module, unaffected the rest of the module geometrical parameters, is to increase the cell width. For the L_{cell} -PCE module sensitivity analysis, ST modules with L_{cell} values of 2 mm, 3 mm and 4 mm were manufactured. This is a relevant milestone for the upscaling of this system.

Table 6.6 shows the influence of L_{cell} on the photovoltaic performance parameters of modules. The V_{oc} values of the modules scale proportionally with the number of series interconnected subcells and do not depend on the length of the subcell (L_{cell}), thus indicating an efficient sequential coating and laser patterning steps. On the one hand, a small reduction in the J_{sc} ($< 1 \text{ mA/cm}^2$) is observed when L_{cell} is increased from 2 mm to 4 mm. This minor J_{sc} reduction could be explained as small thickness variations in sample-to-sample as suggested by the small variations of HPT values. Interestingly, comparing modules with lab cells, the J_{sc} values are not affected ($\approx 11 \text{ mA/cm}^2$) when increasing the active area from 0.08 cm^2 (lab-cell) to 1.1 cm^2 (largest module).

On the other hand, the 2 mm- L_{cell} module shows the highest FF (50.2%), similar to the single devices (50.5%). By contrast, FF is reduced to 44.8% and 43.7% for modules with 3 mm and 4 mm- L_{cell} , respectively. This important FF- L_{cell} dependence is expected as the transport path increases with L_{cell} . This transport-related limitation could be diminished by enhancing the electrical conductivity of the electrodes, which would allow to further increase L_{cell} , thus improving GFF of the module. Again, the limited electrical conductivity of the top electrode is the main responsible of the limited L_{cell} as occurred in the lab-cell section with a noticeable drop in performance in the transition from opaque to semitransparent devices. Considering that the sheet resistance of the top electrode PH1000 is 20 times higher than the bottom ITO electrode, the performance-geometry dependence points to the limited conductivity of PH1000 as the bottleneck for the upscaling of this system.^[256]

Still considering L_{cell} variations, we can see that the overall module PCE is not as sensitive as the FF, since performances over 3.8% were achieved for both 2 and 3 mm- L_{cell} values (Figure 6.15). However, the performance of the 4 mm- L_{cell} modules drops to 3.3% mainly attributed to a low FF.

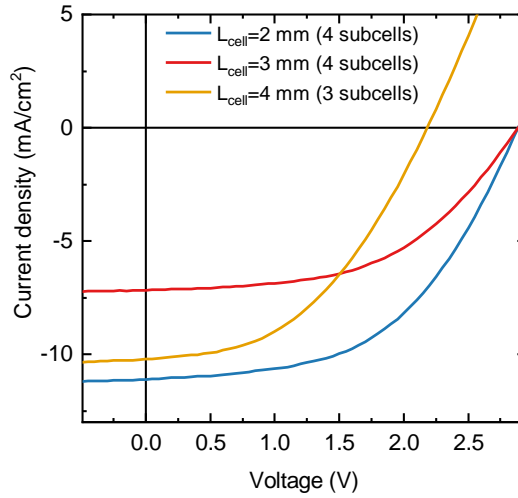


Figure 6.15. JV characteristics of modules with 2, 3 and 4-mm L_{cell} .

Remarkably, 2 and 3 mm- L_{cell} modules reach similar performances to single cells, despite a 9 and 14-fold increase in the active area, respectively with respect to single cells. Consequently, the study allows us to define the cell dimensions so that the module design has a negligible impact on the PCE. We conclude that 90% GFF milestone set at the beginning of this chapter is achieved for two module configurations (3 and 4 mm- L_{cell}). Moreover, these GFF values are similar to the state-of-the-art of laser-patterning modules (90-95%) but using a microsecond and low-cost laser equipment. Moreover, the module high transparency exhibited by this system together with the reliability of the laser patterning approach employed as a potential combination for upscaling semitransparent devices. Finally, further developments in ST electrodes are required to reduce the drop in PCE upon the replacement of evaporated electrodes. Similarly, a more conductive ST electrode would enable to manufacture larger L_{cell} subcells without affecting the FF, and consequently improving the GFF values.

Table 6.6. Photovoltaic ST modules and lab-cell (reference) parameters as a function of the cell length (L_{cell}). The first values refer to the average and standard deviation of four modules while the numbers in brackets refer to the best performing module. The thickness of the photoactive layer was fixed to 120 nm. * AA_{module} corresponds to the active area of a single cell. ^a Refers to the individual subcell assessment of JV curves from Figure 6.19.

| L_{cell} (mm) | N_{cell} | V_{oc} module (V) | V_{oc} subcell (V) | I_{sc} module (mA) | J_{sc} subcell (mA/cm ²) | FF (%) | PCE (%) | GFF (%) | HPT (%) | AA_{module} (cm ²) |
|---------------------------|-------------------|-------------------------------|--------------------------------|--------------------------------|--|----------------------|--------------------|-------------------|-----------------|--|
| 2 | 4 | 2.88 ± 0.02 (2.88) | 0.72 ± 0.01 (0.72) | 1.95 ± 0.05 (1.98) | 10.9 ± 0.3 (11.1) | 50.2 ± 0.3 (51.5) | 3.9 ± 0.1 (4.1) | 87.6 | 35 | 0.71 |
| 3 | 4 | 2.89 ± 0.03 (2.89) | 0.73 ± 0.01 (0.72) | 3.11 ± 0.10 (3.24) | 11.3 ± 0.4 (11.8) | 44.8 ± 0.3 (45.7) | 3.8 ± 0.1 (3.9) | 92.2 | 35 | 1.10 |
| 4 | 3 | 2.18 ± 0.02 (2.19) | 0.72 ± 0.01 (0.72) | 3.72 ± 0.05 (3.70) | 10.3 ± 0.4 (10.3) | 43.7 ± 0.3 (45.5) | 3.3 ± 0.1 (3.4) | 93.2 | 35 | 1.01 |
| 2 ^a | 2 ^a | 1.45 ^a | 0.73 ^a | 2.4 ^a | 11.8 ^a | 47.3 ^a | 4.1 ^a | 84.7 ^a | 30 ^a | 0.397 ^a |
| 2 ^a | 4 ^a | 2.81 ^a | 0.70 ^a | 2.4 ^a | 12.0 ^a | 48.7 ^a | 4.1 ^a | 84.7 ^a | 30 ^a | 0.794 ^a |
| Single cell (Ref) | 1 | - | 0.69 ± 0.05 (0.69) | - | 11.1 ± 0.4 (11.1) | 50.5 ± 2.8 (53.4) | 3.9 ± 0.2 (4.1) | - | 33.4 | 0.08* |

6.4.5 Geometry optimisation by co-local techniques

In order to gain insight into the L_{cell} -PCE dependence, we studied the 2, 3 and 4 mm- L_{cell} modules by means of co-local optoelectrical imaging (Figure 6.16). For the sake of the visualisation of the micron-sized features, we assessed only one of the subcells of the module, as it was done in Figure 6.14, taking advantage of the flexibility of the module layout.

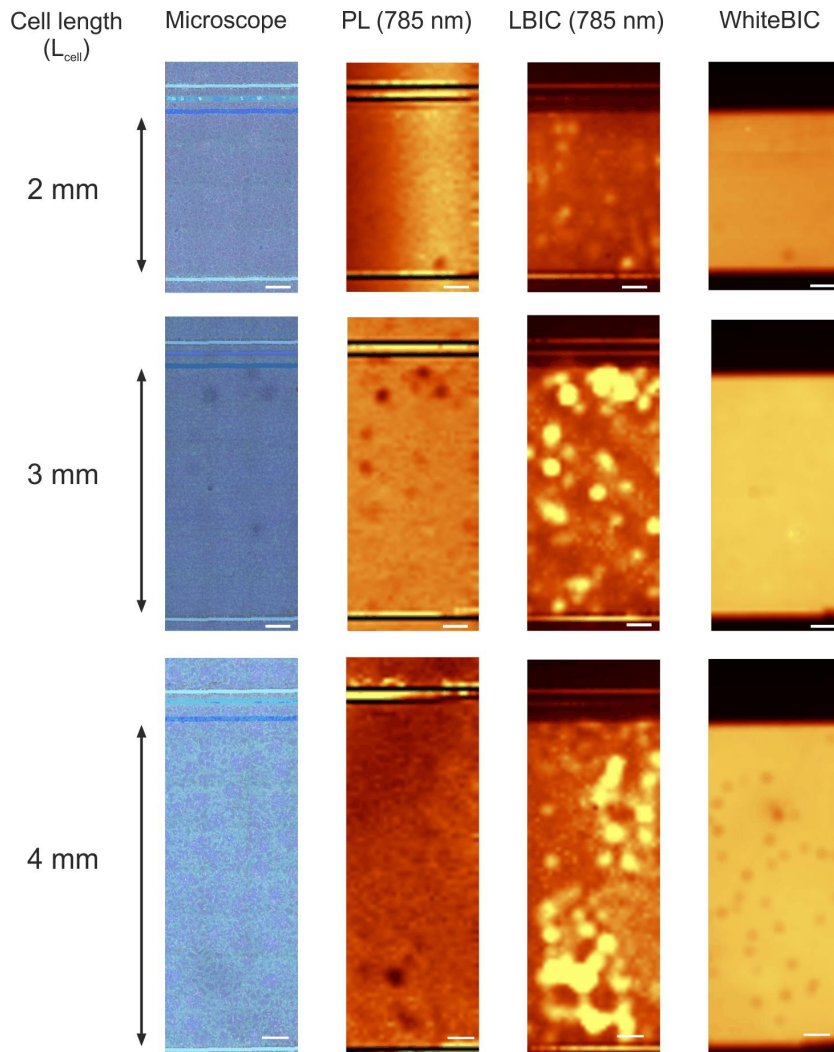


Figure 6.16. Geometry optimisation via co-local electrical and optical mapping. Microscope image, photoluminescence (PL), laser beam induced current (LBIC) excited at 785 nm and with white light LBIC (*whiteBIC*) maps of laser-patterned modules with cell lengths of 2, 3 and 4 mm. The white scale bar corresponds to 300 μm . The scanned width (w_{cell}) was in all cases 1.6 mm. LBIC maps are normalised respect to the 3 mm- L_{cell} module.

In particular, we acquired PL and LBIC maps, together with the photocurrent map using the microscope white light illumination as illumination source also known as *whiteBIC*, similarly as performed in section 4.7.2. *WhiteBIC* photocurrent maps allow us to determine the active area of the module without scattering artefacts. Indeed using broadband light excitation, the *whiteBIC* technique does not generate scattered light and light guiding effects at the patterned grooves (see photocurrent maps in Figure 6.14 and Figure 6.16), owing to the larger spot size of the light beam and the larger focal length with different wavelengths.

To extend the analysis of the co-local maps in the charge transport direction, Figure 6.17 shows the averaged cross-section along the L_{cell} of each of the maps extracted from Figure 6.16.

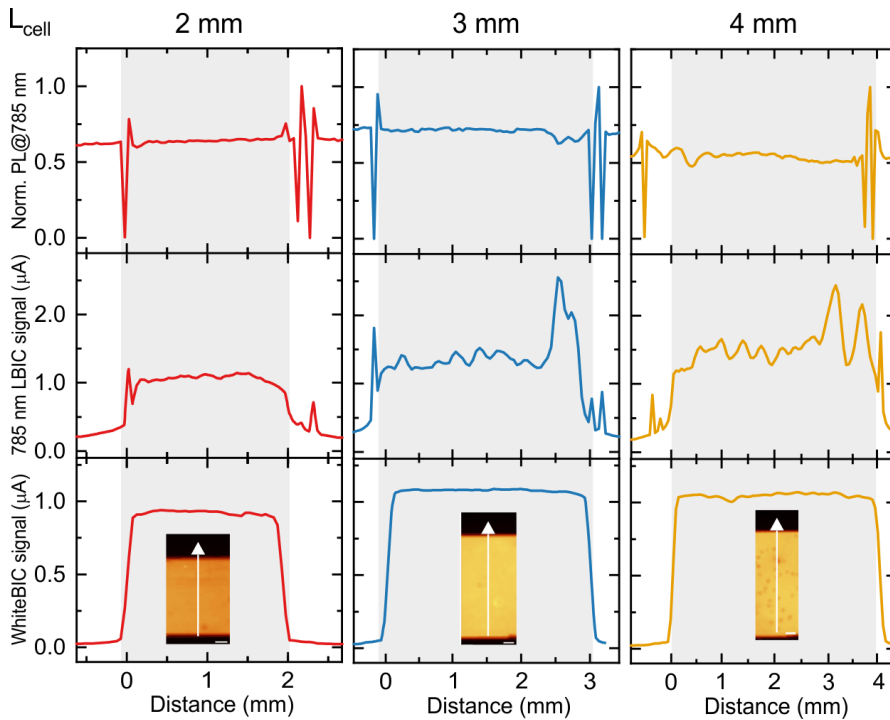


Figure 6.17. Transversal cross-section images from Figure 6.16. Normalised PL, 785 nm LBIC and *whiteBIC* maps for 2, 3 and 4 mm- L_{cell} modules. Inset: *WhiteBIC* maps with an arrow pointing the direction of the averaged cross-section. The grey rectangle is a guide to identify the subcell length.

The co-local maps have some features in common for all L_{cells} of the module. First, despite the large variations of L_{cell} , there is no photocurrent drop along the *whiteBIC* cross-section (Figure 6.17). The homogenous distribution of the photocurrent throughout the L_{cell} suggests that charge collection is independent of module geometry. Second, the black parallel lines at the top of the PL maps in Figure 6.16 are again an indication of an efficient patterned P2 and P3 grooves. This proves the reliability and reproducibility of the patterning process regardless of the module design. Third, the darker areas observed in the PL maps are well correlated with areas of higher photocurrent in the 785 nm LBIC maps but not in the *whiteBIC* photocurrent maps. This could be partially attributed to scattered laser light (defects) since some of the spots are well correlated with dark spots in the microscope image. However, these areas do not have a detrimental effect on the *whiteBIC* photocurrent maps.

Note that, the *whiteBIC* maps also reveal a reduction of the photocurrent at the edge of the PAL. As it can be identified in the P3 magnified microscope image of Figure 6.8(d), this is caused by the burning of the organic material around the edges upon laser patterning. This effect is also visible in the PL maps of Figure 6.16 as well as in the peaks of the PL cross-section (Figure 6.17), associated with a higher PL signal at the groove edges. However, this small reduction of the effective L_{cell} of less than 20 μm is negligible since it only corresponds to a 2.3% area loss in the case of 3 mm- L_{cell} modules.

On the other hand, there are some differences depending on the cell length. For the 2 mm- L_{cell} modules, both PL and 785 nm photocurrent map cross-section show very smooth and flat characteristics revealing a homogenous coating distribution of the photoactive material (Figure 6.17). The profiles are less smooth for the 3 and 4 mm- L_{cell} modules. In particular, the 3 mm- L_{cell} module exhibits the highest *whiteBIC* signal, in agreement with the photovoltaic parameters in Table 6.6, closely followed by the 4 mm- L_{cell} modules.

To sum up, we confirmed the great potential of the use of co-local and non-invasive imaging techniques for the characterisation and optimisation the ST laser patterned modules. We could identify the best module design by combining PL mapping, which assesses the photoactive material properties, together with local photocurrent maps at different excitation wavelengths to evaluate the local performance. In particular, we found that the 3 mm- L_{cell} module is the most suitable design showing excellent coating

homogeneity and performance, while at the same time fulfilling the initial target requirements for upscaling at the beginning this chapter (Table 6.1). More specifically, this module design yields over 90% of GFF while at the same time exhibiting 34% of HPT. Overall, the performance of the ST modules (3.8%, over 1.1 cm²) is as good as in small ST devices (3.9%, 8 mm²). This confirms that the developed laser patterning process is suitable for upscaling the OPV.

6.4.6 PAL thickness tolerance in modules

As it was highlighted before, thickness variations are very likely to occur in large scale printing processes. Previously, we proved that the optimised laser parameters are PAL thickness insensitive in the range from 120-160 nm, see Figure 6.13. Afterwards, we checked the thickness dependence on the performance of modules. To do so, we manufactured modules with 4-serially interconnected subcells with different photoactive layer thicknesses ranging from 120 to 160 nm (Table 6.7). As seen in lab-cell devices, J_{sc} increases from 8.7 to 11.8 mA/cm² as the PAL get thicker going from 120 nm to 160 nm, respectively. Unlike J_{sc} , FF of PAL thicker modules is reduced from 54% to 46%, as expected upon enlargement of charge transport distance. Consequently, PCE varies from 3.3% to 3.8% for PAL thicknesses increase from 120 nm to 160 nm. Note that modules with similar PCE are found for a relative wide thickness window (140-160 nm). Therefore, the performance-thickness tolerance of these photoactive materials processed by blade coating and laser patterning steps are a suitable combination for upscaling.

Table 6.7. Photovoltaic parameters of semitransparent modules consisting of 4 subcells interconnected in series ($L_{cell}= 3$ mm) and lab-devices.

| PAL thickness (nm) | V_{oc} (V) | V_{oc}^* (V) | J_{sc}^* (mA/cm ²) | FF (%) | PCE (%) | HPT (%) | AA (cm ²) |
|--------------------|-----------------|-----------------|----------------------------------|----------------|---------------|---------|-----------------------|
| 120 | - | 0.68 ± 0.01 | 7.7 ± 0.1 | 59.4 ± 3.8 | 3.1 ± 0.1 | 45 | 8 |
| | 2.91 ± 0.04 | 0.73 ± 0.01 | 8.7 ± 0.1 | 53.1 ± 1.3 | 3.3 ± 0.1 | 41 | 1.10 |
| 140 | - | 0.69 ± 0.05 | 11.0 ± 0.5 | 50.5 ± 2.8 | 3.9 ± 0.2 | 33 | 8 |
| | 2.80 ± 0.06 | 0.72 ± 0.01 | 11.3 ± 0.3 | 44.8 ± 0.3 | 3.8 ± 0.1 | 35 | 1.10 |
| 160 | - | 0.69 ± 0.06 | 11.6 ± 0.4 | 49.6 ± 0.1 | 4.0 ± 0.2 | 28 | 8 |
| | 2.82 ± 0.04 | 0.72 ± 0.01 | 11.8 ± 0.2 | 44.9 ± 0.1 | 3.8 ± 0.1 | 28 | 1.10 |

*Parameters corresponding to 1 subcell.

6.4.7 Flexible assessing of modules

Hereafter we analysed the effect of the number the subcells on the module. The flexible design of the module layout, shown in Figure 6.18, enables accessing independently the desired number of interconnected subcells. Figure 6.19(a) depicts the JV characteristics of 2 and 4 interconnected-subcells modules. The invariability of the J_{sc} with the number of the interconnected subcells is a further confirmation that the accurate laser patterning provides an efficient interconnection.

The V_{oc} of the ST modules (Table 6.6) also scales linearly with the number of the interconnected subcells (depending on the design 3 or 4 subcells), being 1.44 V and 2.81V for 2 and 4 subcells, respectively. These results are a relevant milestone in the upscaling of this OPV system, as indicated by the fact that the performance of the module can be maintained upon increasing the active area size, provided a suitable module design is developed. In particular, the record efficiency of the module shown in Figure 6.19(a) is 4.1% for both 2 and 4 interconnected subcells, more details on Table 6.6. Besides the performance, a high transparency degree (35% of HPT) is exemplified in the picture of the ST module in Figure 6.19(b). Noteworthy, the 3 interconnection regions of our ST module, with a width of 300 μm each, are hardly visible by the naked eye.

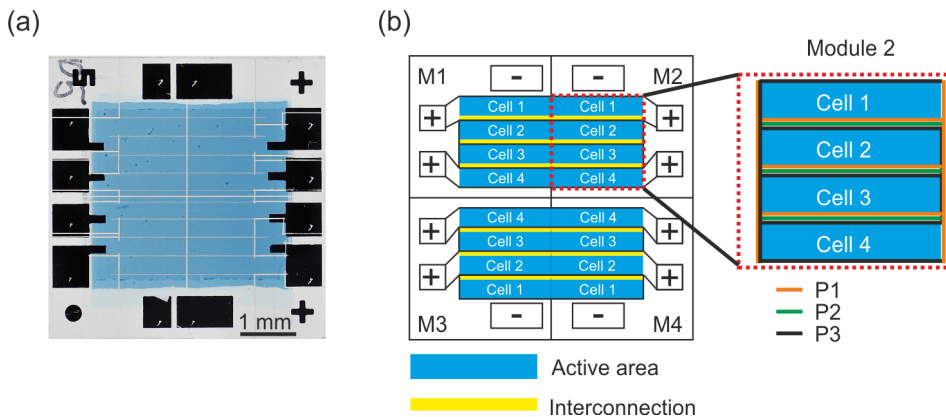


Figure 6.18. The layout of the laser patterning design. (a) Photograph of the sample containing 4 different modules and (b) scheme of the module layout with detailed laser patterned grooves.

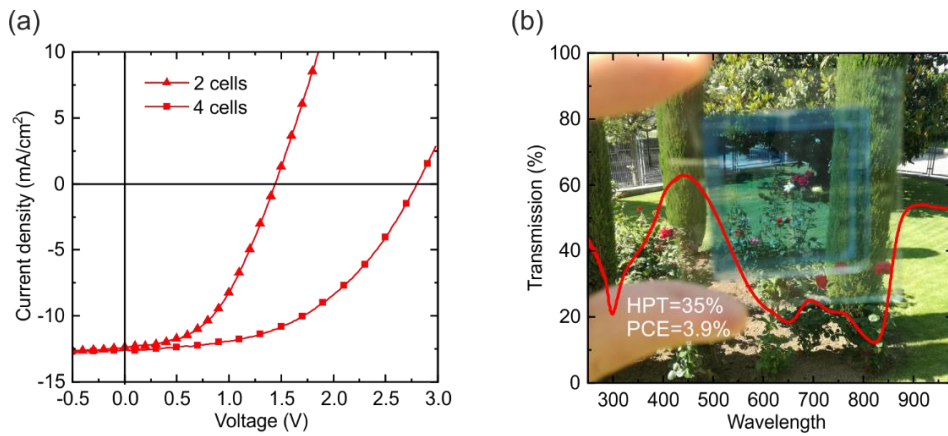


Figure 6.19. Module performance and transparency. (a) JV characteristics of the module of 2 and 4 cells interconnected in series. (b) Transmission spectrum and photograph image (background) of a module based on PBDTZT-stat-DBTT-8:4TICO.

This is an intrinsic advantage of laser patterned ST modules over those fabricated solely by means of slot-die coating and screen printing, where the individual interconnections can be easily noticeable.

6.5 Conclusions

Organic photovoltaics are expected to become a key player in building-integrated photovoltaics (BIPV), especially in semitransparent architectonic elements due to its transparency, performance and design flexibility. We have defined those specific characteristics that an OPV system has to fulfil, based on the experience of Merck Chemicals with customers, including threshold transparency of 30% and appealing colours for architecture such as blue, green or grey. We have studied the candidate system comprising the semiconducting blue polymer PBDTZT-stat-DBTT-8 and the strong NIR absorbing acceptor 4TICO. The full fabrication of the solar cells and modules has been performed following the industrial preferences for low embodied energy technologies including air processing, full solution-process from non-halogenated formulations, low annealing temperatures and no evaporation steps.

Despite the high transmittance required in BIPV applications, which limits the light-harvesting, the fabricated semitransparent modules yield around 4% efficiency, with a geometrical fill factor above 90% and 1 cm² active area. Importantly, the system shows a negligible drop in performance upon area upscaling from 8 mm² to the mentioned value of 110 mm². Moreover, a laser patterning process has been developed and implemented in the fabrication of the modules, to narrow the interconnection length down to 300 µm, and consequently maximise the GFF.

A comprehensive characterisation of the modules has been done with the aid of the combination of advanced co-local optoelectronic imaging techniques, namely laser-beam/white-light induced photocurrent, together with photoluminescence and Raman scattering mapping. These techniques have helped to correlate the local morphological features of the photoactive material with the photocurrent distribution as well as to validate the efficacy of the laser patterning. On the other hand, the moderate module efficiency suggests room for improvement, being the semitransparent top electrode the bottleneck for achieving higher performances. Yet, the results of this work encourage the use of organic semiconductors that extend the light absorption into the infrared as key materials for the photoactive architectonic elements of the future.

Chapter 7 General conclusions and perspectives

This chapter summarises the general conclusions of the thesis and some of the perspectives that arise from this work.

7.1 Conclusions

The results obtained in this thesis have contributed to the lab-to-fab transition for non-fullerene acceptor based OPV. As a first approach, we studied theoretically the aesthetic appearance of OPV by different tuning strategies applied to the photoactive layer, namely thickness interference, donor:acceptor (D:A) stoichiometry and the addition of a third photoactive component. The use of dyes (a simplified model of NFAs) turned out to be the most effective alternative for changing the appearance of photoactive films. Additionally, we combined the colour calculation-based on transfer matrix method together with a genetic algorithm to predict the photovoltaic characteristics (thickness and D:A ratio) that reproduces a desired colour. As an extension of that work, we explore the aesthetics of 5 commercial NFAs when blended with polythiophenes (P3HT). The colour coordinates of P3HT-based blends covers a wide range of the chromaticity diagram, going from the traditional wine-like appearance of PC₆₀BM mixtures, to orange upon blending with O-IDFBR or purple upon blending with O-IDTBR. This fact represents a further confirmation of the validity of our theoretical colour predictions in Chapter 3.

In terms of OPV devices, we aimed to move from fabrication-intensive approaches to measuring-intensive ones. We manufactured photoactive films with intended variations in the parameter(s) of interest. In particular, 1-dimensional (1D) gradients were

demonstrated by applying controlled gradients in thickness and annealing temperature in the photoactive layer. Thanks to the 1D gradients, we managed to accelerate significantly the optimisation process by a factor of 10. Moreover, 1D graded blade-coated devices showed similar efficiencies, in comparison to the state-of-the-art by scalable techniques (Table 1.1). Thus, measuring-intense approaches not only speed-up the screening process but also reach benchmarked results especially for P3HT-based system. Additionally, we combined the large dataset (>1000 data points) of P3HT-based device with the statistic tool ANOVA to rank the manufacturing parameters by their performance sensitivity. We found that the parameters affecting blend morphology including the solvent system and the post-annealing temperature turned out to be more relevant than the casting temperature and photoactive layer thickness. A comprehensive explanation was given correlating the solubility of the material in the different solvent systems (Hansen Solubility Parameters) and annealing effect. On the other hand, we found that the results optimised for the semi-crystalline P3HT by blade-coating cannot be extrapolated to other polymers *a priori* more amorphous such as PBDB-T.

The 1D gradients methodology was extended to 2D parametric libraries manufactured with simultaneous variations of thickness and stoichiometry at the photoactive layer. We demonstrated the reliability and accuracy of our strategy when compared to the conventional approach. To generalise this method, we demonstrated the screening capability of this methodology by identifying the optimum D:A ratio for 12 different systems. It is worth highlighting that each D:A system requires only one heterogeneous sample in which 10.000 data points were extracted with the aid of co-local measurements. Additionally, these results pointed out a correlation between the degree of overlapping in the absorption spectra of donor and acceptor materials and the shape of the photocurrent distribution as a function of the composition. Whereas for coincident absorption characteristic (PTB7-Th:ITIC), the photocurrent values exhibit a normal distribution as a function of the composition, materials with complementary absorption (PBDB-T:EH-ITIC) have a bimodal distribution.

Table 7.1. Results achieved in the thesis benchmarked with the state-of-the-art results

| | System | Deposition | PCE (%) | Area (mm ²) | Ref |
|-----------|-------------------------|------------------|---------|-------------------------|-----------|
| Chapter 4 | P3HT:O-IDTBR | Spin-coating | 6.3 | 5 | [154] |
| | | Inkjet-printing | 6.2 | 3 | [168] |
| | | Blade-coating | 5.6 | 10.4 | [166] |
| | | Blade-coating | 5.6 | 8 | This work |
| | | Inkjet-printing | 6.0 | 200 | [168] |
| | | Slot-die-coating | 5.0 | 5952 | [166] |
| | | Slot-die coating | 1.7 | 108 | This work |
| Chapter 5 | PBDB-T:ITIC | Blade-coating | 10.0 | 3.9 | [224] |
| | PBDB-T:ITIC | Blade-coating | 7.7 | 8 | This work |
| | PBDB-T:O-ITIC | Spin-coating | 12.4 | 3.9 | [224] |
| | PBDB-T:O-ITIC | Blade-coating | 9.3 | 8 | This work |
| | PBDB-T:EH-ITIC | Blade-coating | 8.9 | 8 | This work |
| Chapter 6 | PFBDB-T:O-ITIC | Spin-coating | 10 | 4.5 | [246] |
| | PBTZT-stat-BDIT-8:PCBM | Slot-die | 4.5 | 114.5 | [101] |
| | PBTZT-stat-BDIT-8:4TICO | Blade-coating | 4.7 | 8 | This work |
| | PBTZT-stat-BDIT-8:4TICO | Blade-coating | 3.9 | 110 | This work |

Significant efforts were devoted to the upscaling of OPV from mm²-scale lab devices to cm²-scale prototyping modules. The two technological aspects considered were slot-die mounted on roll-to-roll equipment (Eurecat, Chapter 4) and laser patterning (Merck Chemicals, Chapter 6). To the best of our knowledge, this is the first demonstrator reported in the literature of R2R P3HT:O-IDTBR modules in a flexible substrate. However, there is a big room for improvement to reduce the PCE drop from 5.6% at lab-scale to 1.7% in 108 mm² active area, please refer to Table 7.1.

The second example demonstrated the upscalability of the commercial system PBTZT-stat-BDIT-8:4TICO (chapter 6). In this case, we focused not only on performance but also on achieving a level of transparency (30%) which was identified as the threshold for the integration into photoactive windows. A significant drop in performance was found when moving from evaporated to the solution-process semitransparent electrode. The electrical conductivity of the highly conductive PEDOT (PH1000) was identified as the main responsible because of its significantly lower value compared to the typical conductors. However, a negligible reduction in performance was shown when upscaling

this system from mm²-scale devices to cm²-scale prototyping modules, revealing an efficient laser-patterning and cell-to-cell interconnection.

To pave the way towards the commercialisation of OPV, we studied systematically the shelf-lifetime of 48 P3HT:O-IDTBR devices with variations in the photoactive layer thickness and the effect of the encapsulation. After 3.000 h, thin and encapsulated devices (~80 nm) demonstrated higher stability than thicker ones (~300 nm). The selective photocurrent maps at 488 nm (P3HT contribution) and 785 nm (O-IDTRBR) contribution identified O-IDTBR as the main responsible for the performance drop in thicker PAL films (>200 nm). Further efforts would be necessary to fully understand this phenomenon.

Finally, in terms of summary numbers of this thesis, a total of **30 different OPV systems** have been evaluated throughout the PhD. However, only 21 systems were included in this thesis. Some of the studied systems are listed below including P3HT-based system (10) blended with ITIC, ITIC-M, O-ITIC, EH-ITIC, ITIC-M, O-IDTBR, EH-IDTBR, O-IDFBR, PC₆₀BM and ICBA (some of them reported in chapter 4). The low bandgap polymers PBDB-T (6) and PTB7-Th (6) blended with ITIC, ITIC-M, O-ITIC, EH-ITIC, ITIC-4F, PC₇₀BM. On the other hand, we also evaluated PBDB-T-2Cl:ITIC-4F, PBDB-T-2F:ITIC-4F, PCDTBT:PC₇₀BM and PBTZT-stat-BDIT-8:4TICO.

The developed database during this thesis includes more than **4700** data points with their associated processing conditions generated by the use of 1D gradients. On the other hand, **300.000** data points (12 systems and 25.000 data points each) were measured with the aid of 2D gradients and co-local measurements. Note that the generation of the dataset is only relying on me, whereas the 2D gradient collaborative work with Mr. Xabier Rodriguez. Thus, these numbers support the great screening capabilities of graded-combinatorial approach to screening several materials in a limited time, material and human resources.

7.2 Perspectives

In this thesis, we have dedicated significant efforts to advance towards the upscaling of NFAs in OPV technology. However, several topics still require further investigation.

As an extension of the transfer matrix method developed for aesthetics, the electrical modelling of the full device could help to correlate the aesthetics with the device performance. On the other hand, the genetic algorithm, so far, optimises the composition and thickness for a given pair of photoactive materials. The use of a multi-variable genetic algorithm (MV-GA) could help to optimise the selection of blend materials that consider other relevant factors while mimicking the target aesthetics. For instance, the MV-GA could optimise in terms of cost and photocurrent the election of materials, composition and thickness. Besides, the level of transparency could be considered in the case of using a semitransparent electrode. This latter tool could be very relevant for the OPV implementation as semitransparent architectonic element.

As a potential improvement to explore more efficiently the variable space, 1D gradient approach could be coupled to the so-called design-of-experiment driven by experimental data. The know-how acquired over years experimental scientists could be partially transferred to an artificial intelligence algorithm that could decide based on previous experiments which one would be more meaningful in order to acquire the largest amount of information with minimum resources. To achieve that point, the scientific community should join efforts by sharing their experimental results in a common and open-access repository/database.

Big data produced through 2D-gradient approach could be coupled to artificial intelligence (AI) algorithms. With their aid, we could correlate the photovoltaic performance with fundamental material properties and thus, more robust conclusions could be drawn. One interesting feature of these AI is that they can quantitatively classify the importance of the material descriptors employed in the analysis such as chemical structure (SMILE), material absorption, energy levels, etc. Similarly, AI predictions could help in the design of new chemical materials based on experimental work. Thanks to the synergy between big data applied to material science and AI new frontiers could be explored.

The key technical aspects of upscaling that should be addressed include detailed manufacturing and long-term stability studies. For the former, additional efforts should be dedicated to minimising the drop in performance when moving from top-record spin-coating lab-scale devices, passing by blade coating lab-scale device and to finally fully-roll-to-roll flexible modules. In particular, these key aspects include the use of halogen-free solvent systems, the effect of a non-controlled atmosphere when casting or annealing the OPV device, substitution of the evaporated electrode by efficient transparent solution-process alternatives. The high throughput methodology developed in part during this thesis could significantly help in this endeavour.

Besides the performance, long-term stability should be considered for the commercialisation. Among others, the analysis of the aforementioned terms should be included as well or other factors that affect the long-term stability such as encapsulation materials, thickness effect and analysis under real operating conditions. Again, the use of AI could be very relevant in this field to accelerate the identification of the best candidate.

Appendix A

Input data used in Eq. 3.3 for CIE covered area prediction (Table 3.2). CIE coordinates of the pristine material (x,y) with 3 different thicknesses (50, 100 and 400 nm) and cylindrical coordinates (ρ and θ) centred on the illuminant AM 1.5G given by its CIE coordinates (x,y)=(0.3322, 0.3443).

| Material | Thickness (nm) | x | y | ρ | θ (deg) |
|------------------------|-------------------|--------|---------|--------|-------------------|
| P3HT | 50 | 0.3588 | 0.3044 | 0.0480 | -56.30 |
| P3HT | 100 | 0.4478 | 0.3027 | 0.1229 | -19.79 |
| P3HT | 400 | 0.7095 | 0.2829 | 0.3823 | -9.24 |
| PC ₇₀ BM | 50 | 0.3599 | 0.3521 | 0.0288 | 15.72 |
| PC ₇₀ BM | 100 | 0.3905 | 0.3699 | 0.0637 | 23.70 |
| PC ₇₀ BM | 400 | 0.5726 | 0.3766 | 0.2426 | 7.65 |
| PC ₆₀ BM | 50 | 0.3561 | 0.3639 | 0.0309 | 39.35 |
| PC ₆₀ BM | 100 | 0.3595 | 0.3784 | 0.0437 | 51.31 |
| PC ₆₀ BM | 400 | 0.4627 | 0.4344 | 0.1586 | 34.62 |
| PTB7-Th | 50 | 0.286 | 0.309 | 0.0581 | 217.38 |
| PTB7-Th | 100 | 0.2597 | 0.275 | 0.1003 | 223.71 |
| PTB7-Th | 400 | 0.1667 | 0.09453 | 0.2996 | 236.54 |
| APFOGreen | 50 | 0.3521 | 0.3785 | 0.0396 | 59.81 |
| APFOGreen | 100 | 0.3505 | 0.3921 | 0.0512 | 69.056 |
| APFOGreen | 400 | 0.3757 | 0.4852 | 0.1475 | 72.84 |
| PCDTBT | 50 | 0.3206 | 0.2775 | 0.0678 | 260.12 |
| PCDTBT | 100 | 0.3712 | 0.241 | 0.1104 | -69.31 |
| PCDTBT | 400 | 0.6323 | 0.241 | 0.3174 | -18.99 |
| DPPTTT | 50 | 0.3069 | 0.3507 | 0.0261 | 165.82 |
| DPPTTT | 100 | 0.2837 | 0.3539 | 0.0494 | 168.80 |
| DPPTTT | 400 | 0.1771 | 0.377 | 0.1585 | 168.09 |
| Dye $\lambda_0=450$ nm | 50 | 0.3964 | 0.4061 | 0.0891 | 43.90 |
| Dye $\lambda_0=450$ nm | 100 | 0.4469 | 0.4451 | 0.1527 | 41.30 |
| Dye $\lambda_0=450$ nm | 400 | 0.568 | 0.4258 | 0.2495 | 19.06 |
| Dye $\lambda_0=540$ nm | 50 | 0.3499 | 0.2897 | 0.0574 | -72.03 |
| Dye $\lambda_0=540$ nm | 100 | 0.3958 | 0.2697 | 0.098 | -49.55 |

| Material | Thickness (nm) | x | y | ρ | θ (deg) |
|------------------------|-------------------|--------|---------|--------|-------------------|
| Dye $\lambda_0=540$ nm | 400 | 0.5554 | 0.2366 | 0.2478 | -25.75 |
| Dye $\lambda_0=650$ nm | 50 | 0.274 | 0.3197 | 0.0632 | 202.91 |
| Dye $\lambda_0=650$ nm | 100 | 0.2252 | 0.2756 | 0.1272 | 212.70 |
| Dye $\lambda_0=650$ nm | 400 | 0.1432 | 0.08443 | 0.3213 | 233.97 |
| Dye $\lambda_0=750$ nm | 50 | 0.3171 | 0.3391 | 0.016 | 199.00 |
| Dye $\lambda_0=750$ nm | 100 | 0.2944 | 0.328 | 0.0412 | 203.32 |
| Dye $\lambda_0=750$ nm | 400 | 0.1968 | 0.2738 | 0.1527 | 207.50 |

Appendix B

Transparency metrics and colour characteristics of PBDTZT-stat-DBTT-8 and 4TICO films shown in Figure 6.2. Human perception transmittance (HPT) and average visual transmittance (AVT). Full device transparency highlighted in bold.

| Layers | PAL thickness (nm) | HPT (%) | AVT (%) | Transmission at 550 nm (%) | CIE coordinates (x,y) |
|------------------|--------------------|-----------|-----------|----------------------------|-------------------------|
| ITO | 100 | 90.4 | 92.1 | 90 | (0.3289,0.3359) |
| PAL | | 83.7 | 80.6 | 86 | (0.3102, 0.3352) |
| PAL+PEDOT | 32 | 79 | 76 | 81 | (0.3127, 0.3363) |
| ST device | | 63 | 61 | 65 | (0.304, 0.3313) |
| PAL | | 62 | 60 | 64 | (0.2803, 0.3416) |
| PAL+PEDOT | 71 | 63.2 | 61.1 | 66 | (0.2931, 0.3253) |
| ST device | | 49 | 48 | 50 | (0.285, 0.3195) |
| PAL | | 55 | 53 | 57 | (0.2687, 0.3070) |
| PAL+PEDOT | 88 | 53.8 | 52.7 | 56 | (0.2814, 0.3161) |
| ST device | | 40 | 40 | 42 | (0.2667, 0.3052) |
| PAL | | 40 | 39 | 42 | (0.2445, 0.2905) |
| PAL+PEDOT | 135 | 37.3 | 38.7 | 38 | (0.2457, 0.2803) |
| ST device | | 31 | 32 | 32 | (0.2406, 0.2835) |
| PAL | | 34 | 34 | 35 | (0.2321, 0.2774) |
| PAL+PEDOT | 160 | 31.8 | 33.7 | 32 | (0.2288, 0.2657) |
| ST device | | 26 | 27 | 27 | (0.2273, 0.2713) |
| PAL | | 26 | 27 | 26 | (0.2099, 0.2507) |
| PAL+PEDOT | 200 | 25.7 | 27.3 | 26 | (0.2116, 0.2557) |
| ST device | | 20 | 22 | 20 | (0.2068, 0.2513) |
| PAL | | 21 | 23 | 21 | (0.1959, 0.2373) |
| PAL+PEDOT | 240 | 19.9 | 22 | 20 | (0.1987, 0.2393) |
| ST device | | 14 | 16 | 14 | (0.1884, 0.2284) |
| PAL | | 15 | 18 | 15 | (0.1818, 0.2167) |
| PAL+PEDOT | 300 | 15 | 17.9 | 14 | (0.1837, 0.2125) |
| ST device | | 12 | 14 | 11 | (0.1773, 0.2079) |

Appendix C

Similarly as performed in Chapter 4, one simple way to estimate the PAL thickness in a great number of samples is through absorption measurements, provided a calibration curve is calculated based on profilometry measurements. We found that the optical density at 610 nm (polymer absorption region) scales linearly with both blade speed and PAL thickness, assuming no significant changes occurred in the coating process of the PAL. Once the calibration is carried out, the thickness of the PAL is predictable, thus avoiding the longer and invasive mechanical profilometry measurements.

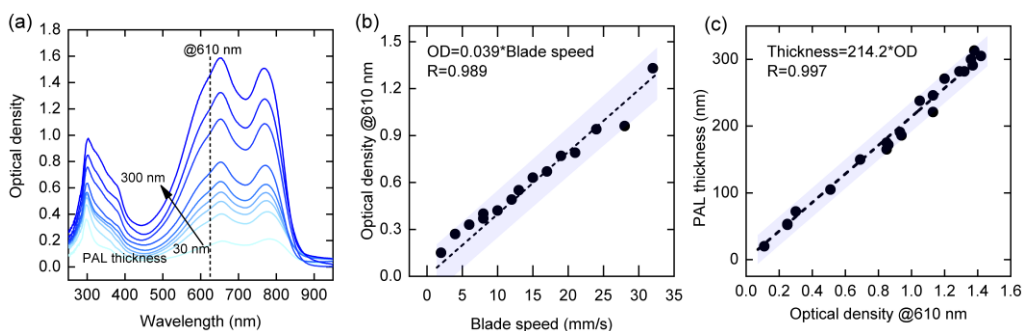


Fig. C.1. Thickness quantification of the bladed-coated films. (a) Optical density spectra as a function of the photoactive layer thickness (b) Optical density value at 610 nm as a function of the blade speed. (c) Thickness of the photoactive layer as a function of the optical density at 610 nm. Dashed lines and confidence band of 98% are plotted to guide the eye.

References

1. E. A. Wrigley, Energy and the English Industrial Revolution, *Philos. Trans. R. Soc. A*, **371**, 20110568, 2013.
2. R. Perez and M. Perez, A Fundamental Look at Supply Side Energy Reserves for the Planet, *The IEA SHC Solar Update*, **50**, 2009.
3. <https://www.ecotricity.co.uk/our-green-energy/energy-independence/the-end-of-fossil-fuels>, (accessed 23/03/2020).
4. <https://www.nationalgeographic.com/environment/global-warming/global-warming-overview/>, (accessed 21/01/2020).
5. S. Pye, F. G. N. Li, J. Price and B. Fais, Achieving net-zero emissions through the reframing of UK national targets in the post-Paris Agreement era, *Nat. Energy*, **2**, 2017.
6. <https://www.epa.gov/climate-indicators/climate-change-indicators-us-and-global-temperature>, (accessed 14/10/2019, 2019).
7. *Renewables 2019 Global status report*, 2019.
8. *Global Energy & CO2 Status Report* <https://www.iea.org/geco/electricity/>, (accessed 14/10/2019, 2019).
9. *The spanish electricity system*, Red Eléctrica española, 2018.
10. J. van Zalk and P. Behrens, The spatial extent of renewable and non-renewable power generation: A review and meta-analysis of power densities and their application in the U.S, *Energy Policy*, **123**, 83-91, 2018.
11. C. J. Cleveland, Net energy from the extraction of oil and gas in the United States, *Energy*, **30**, 769-782, 2005.
12. D. J. Murphy and C. A. S. Hall, Year in review—EROI or energy return on (energy) invested, *Ann. N.Y. Acad. Sci.*, **1185**, 102-118, 2010.
13. M. Lenzen, Life cycle energy and greenhouse gas emissions of nuclear energy: A review, *Energy Convers. Manage.*, **49**, 2178-2199, 2008.
14. D. J. C. MacKay, *Sustainable Energy: Without the Hot Air*, UIT, 2009.
15. C. A. S. Hall, *Provisional results from EROI assessments. The Oil Drum.*, <http://theoil Drum.com/node/3810>, 2008.

16. P. E. Brockway, A. Owen, L. I. Brand-Correa and L. Hardt, Estimation of global final-stage energy-return-on-investment for fossil fuels with comparison to renewable energy sources, *Nat. Energy*, **4**, 612-621, 2019.
17. P. Soltantabar, Annual Energy Outlook, 2015.
18. <https://www.nrel.gov/pv/cell-efficiency.html>, (accessed 20/04/2020).
19. M. A. Green, Silicon solar cells: state of the art, *Philos. Trans. R. Soc. A*, **371**, 20110413, 2013.
20. B. D. Safyanu, M. N. Abdullah and Z. Omar, Review of Power Device for Solar-Powered Aircraft Applications, *J. Aerosp. Technol. Manag.*, **11**, 2019.
21. http://www.esa.int/Enabling_Support/Space_Engineering_Technology/, (accessed 22/03/2020).
22. Z. Yin, J. Wei and Q. Zheng, Interfacial Materials for Organic Solar Cells: Recent Advances and Perspectives, *Adv. Sci.*, **3**, 1500362, 2016.
23. <https://www.nrel.gov/pv/module-efficiency.html>, (accessed 20/03/2020).
24. K. P. Bhandari, J. M. Collier, R. J. Ellingson and D. S. Apul, Energy payback time (EPBT) and energy return on energy invested (EROI) of solar photovoltaic systems: A systematic review and meta-analysis, *Renew. Sustain. Energy Rev*, **47**, 133-141, 2015.
25. J. Gonzalo, D. Domínguez and D. López, On the challenge of a century lifespan satellite, *Prog. Aerosp. Sci.*, **70**, 28-41, 2014.
26. L. Qiu, L. K. Ono and Y. Qi, Advances and challenges to the commercialization of organic-inorganic halide perovskite solar cell technology, *Mater. Today Energy*, **7**, 169-189, 2018.
27. J. Gong, S. B. Darling and F. You, Perovskite photovoltaics: life-cycle assessment of energy and environmental impacts, *Energy Environ. Sci.*, **8**, 1953-1968, 2015.
28. N. Espinosa, M. Hösel, D. Angmo and F. C. Krebs, Solar cells with one-day energy payback for the factories of the future, *Energy Environ. Sci.*, **5**, 5117-5132, 2012.
29. A. Anctil, E. Lee and R. R. Lunt, Net energy and cost benefit of transparent organic solar cells in building-integrated applications, *Appl. Energy*, **261**, 114429, 2020.
30. <https://periodictable.com/Properties/A/CrustAbundance.html>, (accessed 16/03/2020).
31. K. Kakiage, Y. Aoyama, T. Yano, K. Oya, J. Fujisawa and M. Hanaya, Highly-efficient dye-sensitized solar cells with collaborative sensitization by silyl-anchor and carboxy-anchor dyes, *Chem. Commun. (Camb.)*, **51**, 15894-15897, 2015.
32. Q. Zhao, A. Hazarika, X. Chen, S. P. Harvey, B. W. Larson, G. R. Teeter, J. Liu, T. Song, C. Xiao, L. Shaw, M. Zhang, G. Li, M. C. Beard and J. M. Luther, High

- efficiency perovskite quantum dot solar cells with charge separating heterostructure, *Nat Commun*, **10**, 2842, 2019.
33. Q. Liu, Y. Jiang, K. Jin, J. Qin, J. Xu, W. Li, J. Xiong, J. Liu, Z. Xiao, K. Sun, S. Yang, X. Zhang and L. Ding, 18% Efficiency organic solar cells, *Sci. Bull.*, **65**, 272-275, 2020.
 34. A. Urbina, The balance between efficiency, stability and environmental impacts in perovskite solar cells: a review, *JPhys Energy*, **2**, 022001, 2020.
 35. L. Zhan, S. Li, T.-K. Lau, Y. Cui, X. Lu, M. Shi, C.-Z. Li, H. Li, J. Hou and H. Chen, Over 17% efficiency ternary organic solar cells enabled by two non-fullerene acceptors working in alloy-like model, *Energy Environ. Sci.*, 2020.
 36. Z. Liu, P. You, S. Liu and F. Yan, Neutral-Color Semitransparent Organic Solar Cells with All-Graphene Electrodes, *ACS Nano*, **9**, 12026-12034, 2015.
 37. Z. Zhang, R. Lv, Y. Jia, X. Gan, H. Zhu and F. Kang, All-Carbon Electrodes for Flexible Solar Cells, *Appl. Sci.*, **8**, 152, 2018.
 38. J. Yuan, Y. Zhang, L. Zhou, G. Zhang, H.-L. Yip, T.-K. Lau, X. Lu, C. Zhu, H. Peng, P. A. Johnson, M. Leclerc, Y. Cao, J. Ulanski, Y. Li and Y. Zou, Single-Junction Organic Solar Cell with over 15% Efficiency Using Fused-Ring Acceptor with Electron-Deficient Core, *Joule*, **3**, 1140-1151, 2019.
 39. N. Li, I. McCulloch and C. J. Brabec, Analyzing the efficiency, stability and cost potential for fullerene-free organic photovoltaics in one figure of merit, *Energy Environ. Sci.*, **11**, 1355-1361, 2018.
 40. I. Burgués-Ceballos, M. Stella, P. Lacharmoise and E. Martínez-Ferrero, Towards industrialization of polymer solar cells: material processing for upscaling, *J. Mater. Chem. A*, **2**, 17711-17722, 2014.
 41. J. Guo and J. Min, A Cost Analysis of Fully Solution-Processed ITO-Free Organic Solar Modules, *Adv. Energy Mater.*, **9**, 1802521, 2019.
 42. W. Shockley, The Theory of p-n Junctions in Semiconductors and p-n Junction Transistors, *Syst. Tech. J.*, **28**, 1949.
 43. <https://ch301.cm.utexas.edu/>, (accessed 08/04/2020).
 44. S. Li, L. Ye, W. Zhao, S. Zhang, S. Mukherjee, H. Ade and J. Hou, Energy-Level Modulation of Small-Molecule Electron Acceptors to Achieve over 12% Efficiency in Polymer Solar Cells, *Adv. Mater.*, **28**, 9423-9429, 2016.
 45. M. Campoy-Quiles, C. Müller, M. Garriga, E. Wang, O. Inganäs and M. I. Alonso, On the complex refractive index of polymer:fullerene photovoltaic blends, *Thin Solid Films*, **571**, 371-376, 2014.
 46. M. Hiramoto, H. Fujiwara and M. Yokoyama, Three-layered organic solar cell with a photoactive interlayer of codeposited pigments, *Appl. Phys. Lett.*, **58**, 1062-1064, 1991.
 47. T. Zhang, D. B. Dement, V. E. Ferry and R. J. Holmes, Intrinsic measurements of exciton transport in photovoltaic cells, *Nat. Commun.*, **10**, 1156, 2019.

48. C. W. Tang, Two-layer organic photovoltaic cell, *Appl. Phys. Lett.*, **48**, 183-185, 1986.
49. S. Izawa, K. Nakano, K. Suzuki, K. Hashimoto and K. Tajima, Dominant effects of first monolayer energetics at donor/acceptor interfaces on organic photovoltaics, *Adv. Mater.*, **27**, 3025-3031, 2015.
50. G. Yu, J. Gao, J. C. Hummelen, F. Wudl and A. J. Heeger, Polymer Photovoltaic Cells: Enhanced Efficiencies via a Network of Internal Donor-Acceptor Heterojunctions, *Science*, **270**, 1789-1791, 1995.
51. H. Hoppe and N. S. Sariciftci, Organic solar cells: An overview, *J. Mater. Res.*, **19**, 1924-1945, 2011.
52. J. Nelson, Polymer:fullerene bulk heterojunction solar cells, *Mater. Today*, **14**, 462-470, 2011.
53. J. Yuan, Y. Xu, G. Shi, X. Ling, L. Ying, F. Huang, T. H. Lee, H. Y. Woo, J. Y. Kim, Y. Cao and W. Ma, Engineering the morphology via processing additives in multiple all-polymer solar cells for improved performance, *J. Mater. Chem. A*, **6**, 10421-10432, 2018.
54. M. Campoy-Quiles, T. Ferenczi, T. Agostinelli, P. G. Etchegoin, Y. Kim, T. D. Anthopoulos, P. N. Stavrinou, D. D. Bradley and J. Nelson, Morphology evolution via self-organization and lateral and vertical diffusion in polymer:fullerene solar cell blends, *Nat. Mater.*, **7**, 158-164, 2008.
55. Y. Xie, W. Zhou, J. Yin, X. Hu, L. Zhang, X. Meng, Q. Ai and Y. Chen, Post-annealing to recover the reduced open-circuit voltage caused by solvent annealing in organic solar cells, *J. Mater. Chem. A*, **4**, 6158-6166, 2016.
56. R. Po, C. Carbonera, A. Bernardi and N. Camaioni, The role of buffer layers in polymer solar cells, *Energy Environ. Sci.*, **4**, 285-310, 2011.
57. T.-H. Lai, S.-W. Tsang, J. R. Manders, S. Chen and F. So, Properties of interlayer for organic photovoltaics, *Mater. Today*, **16**, 424-432, 2013.
58. Y. Lin, B. Adilbekova, Y. Firdaus, E. Yengel, H. Faber, M. Sajjad, X. Zheng, E. Yarali, A. Seitkhan, O. M. Bakr, A. El-Labban, U. Schwingenschlogl, V. Tung, I. McCulloch, F. Laquai and T. D. Anthopoulos, 17% Efficient Organic Solar Cells Based on Liquid Exfoliated WS₂ as a Replacement for PEDOT:PSS, *Adv. Mater.*, **31**, e1902965, 2019.
59. M. O. Reese, S. A. Gevorgyan, M. Jørgensen, E. Bundgaard, S. R. Kurtz, D. S. Ginley, D. C. Olson, M. T. Lloyd, P. Morvillo, E. A. Katz, A. Elschner, O. Haillant, T. R. Currier, V. Shrotriya, M. Hermenau, M. Riede, K. R. Kirov, G. Trimmel, T. Rath, O. Inganäs, F. Zhang, M. Andersson, K. Tvingstedt, M. Lira-Cantu, D. Laird, C. McGuinness, S. Gowrisanker, M. Pannone, M. Xiao, J. Hauch, R. Steim, D. M. DeLongchamp, R. Rösch, H. Hoppe, N. Espinosa, A. Urbina, G. Yaman-Uzunoglu, J.-B. Bonekamp, A. J. J. M. van Breemen, C. Girotto, E. Voroshazi and F. C. Krebs, Consensus stability testing protocols for organic photovoltaic materials and devices, *Sol. Energy Mater. Sol. Cells*, **95**, 1253-1267, 2011.

60. M. T. Dang, L. Hirsch and G. Wantz, P3HT:PCBM, best seller in polymer photovoltaic research, *Adv. Mater.*, **23**, 3597-3602, 2011.
61. D. Chi, S. Qu, Z. Wang and J. Wang, High efficiency P3HT:PCBM solar cells with an inserted PCBM layer, *J. Mater. Chem. C*, **2**, 4383, 2014.
62. G. Zhao, Y. He and Y. Li, 6.5% Efficiency of polymer solar cells based on poly(3-hexylthiophene) and indene-C(60) bisadduct by device optimization, *Adv. Mater.*, **22**, 4355-4358, 2010.
63. M. Hösel, R. R. Søndergaard, M. Jørgensen and F. C. Krebs, Fast Inline Roll-to-Roll Printing for Indium-Tin-Oxide-Free Polymer Solar Cells Using Automatic Registration, *Energy Technol.*, **1**, 102-107, 2013.
64. S. Zhang, L. Ye, W. Zhao, D. Liu, H. Yao and J. Hou, Side Chain Selection for Designing Highly Efficient Photovoltaic Polymers with 2D-Conjugated Structure, *Macromolecules*, **47**, 4653-4659, 2014.
65. J. Hou, O. Inganäs, R. H. Friend and F. Gao, Organic solar cells based on non-fullerene acceptors, *Nat. Mater.*, **17**, 119-128, 2018.
66. Y. Cui, H. Yao, J. Zhang, T. Zhang, Y. Wang, L. Hong, K. Xian, B. Xu, S. Zhang, J. Peng, Z. Wei, F. Gao and J. Hou, Over 16% efficiency organic photovoltaic cells enabled by a chlorinated acceptor with increased open-circuit voltages, *Nat. Commun.*, **10**, 2515, 2019.
67. Y. Firdaus, V. M. Le Corre, J. I. Khan, Z. Kan, F. Laquai, P. M. Beaujuge and T. D. Anthopoulos, Key Parameters Requirements for Non-Fullerene-Based Organic Solar Cells with Power Conversion Efficiency >20, *Adv. Sci.*, **6**, 1802028, 2019.
68. L. Zhu, W. Zhong, C. Qiu, B. Lyu, Z. Zhou, M. Zhang, J. Song, J. Xu, J. Wang, J. Ali, W. Feng, Z. Shi, X. Gu, L. Ying, Y. Zhang and F. Liu, Aggregation-Induced Multilength Scaled Morphology Enabling 11.76% Efficiency in All-Polymer Solar Cells Using Printing Fabrication, *Adv. Mater.*, **31**, e1902899, 2019.
69. Y. Xu, J. Yuan, S. Zhou, M. Seifrid, L. Ying, B. Li, F. Huang, G. C. Bazan and W. Ma, Ambient Processable and Stable All-Polymer Organic Solar Cells, *Adv. Funct. Mater.*, **29**, 1806747, 2019.
70. R. Zhou, Z. Jiang, C. Yang, J. Yu, J. Feng, M. A. Adil, D. Deng, W. Zou, J. Zhang, K. Lu, W. Ma, F. Gao and Z. Wei, All-small-molecule organic solar cells with over 14% efficiency by optimizing hierarchical morphologies, *Nat Commun*, **10**, 5393, 2019.
71. L. Meng, Y. Zhang, X. Wan, C. Li, X. Zhang, Y. Wang, X. Ke, Z. Xiao, L. Ding, R. Xia, H.-L. Yip, Y. Cao and Y. Chen, Organic and solution-processed tandem solar cells with 17.3% efficiency, *Science*, **361**, 1094-1098, 2018.
72. C.-Y. Liao, Y. Chen, C.-C. Lee, G. Wang, N.-W. Teng, C.-H. Lee, W.-L. Li, Y.-K. Chen, C.-H. Li, H.-L. Ho, P. H.-S. Tan, B. Wang, Y.-C. Huang, R. M. Young, M. R. Wasielewski, T. J. Marks, Y.-M. Chang and A. Facchetti, Processing

- Strategies for an Organic Photovoltaic Module with over 10% Efficiency, *Joule*, **4**, 189-206, 2020.
73. <https://www.fau.eu/2019/11/11/wissenschaft/new-efficiency-world-record-for-organic-solar-modules/>, (accessed 31/01/2020).
74. <https://sunew.com.br/en/>, (accessed 20/01/2020).
75. <https://www.enerthing.com/>, (accessed 20/01/2020).
76. <https://www.armor-group.com/en/ase>, (accessed 20/01/2020).
77. <https://www.heliatek.com/>, (accessed 20/01/2020).
78. R. García-Valverde, J. A. Cherni and A. Urbina, Life cycle analysis of organic photovoltaic technologies, *Prog Photovolt*, **18**, 535-558, 2010.
79. <https://www.epishine.com/>, (accessed 20/01/2020).
80. <https://infinitypv.com/>, (accessed 20/01/2020).
81. <https://www.savvyscience.org/>, (accessed 12/03/2020).
82. http://www.kolonindustries.com/Eng/RnD/rnd05_03.asp, (accessed 04/05/2020).
83. <https://dracula-technologies.com/>, (accessed 12/03/2020).
84. https://www.toyobo-global.com/news/2020/release_117.html, (accessed 26/03/2020).
85. <https://www.solarwindow.com/>, (accessed 04/05/2020).
86. <https://www.eni.com/en-IT/operations/organic-photovoltaic-opv.html>, (accessed 26/03/2020).
87. <http://www.ribestech.it/>, (accessed 12/03/2020).
88. <http://www.opvius.com/en/applications.html>, (accessed 14/04/2020).
89. M. D. Chatzisideris, P. K. Ohms, N. Espinosa, F. C. Krebs and A. Laurent, Economic and environmental performances of organic photovoltaics with battery storage for residential self-consumption, *Appl. Energy*, **256**, 113977, 2019.
90. <http://www.opvius.com/pink-bionic-smart-backpack-inspired-by-solartrees.html>, (accessed 30/07/2019).
91. <http://www.opvius.com/opv-wind-deflector-for-trucks-288.html>, (accessed 30/07/2019).
92. C. L. Cutting, M. Bag and D. Venkataraman, Indoor light recycling: a new home for organic photovoltaics, *J. Mater. Chem. C*, **4**, 10367-10370, 2016.
93. Y. Cui, H. Yao, T. Zhang, L. Hong, B. Gao, K. Xian, J. Qin and J. Hou, 1 cm² Organic Photovoltaic Cells for Indoor Application with over 20% Efficiency, *Adv. Mater.*, **31**, 1904512, 2019.
94. Y. Cui, Y. Wang, J. Bergqvist, H. Yao, Y. Xu, B. Gao, C. Yang, S. Zhang, O. Inganäs, F. Gao and J. Hou, Wide-gap non-fullerene acceptor enabling high-

- performance organic photovoltaic cells for indoor applications, *Nat. Energy*, **4**, 768-775, 2019.
95. D. Chemisana, A. Moreno, M. Polo, C. Aranda, A. Riverola, E. Ortega, C. Lamnatou, A. Domènech, G. Blanco and A. Cot, Performance and stability of semitransparent OPVs for building integration: A benchmarking analysis, *Renew. Energy*, **137**, 177-188, 2019.
96. M. Valimaki, P. Apilo, R. Po, E. Jansson, A. Bernardi, M. Ylikunnari, M. Vilkmann, G. Corso, J. Puustinen, J. Tuominen and J. Hast, R2R-printed inverted OPV modules-towards arbitrary patterned designs, *Nanoscale*, **7**, 9570-9580, 2015.
97. <https://sunew.com.br/en/aplicacoes-da-energia-fotovoltaica/>, (accessed 30/07/2019).
98. <https://www.globalbiotechinsights.com/articles/17751/greenhouses-fitted-with-organic-photovoltaic-film>, (accessed 30/07/2019).
99. <http://www.opvius.com/first-energy-efficient-facade.html>, (accessed 30/07/2019).
100. <https://www.pv-tech.org/news/heliateks-organic-thin-film-technology-used-on-engies-research-center>, (accessed 30/07/2019).
101. S. Berny, N. Blouin, A. Distler, H. J. Egelhaaf, M. Krompiec, A. Lohr, O. R. Lozman, G. E. Morse, L. Nanson, A. Pron, T. Sauermann, N. Seidler, S. Tierney, P. Tiwana, M. Wagner and H. Wilson, Solar Trees: First Large-Scale Demonstration of Fully Solution Coated, Semitransparent, Flexible Organic Photovoltaic Modules, *Adv. Sci.*, **3**, 1500342, 2016.
102. <https://www.heliatek.com/projects/acciona-wind-turbine-spain/>, (accessed 20/01/2020).
103. <https://sunew.com.br/en/cases/natura/>, (accessed 20/01/2020).
104. <https://sunew.com.br/en/cases/shopping-da-bahia/>, (accessed 20/01/2020).
105. <https://www.heliatek.com/projects/biopv-la-rochelle/>, (accessed 20/01/2020).
106. <https://www.heliatek.com/blog/worlds-largest-facade-installed-with-organic-photovoltaics-in-the-port-of-duisburg/>, (accessed 20/01/2020).
107. C. J. M. Emmott, J. A. Röhr, M. Campoy-Quiles, T. Kirchartz, A. Urbina, N. J. Ekins-Daukes and J. Nelson, Organic photovoltaic greenhouses: a unique application for semi-transparent PV?, *Energy Environ. Sci.*, **8**, 1317-1328, 2015.
108. G. Ji, W. Zhao, J. Wei, L. Yan, Y. Han, Q. Luo, S. Yang, J. Hou and C.-Q. Ma, 12.88% efficiency in doctor-blade coated organic solar cells through optimizing the surface morphology of a ZnO cathode buffer layer, *J. Mater. Chem. A*, **7**, 212-220, 2019.
109. W. Zhao, S. Zhang, Y. Zhang, S. Li, X. Liu, C. He, Z. Zheng and J. Hou, Environmentally Friendly Solvent-Processed Organic Solar Cells that are Highly Efficient and Adaptable for the Blade-Coating Method, *Adv. Mater.*, **30**, 2018.

110. L. Zhang, X. Xu, B. Lin, H. Zhao, T. Li, J. Xin, Z. Bi, G. Qiu, S. Guo, K. Zhou, X. Zhan and W. Ma, Achieving Balanced Crystallinity of Donor and Acceptor by Combining Blade-Coating and Ternary Strategies in Organic Solar Cells, *Adv. Mater.*, **30**, 1805041, 2018.
111. F. C. Krebs, Fabrication and processing of polymer solar cells: A review of printing and coating techniques, *Sol. Energy Mater. Sol. Cells*, **93**, 394-412, 2009.
112. W. C. Tsoi, D. T. James, J. S. Kim, P. G. Nicholson, C. E. Murphy, D. D. Bradley, J. Nelson and J. S. Kim, The nature of in-plane skeleton Raman modes of P3HT and their correlation to the degree of molecular order in P3HT:PCBM blend thin films, *J. Am. Chem. Soc.*, **133**, 9834-9843, 2011.
113. A. Perulli, S. Lattante, A. Persano, A. Cola and M. Anni, On the homogeneity of the external quantum efficiency in a free OPV roll-to-roll flexible solar module, *Synth. Met.*, **247**, 248-254, 2019.
114. Y. Galagan, H. Fledderus, H. Gorter, H. H. t Mannelje, S. Shanmugam, R. Mandamparambil, J. Bosman, J.-E. J. M. Rubingh, J.-P. Teunissen, A. Salem, I. G. de Vries, R. Andriessen and W. A. Groen, Roll-to-Roll Slot-Die Coated Organic Photovoltaic (OPV) Modules with High Geometrical Fill Factors, *Energy Technol.*, **3**, 834-842, 2015.
115. P. Kubis, N. Li, T. Stubhan, F. Machui, G. J. Matt, M. M. Voigt and C. J. Brabec, Patterning of organic photovoltaic modules by ultrafast laser, *Prog Photovolt*, **23**, 238-246, 2015.
116. <https://www.rofin.com/en/products/lasers-for-marking/laser-marking-systems/desktop-markers/easymark/>, (accessed 25/07/2019, 2019).
117. M. Wojdyr, Fityk: a general-purpose peak fitting program, *J. Appl. Crystallogr.*, **43**, 1126-1128, 2010.
118. L. A. A. Pettersson, L. S. Roman and O. Inganäs, Modeling photocurrent action spectra of photovoltaic devices based on organic thin films, *J. Appl. Phys.*, **86**, 487-496, 1999.
119. CIE. Commission internationale de l'Eclairage proceedings, 1931.
120. F. X. Blasco Ferragud, Universitat Politècnica de València, 1999.
121. R. A. Janssen and J. Nelson, Factors limiting device efficiency in organic photovoltaics, *Adv. Mater.*, **25**, 1847-1858, 2013.
122. A. Guerrero and G. Garcia-Belmonte, Recent Advances to Understand Morphology Stability of Organic Photovoltaics, *Nanomicro Lett*, **9**, 10, 2017.
123. J. Luke, E. M. Speller, A. Wadsworth, M. F. Wyatt, S. Dimitrov, H. K. H. Lee, Z. Li, W. C. Tsoi, I. McCulloch, D. Bagnis, J. R. Durrant and J. S. Kim, Twist and Degrade—Impact of Molecular Structure on the Photostability of Nonfullerene Acceptors and Their Photovoltaic Blends, *Adv. Energy Mater.*, **9**, 1803755, 2019.

124. Y. Q. Wong, H.-F. Meng, H. Y. Wong, C. S. Tan, C.-Y. Wu, P.-T. Tsai, C.-Y. Chang, S.-F. Horng and H.-W. Zan, Efficient semitransparent organic solar cells with good color perception and good color rendering by blade coating, *Org. Electron.*, **43**, 196-206, 2017.
125. G. Sivakumar, T. Pratyusha, D. Gupta and W. Shen, Doping of Hole Transport Layer PEDOT: PSS with Pentacene for PCDTBT: PCBM Based Organic Solar Cells, *Mater. Today-Proc.*, **4**, 6814-6819, 2017.
126. J. Kong, M. Mohadjer Beromi, M. Mariano, T. Goh, F. Antonio, N. Hazari and A. D. Taylor, Colorful polymer solar cells employing an energy transfer dye molecule, *Nano Energy*, **38**, 36-42, 2017.
127. D. Cui, Z. Yang, D. Yang, X. Ren, Y. Liu, Q. Wei, H. Fan, J. Zeng and S. Liu, Color-Tuned Perovskite Films Prepared for Efficient Solar Cell Applications, *J. Phys. Chem. C*, **120**, 42-47, 2015.
128. G. E. Eperon, S. D. Stranks, C. Menelaou, M. B. Johnston, L. M. Herz and H. J. Snaith, Formamidinium lead trihalide: a broadly tunable perovskite for efficient planar heterojunction solar cells, *Energy Environ. Sci.*, **7**, 982, 2014.
129. B. Suarez, V. Gonzalez-Pedro, T. S. Ripolles, R. S. Sanchez, L. Otero and I. Mora-Sero, Recombination Study of Combined Halides (Cl, Br, I) Perovskite Solar Cells, *J. Phys. Chem. Lett.*, **5**, 1628-1635, 2014.
130. Q. Liu, P. Romero-Gomez, P. Mantilla-Perez, S. Colodrero, J. Toudert and J. Martorell, A Two-Resonance Tapping Cavity for an Optimal Light Trapping in Thin-Film Solar Cells, *Adv. Energy Mater.*, **7**, 1700356, 2017.
131. L. Wen, Q. Chen, F. Sun, S. Song, L. Jin and Y. Yu, Theoretical design of multi-colored semi-transparent organic solar cells with both efficient color filtering and light harvesting, *Sci. Rep.*, **4**, 7036, 2014.
132. M. B. Upama, M. Wright, N. K. Elumalai, M. A. Mahmud, D. Wang, K. H. Chan, C. Xu, F. Haque and A. Uddin, High performance semitransparent organic solar cells with 5% PCE using non-patterned MoO₃/Ag/MoO₃ anode, *Curr. Appl. Phys.*, **17**, 298-305, 2017.
133. G. Xu, L. Shen, C. Cui, S. Wen, R. Xue, W. Chen, H. Chen, J. Zhang, H. Li, Y. Li and Y. Li, High-Performance Colorful Semitransparent Polymer Solar Cells with Ultrathin Hybrid-Metal Electrodes and Fine-Tuned Dielectric Mirrors, *Adv. Funct. Mater.*, **27**, 1605908, 2017.
134. R. Betancur, P. Romero-Gomez, A. Martinez-Otero, X. Elias, M. Maymó and J. Martorell, Transparent polymer solar cells employing a layered light-trapping architecture, *Nat. Photonics*, **7**, 995-1000, 2013.
135. W. Zhang, M. Anaya, G. Lozano, M. E. Calvo, M. B. Johnston, H. Miguez and H. J. Snaith, Highly efficient perovskite solar cells with tunable structural color, *Nano Lett.*, **15**, 1698-1702, 2015.
136. J.-H. Lu, Y.-L. Yu, S.-R. Chuang, C.-H. Yeh and C.-P. Chen, High-Performance, Semitransparent, Easily Tunable Vivid Colorful Perovskite Photovoltaics

- Featuring Ag/ITO/Ag Microcavity Structures, *J. Phys. Chem. C*, **120**, 4233-4239, 2016.
137. Y. Jiang, B. Luo, F. Jiang, F. Jiang, C. Fuentes-Hernandez, T. Liu, L. Mao, S. Xiong, Z. Li, T. Wang, B. Kippelen and Y. Zhou, Efficient Colorful Perovskite Solar Cells Using a Top Polymer Electrode Simultaneously as Spectrally Selective Antireflection Coating, *Nano Lett.*, **16**, 7829-7835, 2016.
138. C. O. Ramirez Quiroz, C. Bronnbauer, I. Levchuk, Y. Hou, C. J. Brabec and K. Forberich, Coloring Semitransparent Perovskite Solar Cells via Dielectric Mirrors, *ACS Nano*, **10**, 5104-5112, 2016.
139. E. S. Arinze, B. Qiu, N. Palmquist, Y. Cheng, Y. Lin, G. Nyirjesy, G. Qian and S. M. Thon, Color-tuned and transparent colloidal quantum dot solar cells via optimized multilayer interference, *Opt. Express*, **25**, A101-A112, 2017.
140. R. Xia, C. J. Brabec, H.-L. Yip and Y. Cao, High-Throughput Optical Screening for Efficient Semitransparent Organic Solar Cells, *Joule*, **3**, 2241-2254, 2019.
141. D. A. G. Bruggeman, Berechnung verschiedener physikalischer Konstanten von heterogenen Substanzen. I. Dielektrizitätskonstanten und Leitfähigkeiten der Mischkörper aus isotropen Substanzen, *Annalen der Physik*, **416**, 636-664, 1935.
142. N. Gasparini, A. Salleo, I. McCulloch and D. Baran, The role of the third component in ternary organic solar cells, *Nat. Rev. Mater.*, 2019.
143. M. S. Vezie, S. Few, I. Meager, G. Pieridou, B. Dorling, R. S. Ashraf, A. R. Goni, H. Bronstein, I. McCulloch, S. C. Hayes, M. Campoy-Quiles and J. Nelson, Exploring the origin of high optical absorption in conjugated polymers, *Nat. Mater.*, **15**, 746-753, 2016.
144. A. M. Leguy, P. Azarhoosh, M. I. Alonso, M. Campoy-Quiles, O. J. Weber, J. Yao, D. Bryant, M. T. Weller, J. Nelson, A. Walsh, M. van Schilfgaarde and P. R. Barnes, Experimental and theoretical optical properties of methylammonium lead halide perovskites, *Nanoscale*, **8**, 6317-6327, 2016.
145. G. Longo, C. Momblona, M.-G. La-Placa, L. Gil-Escrig, M. Sessolo and H. J. Bolink, Fully Vacuum-Processed Wide Band Gap Mixed-Halide Perovskite Solar Cells, *ACS Energy Lett.*, **3**, 214-219, 2017.
146. L. Gil-Escrig, A. Miquel-Sempere, M. Sessolo and H. J. Bolink, Mixed Iodide-Bromide Methylammonium Lead Perovskite-based Diodes for Light Emission and Photovoltaics, *J. Phys. Chem. Lett.*, **6**, 3743-3748, 2015.
147. A. T. Kleinschmidt, S. E. Root and D. J. Lipomi, Poly(3-hexylthiophene) (P3HT): fruit fly or outlier in organic solar cell research?, *J. Mater. Chem. A*, **5**, 11396-11400, 2017.
148. A. Wadsworth, Z. Hamid, M. Bidwell, R. S. Ashraf, J. I. Khan, D. H. Anjum, C. Cendra, J. Yan, E. Rezasoltani, A. A. Y. Guilbert, M. Azzouzi, N. Gasparini, J. H. Bannock, D. Baran, H. Wu, J. C. de Mello, C. J. Brabec, A. Salleo, J. Nelson, F. Laquai and I. McCulloch, Progress in Poly (3-Hexylthiophene) Organic Solar Cells and the Influence of Its Molecular Weight on Device Performance, *Adv. Energy Mater.*, **8**, 1801001, 2018.

149. Solaris Chem Inc, <http://www.solarischem.com/P3HT.html>, (accessed 15/02/2019, 2019).
150. R. Po, A. Bernardi, A. Calabrese, C. Carbonera, G. Corso and A. Pellegrino, From lab to fab: how must the polymer solar cell materials design change? – an industrial perspective, *Energy Environ. Sci.*, **7**, 925, 2014.
151. H. Seyler, J. Subbiah, D. J. Jones, A. B. Holmes and W. W. Wong, Controlled synthesis of poly(3-hexylthiophene) in continuous flow, *Beilstein J. Org. Chem.*, **9**, 1492-1500, 2013.
152. Y. Kim, S. Cook, S. M. Tuladhar, S. A. Choulis, J. Nelson, J. R. Durrant, D. D. C. Bradley, M. Giles, I. McCulloch, C.-S. Ha and M. Ree, A strong regioregularity effect in self-organizing conjugated polymer films and high-efficiency polythiophene:fullerene solar cells, *Nat. Mater.*, **5**, 197-203, 2006.
153. R. Søndergaard, M. Hösel, D. Angmo, T. T. Larsen-Olsen and F. C. Krebs, Roll-to-roll fabrication of polymer solar cells, *Mater. Today*, **15**, 36-49, 2012.
154. S. Holliday, R. S. Ashraf, A. Wadsworth, D. Baran, S. A. Yousaf, C. B. Nielsen, C. H. Tan, S. D. Dimitrov, Z. Shang, N. Gasparini, M. Alamoudi, F. Laquai, C. J. Brabec, A. Salleo, J. R. Durrant and I. McCulloch, High-efficiency and air-stable P3HT-based polymer solar cells with a new non-fullerene acceptor, *Nat. Commun.*, **7**, 11585, 2016.
155. N. Gasparini, M. Salvador, T. Heumueller, M. Richter, A. Classen, S. Shrestha, G. J. Matt, S. Holliday, S. Strohm, H.-J. Egelhaaf, A. Wadsworth, D. Baran, I. McCulloch and C. J. Brabec, Polymer:Nonfullerene Bulk Heterojunction Solar Cells with Exceptionally Low Recombination Rates, *Adv. Energy Mater.*, **7**, 1701561, 2017.
156. R.-Z. Liang, M. Babics, V. Savikhin, W. Zhang, V. M. Le Corre, S. Lopatin, Z. Kan, Y. Firdaus, S. Liu, I. McCulloch, M. F. Toney and P. M. Beaujuge, Carrier Transport and Recombination in Efficient “All-Small-Molecule” Solar Cells with the Nonfullerene Acceptor IDTBR, *Adv. Energy Mater.*, **8**, 1800264, 2018.
157. C.-H. Tan, A. Wadsworth, N. Gasparini, S. Wheeler, S. Holliday, R. S. Ashraf, S. D. Dimitrov, D. Baran, I. McCulloch and J. R. Durrant, Excitation Wavelength Dependent Internal Quantum Efficiencies in a P3HT / Non-Fullerene Acceptor Solar Cell, *J. Phys. Chem. C*, 2018.
158. B. Sanchez-Lengeling, L. M. Roch, J. D. Perea, S. Langner, C. J. Brabec and A. Aspuru-Guzik, A Bayesian Approach to Predict Solubility Parameters, *Adv. Theor. and Sim.*, **2**, 1800069, 2019.
159. D. Baran, R. S. Ashraf, D. A. Hanifi, M. Abdelsamie, N. Gasparini, J. A. Rohr, S. Holliday, A. Wadsworth, S. Lockett, M. Neophytou, C. J. Emmott, J. Nelson, C. J. Brabec, A. Amassian, A. Salleo, T. Kirchartz, J. R. Durrant and I. McCulloch, Reducing the efficiency-stability-cost gap of organic photovoltaics with highly efficient and stable small molecule acceptor ternary solar cells, *Nat. Mater.*, **16**, 363-369, 2017.
160. F. Zhang, Z. Zhuo, J. Zhang, X. Wang, X. Xu, Z. Wang, Y. Xin, J. Wang, J. Wang, W. Tang, Z. Xu and Y. Wang, Influence of PC60BM or PC70BM as

- electron acceptor on the performance of polymer solar cells, *Sol. Energy Mater. Sol. Cells*, **97**, 71-77, 2012.
161. B. Xiao, A. Tang, J. Zhang, A. Mahmood, Z. Wei and E. Zhou, Achievement of High Voc of 1.02 V for P3HT-Based Organic Solar Cell Using a Benzotriazole-Containing Non-Fullerene Acceptor, *Adv. Energy Mater.*, **7**, 1602269, 2017.
 162. B. Xiao, A. Tang, J. Yang, Z. Wei and E. Zhou, P3HT-Based Photovoltaic Cells with a High Voc of 1.22 V by Using a Benzotriazole-Containing Nonfullerene Acceptor End-Capped with Thiazolidine-2,4-dione, *ACS Macro Letters*, **6**, 410-414, 2017.
 163. Y. Qin, M. A. Uddin, Y. Chen, B. Jang, K. Zhao, Z. Zheng, R. Yu, T. J. Shin, H. Y. Woo and J. Hou, Highly Efficient Fullerene-Free Polymer Solar Cells Fabricated with Polythiophene Derivative, *Adv. Mater.*, **28**, 9416-9422, 2016.
 164. J. Yuan, T. Huang, P. Cheng, Y. Zou, H. Zhang, J. L. Yang, S. Y. Chang, Z. Zhang, W. Huang, R. Wang, D. Meng, F. Gao and Y. Yang, Enabling low voltage losses and high photocurrent in fullerene-free organic photovoltaics, *Nat. Commun.*, **10**, 570, 2019.
 165. N. A. Mica, S. A. J. Thomson and I. D. W. Samuel, Electron mobility of non-fullerene acceptors using a time of flight method, *Org. Electron.*, **63**, 415-420, 2018.
 166. S. Strohm, F. Machui, S. Langner, P. Kubis, N. Gasparini, M. Salvador, I. McCulloch, H. J. Egelhaaf and C. J. Brabec, P3HT: non-fullerene acceptor based large area, semi-transparent PV modules with power conversion efficiencies of 5%, processed by industrially scalable methods, *Energy Environ. Sci.*, **11**, 2225-2234, 2018.
 167. B. S. S. Pokuri, J. Sit, O. Wodo, D. Baran, T. Ameri, C. J. Brabec, A. J. Moule and B. Ganapathysubramanian, Nanoscale Morphology of Doctor Bladed versus Spin-Coated Organic Photovoltaic Films, *Adv. Energy Mater.*, **7**, 1701269, 2017.
 168. D. Corzo, K. Almasabi, E. Bihar, S. Macphee, D. Rosas-Villalva, N. Gasparini, S. Inal and D. Baran, Digital Inkjet Printing of High-Efficiency Large-Area Nonfullerene Organic Solar Cells, *Adv. Mater. Technol.*, **4**, 1900040, 2019.
 169. Y. J. Kim, K. H. Park, J. J. Ha, D. S. Chung, Y. H. Kim and C. E. Park, The effect of branched versus linear alkyl side chains on the bulk heterojunction photovoltaic performance of small molecules containing both benzodithiophene and thienopyrroledione, *Phys. Chem. Chem. Phys.*, **16**, 19874-19883, 2014.
 170. M. Azzouzi, J. Yan, T. Kirchartz, K. Liu, J. Wang, H. Wu and J. Nelson, Nonradiative Energy Losses in Bulk-Heterojunction Organic Photovoltaics, *Phys. Rev. X*, **8**, 2018.
 171. C. McDowell, M. Abdelsamie, M. F. Toney and G. C. Bazan, Solvent Additives: Key Morphology-Directing Agents for Solution-Processed Organic Solar Cells, *Adv. Mater.*, **30**, 1707114, 2018.
 172. G. E. B. Archer, A. Saltelli and I. M. Sobol, Sensitivity measures, anova-like Techniques and the use of bootstrap, *J. Stat. Comput. Simul.*, **58**, 99-120, 1997.

173. D. Kekuda, H.-S. Lin, M. Chyi Wu, J.-S. Huang, K.-C. Ho and C.-W. Chu, The effect of solvent induced crystallinity of polymer layer on poly(3-hexylthiophene)/C70 bilayer solar cells, *Sol. Energy Mater. Sol. Cells*, **95**, 419-422, 2011.
174. G.-H. Lim, J.-M. Zhuo, L.-Y. Wong, S.-J. Chua, L.-L. Chua and P. K. H. Ho, A transition solvent strategy to print polymer:fullerene films using halogen-free solvents for solar cell applications, *Org. Electron.*, **15**, 449-460, 2014.
175. S. K. Hau, H.-L. Yip, O. Acton, N. S. Baek, H. Ma and A. K. Y. Jen, Interfacial modification to improve inverted polymer solar cells, *J. Mater. Chem.*, **18**, 5113, 2008.
176. Y. Kim, S. A. Choulis, J. Nelson, D. D. C. Bradley, S. Cook and J. R. Durrant, Device annealing effect in organic solar cells with blends of regioregular poly(3-hexylthiophene) and soluble fullerene, *Appl. Phys. Lett.*, **86**, 063502, 2005.
177. M. Campoy-Quiles, M. I. Alonso, D. D. C. Bradley and L. J. Richter, Advanced Ellipsometric Characterization of Conjugated Polymer Films, *Adv. Funct. Mater.*, **24**, 2116-2134, 2014.
178. C. M. Hansen, University of Copenhagen, 1967.
179. F. Machui and C. J. Brabec, in *In Semiconducting Polymer Composites*, ed. X. Yang, 2013.
180. G. Wang, M. A. Adil, J. Zhang and Z. Wei, Large-Area Organic Solar Cells: Material Requirements, Modular Designs, and Printing Methods, *Adv. Mater.*, 1805089, 2018.
181. E. Voroshazi, B. Verreet, T. Aernouts and P. Heremans, Long-term operational lifetime and degradation analysis of P3HT:PCBM photovoltaic cells, *Sol. Energy Mater. Sol. Cells*, **95**, 1303-1307, 2011.
182. S. Rafique, S. M. Abdullah, K. Sulaiman and M. Iwamoto, Fundamentals of bulk heterojunction organic solar cells: An overview of stability/degradation issues and strategies for improvement, *Renew. Sust. Energ. Rev.*, **84**, 43-53, 2018.
183. J. A. Hauch, P. Schilinsky, S. A. Choulis, R. Childers, M. Biele and C. J. Brabec, Flexible organic P3HT:PCBM bulk-heterojunction modules with more than 1 year outdoor lifetime, *Sol. Energy Mater. Sol. Cells*, **92**, 727-731, 2008.
184. C. H. Peters, I. T. Sachs-Quintana, W. R. Mateker, T. Heumueller, J. Rivnay, R. Noriega, Z. M. Beiley, E. T. Hoke, A. Salleo and M. D. McGehee, The mechanism of burn-in loss in a high efficiency polymer solar cell, *Adv. Mater.*, **24**, 663-668, 2012.
185. N. Grossiord, J. M. Kroon, R. Andriessen and P. W. M. Blom, Degradation mechanisms in organic photovoltaic devices, *Org. Electron.*, **13**, 432-456, 2012.
186. W. R. Mateker and M. D. McGehee, Progress in Understanding Degradation Mechanisms and Improving Stability in Organic Photovoltaics, *Adv. Mater.*, **29**, 2017.

187. R. Rösch, D. M. Tanenbaum, M. Jørgensen, M. Seeland, M. Bärenklau, M. Hermenau, E. Voroshazi, M. T. Lloyd, Y. Galagan, B. Zimmermann, U. Würfel, M. Hösel, H. F. Dam, S. A. Gevorgyan, S. Kudret, W. Maes, L. Lutsen, D. Vanderzande, R. Andriessen, G. Teran-Escobar, M. Lira-Cantu, A. Rivaton, G. Y. Uzunoğlu, D. Germack, B. Andreasen, M. V. Madsen, K. Norrman, H. Hoppe and F. C. Krebs, Investigation of the degradation mechanisms of a variety of organic photovoltaic devices by combination of imaging techniques—the ISOS-3 inter-laboratory collaboration, *Energy Environ. Sci.*, **5**, 6521, 2012.
188. M. Karakawa, K. Suzuki, T. Kuwabara, T. Taima, K. Nagai, M. Nakano, T. Yamaguchi and K. Takahashi, Factors contributing to degradation of organic photovoltaic cells, *Org. Electron.*, 105448, 2019.
189. A. Classen, T. Heumueller, I. Wabra, J. Gerner, Y. He, L. Einsiedler, N. Li, G. J. Matt, A. Osvet, X. Du, A. Hirsch and C. J. Brabec, Revealing Hidden UV Instabilities in Organic Solar Cells by Correlating Device and Material Stability, *Adv. Energy Mater.*, 1902124, 2019.
190. J. Razzell-Hollis, W. C. Tsoi and J.-S. Kim, Directly probing the molecular order of conjugated polymer in OPV blends induced by different film thicknesses, substrates and additives, *J. Mater. Chem. C*, **1**, 6235, 2013.
191. S. van Bavel, E. Sourty, G. de With, K. Frolic and J. Loos, Relation between Photoactive Layer Thickness, 3D Morphology, and Device Performance in P3HT/PCBM Bulk-Heterojunction Solar Cells, *Macromolecules*, **42**, 7396-7403, 2009.
192. <https://riekemetals.com/products-services/compound/2041>, (accessed 20/11/2019).
193. <https://www.sigmaaldrich.com/catalog/product/aldrich/900563?>, (accessed 20/11/2019).
194. F. Padinger, R. S. Rittberger and N. S. Sariciftci, Effects of Postproduction Treatment on Plastic Solar Cells, *Adv. Funct. Mater.*, **13**, 85-88, 2003.
195. M. Prosa, M. Tessarolo, M. Bolognesi, O. Margeat, D. Gedefaw, M. Gaceur, C. Videlot-Ackermann, M. R. Andersson, M. Muccini, M. Seri and J. Ackermann, Enhanced Ultraviolet Stability of Air-Processed Polymer Solar Cells by Al Doping of the ZnO Interlayer, *ACS Appl. Mater. Interfaces*, **8**, 1635-1643, 2016.
196. C. Liao, M. Zhang, X. Xu, F. Liu, Y. Li and Q. Peng, Green solvent-processed efficient non-fullerene organic solar cells enabled by low-bandgap copolymer donors with EDOT side chains, *J. Mater. Chem. A*, **7**, 716-726, 2019.
197. S. Zhang, L. Ye, H. Zhang and J. Hou, Green-solvent-processable organic solar cells, *Mater. Today*, **19**, 533-543, 2016.
198. Z. Ma, B. Zhao, Y. Gong, J. Deng and Z. a. Tan, Green-solvent-processable strategies for achieving large-scale manufacture of organic photovoltaics, *J. Mater. Chem. A*, 2019.
199. M. Sims, D. D. C. Bradley, M. Ariu, M. Koeberg, A. Asimakis, M. Grell and D. G. Lidzey, Understanding the Origin of the 535 nm Emission Band in Oxidized

- Poly(9,9-dioctylfluorene): The Essential Role of Inter-Chain/Inter-Segment Interactions, *Adv. Funct. Mater.*, **14**, 765-781, 2004.
200. P. Apilo, M. Välimäki, R. Po, K.-L. Väisänen, H. Richter, M. Ylikunnari, M. Vilkmann, A. Bernardi, G. Corso, H. Hoppe, R. Roesch, R. Meitzner, U. S. Schubert and J. Hast, Fully Roll-to-Roll Printed P3HT/Indene-C60-Bisadduct Modules with High Open-Circuit Voltage and Efficiency, *Solar RRL*, **2**, 1700160, 2018.
201. B. Hellen da Souza, F. Rodriguez, R. Vilaça and D. Bagnis, 2018.
202. P. Maisch, Lena M. Eisenhofer, K. C. Tam, A. Distler, M. M. Voigt, C. J. Brabec and H.-J. Egelhaaf, A generic surfactant-free approach to overcome wetting limitations and its application to improve inkjet-printed P3HT:non-fullerene acceptor PV, *J. Mater. Chem. A*, **7**, 13215-13224, 2019.
203. P. Mondelli, G. Boschetto, P. Horton, P. Tiwana, C.-K. Skylaris, S. Coles, M. Krompiec and G. E. Morse, Meta-analysis: the molecular organization of non-fullerene acceptors, *Mater. Horiz.*, 2019.
204. P. Cheng, G. Li, X. Zhan and Y. Yang, Next-generation organic photovoltaics based on non-fullerene acceptors, *Nat. Photonics*, **12**, 131-142, 2018.
205. S. Nagasawa, E. Al-Naamani and A. Saeki, Computer-Aided Screening of Conjugated Polymers for Organic Solar Cell: Classification by Random Forest, *J. Phys. Chem. Lett.*, **9**, 2639-2646, 2018.
206. H. Sahu, F. Yang, X. Ye, J. Ma, W. Fang and H. Ma, Designing promising molecules for organic solar cells via machine learning assisted virtual screening, *J. Mater. Chem. A*, **7**, 17480-17488, 2019.
207. F.-C. Chen, Virtual Screening of Conjugated Polymers for Organic Photovoltaic Devices Using Support Vector Machines and Ensemble Learning, *Int. J. Polym. Sci.*, **4538514**, 1-7, 2019.
208. X. Rodríguez-Martínez, A. Sánchez-Díaz, G. Liu, M. A. Niño, J. Cabanillas-Gonzalez and M. Campoy-Quiles, Combinatorial optimization of evaporated bilayer small molecule organic solar cells through orthogonal thickness gradients, *Org. Electron.*, **59**, 288-292, 2018.
209. A. S. Gertsen, M. F. Castro, R. R. Søndergaard and J. W. Andreasen, Scalable fabrication of organic solar cells based on non-fullerene acceptors, *Flex. Print. Electron.*, **5**, 014004, 2020.
210. A. Teichler, S. Holzer, J. Nowotny, F. Kretschmer, C. Bader, J. Perelaer, M. D. Hager, S. Hoepfener and U. S. Schubert, Combinatorial screening of inkjet printed ternary blends for organic photovoltaics: absorption behavior and morphology, *ACS Comb. Sci.*, **15**, 410-418, 2013.
211. A. Teichler, R. Eckardt, S. Hoepfener, C. Friebe, J. Perelaer, A. Senes, M. Morana, C. J. Brabec and U. S. Schubert, Combinatorial Screening of Polymer:Fullerene Blends for Organic Solar Cells by Inkjet Printing, *Adv. Energy Mater.*, **1**, 105-114, 2011.

212. S. Langner, F. Hase, J. D. Perea, T. Stubhan, J. Hauch, L. M. Roch, T. Heumueller, A. Aspuru-Guzik and C. J. Brabec, Beyond Ternary OPV: High-Throughput Experimentation and Self-Driving Laboratories Optimize Multicomponent Systems, *Adv. Mater.*, **32**, 14, 1907801, 2020.
213. J. Alstrup, M. Jorgensen, A. J. Medford and F. C. Krebs, Ultra fast and parsimonious materials screening for polymer solar cells using differentially pumped slot-die coating, *ACS Applied Material & Interfaces*, **2**, 2819-2827, 2010.
214. J.-h. Lee, T. Sagawa and S. Yoshikawa, Fast Screening of the Optimal Polymer Ratio for Organic Solar Cells Using a Spray-Coating Deposition Method for the Fullerene Mixture, *Energy Technol.*, **1**, 85-93, 2013.
215. F. Nickel, C. Sprau, M. F. G. Klein, P. Kapetana, N. Christ, X. Liu, S. Klinkhammer, U. Lemmer and A. Colmann, Spatial mapping of photocurrents in organic solar cells comprising wedge-shaped absorber layers for an efficient material screening, *Sol. Energy Mater. Sol. Cells*, **104**, 18-22, 2012.
216. K. Glaser, P. Beu, D. Bahro, C. Sprau, A. Pütz and A. Colmann, Rapid experimental optimization of organic tandem solar cells: 200 absorber layer thickness combinations on a 4×4 cm² substrate, *J. Mater. Chem. A*, **6**, 9257-9263, 2018.
217. A. Sánchez-Díaz, X. Rodríguez-Martínez, L. Córcoles-Guija, G. Mora-Martín and M. Campoy-Quiles, High-Throughput Multiparametric Screening of Solution Processed Bulk Heterojunction Solar Cells, *Adv. Electron. Mater.*, **4**, 1700477, 2018.
218. A. Harillo-Baños, X. Rodríguez-Martínez and M. Campoy-Quiles, Efficient Exploration of the Composition Space in Ternary Organic Solar Cells by Combining High-Throughput Material Libraries and Hyperspectral Imaging, *Adv. Energy Mater.*, **10**, 1902417, 2019.
219. H. Sahu, W. Rao, A. Troisi and H. Ma, Toward Predicting Efficiency of Organic Solar Cells via Machine Learning and Improved Descriptors, *Adv. Energy Mater.*, **8**, 1801032, 2018.
220. H. Wang, Y. Ji and Y. Li, Simulation and design of energy materials accelerated by machine learning, *Wires. Comput. Mol. Sci.*, **10**, e1421, 2019.
221. R. L. Davis, S. Jayaraman, P. M. Chaikin and R. A. Register, Creating controlled thickness gradients in polymer thin films via flowcoating, *Langmuir*, **30**, 5637-5644, 2014.
222. A. Reale, L. La Notte, L. Salamandra, G. Polino, G. Susanna, T. M. Brown, F. Brunetti and A. Di Carlo, Spray Coating for Polymer Solar Cells: An Up-to-Date Overview, *Energy Technol.*, **3**, 385-406, 2015.
223. X. Meng, L. Zhang, Y. Xie, X. Hu, Z. Xing, Z. Huang, C. Liu, L. Tan, W. Zhou, Y. Sun, W. Ma and Y. Chen, A General Approach for Lab-to-Manufacturing Translation on Flexible Organic Solar Cells, *Adv. Mater.*, **31**, e1903649, 2019.

224. Z. Fei, F. D. Eisner, X. Jiao, M. Azzouzi, J. A. Rohr, Y. Han, M. Shahid, A. S. R. Chesman, C. D. Easton, C. R. McNeill, T. D. Anthopoulos, J. Nelson and M. Heeney, An Alkylated Indacenodithieno[3,2-b]thiophene-Based Nonfullerene Acceptor with High Crystallinity Exhibiting Single Junction Solar Cell Efficiencies Greater than 13% with Low Voltage Losses, *Adv. Mater.*, **30**, 1705209, 2018.
225. H. Sahu and H. Ma, Unraveling Correlations between Molecular Properties and Device Parameters of Organic Solar Cells Using Machine Learning, *J. Phys. Chem. Lett.*, **10**, 7277-7284, 2019.
226. X. Rodríguez-Martínez, M. S. Vezie, X. Shi, I. McCulloch, J. Nelson, A. R. Goñi and M. Campoy-Quiles, Quantifying local thickness and composition in thin films of organic photovoltaic blends by Raman scattering, *J. Mater. Chem. C*, **5**, 7270-7282, 2017.
227. C. Volz, M. Arif and S. Guha, Conformations in dioctyl substituted polyfluorene: a combined theoretical and experimental Raman scattering study, *J. Chem. Phys.*, **126**, 064905, 2007.
228. A. M. Leguy, A. R. Goni, J. M. Frost, J. Skelton, F. Brivio, X. Rodríguez-Martínez, O. J. Weber, A. Pallipurath, M. I. Alonso, M. Campoy-Quiles, M. T. Weller, J. Nelson, A. Walsh and P. R. Barnes, Dynamic disorder, phonon lifetimes, and the assignment of modes to the vibrational spectra of methylammonium lead halide perovskites, *Phys. Chem. Chem. Phys.*, **18**, 27051-27066, 2016.
229. P. Wolfer, P. E. Schwenn, A. K. Pandey, Y. Fang, N. Stingelin, P. L. Burn and P. Meredith, Identifying the optimum composition in organic solar cells comprising non-fullerene electron acceptors, *J. Mater. Chem. A*, **1**, 5989, 2013.
230. C. Müller, T. A. M. Ferenczi, M. Campoy-Quiles, J. M. Frost, D. D. C. Bradley, P. Smith, N. Stingelin-Stutzmann and J. Nelson, Binary Organic Photovoltaic Blends: A Simple Rationale for Optimum Compositions, *Adv. Mater.*, **20**, 3510-3515, 2008.
231. G. H. Gu, J. Noh, I. Kim and Y. Jung, Machine learning for renewable energy materials, *J. Mater. Chem. A*, **7**, 17096-17117, 2019.
232. E. Rezasoltani, A. A. Y. Guilbert, J. Yan, X. Rodríguez-Martínez, M. Azzouzi, F. Eisner, S. M. Tuladhar, A. Wadsworth, Z. Hamid, I. McCulloch, M. Campoy-Quiles and J. Nelson, Correlating the Phase Behavior with the Device Performance in Binary P3HT:NFA Blend Using Optical Probes of Microstructure, *Preprint*, 2020.
233. R. Xue, J. Zhang, Y. Li and Y. Li, Organic Solar Cell Materials toward Commercialization, *Small*, **14**, 1801793, 2018.
234. A. Wadsworth, M. Moser, A. Marks, M. S. Little, N. Gasparini, C. J. Brabec, D. Baran and I. McCulloch, Critical review of the molecular design progress in non-fullerene electron acceptors towards commercially viable organic solar cells, *Chem. Soc. Rev.*, **48**, 1596, 2018.

235. V. V. Brus, J. Lee, B. R. Luginbuhl, S. J. Ko, G. C. Bazan and T. Q. Nguyen, Solution-Processed Semitransparent Organic Photovoltaics: From Molecular Design to Device Performance, *Adv. Mater.*, **31**, 1900904, 2019.
236. J. Halme and P. Mäkinen, Theoretical efficiency limits of ideal coloured opaque photovoltaics, *Energy Environ. Sci.*, **12**, 1274-1285, 2019.
237. J. L. Caivano, Research on color in architecture and environmental design: Brief history, current developments, and possible future, *Color Res Appl*, **31**, 350-363, 2006.
238. K. Forberich, F. Guo, C. Bronnbauer and C. J. Brabec, Efficiency Limits and Color of Semitransparent Organic Solar Cells for Application in Building-Integrated Photovoltaics, *Energy Technol.*, **3**, 1051-1058, 2015.
239. Q. Xue, R. Xia, C. J. Brabec and H.-L. Yip, Recent advances in semi-transparent polymer and perovskite solar cells for power generating window applications, *Energy Environ. Sci.*, **11**, 1688-1709, 2018.
240. K.-S. Chen, J.-F. Salinas, H.-L. Yip, L. Huo, J. Hou and A. K. Y. Jen, Semi-transparent polymer solar cells with 6% PCE, 25% average visible transmittance and a color rendering index close to 100 for power generating window applications, *Energy Environ. Sci.*, **5**, 9551, 2012.
241. M. B. Upama, M. Wright, N. K. Elumalai, M. A. Mahmud, D. Wang, C. Xu and A. Uddin, High-Efficiency Semitransparent Organic Solar Cells with Non-Fullerene Acceptor for Window Application, *ACS Photonics*, **4**, 2327-2334, 2017.
242. K. Liu, T. T. Larsen-Olsen, Y. Lin, M. Beliatis, E. Bundgaard, M. Jørgensen, F. C. Krebs and X. Zhan, Roll-coating fabrication of flexible organic solar cells: comparison of fullerene and fullerene-free systems, *J. Mater. Chem. A*, **4**, 1044-1051, 2016.
243. H. Lu, J. Lin, N. Wu, S. Nie, Q. Luo, C.-Q. Ma and Z. Cui, Inkjet printed silver nanowire network as top electrode for semi-transparent organic photovoltaic devices, *Appl. Phys. Lett.*, **106**, 093302, 2015.
244. C. J. Traverse, R. Pandey, M. C. Barr and R. R. Lunt, Emergence of highly transparent photovoltaics for distributed applications, *Nat. Energy*, **2**, 849-860, 2017.
245. Y. Xie, R. Xia, T. Li, L. Ye, X. Zhan, H. L. Yip and Y. Sun, Highly Transparent Organic Solar Cells with All-Near-Infrared Photoactive Materials, *Small Methods*, **3**, 1900424, 2019.
246. G. Sun, M. Shahid, Z. Fei, S. Xu, F. D. Eisner, T. D. Anthopolous, M. A. McLachlan and M. Heaney, Highly-efficient semi-transparent organic solar cells utilising non-fullerene acceptors with optimised multilayer MoO₃/Ag/MoO₃ electrodes, *Mater. Chem. Front.*, **3**, 450-455, 2019.
247. W. Wang, C. Yan, T. K. Lau, J. Wang, K. Liu, Y. Fan, X. Lu and X. Zhan, Fused Hexacyclic Nonfullerene Acceptor with Strong Near-Infrared Absorption for

- Semitransparent Organic Solar Cells with 9.77% Efficiency, *Adv. Mater.*, **29**, 2017.
248. P. Maisch, K. C. Tam, P. Schilinsky, H.-J. Egelhaaf and C. J. Brabec, Shy Organic Photovoltaics: Digitally Printed Organic Solar Modules With Hidden Interconnects, *Solar RRL*, **2**, 1800005, 2018.
249. P. Maisch, K. C. Tam, L. Lucera, H.-J. Egelhaaf, H. Scheiber, E. Maier and C. J. Brabec, Inkjet printed silver nanowire percolation networks as electrodes for highly efficient semitransparent organic solar cells, *Org. Electron.*, **38**, 139-143, 2016.
250. F. Guo, X. Zhu, K. Forberich, J. Krantz, T. Stubhan, M. Salinas, M. Halik, S. Spallek, B. Butz, E. Spiecker, T. Ameri, N. Li, P. Kubis, D. M. Guldi, G. J. Matt and C. J. Brabec, ITO-Free and Fully Solution-Processed Semitransparent Organic Solar Cells with High Fill Factors, *Adv. Energy Mater.*, **3**, 1062-1067, 2013.
251. Y. Wang, B. Jia, F. Qin, Y. Wu, W. Meng, S. Dai, Y. Zhou and X. Zhan, Semitransparent, non-fullerene and flexible all-plastic solar cells, *Polymer*, **107**, 108-112, 2016.
252. F. Guo, P. Kubis, T. Przybilla, E. Spiecker, A. Hollmann, S. Langner, K. Forberich and C. J. Brabec, Nanowire Interconnects for Printed Large-Area Semitransparent Organic Photovoltaic Modules, *Adv. Energy Mater.*, **5**, 1401779, 2015.
253. C. C. Chen, L. Dou, R. Zhu, C. H. Chung, T. B. Song, Y. B. Zheng, S. Hawks, G. Li, P. S. Weiss and Y. Yang, Visibly transparent polymer solar cells produced by solution processing, *ACS Nano*, **6**, 7185-7190, 2012.
254. L. Lucera, F. Machui, H. D. Schmidt, T. Ahmad, P. Kubis, S. Strohm, J. Hepp, A. Vetter, H. J. Egelhaaf and C. J. Brabec, Printed semi-transparent large area organic photovoltaic modules with power conversion efficiencies of close to 5 %, *Org. Electron.*, **45**, 209-214, 2017.
255. J. E. Carlé, M. Helgesen, O. Hagemann, M. Hösel, I. M. Heckler, E. Bundgaard, S. A. Gevorgyan, R. R. Søndergaard, M. Jørgensen, R. García-Valverde, S. Chaouki-Almagro, J. A. Villarejo and F. C. Krebs, Overcoming the Scaling Lag for Polymer Solar Cells, *Joule*, **1**, 274-289, 2017.
256. L. Lucera, P. Kubis, F. W. Fecher, C. Bronnbauer, M. Turbiez, K. Forberich, T. Ameri, H.-J. Egelhaaf and C. J. Brabec, Guidelines for Closing the Efficiency Gap between Hero Solar Cells and Roll-To-Roll Printed Modules, *Energy Technol.*, **3**, 373-384, 2015.
257. P. Kubis, L. Lucera, F. Machui, G. Spyropoulos, J. Cordero, A. Frey, J. Kaschta, M. M. Voigt, G. J. Matt, E. Zeira and C. J. Brabec, High precision processing of flexible P3HT/PCBM modules with geometric fill factor over 95%, *Org. Electron.*, **15**, 2256-2263, 2014.
258. L. Lucera, F. Machui, P. Kubis, H. D. Schmidt, J. Adams, S. Strohm, T. Ahmad, K. Forberich, H. J. Egelhaaf and C. J. Brabec, Highly efficient, large area, roll coated flexible and rigid OPV modules with geometric fill factors up to 98.5%

- processed with commercially available materials, *Energy Environ. Sci.*, **9**, 89-94, 2016.
259. I. Jeon, R. Sakai, S. Seo, G. E. Morse, H. Ueno, T. Nakagawa, Y. Qian, S. Maruyama and Y. Matsuo, Engineering high-performance and air-stable PBTZT-stat-BDIT-8:PC61BM/PC71BM organic solar cells, *J. Mater. Chem. A*, **6**, 5746-5751, 2018.
260. S. Dai and X. Zhan, Nonfullerene Acceptors for Semitransparent Organic Solar Cells, *Adv. Energy Mater.*, **8**, 1800002, 2018.
261. J. Yuan, Y. Zhang, L. Zhou, G. Zhang, H.-L. Yip, T.-K. Lau, X. Lu, C. Zhu, H. Peng, P. A. Johnson, M. Leclerc, Y. Cao, J. Ulanski, Y. Li and Y. Zou, Single-Junction Organic Solar Cell with over 15% Efficiency Using Fused-Ring Acceptor with Electron-Deficient Core, *Joule*, **3**, 4, 1140-1151, 2019.
262. N. Bauer, Q. Zhang, J. Zhao, L. Ye, J.-H. Kim, I. Constantinou, L. Yan, F. So, H. Ade, H. Yan and W. You, Comparing non-fullerene acceptors with fullerene in polymer solar cells: a case study with FTAZ and PyCNTAZ, *J. Mater. Chem. A*, **5**, 4886-4893, 2017.
263. Y. Xia and J. Ouyang, Significant different conductivities of the two grades of poly(3,4-ethylenedioxythiophene):poly(styrenesulfonate), Clevios P and Clevios PH1000, arising from different molecular weights, *ACS Appl. Mater. Interfaces*, **4**, 4131-4140, 2012.
264. M. Koppitz, N. Hesse, D. Landerer, L. Graf von Reventlow, E. Wegner, J. Czolk and A. Colmann, Organic Solar Modules: Fully Doctor Bladed on Glass in Air, *Energy Technol.*, **5**, 1105-1111, 2017.
265. R. Abbel, I. de Vries, A. Langen, G. Kirchner, H. t'Mannetje, H. Gorter, J. Wilson and P. Groen, Toward high volume solution based roll-to-roll processing of OLEDs, *J. Mater. Res.*, **32**, 2219-2229, 2017.
266. P. Kubis, J. Winter, A. Gavrilova, M. Hennel, S. Schlosser, I. Richter, A. Distler, M. Heyder, S. Kery, P. Lenk, S. Geiger, C. J. Brabec, H. P. Huber and H.-J. Egelhaaf, All sub-nanosecond laser monolithic interconnection of OPV modules, *Prog Photovolt*, **27**, 479-490, 2019.